EXPERIMENTAL AND NUMERICAL INVESTIGATIONS OF IMPACT SPLITTING OF NATURALLY BEDDED LAYERED SLATE ROCK

MD. RABIUL ALAM

Experimental and Numerical Investigations of Impact Splitting of Naturally Bedded Layered Slate Rock

by

© Md. Rabiul Alam, B.Sc.Eng., M.Eng.

A thesis submitted to the School of Graduate
Studies in partial fulfillment of the
requirements for the degree of
Doctor of Philosophy

Faculty of Engineering and Applied Science
Memorial University of Newfoundland
August, 2005

St. John's Newfoundland Canada

Your file Votre référence
ISBN: 978-0-494-15657-5
Our file Notre référence
ISBN: 978-0-494-15657-5

Acknowledgements

I am grateful to my supervisor, Dr. A. S. J. Swamidas and sincerely appreciate his continuous guidance, helpful suggestions, sympathetic cooperation and expert counsel at all stages of the development of this thesis. I am also thankful to him for helping me financially during my Ph.D. days though I didn't receive any financial support from the School of Graduate Studies.

I would like to thank Dr. K. Munaswamy, my thesis co-supervisor, for his continuous financial support, valuable suggestions and constructive criticism at various stages of my thesis development. Also heartfelt thanks to Dr. John Gale who gave me an opportunity to use the equipment in his laboratory and as well assisted me in providing a geological orientation for my thesis investigations.

Thanks are also due to Dr. M. R. Haddara, former Associate Dean, Faculty of Engineering and Applied Science, who facilitated my admission to the Ph.D. program soon after my M. Eng. degree, and as well helped me in many ways.

I am also deeply grateful to all teachers who taught theory courses (Drs. S. Adluri, G. Sabin, and others acknowledged earlier) during my graduate days.

Special thanks are due to Mr. Austin Bursey for his assistance in setting up experiments in the strength laboratory of the faculty.

I would also like to thank Carew Services, Portugal Cove, St. John's, and Hurleys Slateworks Company, Manuels, St. John's, NL, Canada for their generous and often free supply of slate material for my thesis experiments.

Finally, my sincere appreciation to my uncle Mr. A. K. M. Fazlul Hoque and my parents, for their continuous encouragement and valuable advice during my long period of stay in Canada.

Abstract

In this thesis investigation, experimental and numerical studies were carried out to determine the axial impact splitting loads and the splitting process of naturally bedded layered slate rocks. This effort was undertaken to examine an alternate slate mining procedure so that the wastage in slate can be reduced from the present-day 95%. This was the first effort made in the use of this procedure for slate excavation.

Experimental impact forces were determined by carrying out splitting tests on different sizes of slate blocks from small to intermediate scales, using a hydraulic actuator with a wedge-shaped indenter in the laboratory. Generally the slate blocks split parallel to their natural bedding planes, exhibiting clean and even split faces. Thus the use of this procedure for slate mining will minimize the damage produced by the use of optimum explosives; this reduction in wastage has been approximately estimated to be nearly 20% to 25% less than the present-day 95%. It has been observed in some cases that breaking loads were not consistent with the sizes of blocks (probably due to the presence of pre-existing flaws within the block). Some of the larger blocks needed lesser loads to break than those found for relatively smaller blocks.

Numerical analyses were carried out to predict the impact splitting loads required to split a finite sized layered slate rock based on the observed mechanism of plane crack propagation in plane strain and three-dimensional slate blocks, obtained from impact splitting of slate blocks in the laboratory. In order to characterize the material for numerical analysis, properties of the slate material, such as elastic moduli, Poisson's ratio, compressive and tensile strengths, coefficient of friction (between slate and steel),

plane strain fracture toughness, hardness, crack propagation velocity etc., were determined after carrying out extensive experimental investigations. The experimental values obtained in this study were generally within the ranges specified for slates of other origins. It must also be mentioned here that the results presented in this thesis on the physical and mechanical properties of slate are the first study carried out on slates of Newfoundland origin.

ABAQUS finite element software was used to simulate the entire wedge impact splitting process during numerical analysis. Mode I (plane strain opening mode) dynamic crack propagation was simulated numerically by the sequential releasing of the restraining node on the symmetric plane of the analyzed specimen. Mode I stress intensity factors (K_I) were determined for different crack lengths and two types of crack propagation velocities. It was found that the crack propagation velocities had little (less than 10%) or almost no effect on the variation of the mode I stress intensity factors (SIFs). The possibility of crack propagation was determined by comparing K_I with the plane strain fracture toughness (K_{IC}). For a chosen slate block, the mode I stress intensity factor was obtained to be almost the same as its fracture toughness, when the experimental impact splitting load was applied on it. Also in a three-dimensional splitting scenario, a parabolic crack front was required to model an equal fracture toughness (or stress intensity factor) value all along the crack front.

Numerical results on the effect of size of the specimen (width and depth) on the mode I stress intensity factor were also examined and a correlation equation was established between the mode I stress intensity factor, splitting force and plane strain geometry of the

slate block. Breaking loads calculated using the correlation equation for plane strain fracture toughness were compared with those obtained from experimental work. The differences between the numerical and experimental impact forces were found to vary between + 0.78 to – 32.34%. A field problem, considering the separation of a large sized slate slab from its intact state, was also analyzed numerically. The breaking load obtained from this study was compared with those obtained from the developed correlation equation. A good agreement (difference was less than 15%) was obtained between them. A discussion is also given concerning the possible reduction of wastage by the use of this process as a slate mining procedure.

Contents

List of Tables

List of Figures

List of Symbols

a	Crack depth
AEM	Analytical Electron Microscopy
ASTM	American Society for Testing and Material
B	Distance from released node to crack tip
c	Half length of crack
c_0	Initial half crack length
C_{ijkl}	Elastic constants
G_{eff}	Effective shear modulus of elasticity
d	Depth of the specimen
D	Constitutive matrix
d.o.f	Degrees of freedom
E	Young's modulus of elasticity
E_{eff}	Effective Young's modulus of elasticity
F	Force having large magnitude; also denotes gauge factor
F_0	Reaction force
$\overline{F}$	Impulse
FEM	Finite element method
G	Strain energy release rate
G_{IC}	Critical strain energy rate
ISRM	International Society for Rock Mechanics
$[J]$	Jacobian Matrix

k	Stiffness of the body
K^e, $[k]$	Element stiffness matrix
[K]	Stiffness matrix
K	Stress Intensity Factor
K_I	Mode I stress intensity factor
K_{Id}	Mode I dynamic stress intensity factor
K_{II}	Mode II stress intensity factor
K_{III}	Mode III stress intensity factor
K_{IC}	Plane strain fracture toughness
LEFM	Linear elastic fracture mechanics
m	Mass
MK	Malluck and King
N	Shape function
NEFM	Nonlinear Elastic Fracture Mechanics
P(t)	Time dependent impact splitting force
RFN	Rydholm, Fredriksson, and Nilsson
r	Radius of curvature
SEM	Scanning Electron Microscope
SIF	Stress Intensity Factor
STEM	Scanning Transmission Electron Microscope
t	Thickness of the body
T	Tension vector/time period
TEM	Transmission Electron Microscopy

u, v, w	Displacement in global x, y, z directions
u_i, v_i, w_i	Displacement in global x, y, z directions at node I
U	Strain energy
v	Crack velocity
v_1, v_2	Velocities
v_T	Terminal fracture velocity
v_L	Velocity of longitudinal wave propagation
W_k	Kinetic energy
Δ	Distance between nodes
ε_x, ε_y & ε_z	Normal stains in local x, y and z directions
ε_{kl}	Strain tensors
γ_s	Surface tension
γ_{xy}, γ_{yz} & γ_{zx}	Shear strains
ν	Poisson's ratio
σ	Average tensile stress
σ_1, σ_2 and σ_3	Principal stresses
σ_u	Ultimate tensile strength
σ_m	Maximum tensile stress
σ_{in}	Value of σ when crack propagation initiates
σ_{ij}	Stress tensors
ω	Natural Frequency
ζ, η, z'	Natural coordinate set

Chapter 1

Introduction

1.1 General

The experimental and numerical studies of destructive phenomena of impact events such as tools drop, flying debris/bird impact on the envelope of aircraft, car crashes, mortar bullets/missiles propelled onto the structural envelope, etc., have been carried out by a number of researchers. However, the beneficial use of this impact event (force) in engineering applications has not been given much consideration yet. There are many areas in which the impact event is used to generate beneficial effects. When it is necessary to quarry a sedimentary/metamorphic rock (sandstone, mudstone, slate, schist, etc.), and to break them into smaller sizes for the purpose of building construction (load bearing wall, slate roof, paving, etc.) or to construct an underground tunnel in rocky region by cutting or breaking rocks, the use of impact force becomes very important. Some laboratory tests that determine mode I dynamic fracture toughness of layered composite materials in laboratory, also use axial impact forces. Very few investigations

have been carried out in this field. Sun and Han (2001) determined mode I dynamic fracture toughness of composites using a Kolsky bar. They applied wedge insertion fracture (WIF) method to carry out the dynamic test using a Kolsky bar apparatus. A laboratory study on pellet impact and water jet erosion technique to break rock for making a tunnel through hard rock was discussed by Singh (1970).

Two distinct types of engineering problems have been observed while dealing with rocks in nature. One deals with the prevention of failure of rock mass to protect structures made in the rocky regions such as caverns, underground tunnels, etc. The other type of problem tries to take advantage of fracturing using hydraulic fracturing and rock fragmentation by cutting or splitting or blasting. The latter deals with mining, drilling and excavating of rocks. To quarry layered rocks such as slate, schist, sandstone, coal, etc., from a mine, blasting procedures using detonating materials have been generally used for a long time. In addition to blasting which destroys a major portion of the virgin rock, other mechanical procedures are also recently being used to get an efficient and economic form of excavation. Mechanical procedures in rock extraction are advantageous over blasting enhancing the continuity of operations, clean-cut excavation profile, safety and minimum wastage. Some studies based on experimental and theoretical observations have been carried out in the last few decades on the rock breaking using mechanical procedures. Whittaker and Szwilski (1973) examined the principle of rock cutting by impact action. They discussed theoretical aspects of cutting with particular reference to the tensile splitting theory. They have given the use of an experimental rig of the pendulum type designed to break different types of rocks. They have also focussed their attention on impact ripping to cut rock. They mentioned that the relationship between explosive

energy and rock strength is important to design impact ripping machines together with their cutting tools. They reported that their impact cutting experiments gave close agreement with the tensile breakage theory of Evans (1962). Nishimatsu (1972) developed a theory on the mechanics of rock cutting based on the observation of the process of rock cutting and some simplifying assumptions. He has proposed a formula for determining the breaking force of rocks, based on Mohr's failure criterion, the depth of cut and the geometry of cutting tool. He used an inclined cutting tool (width of the cutting edge was much greater than the depth of cut) for rock breaking at a cutting speed of about 0.4 m/min.

During the excavation of rock from the ground or extraction of rock from a quarry applying mechanical procedures, it is seen that special machinery is needed to cut it. Throughout the past various quarrying techniques and equipments have been developed continuously and improved allowing quarriers to increase their net profits by increasing the amount of stone that can be quarried without much wastage. Some industries have developed new technologies that have revolutionized these industries. They use diamond wire machines, Chain saw (CH60), Diesel workhorse TDD 100, single multiple wire machine, polywire machine, GU50 Chainsaw machine and so on. All of these machines are simple mechanically and have relatively lower cost, high reliability, easy maintenance, high cutting speeds and sophisticated controls systems. Some of these machines such as Diesel workhorse TDD 100 can cut anything of any size, and derrick cranes, used to cut 50-ton rough blocks in some countries, are built with booms up to 70 meters long. A single multiple wire machine can be set not only in processing areas, but also in the quarry, even outdoors. This machine can cut to a smaller slab any type of stone

block. Polywire can cut rock to any desired block shape without much production loss. Some of these machines have a full set of safety, surveillance and messaging systems, to ensure easy operation and diagnostics. The Model GU50 Chainsaw Machine is designed to save time in shifting of the machine as it moves on tracks. The cutting arm is capable of making both horizontal and vertical cuts in different planes, as well as "back cut" cuttings. This machine is adaptable to the narrow rooms of underground quarries and can be custom-built to fit these dimensions. It can make dry cuts in many types of stone, except granite (www.stoneworld.com, 2003).

Reduction of slate rock to smaller-sized tiles in quarries is basically a process of rock fragmentation. Initially large sized slate blocks are obtained in quarries through the dynamiting of rock masses. Thereafter, it is broken into smaller sizes using either saw cut or other breaking methods. A recent (United Kingdom Production of Minerals, 2004) publication puts the ratio of usable to unusable slate during the use of presently available quarrying methods as 1:20 (approximately 95%).

As a result of these improvements made in quarrying technology and the contributions of many quarrying equipment manufacturers, the stone industry has advanced significantly within the last few years. Consequently, the slate manufacturing industries are also trying to supply low cost building materials by minimizing the quarrying and processing costs. Although a lot of sophisticated quarrying and processing technologies have been developed and used to advantage in slate manufacturing industries, new methods are constantly being made available to help quarries streamline their businesses and increase their profits. In this regard, dynamic impact load based quarrying and processing method

is still not being used. This method could also be applied to quarry and break naturally bedded layered materials. In this method dynamic (impact) load is used in a systematic manner to quarry and process building rock materials such as slate. The present study has been focused on the development of a breaking method of layered slate rock based on experimental and numerical studies of impact splitting of slate material to produce slate tiles/products more efficiently without much wastage. The events associated with rock failure under impact splitting are the crushing of material at the beginning of impacting procedure and the propagation of plane crack through the rock, parallel to the layer. Since impact is a fast dynamic event, there should be sufficient time to propagate the crack to the required depth though the time required to initiate crack is short. Crack propagation is the dominant event for impact splitting of slate rock. Therefore, much attention needs to be given for the experimental analysis and the numerical simulation of dynamic crack propagation in the slate block.

1.2 Objectives of the Present Study

The objectives of the present study were to determine the breaking loads of different sizes of slate blocks experimentally and numerically from the mechanism of impact splitting of slate rocks with the intention of developing a useful mathematical model for computing the breaking loads for plane strain condition. Such a model could be used to explain the effects of size on the splitting forces of laboratory specimens and be helpful in interpreting large scale field problems utilizing impact rock breaking. The study carried out for this research consisted of two parts. In the first part, experimental investigations of different physical and mechanical properties of slate rock, crack propagation velocities and impact splitting forces of different sizes of slate blocks were carried out. The material

used in these tests was the natural slate obtained from Carew Services, Portugal Cove, St. John's and Hurleys Slateworks Company (free samples supplied), Manuels, St. John's, NL, Canada.

The second part of the study consisted of analyzing impact splitting of slate blocks numerically using ABAQUS finite element software. Stress intensity factors for each time dependent crack extension and geometry of slate block were determined corresponding to splitting force determined experimentally and compared with the experimentally determined plane strain material fracture toughness. This was carried out for both small-scale and large-scale cleaving of naturally bedded slates. Based on the results obtained from numerical analysis for plane strain problems a correlation between impact force required to split any finite sized slate block, mode I stress intensity factor and the geometry of the block has been developed.

1.3 Organization of the Thesis

The following outline provides a brief description of the contents of the thesis:

Chapter 2 covers the literature survey based on general studies on impact event, introduction to slate rock and its existing quarrying and processing techniques, and failure theories for brittle materials. Fracture mechanics based crack analysis including crack initiation and propagation phenomena is also presented in this chapter; in addition, it also covers the literature survey on the static and dynamics stress intensity factors, and their experimental measurement techniques.

Chapter 3 deals with the finite element theory concerning the use of eight-noded isoparametric plane strain elements and eight-noded isoparametric brick elements, used to model the slate blocks. It also covers the theory relating to effective elastic moduli and the sequential node release technique used in the numerical analysis.

Chapter 4 deals with the experimental procedures used to measure different physical and mechanical properties and the breaking loads used to split different sizes of slate blocks. Microscopic observations of slate material using Scanning Electron Microscope are also provided in addition to other detailed experimental procedures. It also discusses crack propagation velocity and the experimental procedure used to determine it.

The numerical investigation of impact splitting process of different sized plane strain slate blocks using finite element method is given in Chapter 5.

The finite element analysis of 3D slate blocks, whose sizes are greater than the plane strain slate blocks, is given in Chapter 6.

Chapter 7 presents the correlation study between the mode I stress intensity factor, the geometry of the slate block and the impact splitting load.

Analytical treatment of impact splitting of a slate rock in the field is detailed in Chapter 8.

Conclusions drawn from this thesis investigation, contributions made in the thesis, as well as areas for further research, are discussed in Chapter 9.

Chapter 2

Literature Review on the Impact Splitting of Layered Slate Rock

2.1 General Studies on Impact Events

Impact is a short duration phenomenon. It occurs so quickly that it is often difficult to follow what is happening and the evidence it leaves behind. It could destroy any structure within a very short time and create a significant damage to human life. Over the last fifty years, significant developments in sensitive instrumentation and computational capabilities have made it possible to examine the impact phenomenon in greater detail; hence considerable amount of attention is being paid recently to the impact response of structures.

Generally studies on impact events are carried out based on their destructive and beneficial effects on structures. The essential characteristics and the various areas of research explored by the past researchers on these effects are discussed briefly in this section.

Impact events are classified as low velocity and high velocity impact events. In case of low velocity impact, a large object barges onto the structure with a low velocity. Usually the tool-drop problems are considered to belong to this category. Low velocity impact causes small deformation in the body and occurs solely over a small region adjacent to the contact area. When this impact acts on a layered composite structure, damage is initiated by matrix cracks which create delaminations at the interfaces between plies. Due to high contact stresses matrix cracks start on the impact face of the specimen in a stiff structure. Damage propagates downward as a pine tree pattern, as shown in Figure 2.1(a), by a succession of inter-ply cracks and interface delaminations. However, matrix cracking in the lowest ply of the thin specimen that is caused by bending stresses in a flexible structure, progresses from the nonimpact face up towards the impact area by giving a reverse pine tree appearance [see Figure 2.1(b)]. Since a large number of matrix cracks and delaminations are developed in the impact zone and redistribution of stresses occurs due to the introduction of each new crack, it is not rational to attempt to model every detail of damage development during the dynamic analysis of the impact event.

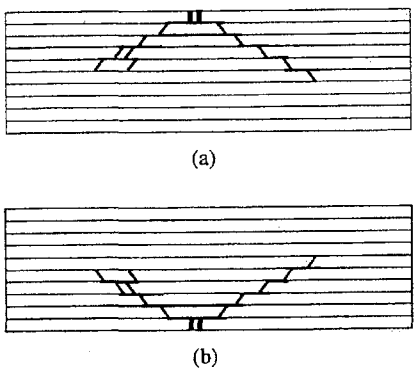

Figure 2.1: Low velocity impact generating: (a) Pine tree pattern due to high contact stresses on a very stiff structure; and (b) Reverse pine tree damage pattern due to large bending stresses (Abrate, 1998) in a flexible structure.

The impacts that result in complete perforation of the target are referred to as high velocity impacts. In this case complete perforation is achieved when the deformations of the target are localized in a small region near the point of impact. Therefore, high velocity impacts are stated to occur when the ratio between impact velocity and the velocity of compressive waves propagating through the thickness is larger than the maximum strain to failure in that direction (Abrate, 1998). This means that the overall damage is introduced during the travel time of the first few compressive waves through the thickness when overall target motion is not yet well-known. The local deformations that occur due to impact depend on the incident relative velocity at the point of initial contact as well as on the hardness of the colliding bodies. In case of high velocity impact, large local deformations are developed near the contact area, which result from plastic flow. If the target is made of nonyielding material then the impacting object could be crushed or liquefied laterally along the face of target or remain coherent depending on the impact velocities. Therefore, there is a critical impact velocity below which the impacting object such as a rigid-plastic missile would remain coherent and intact; above this velocity it is crushed into very small pieces or powder.

The most important step in impact analysis is the evaluation of the contact force generated during impact. If the impact velocity is too high and mass of the impactor is small then there is a possibility to develop local nonlinearities. In this case a local nonlinear contact law must be enunciated while carrying out the analysis of the impact problem. However, this problem is not easy to solve using simple mathematical procedures of differential/integral equations. Numerical methods are often required. Sun and Jih (1995) investigated the quasi-static characteristics of impact response and impact-

induced delamination crack propagation in graphite/epoxy laminates subjected to low-velocity heavy mass impact. They used a single degree of freedom spring mass model to predict the contact force history. Thereafter, they applied the peak contact force in conjunction with a linear beam model to calculate the strain-energy release rate. They obtained the delamination size when the strain-energy release rate reached interlaminar fracture toughness value. They obtained very good agreement between theoretically predicted delamination size and those from experimental results. In the spring-mass model they represented the impactor and the beam by two rigid masses and the associated deformation characteristic by a spring. They considered spring stiffness to be equal to the static stiffness of the given layered beam under a load applied at the mid-span.

Generation of waves is an important phenomenon that is very closely associated with the applied impact forces. Waves are dynamic disturbances that propagate in a medium which may be air, water or solid. Waves in solids are invisible to human eyes and inaudible to human ear. However, waves in solids are real, physical, and very important to engineering applications. To analyze and simulate the phenomena of waves in solids, mathematical and numerical concepts are required. In contrast to vibration, which is a motion of waves with very long wavelengths, the wave generation and propagation phenomena is primarily due to localized disturbance of the structure. Waves are produced due to the generation and propagation of a localized mechanical disturbance whereas vibration is the global motion of the entire structure. However, the mathematical derivations of both vibration and wave motion are governed by the same dynamic equations of motion. Waves in an anisotropic material exhibit anisotropic characteristics. This means that their properties (such as velocity) are direction-dependent (Liu and Xi,

2002). Boundary conditions and interface characteristics of solids (such as laminates) are important factors that affect the wave propagation in a structure. Their presence causes waves to reflect and/or refract; they may also diffract depending on the nature of homogeneity within the medium. Velocities of generated waves depend on the frequencies of local excitation and the shapes of the propagated wave changes continually during the propagation process. The complexity of the structural geometric domain and the material inhomogeneity within the domain influence the wave propagation phenomenon.

When a structural component is subjected to impact or shock loading, transient stress waves are generated at the impact location, and the propagation of these waves can generate very high stresses especially in the local regions surrounding mechanical defects or cracks. Nemat-Nasser (1972) developed general variational methods for wave generation and propagation in elastic composites. Moon (1973) has given an analytical computational technique for the generation and propagation of one-dimensional transient waves in anisotropic plates. He calculated the stresses and displacements that were induced in anisotropic plates by short-duration line impact forces. Kassir and Bandyopadhyay (1983) discussed the impact response of a cracked orthotropic medium. They determined the elastodynamic responses of an orthotropic solid containing a crack under the action of impact loading. Their aim was to determine the distribution of stresses and displacements throughout the solid by focusing particular attention on the influence of material orthotropy on the amplification of the dynamic stress-intensity factor and the elapsed time required to attain the peak value. They found that the dynamic overshoot in stresses for orthotropic materials was smaller for the shearing mode and occurred at a

shorter time than the case for the normal loading. Sansalone, et. al. (1987) carried out finite element studies of transient wave propagation. They showed the versatility and usefulness of the finite element method for solving stress wave propagation problems.

Beneficial effects of impact force are seen in excavating/quarrying rocks (sandstone, marble, slate, etc.), driving pile into the ground, breaking stones and bricks for aggregates or constructing underground tunnel in rocky region, mode I fracture toughness test of any material in the laboratory, etc. Some studies on these fields are detailed in the investigations of Whittaker and Frith (1990) for rock fragmentation, experimental determination of mode I stress intensity factor of layered composite materials by Sun and Han (2001), and rock breaking using pellet impact by Singh (1970).

2.2 Mathematical Definition of Impulse

Impulse is a nonperiodic exciting force having a variation of magnitude (in general) with respect to time. It acts on the structure for a specific period of time and then ceases. Mathematically, it can be defined as a force that has a large magnitude F and acts for a very short time Δt. It is expressed using the momentum principle and found to be equal to the change in momentum of the system when the impacting mass is constant. Therefore, impulse can be written as,

$$\text{Impulse} = F\Delta t = mv_2 - mv_1 \tag{2.1}$$

where v_1 and v_2 are the velocities of the mass m before and after the application of the impulse, respectively.

In general, the impulse ($\overline{F}$) is written as,

$$\overline{F} = \int_t^{t+\Delta t} F dt \tag{2.2}$$

2.3 Applied Structural Mechanics for Engineering Structures

During the last few decades sophisticated theoretical and experimental studies have been carried out to establish the fracture mechanics foundations; this was required to understand the brittle failure of structures made of high strength metal alloys and other artificial man made materials. Since these fracture mechanics principles were developed to characterize behaviour of generalized materials, they are equally applicable to explain the phenomenon of rock fracture. Slate is a naturally formed layered material. Procedures that have been applied for man made layered composite materials utilized in aircrafts, missiles, rockets, ships, automobiles, building structures and instrumentation panels are equally applicable to the analysis slate material. Therefore, the literature explored in the succeeding part of this section includes some studies based on earlier research carried out on impact response of laminated plates and beams.

To analyze the dynamic behavior of layered composites, the composite is modeled as a layered body with the constituent layers composed of homogeneous, linearly elastic material. The layers may be assumed to be isotropic or have some specified anisotropy. Then initial/boundary value problems are generated for such a body within the framework of the classical theory of elasticity; however it is very difficult to obtain exact solutions for the non-homogeneous material. Sometimes effective modulus theory is used to analyze the behavior (static/dynamic) of a layered material. This method is suitable when the wavelengths of interest are considerably greater than the characteristic layer thickness. This theory will be invalid when the wavelengths are equal or less than the layer thicknesses. Successive reflection and refraction of these short waves from the layer interfaces tend to break down the structure of progressive waves. This leads to a marked

dispersive effect and the effective modulus theory cannot predict this effect. A number of approximate theories have appeared in the literature to take into account this dispersive effect. All these theories are collectively called as microstructural theories.

Delph and Herrmann (1983) developed an effective dispersion theory for layered composites. It is a new micostructural theory for wave propagation in periodically layered solids. There are some restrictions to this theory. This theory is valid for one-dimensional wave propagation normal to the layering and for two-dimensional wave propagation under the condition of anti-plane strain. Hegemier and Nayfeh (1973) developed another theory that mitigated some disadvantages of effective modulus concept. They developed a continuum theory for wave propagation in laminated composites. They discussed wave propagation of laminated composites with elastic, periodic microstructures in case of wave propagation normal to the laminates. This theory was based upon an asymptotic scheme that assumes dominant signal wavelengths to be quite large compared to the typical composite microdimensions. They obtained displacements and stress distributions within each layer. Hegemier and Bache (1973) extended the same theory for wave propagation parallel to the laminates. Christensen (1975) discussed wave propagation in layered elastic media. His primary interest was the characterization and methodology for studying wave propagation in heterogeneous materials.

Beams of different materials, with each layer bonded or just contacting without an adhesive can be used to construct multilayered structures. The design of these types of structures against impact loading would require a detailed study of the motion of stress waves in structures with bonded or adhesives layers, considering the effect of materials,

the possible failure mode and the overall structural response, such as the transient shear and bending deformations. Xia (1988) analyzed the behavior of a two-layered beam under impact loading. He proposed a dynamic model for multilayered beams under impact loading in his paper. His model was based on Timoshenko beam theory; however he accommodated interlayer slip. He investigated different impact loads as well as different interfacial situations and determined the transient behavior of a two-layered beam using the method of characteristics to solve the governing dynamic equations. However, delamination resistance was not considered in his study. He considered the same material to be used for the two layers in his investigation. He found that shear failure occurred in the adhesive region and that the adhesive material had a large effect on the interlayer stresses. Xia and Ruiz (1989) examined the response of layered plates to the impact of a blunt projectile. They found from their study that the elastic dynamic stiffness is the important parameter in determining the initial rise of the contact force and mode of failure. They also found out that mode of failure and energy absorption capacity are influenced by the material properties, thickness of layers and stacking sequence. They observed when the impact of a projectile occurred on multilayers with different materials like aluminium alloy and stainless steel, the first layer always failed through localised shear. They also observed failure to occur through tearing rather than through adiabatic shear, when the projectile punched through the target. In this case the maximum contact force reached during the impact was not only a function of the kinetic energy of the projectile and the material hardness but also of the structural stiffness of the target.

Tedesco, et. al. (1987) presented the results of a preliminary numerical study to evaluate the effectiveness of a layered structure to resist blast effects of non-nuclear weaponry.

Their primary concern was the capability of layered structures to substantially reduce or eliminate the incidence of splitting on the interior of the concrete shelter walls by diminishing the intensity of the blast-induced, compression stress wave that propagated through the wall. They found that layered structures reduced or eliminated the incidence of spalling on the interior of the concrete shelter walls by diminishing the intensity of the blast-induced, compression stress waves which propagated through the wall.

The numerical simulation of the splitting phenomenon is not an easy task. During the past three decades two-dimensional finite element analyses of mode I fast crack propagation in linear elastic isotropic bodies have been examined and a number of papers and reports have been published. Most of the researchers have taken advantage of elastodynamic symmetry about the crack tip trajectory to simulate the rapid crack propagation phenomenon by sequential release of nodes along one side of the finite-element model (Malluck and King 1980, Mall et. al. 1980, Sun and Hun 2001). They used small sized regular elements because of constant stiffness and inertia properties at the crack tip location; the crack tip stress singularity is not properly represented in the finite element model. This technique has also been used by Jih and Sun (1990) to simulate the crack advancement in running crack problems. Numerical modeling of dynamic crack propagation in finite bodies, using moving singular elements, was carried out earlier by Nishioka and Atluri (1980). Mall and Luz (1980) simulated fast fracture problems using eight-noded elements, based on the concept of the sequential release of nodes along the crack path. They analyzed a uniformly expanding crack in a square region subjected to uniform tension on the edges parallel to the crack path. They used very stiff massless truss elements to constrain the vertical nodal displacement along the crack path. They

computed energy release rate for each increment of crack extension from the global energy balance involving strain energy, kinetic energy and potential of remote loads. In order to avoid displacement incompatibility, both corner and midside nodes were released simultaneously. They concluded that eight-noded elements can be safely employed for crack propagation problems only when both the corner and midside nodes are released simultaneously. The sequential node releasing technique, along the crack front, has been applied in the present study to simulate crack propagation.

2.4 Naturally Bedded Layered Media: Slates

The material examined in this study is a naturally bedded layered slate rock. A brief description of its composition, geology, formation history, characteristics, quarrying technique and processing procedure in the industries are presented in the succeeding sections to develop a characteristic understanding of its splitting process.

2.4.1 Introduction

As roofing materials and techniques have advanced, centuries-old traditional roofing methods have been conserved and this knowledge carries answers to many problems found even today in modern day construction. In spite of the fact that these are centuries old, these methods are still widely used and practiced today in Europe and America due to their established technology and efficiency. These old methods have been saved for many reasons, including respect for regional traditions of architecture, and the conservation of historical monuments.

Slate is a fine grained, crystalline rock resulting from sediments of clay and fine silt that are deposited on the seabed, that can be easily split into almost parallel uniform layers.

Slate was formed in the Paleozoic Era, as early as 570 million years ago. The sedimentary clay and silt particles were gradually consolidated into bedded deposits of shale by superimposed materials. The bedded deposits of shale were subsequently folded, crumpled, and compressed by the mountain building forces. At the same time the original clays were changed into new minerals such as mica, chlorite, and quartz by intense heat and pressure. By such mechanical and chemical processes, bedded clays were transformed, or metamorphosed, into slate. The process of forming slate consumes whole geological ages. The metamorphic geological changes necessary to produce slate are dependent upon movements in the earth's crust and the heat and pressure generated thereby. This is why slate is available only in certain mountainous regions. The composition, structure and durability of slate are not uniform because the degree to which their determinant minerals are altered is neither uniform nor consistent. Its quality from dense to soft also varies depending on the quarry it comes out, its thickness and density. The physical properties of the rocks, composed of slates, are defined by the minerals contained, the building blocks of rocks, and their characteristic crystalline structures. Slate consists of minerals that are stable and resistant to weathering and are therefore generally of high strength, low porosity and low absorption. The low absorption and low porosity of slate mitigates the deleterious action of frost and makes it well adapted for different purposes such as roofing and paving. Quartz, chlorite and sericite are the main components of slate. The durability characteristics of different slates are given in Table 2.1.

Slates of a variety of colors are available. Grey, blue grey, black, various shades of green, deep purple, brick and red are the most common. Black color in slate is present due to the presence of carbonaceous matter, derived from the decay of marine organisms from

Table 2.1: Durability of different slates

Name of slate according to place	Life span
Vermont and New York slates	125 years
Buckingham Virginia slates	175 years
Pennsylvania Soft Vein slates	Excess of 60 years
Pennsylvania Hard Vein slates	Roughly 100 years
Peach Bottom slates	At least 200 years

ancient sea floors. Compounds of iron generate the red, purple, and green colored slates. Deep blueblack color slate is found in Maine, Virginia and the Peach Bottom district of York Country, Pennsylvania, U. S. A. Due to the high mica content, slate in Virginia has a distinctive lustrous appearance. The slate producing regions of New York, U.S.A, which centers on Granville and Middle Granville, are particularly important because they contain one of the few commercial deposits of red slate in the world. According to the stability of color, slates are classified as fading or unfading. Fading slates change to new shades or may streak within a short time, after exposure to atmosphere, due to the presence of fine grained disseminated pyrite. Varieties of slates depending on the density, coefficient of water absorption, mechanical flexural strength, resistance to frost, color, etc. are obtained in nature. However, their principal characteristic, viz., the planar structure that allows splitting slate into thin parallel layer is the same. Cleavage and grain are usually considered as the two most important structural properties of slate. A well-developed cleavage, defined by mineral grains in preferred orientations, characterizes slates.

2.4.2 Geology and Microstructure of Slate

From a geological point of view, a fine-grained hardened rock that splits readily into thin plates or any hard argillaceous rock with a tendency to split along the bedding plane is usually called slate. The most perfect splitting, however, occurs in those rocks which have been further hardened by lateral pressure and have at the same time had imposed on them a cleavage plane at right angles to the pressure direction; the splitting is then along this cleavage plane. The breaking of slate rock into thin lamina (or plates) occurs frequently in a different direction from that of the original strata in which the sedimentation process occurred.

There are two types of cleavages developed in rock in nature. These are slaty cleavage and fracture cleavage. The slaty cleavage is usually developed in fine-grained rocks as a result of great lateral pressure, the planes of splitting lying nearly parallel to the axial planes of folds and independent of the original bedding planes (Challinor, 1967). This type of cleavage develops due to: (i) minute flaky minerals re-orientating themselves, with, probably, some shearing, (ii) the growth of new flaky minerals similarly orientated (an incipient schistosity), and (iii) the flattening of mineral particles by pressure. Sometimes it may be possible to trace the original bedding in the cleavage surfaces and edges in slate type rock. The most natural position of the lamina or cleavage of the slate appears to be vertical; but it is to be found in various degrees of inclination, both with respect to the horizontal, and with respect to the planes of stratification. Fracture cleavage develops mainly in fine-grained plastically deformed rocks, splitting along closely spaced, but individually distinct, parallel planes. In this cleavage the splitting does not depend on the mineral arrangement. Cleavage planes are usually shear planes, along which slight

movement has occurred; or they may be planes of weakness corresponding to attenuated limbs or axial planes of very small folds. Though tending to lie parallel to the axial planes of folds, the orientation is not nearly so constant as that of true cleavage. The factors that determine this orientation are more complicated. This cleavage is also called false cleavage. It includes strain slip cleavage and may also be a form of jointing: where closely spaced tight joints give the rock a capacity to part along parallel surfaces, the structure may be designated as fracture cleavage.

Bakewell (1815) mentioned that "slate is composed of straight parallel thin plates or lamina." It divides into layers or plates. It is the result of crystallization, or of the internal arrangement of the particles. The division of the laminae of slate is frequently in a different direction from that of the strata. Slate-rocks vary in their quality, and pass by transition into flinty slate, which appears to differ from common slate by containing a greater proportion of siliceous earth. He showed that crystallization is the origin of slaty cleavage. Sedgwick (1835) showed that slaty cleavage is quite distinct from bedding, and develops due to some post-depositional changes, which he attributed to "crystalline and polar (glacial or hostile) forces acting on the whole mass simultaneously, in given directions, and with adequate power".

Darwin (1846) recognized a genetic relationship between slaty cleavage and foliation. He mentioned that both of these are parts of the same process, i.e., in cleavage there being only incipient separation of the constituent minerals, and in foliation there being much more complete separation and crystallisation. In most extensive metamorphic areas, the foliation is the extreme result of that process of which cleavage is the first effect.

Sharpe (1849) noted that the cleavage was always parallel to the plane of flattening. He considered that the minute constituent particles of slate, like the fragments in the tuffs (any soft porous stone or consolidated fine volcanic ash), were deformed so that their short dimensions were more or less perpendicular to the cleavage planes, which are oriented parallel to the flattest faces of these particles.

Slaty cleavage associated with bulk flattening of rocks was found by Sorby (1853, 1856a). He was able to make microscopic examination of Cambrian slates of North Wales. He found that it is composed of largely minute mica flakes, approximately 2.54×10^{-5} m in maximum length and 2.54×10^{-6} m thick, with a very pronounced and preferred orientation, so that on an average their short dimensions were perpendicular to the cleavage planes. He concluded that the flat particles tended to align themselves perpendicular to the compression direction, and that longer fragments tended to align themselves along the expansion direction, giving the rocks a definite grain orientation along the cleavage plane during the process of deformation. He also mentioned that many slates appear to be recrystallised. Transmission Electron Microscopy (TEM), Analytical Electron Microscopy (AEM), Scanning Transmission Electron Microscope (STEM) are usually used in the microstructural study of slates. Power X-ray diffraction and optical studies and electron microprobe analysis are also used in measuring the average properties of many grains. Recent TEM studies have enhanced the understanding of the formation of slaty cleavage in rocks. White and Johnston (1981) found from slate studies, using TEM technique, that two processes contribute to the development of cleavage. These are crystallisation and mechanical rotation. They found crystalization

occurring in the hinge areas of folds and mechanical rotation occurring in the limbs of fold; they found the siting of the Phyllosilicate-rich domain (P-domains), along which the cleavage occurred, and their initial spacing was controlled by microcrenulations (or micro-notches) that occur along these cleavage planes.

White and Johnston (1981) also performed detailed optical studies on ultra thin sections ($\cong$ 5 μm thick) and undertook detailed microstrucural studies on AE1 EM7 high voltage TEM, operating at 1000 kV and used a Jeol 120CX STEM fitted with a Link Energy-dispersive X-ray system for micro-analytical studies. This technique enabled them to carry out quantitative analyses of very small grains (< 0.1 μm). They concluded that the cleavage developed from the pre-existing microcrenulations mainly by crystallization processes, which were generated by pressure solution and mechanical rotation of grains.

Using transmission electron microscopy techniques it is possible to take direct image of the layers that can be used to characterize the specific nature of individual layers or packets of layers. Still, this does not generally permit identification of trioctahedral and /or dioctahedral planes of shear orientation occurring along the shear cleavage planes. However, with high-resolution analytical electron microscopy performed with a scanning transmission electron microscope, which is operated in TEM mode, it is possible to achieve analytical resolution approaching 300 A^0 (approximately 30 layers of 10 A^0 – 10^{-10} m - structure). Lee, et. al. (1984) applied TEM/STEM and AEM techniques to examine the mudstone to slate transition in the Martinsburg formation at Lehigh Gap, Pennsylvania. They mentioned that chlorite and white mica occur in a variety of intergrowths at all scales, from both regular and random intergrowths at the individual

layer scale to interstratified packets of chlorite and muscovite in a grain size greater than 1μm. In samples which have well developed slaty cleavage the majority of the phyllosilicate grains, whether oriented parallel to bedding or to cleavage are also in sizes below the level of resolution by electron microprobe. However, they retain the large grains parallel to bedding, and also contain grains of equivalent size parallel or subparallel to the plane of cleavage. At a TEM level (<0.1 μm) these cleavage planes consist of white mica, chlorite, and interlayer chlorite-white mica. It can appear as well defined and differentiated subunits of white mica and chlorite. Only white micas and chlorites appear to be homogenous at the optical level of resolution. The powder X-ray diffraction patterns also verify that the only detectable phyllosilicates occurring in all samples are chlorite and white mica.

White and Knipe (1978) reported a microstructural study on cleavage development in selected slates. They used high voltage transmission electron microscopy to detail the microstructural study carried on three types of slates. All these slates contained a low percentage of quartz and carbonate and had domains of orientated phyllosilicates (cleavage lamellae). The materials in between these lamellae are lenticular domains that contain deformed phyllosilicates and that are enriched in secondary minerals. After examination by electron micrographs, they found that the initiation of cleavage lamellae occurred along zones of intense deformation, viz., along kinks and microfolds that form from initial crenulations. They also observed strain induced crystallization and the growth of metamorphically stable phyllosilicates together with mechanical rotation of the phyllosilicates during cleavage development. Once cleavage was initiated it extended laterally into the lenticular domains as deformation proceeded. They examined

interference between adjacent phyllosilicates during deformation and stated that resultant extension sites were often enriched in secondary minerals. They laid emphasis on the importance of mechanical rotation for cleavage development. They classified slates into two types depending on the microstructural study of cleavage. These were: (i) cleavage developed in slates due to well defined planar discontinuities such as cleavage lamellae, which enclosed lenticular domains of quartz, calcite, feldspar and phyllosilicates with their planes at a high angle to cleavage; and (ii) cleavage due to the preferred orientation of nearly all platy minerals together with a preferred dimensional orientation of quartz and carbonates parallel to the platy minerals. Syntectonic crystallization and the preferred growth of new platy minerals approximately parallel to the flattening could be a possible mechanism for cleavage formation. They stated that this slaty cleavage was divided into two groups such as (i) cleavage without syntectonic phyllosilicate recrystallization generally called crenulation cleavage; and (ii) cleavage with syntectonic phyllosilicate recrystallization. Solution of grains along cleavage planes and precipitation of material within the cleavage lamellae with increasing syntectonic metamorphism modified the crenulation fabric. If metamorphism increased further then the crenulation fabric was gradually demolished. Slaty cleavage fabrics were usually developed by mechanical and chemical processes.

The above discussions describe the various features that contribute to crack development in slate material. However, the laboratory splitting process (crack propagation into the material) could also be happening as a result of the processes described above. From the study mentioned above it is seen that easy splitting of slate into two parts happens due to the following reasons:

(i) presence of minute flaky minerals that had re-orientated themselves along defined planes, with, probably, some shearing action;

(ii) growth of new flaky minerals similarly orientated (an incipient schistosity); and

(iii) flattening of mineral particles and grain orientation perpendicular to compression direction due to intense pressure and consequent deformation.

2.4.3 Quarrying Slate

In the past, slate was obtained from the earth's surface downward through open wells. However, this process is achieved today through underground mining, reached by a series of shafts and tunnels (www.traditionaltimberframe.com, 2005). The layers of the slate are generally near vertical (some geological formation photographs are shown in Figures A1-A3 in Appendix A), and are quarried with the aid of dynamite from the base in an upward direction. Open quarry and underground tunnel techniques (shown in Figures A4 and A5) are also using to extract slate. Large blocks weighing several tons are cut and brought through the shafts to the earth's surface. Large block of slate can also be obtained by sawing (diamond saw) of slate from the earth's surface downward in incremental of "steps" which could be in the range of 30 m intervals.

2.4.4 Geology of Slate in Newfoundland

Bonavista formation and Britannia Cove deposit are the main geological sources for slate in Newfoundland [Figure 2 (a)]. Bonavista Formation consists of red, green and purple slate, shale, thin limestone beds and local quartz-pebble conglomerate at the base [see Figure 2.2 (b)]. The Bonavista Formation also has links to several other potential slate deposits at Keels and Random Island. Blackwood (1993) has given the location of the Britannia Cove deposit.

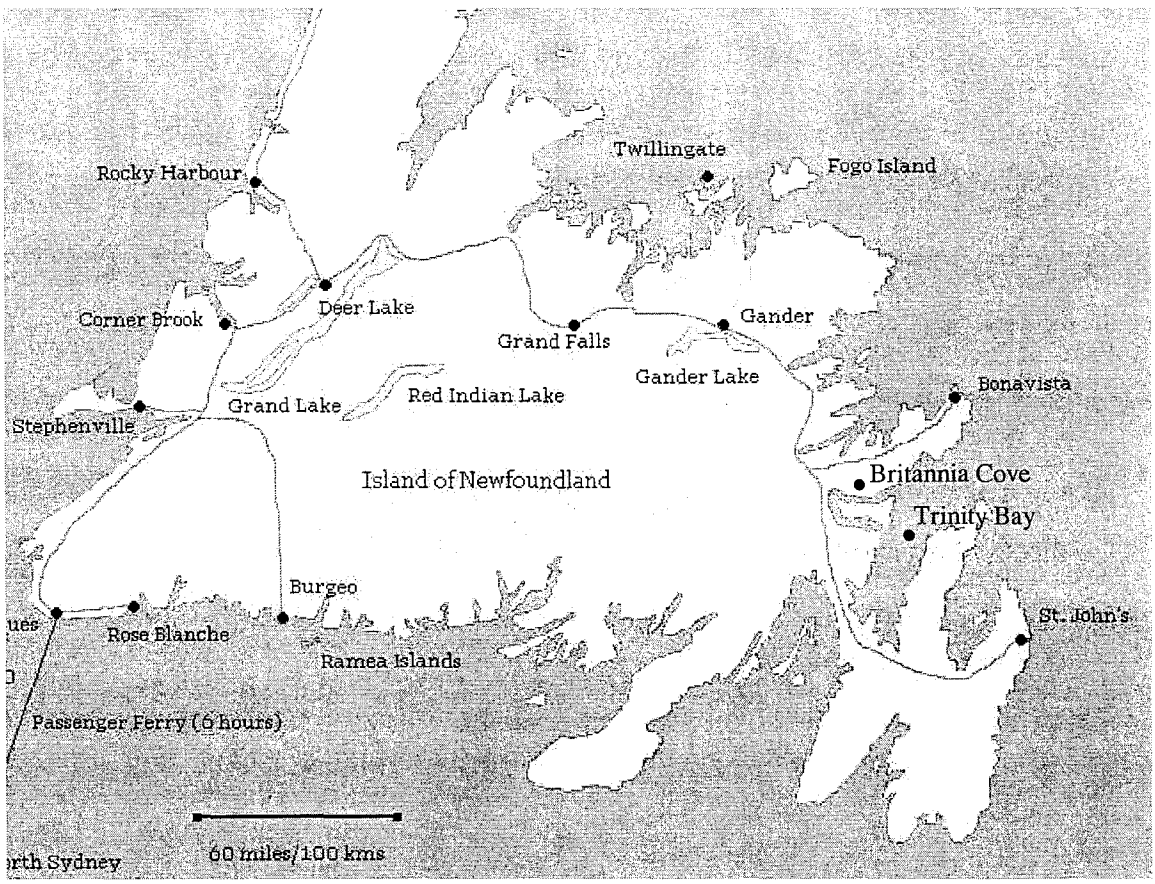

Figure 2.2 (a): Map of Newfoundland, Canada (http://gocanada.about.com/od/maps newfoundland/, 2005)

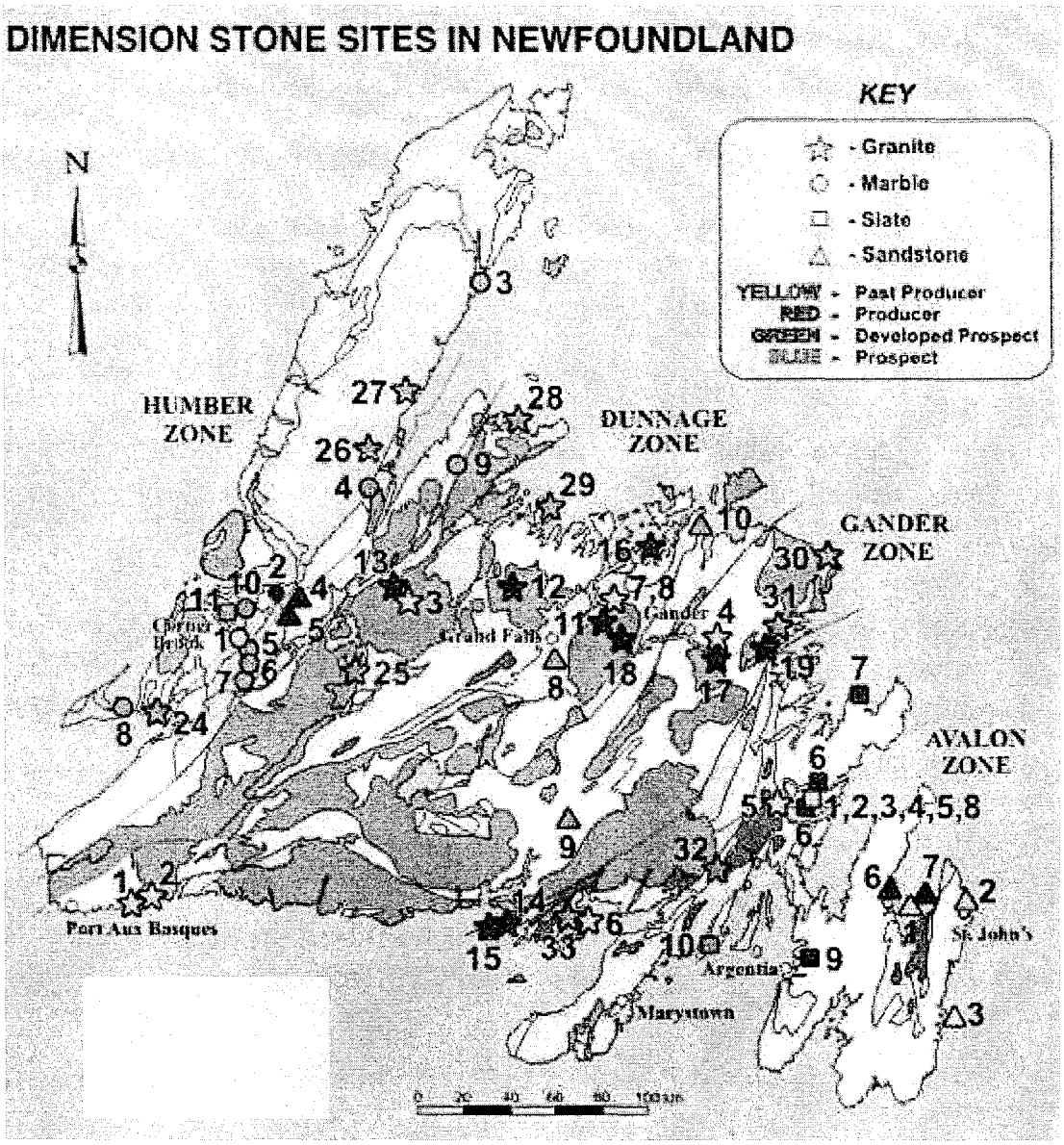

□ Locations of Slate Quarry

Figure 2.2 (b): Dimension stone sites in Newfoundland, Canada [1 - Winter Quarry, 2 - Allison Quarry, 3 - Grieve Quarry, 4 - Black Duck Cove, 5 - Great Cove, 6 - Britannia Cove/Nut Cove, 7 - Keels, 8 - Random Island, 9 - Long Harbour, 10 - Paradise Sound, 11 - Summerside/Curling (number indicates the quarry locations on the map shown above)]. (http://www.nr.gov.nl.ca/mines&en/geosurvey/dimension/dimension.stm, 2000)

He mentioned that Britannia Cove deposit sits in the hinge of a 1.5 to 2.0 km long, tight, north-northeast trending, 5^0 to 30^0 south-southeast plunging syncline and has approximately 65 years of reserves. The deposit consists of approximately 60 to 65 percent purple slate and 30 to 35 percent green slate. He also mentioned that red-purple and blue-green slate and minor grey slate are also available there.

2.4.5 Introduction to Newfoundland Slate Quarries and the Manufacturing Companies

Newfoundland and Labrador is the only province in Canada that has slate quarries. Quarrying of slate was first started in Newfoundland in 1847 at Great Cove, near Brigus, owned by Charles Fox Bennett (Martin, 1983) for local consumption. Purple, green and red slates were available in the Random Sound area of Trinity Bay. A high quality slate for roofing material was discovered on the north side of Smith Sound. It has been reported by Martin (1983) that the first slate quarry in Trinity Bay was opened in the 1850s on the north shore of Smith Sound. Slate obtained from these quarries was supplied both to local and export market until 1900. In 1860, another quarry was opened by John Currie, a Welsh slater adjacent to the Britannia Cove quarry. John Currie operated this quarry until 1899. Thereafter, A. J. Harvey purchased this quarry. Harvey subsequently formed the Newfoundland Slate Company Limited. This company acquired the Carberry quarry in 1900 and renovated the operation and continued the exporting of slate until 1906 when it was closed due to misfortune, fire and poor market. Many building roofs in St. John's, specially in the older portions, were built using Britannia Cove slate. Another three smaller slate quarries also operated occasionally on Random Island with the last quarry closing in 1910. Murray and Howley (1909) reported that an amount of 153,702 squares of finished roofing slate were produced between 1865 and

1909, and most of them were shipped to England. In the west coast of Newfoundland, Summerside, north of Corner Brook, and Birchy Bay also had some slate quarries. [http://www.gov.nf.ca/mines&en/geosurvey/dimension/dimension.stm]

In mid 1980s, the inactive slate quarry was activated. In 1991, Newfoundland Slate Inc. formed a joint venture with Miller-McAsphalt Group, Ontario, and started to distribute slate to the European markets with the aid of interested French producers. It was continued until 1994. In 1995 Newfoundland Slate Inc. developed their own market and produced slate tiles of around 4700 tonnes. They produced purple and green roofing slates (trade name was Trinity Slate), flooring tiles and flagstones. However, this operation was closed again in 1998.

In 2000, Hurley Slateworks Company (Britannia Cove quarry) reactivated the quarry by building a new roofing slate production facility adjacent to the quarry. They are producing varieties of gift products such as paper weight, clock, pen cup, etc., in addition to roofing/flooring tiles and supplying their finished products in 12 countries.

In addition to slates many other sedimentary rocks also consist of very thin layers. Among them sandstone, mudstone, gabbro, etc., are also available in Newfoundland. All of them are fine grained rocks and have a variety of colors. Impact splitting could also be employed on these types of rocks (http://www.msnucleus.org/membership /html/jh/earth/sedimentary/ lesson4/sedimentary4b.html, 2005).

2.4.6 Manufacturing Process of Slate

Slate is a natural stone that has the characteristic of a well-developed defoliation plane, allowing for easy splitting into layers parallel to that plane. The principal characteristic of this type of stone is the planar structure that allows its splitting into thin plates that are directly used as roofing or paving tiles. The existence of a slate quarry is recorded in the Doomesday Book, made by order of William the Conqueror in the year of 1086 (http://www.traditionaltimberframe.com). The adaptation of slate for usable purposes is so closely linked that it is impossible to separate it from its beginning. The formation processes of nature have gifted slate with certain commercially agreeable properties which have had a deep influence on the methods by which slate was quarried and manufactured, as well as its suitability for use in different purposes. The manufacturing process of commercial slate using traditional method is in four steps: cutting, sculpting, splitting and trimming (Figure 2.3). In the cutting process, large irregular blocks of slate are brought to the earth's surface and unloaded. Then these blocks are first cut with a saw across the grain in sections slightly longer than the length of the structural elements. Thereafter, these blocks are sculpted or split along the grain of the slate, to widths slightly larger than the widths of finished slates. A mallet and a broad-faced chisel are usually used in sculpting. In the splitting area, the slightly oversized blocks are split along their cleavage planes to the desired thickness. The splitter's tools consisting of a wooden mallet and two splitting chisels are used for prying the block into halves and repeating this process until the desired thinness is reached. The final step provides the finished dimension (length and width) of slates, making them a standard square or rectangular in

form. Bevels are also created on the edges of the slates during this process, duplicating the esthetics of traditionally hand cut slates.

Since the manufacturing process of this product using explosives is mostly manual, being noisy, powdery and unsafe for the workers, an alternative method of manufacturing slate is very important to improve working conditions and processing procedure. Boutinguiza, et. al. (2002) explored the capabilities of the CO_2 laser to cut slate tiles for improving the working conditions of the quarry and as well the quality of the products made of slate. They used a 1.5 kW CO_2 laser to carry out different operations. They studied the influence of some processing parameters such as average power, and assist gas pressure on the geometry and the quality of the cut. They showed that the CO_2 laser is a feasible tool for successful cutting of slate. They have satisfactorily cut slate tiles to thicknesses ranging from 3 to 13 mm by using a 1.5 kW CO_2 laser. In this method the quality of the cut is in direct relation to the cutting speed and the average laser power used. The maximum cutting speed decreases if the material thickness is increased. Some slate manufacturing companies such as Delabole Slate company were recently using a diamond wire saw and Tiger wire to create a cleaner and safer working environment (Daniel, 1993). They found a cleaner environment at the quarry by providing much less wastage of nonrenewable natural resources and a safer environment without the use of explosives. However, there was also another economic benefit to this operation. They could extract different qualities of slate present in the quarry selectively and with great precision and this process yielded a higher recovery rate of high integrity material (Daniel, 1993). This company has used diamond wire sawing with an electric powered machine from 1987. More recently they have been using a more powerful Pellegrini TDU

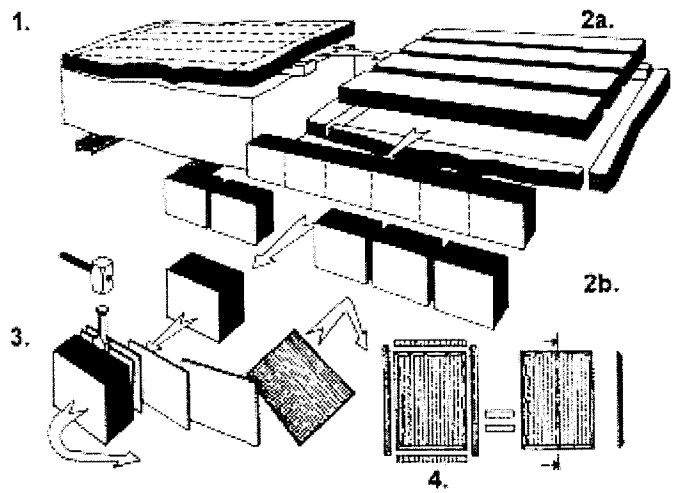

Figure 2.3: Slate manufacturing steps: 1.Cutting; 2. (a) 1st Sawing; 2. (b) 2nd Sawing; 3. Splitting; and 4. Finishing. (http://www.traditionaltimberframe.com, 2005)

100 diesel machine and hydraulic splitter. In the hydraulic splitter method, rocks are split by inserting steel plugs (known as plug-and-feather assembly) into holes drilled into the rock body and applying hydraulic pressure thereafter. These insertions crack open the rock between the holes and sequently separate the rock from the parent rock. Lateral forces are also applied transversely inside the holes, drilled into the rock, by the hydraulic splitters (www.concretenetwork.com, 2004) and www.ur.com, 2004). Many industries also use instrumented hydraulic splitters (which apply shear type load on the rock specimens) to split stone (www.ceejaytool.com, 2005). Some photographs of rock and concrete breaking by using hydraulic splitters are shown in Appendix A (Figures A7-I and A7-II). In this case wastage is minimized and fairly smooth breaking surfaces are obtained. Using these instruments they have produced cost reduction and time saving while trying to clear up the overburden; thereafter they use selective cutting into the

quarry face, so that they can extract blocks in a planned sequence. Tiger wire saw is the improved quality of the diamond wire saw in terms of life and cutting rate.

2.4.7 Processing of Slate in Hurley's Slateworks Company

Hurley's Slateworks Company, Burgoyne's Cove, NF, is producing tiles for roofing and paving from naturally occurring slate material. They obtain large, irregular blocks of slate from quarry by using explosives. Thereafter, they cut it using the machinery shown in Figure A6-I. That machinery can cut reasonably large blocks of slate to a smaller size applying force across the grain. Then they cut it with a saw across the grain into sections slightly longer than the length of the finished roofing slate as shown in Figure A6-II. Next the blocks are split manually along the grain of the slate, progressively to widths slightly larger than the widths of finished slates, as shown in Figures A6-III to A6-V. In this stage skilled artisans split the slate block using a broad faced chisel and a mallet. In the splitting area, the slightly oversized blocks are split along their cleavage planes to the desired shingle thickness. The splitters pry open the block into halves and repeat this process until the desired thinness is reached. Since the slate layer is very thin they can split to any desire size (in thickness direction) by striking along the layer direction. The last step involves trimming the slate tile to the desired size. The complete process of preparing the slate tiles is shown in Figures A6 (I-VII) in Appendix A.

2.5 Failure Theory for Brittle Materials

2.5.1 Brittle and Ductile Material

When a material deforms permanently or it fractures into two or more parts, it is considered to have failed. A combination of stresses contributes to cause failure of the

material. Natural materials may be grouped as brittle or ductile. In general, when the resistance against shearing is greater than the resistance to separation (tension), it is considered as brittle. The opposite phenomenon is considered as ductile. Tensile stress is generally considered as the governing stress associated with the failure of brittle materials, whereas failure of ductile materials is caused by shear stresses.

2.5.2 Failure Mechanisms of Brittle Materials

Material is said to be brittle when a little or almost zero plastic deformation is observed in its failure process. Two principle modes of failure are observed in brittle materials. These are shear fracture and extension fracture. Beside these, grinding and frictional sliding could also be considered as failure mechanisms of the material. However, these modes of failures are basically the combination of the above two fundamental failure modes. Shear fracture is the result of the relative displacement parallel to the plane of failure. It is the governing failure mechanism of ductile materials such as mild steel. The failure plane is generally inclined at an angle of less than 45^0 to the maximum compressive principle stress. It is the dominant mode of macroscopic brittle failure in traxial compression tests at the lowest confining pressures. The micro level definition of extension fracture/cleavage could be stated as the separation of the atoms or molecules to such a distance that no interatomic forces act to bring back together the atoms. This is the dominant mode of failure of many rock materials, specially layered rocks such as, sandstone, slate, etc. The physical characteristic of the extension fracture is the separation of material normal to the failure surface, which is generally oriented normal to the least principal stress. Axial splitting or axial cleavage that normally originates from the local transverse stresses at flaws or heterogeneities (aggregate nature) is also an extension

fracture. Extension fracture can be developed both under tensile and/or compression loading (Paterson, 1978). The general failure modes of brittle material under tensile and compressive loading are shown in Figure 2.4.

Extension fracture under compressive loading develops mainly due to the extension of local transverse tensile stresses in addition to axial compressive stresses at a favourable orientation (axially) of any flaws (circular or elliptical holes, material/plane discontinuity, cracks, etc.). If no resistance (such as confining pressure) is applied against such tensile stress, crack will start to propagate from the flaws parallel to the axis of specimen.

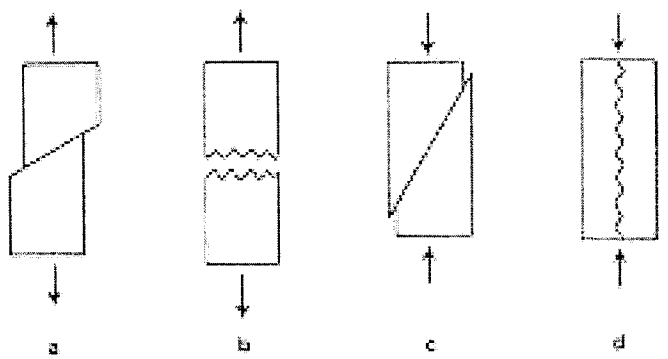

Figure 2.4: (a) Shear fracture in extension test, (b) Extension fracture in extension test, (c) Shear fracture in compression test and (d) Extension or axial splitting fracture in compression test (Paterson, 1978).

In case of inclined flaws the maximum tensile stress component no longer occurs at the end of the major diameter (of the inclined elliptical flaw) but it starts from a point where the normal to the flaw surface is more nearly parallel to the specimen axis. However, the flaw will not tend to propagate in its own plane but swing into an orientation that is more nearly parallel to the axis of loading (Hoek and Bieniawski, 1965).

2.5.3 General Discussion of Brittle Failure Theories

Brittle failure theories are mainly divided into two groups based on their empirical and theoretical contributions. Most of the empirical expressions of crack failure are included in the first group. Mohr's and Coulomb failure criteria and critical maximum tensile stress/strain criterion (applicable to extension failure) are the examples of this group. Although these theories discuss some physical terms, such as limits on stresses in certain planes or limits on strain energy, they discuss very little about the physical failure mechanism. Their main objective is to provide a support for calculating failure conditions under practical situations. Therefore, they are applicable only for strength failure condition cases. In Coulomb failure criterion (maximum shear stress criterion) failure is assumed to occur when maximum shear stress reaches the material shear strength. Failure plane is the plane bisecting the angle between maximum and minimum principal stresses (Vutukuri, et. al. 1974). This criterion is good for isotropic materials. But many rocks that exist in nature (for example, slate, schist, etc.) are not isotropic, and have preferred orientation of planes of weakness or other pronounced fabric. In these cases, consideration of anisotropy in brittle behavior is important.

The second group of failure theories has developed theoretical models of the brittle fracture process to represent actual physical mechanism of fracture. These models contribute to the physical understanding of fracture by providing a firm basis for establishing failure criteria applicable to the general states of stresses. Griffith theory for brittle fracture is the appropriate example for this group.

2.5.4 Failure Theories

The theories used to predict the strength of rock are generally classified as the maximum tensile stress theory, Griffith's theory and statistical theories. A plausible explanation of the variations of the apparent tensile strength with the consideration of size effect (varying volume of rock) and shape effect (various test methods) is offered by the statistical theories. Weibull (1939) theory is used as statistical theory mostly applied to rock failure. Statistical theory will not be discussed here since it is not used in the present study. A brief discussion of maximum tensile stress theory and Griffith's theory is given below;

2.5.4.1 Maximum Tensile Stress Theory

Crack will propagate in a solid when maximum tensile principal stress in a small region around the crack tip reaches the ultimate tensile strength of the material. In that region stresses are assumed to be constant and equal to the ultimate tensile stress. This small local region is named as micro crack processing zone for brittle materials (Peterson, 1978). The mathematical expression for this criterion is written as,

$$\sigma_u = Max\left(|\sigma_1|, |\sigma_2|, |\sigma_3|\right) \qquad \text{(at fracture)} \qquad (2.3)$$

where the notation *Max* indicates that the largest value of the three principal stresses separated by commas is considered. σ_u represents the ultimate tensile strength of the material and σ_1, σ_2 and σ_3 are the principal stresses perpendicular to one another.

2.5.4.2 Griffith Theory

Before discussing Griffith's theory it is necessary to describe the nature of Griffith cracks considered by him for explaining the theory. Griffith mentioned that typical brittle materials inherently contain submicroscopic cracks and/or other heterogeneous discontinuities. They exist in the volume of material with a random orientation and at locations of local stress concentration. Fracture initiation basically starts from those flaws. These types of flaws are called Griffth cracks. In order to prove his theory Griffith carried out a series of tests on varying thickness specimens. He observed greater strength in thin specimens than those obtained from thick specimens. He explained that the reason could be the presence of microscopic flaws, which are less in thin specimens and more in thick specimens. In order to predict theoretical fracture strength of brittle solids, Griffith considered a narrow elliptical hole in a thin plate to simulate the inherent micro crack. Thereafter, he established a relationship between fracture strength and the crack size based on the stress analysis developed by Inglis (1913).

2.5.4.3 Theoretical Development of Griffith Theory

The statement "materials contain flaws (micro-cracks) and tensile failure happens due to the extension of the flaws" was postulated first by Griffith in 1921 (Gdoutos, 1990). He obtained this idea during the experiments he conducted on the deformation of the theoretical strength of glass, an apparently homogeneous and isotropic material. When the material was stressed either by tensile or compressive load, large tensile stress concentrations occurred around the tips of favourably oriented cracks (shown in Figure 2.5). When the tip tensile stress reached the ultimate strength of the material, the crack started to extend, and ultimately failure occurred (Vutukuri, et. al. 1974).

Inglis (1913) mentioned that the maximum tensile stress σ_m developed at or around the tips of the elliptical hole in a flat plate of unit thickness subjected to an average tensile

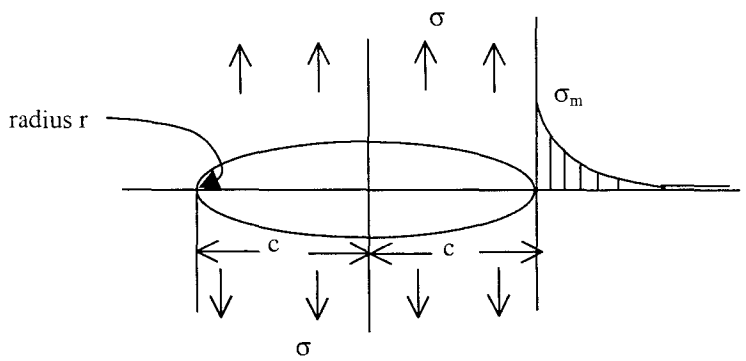

Figure 2.5: Stress distribution at the end of the elliptical hole (Vutukuri, et. al. 1974)

stress σ in a direction perpendicular to the major axis to be equal to,

$$\sigma_m = 2\sigma\left(\frac{c}{r}\right)^{1/2} \tag{2.4}$$

where, r is the radius of curvature at the ends of the major axis, and c is the half length of crack along the major axis; the stress was proportional to $r^{1/2}$.

Griffith also stated that when crack extended, new surfaces were created and energy was absorbed by these surfaces. He compared this energy to the surface energy of the fluid. Griffith established the energy balance analysis for materials subjected to stable crack extension phenomenon by equating energy supplied by the change of strain energy within the solid and the change in potential energy of the applied forces for an infinitesimally

small change in crack length to the energy absorbed by the creation of the new crack surfaces. He mentioned that if the released elastic strain energy (the energy pumped into the fracture zone from the elastic bulk of the solid) of the body was more than the absorbed energy by the creation of the new crack surfaces, a crack would extend. The elastic strain energy released by the extension of a crack in a thin plate of unit thickness was given by

$$W_e = \frac{\pi c^2 \sigma^2}{E} \tag{2.5}$$

and the surface energy absorbed by the creation of the new crack was given by (Griffith, 1921)

$$W_s = 4c\gamma_s \tag{2.6}$$

where, γ_s is the surface tension and E is the Young's modulus of elasticity. Therefore, the total energy decrease due to the extension of crack could be written as,

$$W = W_e - W_s = \frac{\pi c^2 \sigma^2}{E} - 4c\gamma_s \tag{2.7}$$

By minimizing the total energy, Griffith found the tensile stress σ to cause crack growth to be,

$$\sigma = \left(\frac{2\gamma_s E}{\pi c} \right)^{1/2} \geq \sigma_t \tag{2.8}$$

where, σ_t is the ultimate tensile strength of the material.

Griffith also provided the condition for stable crack growth as,

$$\sigma > \left(\frac{2\gamma_s E}{\pi c} \right)^{1/2} \tag{2.9}$$

In case of unstable crack growth, fracture condition will not follow any particular relation between c and σ. In addition, crack propagation velocity will also play another role. In this case crack propagation cannot be controlled by controlling the applied load. When significant amount of energy was available and propagation velocity exceeded the maximum speed, the crack would start to branch out and follow several paths (Vutukuri, et. al. 1974). Griffith theory is particularly suitable to the case of rock failure resulting from compressive stresses.

The energy based Griffith formula concerns stationary crack. However, in dynamic crack propagation, this formula needs to be updated by including the terms for kinetic energy absorption. This energy is absorbed when material on one side of crack gets a motion relative to that on the other side. The stress field is also modified around the crack tip at high crack velocities.

2.6 Fracture Mechanics

The failure process in which new surfaces are created in the form of cracks in a material or existing crack surfaces are extended is defined as fracture. Fracture mechanics offers a mechanistic and a rational understanding of the mechanism of fracture over the other strength predicting methods of the materials. It is a logical extension of Griffith energy balance analysis of crack growth. It covers the shortcomings of Griffith's analysis. Griffith didn't consider absorbed energy due to localized crack non-linearity, in his energy balance criterion. However, this is taken into consideration in this approach. Griffith's method is essentially valid for a perfectly elastic-brittle material and cannot be used for situations where high local plastic deformations occur at the crack tip. Orowan

(1947) and Irwin (1948) proposed that Griffith method could be used in the case of limited plastic deformation (non-linearities are confined to a small region surrounding the crack tips) at the crack tip if plastic surface work is included in energy balance method. Materials that belong to a limited zone of plastic deformation can be characterized by their fracture process using the critical strain energy release rate. If the critical strain energy release rate, the size and the location of the longest expected flaw in the body are known, it is possible to predict the maximum stress that a body can resist. Therefore, critical strain energy release rate could be considered as an important factor in dealing with fracture mechanics problems. Critical strain energy release rate (G_c) is not constant with test geometry. Brown and Srawley (1965) mentioned that in materials having a large plastic zone at the crack tip in comparison to the crack dimension and the thickness of the specimen, G_c is not invariant.

The aim of fracture mechanics is to establish a quantitative measure for a crack of given size to initiate and propagate in an adverse manner under service loading and therefore to determine the degree of safety against the failure by fracture that the structure possesses (Whittaker, et. al. 1992). Linear elastic fracture mechanics (LEFM), non-linear elastic fracture mechanics (NEFM), dynamic fracture mechanics, etc., are the branches of fracture mechanics. The proposed failure criteria in LEFM and NEFM are critical strain energy release rate, critical stress intensity factor, the J-integral, the crack opening displacement and the strain energy density criteria. All criteria except strain energy release rate are restricted to symmetry between the applied load and crack plane and self similar crack growth. Therefore, crack growth direction and shape of the crack growth have to be known prior to use of criteria. Since slate rock material is brittle and fracture

process zone is small and crack growth seems to be almost in a plane (from experimental observation), the concept of LEFM is used to analyze the crack propagation in slate.

Linear elastic fracture mechanics is based on an assumption of small scale yielding, i.e.,when non-linear plastic zone near the crack tip is sufficiently small in comparison to the geometry of crack and any other characteristic dimensions, such as specimen thickness. In LEFM, it is assumed that the process leading to the onset of crack growth and final instability leading to catastrophic fracture are similar (Gdoutos, 1990). Therefore, a single parameter is sufficient to describe the fracture process. Gdoutos mentioned that the critical value of this parameter represents the fracture toughness and corresponds to the onset of unstable fracture process. Stress intensity factor is used to characterize uniquely the crack tip stresses/displacements fields and fracture behaviour of the material in LEFM. Therefore, it is necessary to place particular attention to the stress intensity factors to describe linear elastic fracture mechanics well.

2.6.1 Stress Intensity Factor (SIF)

According to the Griffith's finding, tensile stress across the plane becomes infinite for a narrow crack having zero crack tip radius (due to $r^{-1/2}$ singularity). However, the existence of infinite stress in the material is impossible because no material can resist infinite stress. Its prediction is only a consequence of the mathematical analysis which is based on the assumptions of linearity in the constitutive equations and of infinitesimal strains, both of which are not accepted at the crack tip region. Stress intensity factor (K) is a single parameter characterization of crack tip elastic stresses, strains and displacements in LEFM. It is essentially a measure of elastic stress fields close to the

crack tip. It is dependent only on the remote stress field and the crack size for infinite specimens and in addition body geometry for finite specimens. For a finite body, theoretical determination of stress intensity factors is difficult due to the presence of boundary conditions (Gdoutos, 1990). Critical value of the stress intensity factor, which is a measure of crack growth of solid is called fracture toughness (a material property for plane strain condition) and is represented by K_{IC}. It can be determined experimentally using different methods (three point bending test, four point bending test, compact tension test, chevron notched short rod method, wedge loaded compaction test, etc.) established by ASTM (American Society for Testing and Materials) and ISRM (International Society for Rock Mechanics).

In a three-dimensional body with an arbitrary loading system, to define the stress state around the crack, three stress intensity factors are required. These stress intensity factors correspond to three basic deformation modes such as opening, shearing and tearing modes of the crack plane as shown in Fig. 2.6.

Opening mode i.e., mode I corresponding stress intensity factor is represented as K_I. Similarly mode II (shearing) and mode III (tearing) corresponding stress intensity factors are K_{II} and K_{III}.

Among all the three modes, mode I stress intensity factor is the most significant one and is used extensively. In particular, the studies concerning rock fracture mechanics primarily use the mode I stress intensity factor. The onset of unstable fracture propagation criteria of brittle material is also based on its critical value (fracture toughness) (Bieniawski, 1966).

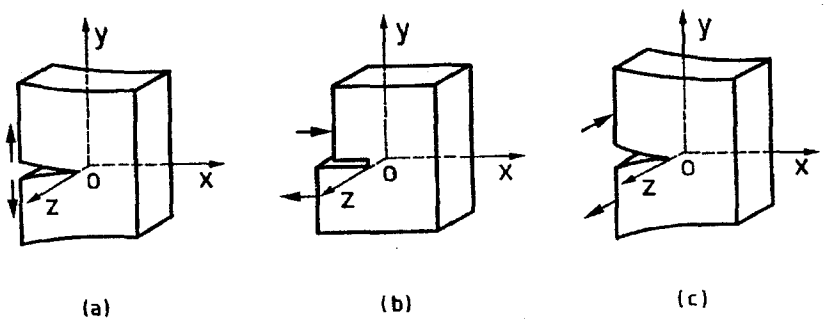

Figure 2.6: The three basic modes of crack extension; (a) Opening mode, I, (b) Sliding mode, II, and (c) Tearing mode, III, (Gdoutos, 1993)

2.6.2 Stress Intensity Factor based Fracture Criterion

Stress intensity based fracture criteria is equivalent to the energy based fracture criteria. Irwin (1957) established relationships between the mode I stress intensity factor and energy release rate based on the assumption that crack extension will be in the plane of crack. For a homogeneous isotropic material, these relationships are,

$$K_I = \sqrt{\frac{EG}{1-\nu^2}} \text{ for plane strain}$$

$$K_I = \sqrt{EG} \text{ for plane stress} \qquad (2.10)$$

where, G is the strain energy release rate. Crack growth direction cannot be determined using stress intensity method. It can be predicted using a stress criterion that can be expressed in terms of stress intensity factors. Fracture starts to propagate when stress intensity factor reaches its critical value, K_{IC}, or strain energy release rate reaches its critical value, G_{IC}, due to applied forces. K_{IC} is referred as plane strain fracture toughness of the material.

2.6.3 J integral - A Fracture Criteria

In linear elastic fracture mechanics it is assumed that crack tip plasticity is very small. However, this is not the true for all materials, specially in ductile materials. In this case crack tip plastic zone cannot be neglected and hence, its influence on the energy release rate needs to be considered. To include plasticity effect into the energy release rate, it is necessary to develop an exact elastic plastic solution of the crack-tip stress field. Such a solution could be provided using a method, which is based on the path independent integrals. It can determine crack tip quantities such as, energy release rate or stress intensity factor not only for an elastic field but also for an elastic-plastic field. It is an analyzing tool for fracture that can provide intense insight into the nature of crack tip fields in nonlinear elastic or plastic solids. It can be evaluated experimentally and its critical value may be used as an attractive elastic-plastic fracture criterion (Begley and

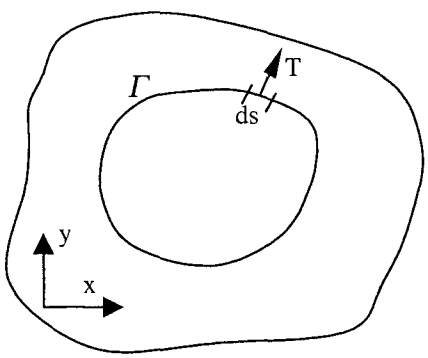

Figure 2.7: Definition of J integral (Broek, 1974)

Landes, 1972). It could be said that this method is an extension of linear elastic fracture mechanics to account for large-scale inelastic effects (Broek, 1974).

J integral is defined as,

$$J = \int_{\Gamma}\left(Wdy - T\frac{\partial u}{\partial x}ds \right) \tag{2.11}$$

where, Γ is a closed contour followed counterclockwise in an area surrounding a stress solid. T is the tension vector perpendicular to the normal at a point on surface Γ in an outside direction; it can be written as,

$$T_i = \sigma_{ij} n_j \tag{2.12}$$

u is the displacement in x direction and ds is an element of Γ, W is the strain energy per unit volume and represented as,

$$W = W(x, y) = W(\varepsilon) = \int_0^{\varepsilon} \sigma_{ij} d\varepsilon_{ij} \tag{2.13}$$

For a closed contour, J can be shown equal to zero.

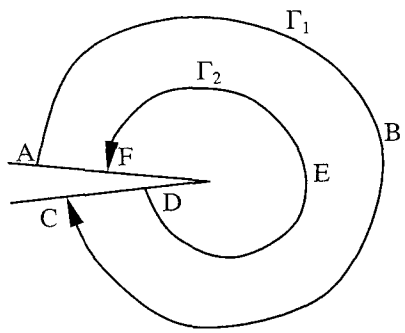

Figure 2.8: Contour around crack tip

Consider a closed contour *ABCDEFA* around the crack tip as shown in Figure 2.8. Since in elastic case J integral is apparently equivalent to energy release rate, the total energy release rate will be equal to the sum of contribution of all parts along the path to the integral. The parts *CD* and *AF* are traction free, $T = 0$, and $dy = 0$, therefore, contribution to the J-integral is zero. Since J integral is zero for a closed contour, therefore, the

contribution of *ABC* must be equal to the contribution of *DEF*. Therefore, it is independent of whatever path is chosen. In Figure 2.8 (b) it is seen that the paths *ABC* and *DEF* are not exactly closed curves; they end at the crack edges, also satisfying the path independent criteria.

In linear elastic material, J-integral is related to the stress intensity factors. For homogeneous isotropic materials the relationships between J-integral and stress intensity factors are defined as (ABAQUS, 2002),

$$J = \frac{1}{E}(K_I^2 + K_{II}^2) + \frac{1}{2\eta}K_{III}^2 \quad \textit{for plane stress case}; \text{ and}$$

$$J = \frac{1-\nu^2}{E}(K_I^2 + K_{II}^2) + \frac{1}{2\eta}K_{III}^2 \quad \textit{for plane strain, axisymmetry and three dimensional cases} \tag{2.14}$$

For crack at the interface of two dissimilar isotropic materials the above relationship is written as (ABAQUS, 2002),

$$J = \frac{1-\beta^2}{E^*}(K_I^2 + K_{II}^2) + \frac{1}{2\eta^*}K_{III}^2 \tag{2.15}$$

where

$$\frac{1}{E^*} = \frac{1}{2}\left(\frac{1}{\bar{E}_1} + \frac{1}{\bar{E}_2}\right), \qquad \frac{1}{\eta^*} = \frac{1}{2}\left(\frac{1}{\eta_1} + \frac{1}{\eta_2}\right),$$

$$\beta = \frac{\eta_1(\kappa_2 - 1) - \eta_2(\kappa_1 - 1)}{\eta_1(\kappa_2 + 1) + \eta_2(\kappa_1 + 1)}, \tag{2.16}$$

and $\kappa_i = 3 - 4\nu_i$, $\overline{E}_i = \frac{E_i}{1-\nu_i^2}$ for plane strain, axisymmetry and three dimensional cases,

and $\kappa_i = \frac{(3-\nu_i)}{(1+\nu_i)}$, $\overline{E}_i = E_i$ for plane stress, and η_i is shear modulus of elasticity with

$i = 1, 2.$ (2.17)

2.6.4 Contour Integral

When an integral is determined by performing integration around a given contour in the complex plane it is called contour integral. Integral is computed by summing the values of the complex residues inside the contour. Details of mathematical explanation of contour integral is available in any calculus and analysis books or in web site (mathworld.wolfram.com/ContourIntegration.html, 2005). Contour integrals are valid for two and three dimensional analyses. Contour integral can be expanded to area integral (for two dimensions) as well as to volume integral (for three dimensions) over a finite domain surrounding the crack front using divergence theorem. ABAQUS finite element software follows this domain integral method to calculate contour integrals. Contour integral option in ABAQUS is used to evaluate the J-integral, the stress intensity factors, the C_t integral and the T stress in fracture mechanics with some limitations mentioned in ABAQUS keynote manual or user manual on using elements (ABAQUS, 2002). It can also be used to calculate crack propagation direction at initiation during the evaluation of stress intensity factors. It is possible to evaluate several contour integrals at each location along the crack front. Such an evaluation is thought of as the virtual motion of a block of material surrounding the crack tip or crack front in finite element evaluation. Each block of material is defined by contours and each contour represents a ring of elements around

the crack tip or crack front from one face to the opposite face of crack. Each new ring of elements is defined to surround of previous contour. An evaluation of contour integral is provided by each contour. Therefore, the number of contour integral evaluations is equal to the number of such rings of elements considered. For a crack under mixed mode loading, ABAQUS directly calculates the stress intensity factors by interaction integral method (available in ABAQUS theory manual, version 6.4) and is applicable for both linear isotropic and anisotropic materials.

2.6.5 Fracture Initiation and Fracture Propagation

As mentioned earlier, for practical purpose the tensile strength criteria is used as crack initiation criteria because of absence of crack closure phenomenon and simultaneous occurrence of strength failure and rupture. However, fracture initiation, strength failure and rupture take place at different stress levels under compressive stress conditions (Hoek and Bieniawski, 1965). Therefore, it is necessary to investigate crack propagation phenomena by considering all of the events separately in rock fracture processes where applied stress is compressive. The entire process of brittle fracture propagation in rock under compressive stress can be divided into four stages such as, onset of fracture propagation i.e., fracture initiation, critical energy release, strength failure and rupture.

Fracture initiation: Griffith (1921) mentioned that for open cracks without friction and a specific limit, i. e., $\infty \leq \frac{\sigma_3}{\sigma_1} \leq 0.33$, fracture initiation occurs when the minor principal stress is equal to the uniaxial tensile strength, $\sigma_3 = \sigma_t$.

Critical Energy Release: It is obtained from experimental evident that the propagation of brittle fracture consists of two processes: a slow process called stable fracture propagation and a fast process called unstable fracture propagation (Bieniawski, 1967). According to Irwin's hypothesis, during fracturing, critical energy release G_c a characteristic property of the material, and could be a condition for determining the transition from stable to unstable fracture propagation. Bieniawski (1967) has given the following criteria for unstable crack propagation for tension (equation 2.18a) and compression (equation 2.18b).

$$\sigma_u = \sqrt{G_c E / \pi c_u} \tag{2.18a}$$

$$\sigma_u = \sqrt{G_c E / \pi c_u \sin^2 \psi \cos^2 \psi} \tag{2.18b}$$

where σ_u is the uniaxial applied stress at the onset of unstable fracture propagation, c_u is the corresponding crack half-length, G_c is the critical energy release rate and ψ is the angle between the crack plane and direction of compression. Many researchers have verified experimentally the concept of critical energy release rate established by Irwin's approach and used it to design different structures such as pressure vessels, steam turbine generator rotors, ships, aircraft, etc. Bieniawski applied this concept to rock. He also proved experimentally that the stress level at critical energy release represents the long term strength of rock material. He obtained from his study on unstable fracture propagation process that fracture propagation velocity increases fast and reaches its maximum value when stress level approaches its failure strength. However, when stress level reaches its failure strength, fracture propagation velocity becomes a constant (Schardin 1959, Bieniawski 1966). He mentioned that crack starts to propagate at low velocity at the starting of the stable fracture propagation. He also pointed out that the

constant velocity obtained at failure strength is related to the velocities of the three elastic waves, i.e., longitudinal, shear, and Rayleigh.

Beniawski considered influence of specimen size on the fracture propagation process of rock. He found that the fracture initiation stress in a rock decreased with increase of the size of the specimen; but the increase was much less when he carried out tests on different sizes of soft coal rock. He reported that the discontinuities of small specimens are more active and fracture will propagate from this discontinuity at a low stress level. For large specimens, material surrounding the discontinuity offers some resistance during fracture initiation; therefore, the effect of a discontinuity will be less pronounced.

2.7 Fracture Dynamics

Rock broken by explosives or by applying instrumented impact force, hydraulic fracturing, earthquake effect, etc., are dynamic events associated with the field of structural geology. In case of impact loading such as explosive propulsion or projectile impact, if time to reach the load from its zero magnitude to peak value is less than half of the fundamental natural period of the body, dynamic effect becomes significant (Gdoutos, 1990, page 241). It is indicated in the elastodynamic analysis of crack problem that the stresses and displacements developed in dynamic loading may be different than those obtained during its static loading. Dynamic values are higher than static values at critical locations of the body. The intersection of elastic wave at the crack surfaces and other body boundaries may be the reasons for the higher values (Shi, et. al. 1972, Shi 1977, Gdoutos 1990). Among other reasons, properties of the material such as yield strength and ultimate strength of metal are very sensitive to the rate of loading. They increase if

the rate of loading increases. At high rates of loading their values increase near the crack in such a way that there will not be enough time to develop yielding and therefore, energy is released within a very short time leading to rapid crack propagation. Fracture dynamics deals with fracture events associated with a propagating crack due to applied dynamic forces by considering kinetic energy (inertia effect) developed due to movement of newly created fracture surfaces. It includes fracture process under static stress conditions (gradually increasing load) as well as dynamic stress conditions (shock or impact loads) (Bieniawski, 1968b). Bieniawski reviewed many research studies related to this area. He reported that the dynamic stress distribution around the propagating crack under static loading conditions differs negligibly from that under dynamic loading conditions. To study fracture dynamics of rock it is necessary and important to discuss the three following events:

i) the stability of fracture propagation

ii) the terminal fracture velocity

iii) the dynamic stress state created by a propagation crack

2.7.1 Stability of Fracture Propagation in Rock

It has been shown from earlier studies that fracture initiation occurs based on the Griffith's energy balance criteria given by,

$$\sigma = \sigma_{in} = \sqrt{2\gamma E / \pi c_0} \tag{2.19}$$

where

σ = applied uniaxial tensile stress

σ_{in} = value of σ when crack propagation initiates

γ = surface energy per unit length of the crack

E = Young's modulus of elasticity

c_0 = half-length of the pre-existing (Griffith) crack

and fracture propagation takes place when,

$$\sigma > [\sigma_{in} = \sqrt{2\gamma E / \pi c_0}] \tag{2.20}$$

The latter criterion is known as a criterion for stable crack propagation. Fracture propagation remains stable as long as a definite relationship between applied stress (σ) and half-crack length (c) is maintained and satisfy the condition $\sigma > \sigma_{in}$. Irwin's hypothesis (1948) has given the following relationship between σ and c for brittle metals,

$$\sigma = \sqrt{GE / \pi c} \tag{2.21}$$

where G is the released energy per unit surface area of crack. Bieniawski (1967) applied this relation to rock material. The concept behind this relation is, a certain amount of energy (G) is released from the stored energy of a structure and used to form additional crack surface area. The rate at which energy is released will be same as the rate at which energy is absorbed by the process of crack extension. Here, G is not constant, and its value depends upon the values σ and c at any instant.

Bieniawski mentioned that the differences between Irwin's and Griffith's σ - c relations are that while Griffith formula is a criterion for crack initiation, Irwin's formula gives a functional relationship between σ and c, describing a law for stable fracture propagation. Bieniawski found that Irwin's formula would no longer be valid when fracture propagation is unstable due to influence of other factors such as crack propagation velocity. Irwin mentioned that the relationship shown in Eqn. (2.21) could be used as a

criterion for the transition of stable to unstable fracture propagation. He mentioned that when energy release per unit crack surface *(G)* reaches critical value *(G_c)* unstable fracture propagation starts. He also mentioned that G_c is a characteristic material property. He proposed a criterion for the onset of unstable fracture propagation by plane stress or strain equation 2.18 mentioned earlier. Using the equation 2.18, the critical energy release for stress condition is written as,

$$G_c = \frac{\pi \sigma_u^2 c_u}{E} \tag{2.22}$$

For plane strain condition, it can be written as,

$$G_c = \frac{(1-\nu^2)\pi \sigma_u^2 c_u}{E} \tag{2.23}$$

where ν is Poisson's ratio. It is possible to determine G_c for a particular material experimentally by knowing the σ_u and c_u at the onset of the unstable crack propagation. Many researchers have measured apparent fracture toughness of rock experimentally using different methods. Klepaczko, et. al. (1984) determined fracture toughness of Canadian coal under quasi-static and impact loading. They used a wedge loaded compact tension specimen for all tests. A servohydraulic testing machine was used to carry out quasi-static test and split Hopkinson Bar was used for the dynamic test. They reported that dynamic apparent fracture toughness could be higher than its quasi-static value by one order of magnitude. Experimental analysis of crack growth in granite was presented by Labuz, et. al. (1985). They used the conventional linear elastic fracture mechanics techniques to calculate the apparent fracture toughness of granite at various crack lengths. They mentioned that fracture process zone was large for large grain-size rock after performing extensive closed-loop, strain-controlled fracture tests. They considered

inelastic part to calculate an apparent fracture toughness of smaller specimens for obtaining a more realistic estimate of fracture parameter.

2.7.2 Fracture Velocity

The theoretical quantitative measure of the speed of rapid crack growth was proposed by Mott in 1948. The kinetic energy disregarded in Griffith energy balance equation was included into the total energy of the system to calculate the speed of the moving crack. Mott analyzed an infinite plate with a central crack subjected to a uniform time-independent uniaxial stress perpendicular to the crack plane based on the following assumptions:

(i) The stress and displacement fields for the dynamic problem were the same as those for the static problem, with the same crack length.

(ii) The crack was travelling at a constant speed

(iii) The crack speed was small compared to the shear wave speed in the body

He determined the kinetic energy for plane stress problems to be,

$$W_k = k\rho c^2 v^2 \sigma^2 / 2E^2 \tag{2.24}$$

where, W_k = kinetic energy

k = a proportional constant

ρ = mass density of the material

c = half length of crack

v = crack velocity

σ = applied stress

E = modulus of elasticity

After adding the above equation to the Griffith original energy balance approach and applying some mathematical operations, the expression for crack speed was obtained as,

$$v = \sqrt{\frac{2\pi}{k}}\sqrt{\frac{E}{\rho}}\left(1-\frac{c_0}{c}\right) \tag{2.25}$$

where c_0 is the initial half crack length

In the above equation it is seen that when $c>>c_0$ i.e., crack velocity approaches its asymptotic value (almost constant). He named this velocity as the terminal fracture velocity and expressed it as,

$$v_T = \sqrt{\frac{2\pi}{k}}\sqrt{\frac{E}{\rho}} = \sqrt{\frac{2\pi}{k}}v_L \tag{2.26}$$

where v_L = velocity of longitudinal wave propagation in rod made of the same material. Detailed derivation regarding this problem is available in Gdoutos (1993) and Broek (1974).

2.7.3 Experimental Techniques to measure Crack Propagation Velocity

Measurement of crack propagation velocity under dynamic loading situation is a very difficult task. Initially it was measured by placing a series of conducting wires at certain intervals along the crack path and perpendicular to the crack plane. These wires formed one part of a bridge, which was connected to an oscilloscope. Once crack started to propagate wires also started to break one by one. Time between two successively broken wires was obtained from the time mark indicated in the oscilloscope. However, nowadays, availability of crack gauges or strain gauges or semi conductor strain gauges with a sophisticated data acquisition system has made this measurement a little easier. Their operating principles are almost the same as those of the wire conductors. The other

method that is widely used to determine crack velocity is the high speed photography. In this technique crack velocity is measured by taking photograph from a high speed camera capable of 10^6 frame per sec (approximately). Although it is suitable for transparent materials, it can also be used for nontransparent materials after polishing the surface of the specimens.

2.7.4 Dynamic Stress Field around a Rapidly Propagating Crack

To determine the ultimate stability of mining excavations and civil engineering rock structures it becomes essential to know the stress distribution around a propagating crack. It is an integral part of fracture dynamics of a rock mass. The theoretical development of dynamic stresses has been carried out mainly to study the brittle fracture of metal. However, these analyses are also applicable to rock. Constant velocity crack problem was carried out by many researchers (Shi and Chen 1972, Nillson 1972). When crack velocity varies with time, the solution of the crack problem becomes difficult to solve with the realistic solution procedures. Tsai (1973) and Kostrov (1975) studied finite length crack propagating problem with acceleration under plane extensional loading. A formulation of the problem of a rapidly propagating crack is given by Gdoutos (1990). He also presented the near crack-tip stress and displacement fields. The mathematical expression of singular stresses and displacements fields for a homogeneous, isotropic material are,

$$\sigma_{11} = \frac{K(t)B}{\sqrt{2\pi r}}\left[\left(1+2\beta_1^2-\beta_2^2\right)\sqrt{\frac{r}{r_1}}\cos\frac{\theta_1}{2} - \frac{4\beta_1\beta_2}{1+\beta_2^2}\sqrt{\frac{r}{r_2}}\cos\frac{\theta_2}{2}\right]$$

$$\sigma_{22} = \frac{2K(t)B}{\sqrt{2\pi r}}\left[-\left(1+\beta_2^2\right)\sqrt{\frac{r}{r_2}}\cos\frac{\theta_1}{2} + \frac{4\beta_1\beta_2}{1+\beta_2^2}\sqrt{\frac{r}{r_2}}\cos\frac{\theta_2}{2}\right]$$

$$\sigma_{12} = \frac{2K(t)B\beta_1}{\sqrt{2\pi r}}\left[\sqrt{\frac{r}{r_1}}\sin\frac{\theta_1}{2} - \sqrt{\frac{r}{r_2}}\sin\frac{\theta_2}{2}\right] \tag{2.27}$$

$$B = \frac{1+\beta_2^2}{4\beta_1\beta_2 - \left(1+\beta_2^2\right)^2} \qquad \beta_1^2 = 1-\frac{v^2}{c_1^2}, \qquad \beta_2^2 = 1-\frac{v^2}{c_2^2}$$

where, $K(t)$ = time dependent stress intensity factor, v is the crack speed, c_1 and c_2 are dilatation and shear wave speeds, r_1, r_2 and θ_1, θ_2 are related by the following expression,

$$\begin{aligned} z_1 &= x + i\beta_1 y = r_1 e^{i\theta_1} \\ z_2 &= x + i\beta_2 y = r_2 e^{i\theta_2} \end{aligned} \tag{2.28}$$

where, z_1 and z_2 are the complex variable functions.

The velocity fields of the particles near the crack tip are,

$$\begin{aligned} \dot{u}_1 &= -\frac{K(t)Bv}{\sqrt{2\pi r}\mu}\left[\sqrt{\frac{r}{r_1}}\cos\frac{\theta_1}{2} - \frac{2\beta_1\beta_2}{1+\beta_2^2}\sqrt{\frac{r}{r_2}}\cos\frac{\theta_2}{2}\right] \\ \dot{u}_2 &= -\frac{K(t)Bv}{\sqrt{2\pi r}\mu}\left[\sqrt{\frac{r}{r_1}}\sin\frac{\theta_1}{2} - \frac{2}{1+\beta_2^2}\sqrt{\frac{r}{r_2}}\sin\frac{\theta_2}{2}\right] \end{aligned} \tag{2.29}$$

2.7.5 Relationship between Dynamic Stress Intensity Factor and Strain Energy Release Rate

For a homogeneous isotropic material (Sih 1970, Gdoutos 1990),

$$G = \left[\frac{\beta_1\left(1-\beta_2^2\right)}{4\beta_1\beta_2 - \left(1+\beta_2^2\right)^2}\frac{1}{2\mu}\right]K^2(t) \tag{2.30}$$

where, μ = shear modulus, G = strain energy release rate and $K(t)$ = dynamic stress intensity factor, β_1 and β_2 are mentioned in equation (2.27). In order to obtain the fracture criteria, it is assumed that when strain energy release rate reaches its critical value that is

equivalent to the critical stress intensity factor, dynamic crack propagation starts. For fracture criteria, it is written as,

$$K(t) = K_{ID}(v,t) \tag{2.31}$$

where, $K_{ID}(v,t)$ represents material resistance to propagate dynamic crack and is assumed as a material property. Dynamic stress intensity factor $K(t)$ which is a function of loading, crack length and geometrical configuration of the cracked body is determined based on the solution of the elastodynamic problem. But K_{ID} is determined experimentally and is dependent on the crack speed and environmental conditions. Dally (1979) reported that K_{ID} depended on the crack speed. Its value was speed independent at low speed (<300 m/s for metals and polymers) but increased as the crack speed increased.

For a moving crack in a homogeneous orthotropic material total energy release rate, stress intensity factors and crack speed are related by the following expression (Yang, et. al. 1991),

$$G = \frac{1}{4}\left(H_{22}K_I^2 + H_{11}K_{II}^2 + H_{33}K_{III}^2\right) \tag{2.32}$$

where H_{11}, H_{22} and H_{33} are elements of a 3 × 3 Hermitian matrix H expressed in terms of material parameters and crack speed v. For mode I case,

$$G_1 = \frac{1}{4}H_{22}K_I^2 \tag{2.33}$$

where,

$H_{22} = \dfrac{2}{C_{66}R}\eta_{22}\sqrt{2(1+s)/\xi}$ in which R is the Rayleigh wave function

$$R = \eta_{22}\left(\eta_{22}\xi - \rho v^2 / C_{66}\right) - \eta_{12}^2(1 - \rho v^2 / C_{66})/\xi \tag{2.34}$$

and

$$s = \frac{1-\rho v^2/C_{66}+\eta_{11}\eta_{22}(1-\rho v^2/C_{11})-(1+\eta_{12})^2}{2\sqrt{\eta_{11}\eta_{22}(1-\rho v^2/C_{66})(1-\rho v^2/C_{11})}}$$

$$\xi = \sqrt{(1-\rho v^2/C_{11})(1-\rho v^2/C_{66})\eta_{11}/\eta_{22}}\ ,$$

$$\eta_{\alpha\beta} = C_{\alpha\beta}/C_{66},\quad \alpha,\beta = 1, 2. \tag{2.35}$$

where C_{12}, C_{11}, C_{22} and C_{66} are elements of the elastic constants of the orthotropic material. Substituting all the terms into equation (2.33).

$$G_I = \frac{C_{22}}{\sqrt{2}C_{66}^2}\sqrt{(1+s)/\xi K_I^2} \tag{2.36}$$

2.8 Summary

In this chapter a study of impact responses of man made layered materials (layered composite materials) and naturally formed layered materials have been presented based on studies carried out during the last few decades. Geological formations of slate and their characteristic properties, quarry techniques and the industry process of making slate tiles have been discussed. Geographic locations of Newfoundland slate quarries and the types of slate existing in each quarry have been discussed with a brief introduction of quarry management. The failure criteria which are appropriate for rock fracture process such as maximum normal stress criteria, Griffith criteria and fracture mechanics based criteria have been presented highlighting Griffith theory of brittle fracture. Introduction to LEFM with a detailed description of stress intensity factor, its application to analysis of crack growth, and its advantages over critical strain energy release rate have been discussed. Fracture dynamics of brittle materials, criteria for dynamic crack growth and associated factors, dynamic rock cutting process, and experimental methods to determine dynamic stress intensity factors have

been reviewed. While reviewing linear elastic fracture mechanics it is seen that fracture propagation of rock can be predicted using LEFM principles. However, crack initiation cannot be predicted by LEFM due to the development of fracture process zone at the crack tip prior to the propagation of crack into the body.

Chapter 3

Theoretical Background

3.1 General

In this study finite element method is used as the numerical analysis tool to investigate splitting process of slate rock. Many researchers have used this method in studies of cracked bodies to determine crack tip energy release rate, stress intensity factors and other field variables such as stresses, strains, displacements, etc., (Browning, et. al. 2001, Craig, et. al. 1998, Jih and Sun 1990, Shih, et. al. 1986). For stable or unstable running crack problems this method has been used with desired accuracy (Malluck and King 1980, Mall, et. al. 1980, Sun and Hun 2001). Finite element method together with other theoretical developments relevant to the present research are discussed in the following sections to clarify the essential issues involved in the modelling and analysis of the problem. Material classifications, effective modulus theory, behaviour of the cracked body under external loads, finite element formulation of eight-noded isoparametric plane strain element and eight-noded isoparametric solid element and node releasing technique are discussed in this chapter.

3.2 Material classifications in the theory of elasticity

Materials are generally classified as isotropic and anisotropic. In *isotropic material* elastic constants (Young's modulus of elasticity, Poisson's ratio, shear modulus of elasticity) are independent of the co-ordinate system. In reality no material is perfectly isotropic at microscopic level. However, for engineering analysis, most of the materials are considered at macroscopic levels; even laboratory tests are carried out at the same level. In anisotropic materials, elastic constants are dependent on the co-ordinate system, i.e., they change with the changes of the coordinate system. 21 independent elastic constants are required to describe their elastic characteristics properly. These independent constants (instead of 36 elastic constants) are limited by the symmetry of the stress and strain tensors. There are some special forms of anisotropic materials, either man made or naturally formed, which are called *transversely isotropic* and *orthotropic*. In transversely isotropic material, elastic properties in one plane are isotropic and elastic properties perpendicular to this plane are different. In orthotropic material, three mutually perpendicular planes of material symmetry exist. The independent elastic constants needed to describe transversely isotropic material are 5 and for an orthotropic material they are 9. From experimental measurement slate has been observed to conform to a transversely isotropic material characterization.

3.3 Constitutive Equations

Stress and strain relationship within elastic limit (primarily) is obtained through constitutive equations. The general form of this equation is given in tensor notations as,

$$\sigma_{ij} = C_{ijkl}\varepsilon_{kl} \tag{3.1}$$

where, σ_{ij} are the stresses and ε_{kl} are the strains. C_{ijkl} are the elastic constants, it is also called elastic moduli or stiffnesses. It generally requires 36 constants; however, for symmetry conditions, the total independent constant coefficients would get reduced to 21 for a fully anisotropic material, and to 5 for a transversely isotropic material. The elastic constitutive matrix for isotropic, transversely isotropic and orthotropic materials is given in Appendix B.

3.4 Modulus-Anisotropy (Effective Modulus Theory)

Rocks usually consist of a large number of different minerals. Therefore, their elastic moduli (Young's modulus of elasticity, Poisson's ratio and shear modulus of elasticity) vary from point to point. Even if it consisted of a layered material, it could have different mineral compositions in each layer and therefore, different elastic moduli would be required to characterize it properly. The analysis of rock considering different point to point elastic moduli of individual mineral/layer is almost impossible. Effective modulus is sometimes considered as a characteristic modulus of the rock mass and used in mechanical analysis in place of point to point elastic moduli of individual mineral or layer. This effective moduli values, therefore, are dependent upon the contribution of the individual mineral, their relative proportion, shape and orientation and if it is layered rock, the composition of each layer and their orientation. Theoretical analysis of treating rock as a composite material has been limited only to a two-phase system where it is assumed that it consists of elastic granular inclusions surrounded by a matrix having different elastic properties. Many researchers have proposed a number of equations for this (Paul 1960, Lama 1969). However, in most of the cases their application to real problems has not been carried out satisfactorily; but the concept has helped to

demonstrate the existence of modulus anisotropy in rocks, which have preferred orientation of grains of varying shapes. In this sense the layered rock could be considered, as a multi-phase system. The experimental determination of elastic moduli in each layer of the layered rock is very difficult due to thinness of its thickness. Therefore, it is important to use effective modulus for further analysis. The elastic moduli determined experimentally could be considered as effective elastic moduli. Because the moduli are determined for a block of rock that consists of many layers, the entire block deformations perpendicular to the layer direction under an applied load will be the sum of the deformations of the individual layers. From experiments it is only possible to measure total deformation in the direction of applied load and not that of individual layer. Therefore, modulus of a rock specimen determined in an experiment could be considered as an effective modulus. The total applied load will be the sum of the load carried by the individual layers (Lama and Vutukuri, 1978). In the following sections effective Young's modulus of elasticity and shear modulus of elasticity are illustrated for two cases.

Case I - When load is applied perpendicular to the bedding plane

If a layered rock consists of n number of layers having thickness S_1, S_2, S_3 .....S_n and Young's modulus of elasticity E_1, E_2, E_3.....En and subjected to a stress σ in the direction perpendicular to the layering, the deformation of each layer can be written as,

$$\Delta S_1 = \frac{\sigma . S_1}{E_1}$$

$$\Delta S_2 = \frac{\sigma . S_2}{E_2}$$

$$\Delta S_3 = \frac{\sigma . S_3}{E_3}$$
$$---------$$
$$---------$$
$$\Delta S_n = \frac{\sigma . S_n}{E_n} \qquad (3.2)$$

Since the total deformation of the body along the direction of the applied stress will be the sum of the deformation of each plane, therefore, total deformation can be written as,

$$\text{Total deformation} = \sum_{i=1}^{n} \Delta S_i = \left(\frac{\sigma S_1}{E_1} + \frac{\sigma S_2}{E_2} + \frac{\sigma S_3}{E_3} + ------ \frac{\sigma S_n}{E_n} \right)$$

$$\text{or,} \quad \frac{\sum_{i=1}^{n} \Delta S_i}{\sigma} = \left(\frac{S_1}{E_1} + \frac{S_2}{E_2} + \frac{S_3}{E_3} + -------- \frac{S_n}{E_n} \right)$$

$$\text{or,} \quad \sum_{i=1}^{n} S_i \times \frac{\sum_{i=1}^{n} \Delta S_i}{\sum_{i=1}^{n} S_i} \times \frac{1}{\left(\frac{S_1}{E_1} + \frac{S_2}{E_2} + \frac{S_3}{E_3} + ------ + \frac{S_n}{E_n} \right)} = \sigma \qquad (3.3)$$

Since strain is defined as, $\varepsilon = \frac{\sum_{i=1}^{n} \Delta S_i}{\sum_{i=1}^{n} S_i}$ therefore, $E_{eff} = \frac{\sum_{i=1}^{n} S_i}{\left(\frac{S_1}{E_1} + \frac{S_2}{E_2} + \frac{S_3}{E_3} + ---- \frac{S_n}{E_n} \right)}$

could be written as an effective Young's modulus of elasticity. Therefore,

$$\therefore \sigma = E_{eff} \times \varepsilon \qquad (3.4)$$

In case of equal layer thickness, it can be written as,

$$S_1 = S_2 = S_3 \ldots\ldots\ldots = S \text{ and } \sum_{i=1}^{n} S_i = nS \qquad (3.5)$$

Therefore,

$$E_{eff} = \frac{n}{\left(\frac{1}{E_1} + \frac{1}{E_2} + \frac{1}{E_3} + ----\frac{1}{E_n}\right)} \tag{3.6}$$

Similarly it can also be stated that effective shear modulus of elasticity (G_{eff}) is given by,

$$G_{eff} = \frac{\sum_{i=1}^{n} S_i}{\left(\frac{S_1}{G_1} + \frac{S_2}{G_2} + \frac{S_3}{G_3} \ldots\ldots \frac{S_n}{G_n}\right)} \tag{3.7a}$$

where, G_1, G_2, G_3...and G_n are the shear modulus of elasticity of the individual layer.

For the case of equal layer thicknesses,

$$G_{eff} = \frac{n}{\frac{1}{G_1} + \frac{1}{G_2} + \frac{1}{G_3} + \ldots\ldots\ldots + \frac{1}{G_n}} \tag{3.7b}$$

Case II - When load is applied parallel to the bedding plane

In this case, stress distribution within the specimen will vary, but each layer will experience uniform strain. Therefore, total applied force per unit width of the specimen will be the sum of load carried by individual layer. Therefore, it can be written as,

$$F = F_1 + F_2 + F_3 + \ldots\ldots\ldots F_n \tag{3.8}$$

If the thickness of the individual layer is considered as S_1, S_2, S_3,.....S_n and displacement of each layer is considered as Δl, then equation (3.8) can be written for case II as,

$$F = \frac{\Delta l E_{eff} \sum_{i=1}^{n} S_i}{l} = \frac{\Delta l S_1 E_1}{l} + \frac{\Delta l S_2 E_2}{l} + \frac{\Delta l S_3 E_3}{l} + \ldots\ldots\ldots\ldots + \frac{\Delta l S_n E_n}{l}$$

$$\therefore E_{eff} = \frac{S_1E_1 + S_2E_2 + S_3E_3 + ... + S_nE_n}{\sum_{i=1}^{n} S_i} \tag{3.9}$$

In case of equal layer thickness, say, $S_1 = S_2 = S_3 = ... = S$

Therefore, the above equation (3.9) can be written as,

$$E_{eff} = \frac{E_1 + E_2 + E_3 + ... + E_n}{n} \tag{3.10}$$

Similarly, it can be shown that,

$$G_{eff} = \frac{S_1G_1 + S_2G_2 + S_3G_3 + ... + S_nG_n}{\sum_{i=1}^{n} S_i} \tag{3.11}$$

For equal layer thickness,

$$G_{eff} = \frac{G_1 + G_2 + G_3 + ... + G_n}{n} \tag{3.12}$$

3.5 Analysis of Physical System Containing Flaws – An Analytical Approach

The determination of energy supplied by the external forces for deformation of elastic bodies of arbitrary shape is discussed in this section. All bodies are assumed as homogeneous, isotropic and linearly elastic and analysis is done only for two-dimensional problems, either plane stress or plane strain. Assume a body containing a crack of length $2c$ acted upon by a single force, F. Due to this force a displacement δ will be produced at the point of application of force. If k is the stiffness of the body in linear elastic limit, it can be defined as $k = F / \delta$. In general this is a decreasing function of crack length. The variation of stiffness with respect to crack length is shown in Figure 3.1 (Hardy, 1973). The force displacement curve is also shown in the same figure.

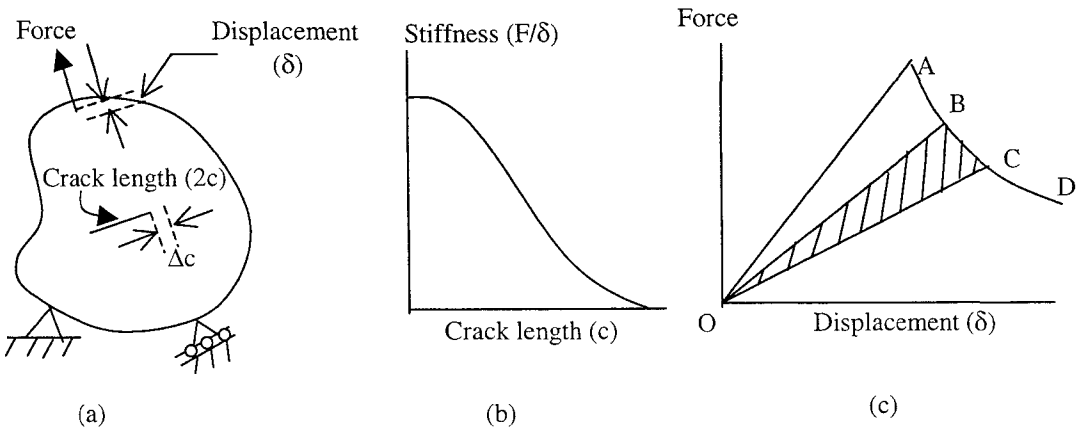

Figure 3.1: Typical crack growth experiment (Hardy, 1973)

The force-displacement curve consists of two parts, initial elastic loading curve and the loci of points for which crack extension occurs. The initial elastic loading path continues until it meets the loci of points of crack extension. The complete force-displacement curve is shown in Figure 3.1 (c). The line *OA* represents the initial elastic loading and its slope is the initial stiffness of the cracked body of crack length equal to *2c*. At point *A* crack growth starts, therefore, *ABCD* represents the locus of points of crack growth. This curve can be obtained by balancing the energy at fracture (equating the change in strain energy of the body and potential energy of the force with the energy absorbed by the body for all increments of crack growth).

The energy absorbed by the body for a change of crack area can be written as, $\gamma\Delta c$ where γ is the specific work of fracture and Δc is the extended crack length. The change in strain energy due to the extension of crack of a length Δc is equal to the area of the shaded part of Figure 3.1 (c). Therefore, at fracture initiation, the energy balance is written as,

$$\text{area } OBC \text{ (incremental work done during crack growth } \Delta c) \geq \gamma\Delta c \qquad (3.13)$$

A unstable crack will be started or stopped when the following criteria is fulfilled

$$\frac{dw_f}{dc} = F\frac{d\delta}{dc} - \frac{dU}{dc} \geq \gamma \tag{3.14}$$

where w_f is the energy available to cause fracture, $F\frac{d\delta}{dc}$ is the change in potential energy of the force F with respect to change in crack length, $\frac{dU}{dc}$ is the change in strain energy (U) of the body as crack grows (strain energy release rate for the fixed grip conditions) and γ is the specific work of fracture. If external force is applied through fixed grips then deflection δ is constant, however force F will decrease due to the growth of crack. Therefore, for fixed grips external loading condition it can be written for elastic body as, $\frac{d\delta}{dc} = 0$ and $U = \frac{F\delta}{2} = \frac{F^2}{2k}$. Hence the equation (3.14) can be expressed as,

$$\frac{dw_f}{dc} = -\frac{dU}{dc} = -\frac{d(F^2/2k)}{dc} \tag{3.15}$$

Since $\delta = \frac{F}{k} = \text{constant}$, therefore,

$$\frac{1}{k}\frac{dF}{dc} = -F\frac{d}{dc}\left(\frac{1}{k}\right) \tag{3.16}$$

After substituting equation (3.16) into the equation (3.15) and applying some mathematical rules, equation (3.15) can be written as,

$$\frac{dw_f}{dc} = -\frac{dU}{dc} = \frac{F^2}{2}\frac{d}{dc}\left(\frac{1}{k}\right) \tag{3.17}$$

Some researchers have also shown the same result for constant load conditions.

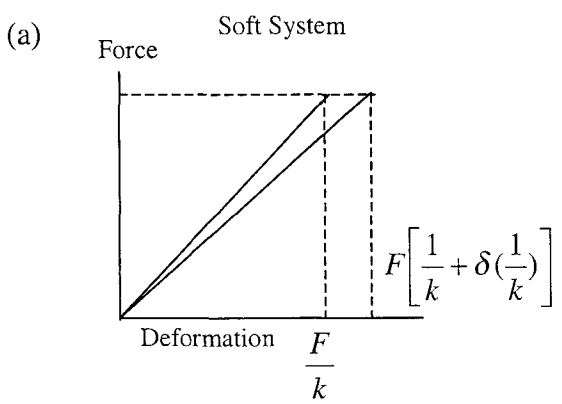

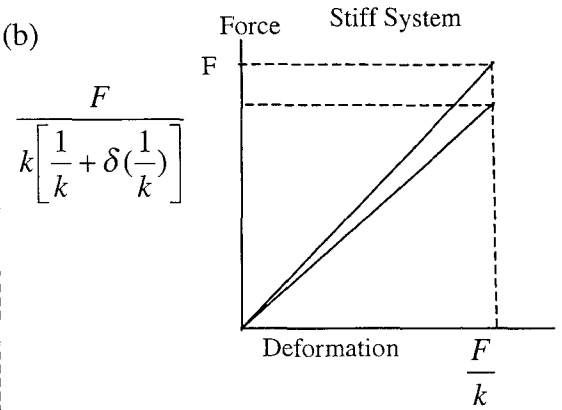

Energy change = $\frac{F}{2}\left\{F\left[\frac{1}{k}+\delta\left\{\frac{1}{k}\right\}\right]-\frac{F}{k}\right\}$

$= \frac{F^2}{2}\delta\left\{\frac{1}{k}\right\}$

Energy change =

$$\frac{F}{2k}\left\{F-\frac{F}{k}\left[\frac{1}{\frac{1}{k}+\delta\left[\frac{1}{k}\right]}\right]\right\}$$

$$=\frac{F^2}{2k}\left\{1-\frac{1}{1+k\delta\left[\frac{1}{k}\right]}\right\}$$

$$= \frac{F^2}{2}\delta\left\{\frac{1}{k}\right\}$$

Figure 3.2: Illustration of the effect of stiffness of the force in the fracture criterion. (Hardy, 1973)

The above discussion on fracture criteria is based on the application of the single load condition. However, this criterion will not change when a body is subjected to *n* forces. When n forces are acting on a body, equation (3.14) is written as,

$$\frac{dw_f}{dc} = F_i \frac{d\delta_i}{dc} - \frac{dU}{dc} \tag{3.18}$$

where F_i are the forces applied at points i, δ_i are the displacements in the direction of F_i at the points i and $i = 1, 2, \ldots\ldots n$. δ_i are related to F_i by the following relation,

$$\delta_i = \lambda_{ij} F_j \tag{3.19}$$

where λ_{ij} is the influence coefficients called compliances. Its values depend on the geometry of the body and the crack length. The strain energy for n applied forces is written as,

$$U = \frac{1}{2} F_i \delta_i = \frac{1}{2} \lambda_{ij} F_i F_j \tag{3.20}$$

After substituting displacement and strain energy expressions from equation (3.19) and (3.20) to (3.18), it can be written as,

$$\begin{aligned} \frac{dw_f}{dc} &= F_i \frac{d\delta_i}{dc} - \frac{1}{2}\frac{d}{dc}\left(F_i \delta_i\right) \\ &= F_i \frac{d}{dc}\left(\lambda_{ij} F_j\right) - \frac{1}{2}\frac{d}{dc}\left(\lambda_{ij} F_i F_j\right) \\ &= F_i F_j \frac{d}{dc}\lambda_{ij} + F_i \lambda_{ij} \frac{d}{dc} F_j - \frac{1}{2}\left(F_i F_j \frac{d}{dc}\lambda_{ij} \right) \\ &\quad + \lambda_{ij} F_j \frac{dF_i}{dc} + \lambda_{ij} F_i \frac{dF_j}{dc} \end{aligned} \tag{3.21}$$

By applying the Maxwell's reciprocal rule $\lambda_{ij} = \lambda_{ji}$ and canceling all terms involving dF_i the equation (3.21) can be written as,

$$\frac{dw_f}{dc} = \frac{1}{2} F_i F_j \frac{d\lambda_{ij}}{dc} \tag{3.22}$$

It is seen from equation (3.22) that the available fracture energy is independent of the type of the application of the force. For a single force system equation (3.22) can be written as,

$$\frac{dw_f}{dc} = \frac{1}{2} F^2 \frac{d\lambda}{dc} = \frac{1}{2} F^2 \frac{d}{dc}\left(\frac{1}{S}\right) \tag{3.23}$$

This is identical to equation (3.17). When applied forces are kept constant the equation (3.22) can be written as,

$$\frac{dw_f}{dc} = \frac{1}{2} F_i F_j \frac{d\lambda_{ij}}{dc} = \frac{d}{dc}\frac{\left(F_i F_j \lambda_{ij}\right)}{2} = \frac{dU}{dc} \tag{3.24}$$

This shows that the energy available to cause fracture is identical to the strain energy release rate. It can be concluded that the application of the energy balance criterion to the bodies, acted upon by a system of forces, could be applied without considering the potential energy changes associated with the applied loads.

3.6 Finite Element Analysis

3.6.1 General

In finite element analysis, the structure under external loads and/or internal body forces is divided into a finite number of elements connected to one another through nodes. According to the philosophy of finite element method nodal displacements of the elements are determined first by inverting of the global stiffness matrix (K), and then multiplying $(K)^{-1}$ by the load vector. Global stiffness matrix is formed from the known element stiffness matrix by the principle of superposition. All loads and boundary conditions are assumed to act through the nodal points. Once displacements and stiffness

matrix are known, the strain energy of the body would be determined directly from the following relationship as,

$$U = \frac{1}{2}\{\delta\}^T [K]\{\delta\} \tag{3.25}$$

where U is the total strain energy of the body, $\{\delta\}$ is the displacement vectors and [K] is the stiffness matrix. By increasing the number of elements within the body, it is possible to improve the accuracy of any field variable. In case of crack problems, reasonable accuracy of field variables (displacements, stresses, strains, etc.) near the crack tip could be achieved either by increasing the density of the elements or using crack tip singular elements in static crack problems. In running crack problems, the application of crack tip singular elements seem to be quite difficult as one needs to keep on changing the nodal coordinates of all the crack tip elements (one side of all elements joining at the crack tip is cracked and the midside nodes on this side need to be moved to the one quarter point nearest the crack tip); therefore, conventional elements with high element density near the crack propagation region are preferred (instead of singular elements) to analyze the problem. Many researchers have used FEM to determine stress intensity factor/energy release rate at the crack tip using conventional elements (Chan, et. al. 1970, Weber 1971, Sun and Hun 2001). Mall and Luz (1980) simulated fast fracture problems using eight-noded 2D elements, based on the concept of the sequential release of nodes along the crack path. They analyzed a uniformly expanding crack in a square region subjected to uniform tension on the edges parallel to the crack path. They used very stiff massless truss elements to constrain the vertical nodal displacements along the crack path. They computed energy release rate for each increment of crack extension from the global energy balance involving strain energy, kinetic energy and potential energy of remote

loads. In order to avoid displacement incompatibility, both corner and midside nodes were released simultaneously. They concluded that eight-noded elements can be safely employed for crack propagation problems with relaxation technique only when both corner and midside nodes are released simultaneously. The sequential node release technique along the crack front, using conventional 8 noded isoparametric rectangular and 6 noded triangular plane strian elements (in two dimensions) and 8 noded isoparametric brick and 6 noded wedge elements (in three dimensions), has been applied in the present study to simulate crack propagation in plane strain/non plane strain analysis. The finite element formulation for these elements is given below.

3.6.2 Isoparametric Formulation of Two-Dimensional Plane Strain Element

In plane strain problem strains (ε_z, γ_{xz} and γ_{yz}) perpendicular to the plane are assumed to be zero or constant. Examples of plane strain problems are dam, pipe, retaining wall, etc. In this problem the body's cross section has to be constant along the length direction (z) and load acts only either in x or y or x and y directions of plane xy and has to be constant along the length direction. The advantage of plane strain problem is that one needs to discretize the cross section only due to its identical section along the transverse z-direction; thickness of the cross section is considered as unity. Six noded linear strain triangular and eight noded quadrilateral isoparametric elements (Figure 3.3) are used to analyze plane strain problems in the present study. The formulation of six noded linear strain triangle is available in any text book (Logan, 2002). Therefore, it is not described in the present study. In this section isoparametric formulation of eight noded quadrilateral element is presented. The shape functions used to describe element geometry are also used to define the displacements within the element for this case. It can be used to create

nonrectangular side as well as curved sides by using higher order elements which brings convergence at a faster rate using fewer elements.

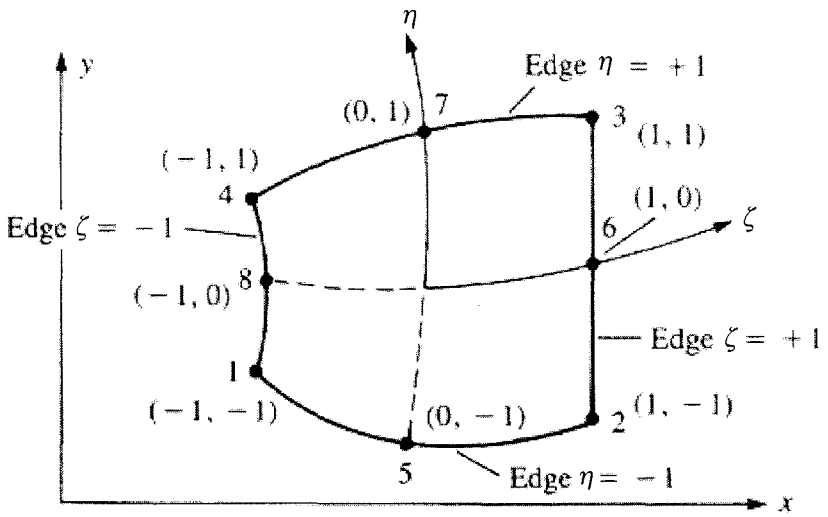

Figure 3.3: Quadratic isoparametric element (Logan, 2002)

The shape functions for the corner nodes, using compact index notation, are assumed as,

$$N_i = \frac{1}{4}(1+\zeta\zeta_i)(1+\eta\eta_i)(\zeta\zeta_i+\eta\eta_i-1) \tag{3.26}$$

where i is the number of shape functions used (i = 1, 2, 3, 4),

ζ_i = -1, 1, 1, -1 (i = 1, 2, 3, 4)

η_i = -1, -1, 1, 1 (i = 1, 2, 3, 4)

For mid side nodes

$$N_i = \frac{1}{2}(1-\zeta^2)(1+\eta\eta_i) \qquad \eta_i = -1,1 \qquad (i = 5, 7)$$

$$N_i = \frac{1}{2}(1-\zeta\zeta_i)(1+\eta^2) \qquad \zeta_i = 1,-1 \qquad (i = 6, 8) \tag{3.27}$$

where ζ and η are natural coordinates. Variation of shape functions should be N_i = 1 at node i, and N_i = 0 at all the other nodes.

The element geometry is defined in global coordinate system as,

$$\begin{Bmatrix} x \\ y \end{Bmatrix} = \begin{bmatrix} N_1 & 0 & N_2 & 0 & N_3 & 0 & N_4 & 0 & N_5 & 0 & N_6 & 0 & N_7 & 0 & N_8 & 0 \\ 0 & N_1 & 0 & N_2 & 0 & N_3 & 0 & N_4 & 0 & N_5 & 0 & N_6 & 0 & N_7 & 0 & N_8 \end{bmatrix} \times \begin{Bmatrix} x_1 \\ y_1 \\ x_2 \\ y_2 \\ . \\ . \\ y_8 \end{Bmatrix} \tag{3.28}$$

The displacement functions are written as,

$$\begin{Bmatrix} u \\ v \end{Bmatrix} = \begin{bmatrix} N_1 & 0 & N_2 & 0 & N_3 & 0 & N_4 & 0 & N_5 & 0 & N_6 & 0 & N_7 & 0 & N_8 & 0 \\ 0 & N_1 & 0 & N_2 & 0 & N_3 & 0 & N_4 & 0 & N_5 & 0 & N_6 & 0 & N_7 & 0 & N_8 \end{bmatrix} \times \begin{Bmatrix} u_1 \\ v_1 \\ u_2 \\ v_2 \\ . \\ . \\ v_8 \end{Bmatrix} \tag{3.29}$$

i. e.,

$$\begin{aligned} u &= N_1u_1 + N_2u_2 + N_3u_3 + N_4u_4 + N_5u_5 + N_6u_6 + N_7u_7 + N_8u_8 \\ v &= N_1v_1 + N_2v_2 + N_3v_3 + N_4v_4 + N_5v_5 + N_6v_6 + N_7v_7 + N_8v_8 \end{aligned} \tag{3.30}$$

Therefore,

$$\varepsilon_x = \frac{\partial u}{\partial x} = \frac{\partial N_1}{\partial x}u_1 + \frac{\partial N_2}{\partial x}u_2 + \frac{\partial N_3}{\partial x}u_3 + \ldots\ldots + \frac{\partial N_8}{\partial x}u_8$$

$$\varepsilon_y = \frac{\partial v}{\partial x} = \frac{\partial N_1}{\partial x}v_1 + \frac{\partial N_2}{\partial x}v_2 + \frac{\partial N_3}{\partial x}v_3 + \ldots\ldots + \frac{\partial N_8}{\partial x}v_8$$

and,

$$\gamma_{xy} = \frac{\partial u}{\partial y} + \frac{\partial v}{\partial x} = \frac{\partial N_1}{\partial y}u_1 + \frac{\partial N_1}{\partial x}v_1 + \frac{\partial N_2}{\partial y}u_2 + \frac{\partial N_2}{\partial x}v_2 + \ldots\ldots + \frac{\partial N_8}{\partial y}u_8 + \frac{\partial N_8}{\partial x}v_8 \qquad (3.31)$$

The strain displacement relationship is,

$$\{\varepsilon\} = \begin{Bmatrix} \varepsilon_x \\ \varepsilon_y \\ \gamma_{xy} \end{Bmatrix} = \begin{Bmatrix} \dfrac{\partial u}{\partial x} \\ \dfrac{\partial v}{\partial y} \\ \dfrac{\partial u}{\partial y} + \dfrac{\partial v}{\partial x} \end{Bmatrix} \qquad (3.32)$$

$$\begin{Bmatrix} \varepsilon_x \\ \varepsilon_y \\ \gamma_{xy} \end{Bmatrix} = \begin{bmatrix} \dfrac{\partial N_1}{\partial x} & 0 & \dfrac{\partial N_2}{\partial x} & 0 & \ldots\ldots & \dfrac{\partial N_8}{\partial x} & 0 \\ 0 & \dfrac{\partial N_1}{\partial y} & 0 & \dfrac{\partial N_2}{\partial y} & \ldots\ldots & 0 & \dfrac{\partial N_8}{\partial y} \\ \dfrac{\partial N_1}{\partial y} & \dfrac{\partial N_1}{\partial x} & \dfrac{\partial N_2}{\partial y} & \dfrac{\partial N_2}{\partial x} & \ldots\ldots & \dfrac{\partial N_8}{\partial y} & \dfrac{\partial N_8}{\partial x} \end{bmatrix} \begin{Bmatrix} u_1 \\ v_1 \\ u_2 \\ v_2 \\ \ldots \\ \ldots \\ u_8 \\ v_8 \end{Bmatrix} \qquad (3.33)$$

Using equation (3.33), the strain-displacement equation can be written as,

$$\{\varepsilon\} = [B]\{d\} \qquad (3.34)$$

where {d} as the nodal displacements vector.

From equation (3.33) it is seen that shape functions need to be derived with respect to global coordinates. The derivative of shape functions with respect to global coordinate can be obtained if its derivative with respect to natural coordinates is known. Since, shape

functions are written in terms of natural coordinates, therefore its derivative is known. However, by applying chain rule the derivative with respect to global coordinates can be obtained.

$$\frac{\partial N_1}{\partial \zeta} = \frac{\partial N_1}{\partial x}\frac{\partial x}{\partial \zeta} + \frac{\partial N_1}{\partial y}\frac{\partial y}{\partial \zeta}$$
$$\frac{\partial N_1}{\partial \eta} = \frac{\partial N_1}{\partial x}\frac{\partial x}{\partial \eta} + \frac{\partial N_1}{\partial y}\frac{\partial y}{\partial \eta} \tag{3.35}$$

or

$$\begin{Bmatrix} \frac{\partial N_1}{\partial \zeta} \\ \frac{\partial N_1}{\partial \eta} \end{Bmatrix} = \begin{bmatrix} \frac{\partial x}{\partial \zeta} & \frac{\partial y}{\partial \zeta} \\ \frac{\partial x}{\partial \eta} & \frac{\partial y}{\partial \eta} \end{bmatrix} \begin{Bmatrix} \frac{\partial N_1}{\partial x} \\ \frac{\partial N_1}{\partial y} \end{Bmatrix} \tag{3.36}$$

$$\therefore \begin{Bmatrix} \frac{\partial N_1}{\partial x} \\ \frac{\partial N_1}{\partial y} \end{Bmatrix} = [J]^{-1} \begin{Bmatrix} \frac{\partial N_1}{\partial \zeta} \\ \frac{\partial N_1}{\partial \eta} \end{Bmatrix} \tag{3.37}$$

where J is called Jacobian Matrix. Therefore, the constitutive relationship can be written as,

$$\sigma = D\varepsilon \tag{3.38}$$

where D is called the stress/strain matrix or constitutive matrix. The constitutive matrices for isotropic and transversely isotropic plane stress or plane strain idealization are given in Appendix B.

The element stiffness matrix is then calculated as,

$$K^e = \int_{V_e} B^T DB dV = t\int_{-1}^{1}\int_{-1}^{1} B^T DB|J|d\zeta d\eta \tag{3.39}$$

where t is the thickness of the body; numerical integration using Gaussian-quadrature method is utilized in evaluating the individual terms of the stiffness matrix.

3.6.3 Isoparametric Formulation of Three Dimensional Brick Element

The term *3D* solid means a three-dimensional solid. Due to the three-dimensional coordinate representation they are unrestricted as to shape, loading, material properties, and boundary conditions. A consequence of this generality is that all six possible stresses (three normal and three shear stresses) and the displacement fields involving all three possible components, u, v, and w are taken into account. Tetrahedral and hexahedral elements, with three translational degrees of freedom (*d.o.f*) per node, are usually considered as typical finite elements for *3D* solids. The general three-dimensional bodies that require more precise analysis (stress-strain, displacement) which is not possible through two-dimensional and/or axisymmetric analyses would be analyzed using these elements. The isoparametric formulation of the stiffness matrix for 8 noded brick elements is given below; twenty-noded elements were not considered in the study since it would be impossible to solve the problems considered in this study due to computer space limitations. The natural coordinates represented by ζ, η and z′, are shown in Figure 3.4.

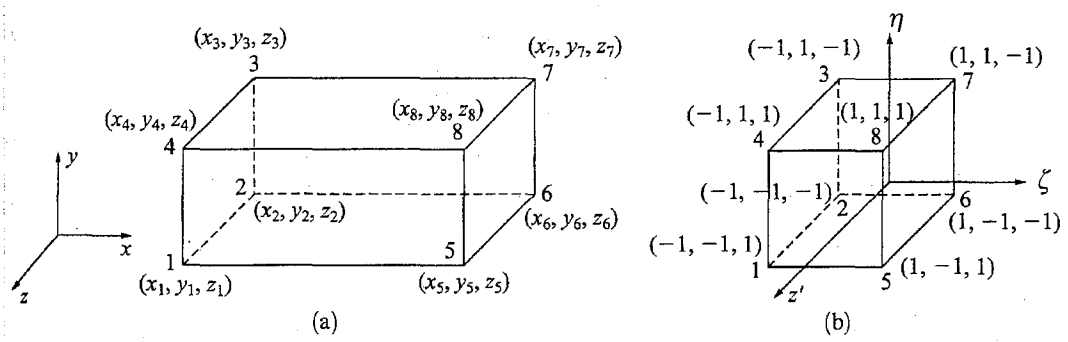

Figure 3.4: Node numbering, global-coordinate system (a) and the isoparametric co-ordinate (b) representation of linear hexahedral element (Logan, 2002).

The element geometry is defined in global coordinates by the following relation,

$$\begin{Bmatrix} x \\ y \\ z \end{Bmatrix} = \sum_{i=1}^{8} \left(\begin{bmatrix} N_i & 0 & 0 \\ 0 & N_i & 0 \\ 0 & 0 & N_i \end{bmatrix} \right) \begin{Bmatrix} x_i \\ y_i \\ z_i \end{Bmatrix} \tag{3.40}$$

where N_i (i=1,2,3....8). The shape functions are written as,

$$N_i = \frac{(1+\zeta\zeta_i)(1+\eta\eta_i)(1+z'z_i')}{8} \tag{3.41}$$

The displacement functions are defined as,

$$\begin{Bmatrix} u \\ v \\ w \end{Bmatrix} = \sum_{i=1}^{8} \left(\begin{bmatrix} N_i & 0 & 0 \\ 0 & N_i & 0 \\ 0 & 0 & N_i \end{bmatrix} \right) \begin{Bmatrix} u_i \\ v_i \\ w_i \end{Bmatrix} \tag{3.42}$$

where N_i are the same functions that are defined in equation (3.41)

The strain displacement relationship is given by,

$$\{\varepsilon\} = \begin{Bmatrix} \varepsilon_x \\ \varepsilon_y \\ \varepsilon_z \\ \gamma_{xy} \\ \gamma_{yz} \\ \gamma_{zx} \end{Bmatrix} = \begin{Bmatrix} \dfrac{\partial u}{\partial x} \\ \dfrac{\partial v}{\partial y} \\ \dfrac{\partial w}{\partial x} \\ \dfrac{\partial u}{\partial y} + \dfrac{\partial v}{\partial x} \\ \dfrac{\partial v}{\partial z} + \dfrac{\partial w}{\partial y} \\ \dfrac{\partial w}{\partial x} + \dfrac{\partial u}{\partial z} \end{Bmatrix} \tag{3.43}$$

Using equation (3.42), equation (3.43) can be written as,

$$\{\varepsilon\} = [B]\{d\} \tag{3.44}$$

where $[B] = [\underline{B}_1 \quad \underline{B}_2 \quad \underline{B}_3 \quad \underline{B}_4 \quad \underline{B}_5 \quad \underline{B}_6 \quad \underline{B}_7 \quad \underline{B}_8]$

Therefore, $\underline{B}_1$ can be written as,

$$\underline{B}_i = \begin{bmatrix} N_{1,\zeta} & 0 & 0 \\ 0 & N_{1,\eta} & 0 \\ 0 & 0 & N_{1,z'} \\ N_{1,\zeta} & N_{1,\eta} & 0 \\ 0 & N_{1,z'} & N_{1,\eta} \\ N_{1,z'} & 0 & N_{1,\zeta} \end{bmatrix} \tag{3.45}$$

where the comma after the subscript indicates differentiation with respect to the variable that follows. Therefore, in index form the coefficient of $[B]$ matrix can be shown to be,

$$\underline{B}_i = \begin{bmatrix} N_{i,\zeta} & 0 & 0 \\ 0 & N_{i,\eta} & 0 \\ 0 & 0 & N_{i,z'} \\ N_{i,\zeta} & N_{i,\eta} & 0 \\ 0 & N_{i,z'} & N_{i,\eta} \\ N_{i,z'} & 0 & N_{i,\zeta} \end{bmatrix} \tag{3.46}$$

The element stresses are related to the element strains by,

$$\{\sigma\} = [D]\{\varepsilon\} \tag{3.47}$$

where $[D]$ is the constitutive matrix. The constitutive matrix for three-dimensional elastic isotropic material and transversely isotropic material are given in Appendix B.

The element stiffness matrix is written as,

$$[k] = \int_{-1}^{1}\int_{-1}^{1}\int_{-1}^{1} [B]^T [D][B] J | d\zeta d\eta dz' \tag{3.48}$$

where Jacobian matrix $[J]$ in local coordinate (ζ, η, z') system is given by,

$$[J]=\begin{bmatrix} \frac{\partial x}{\partial \zeta} & \frac{\partial y}{\partial \zeta} & \frac{\partial z}{\partial \zeta} \\ \frac{\partial x}{\partial \eta} & \frac{\partial y}{\partial \eta} & \frac{\partial z}{\partial \eta} \\ \frac{\partial x}{\partial z'} & \frac{\partial y}{\partial z'} & \frac{\partial z}{\partial z'} \end{bmatrix} \tag{3.49}$$

$|J|$ is the determinant of the Jacobian matrix, $[B]$ the element matrix in isoparametric natural coordinate system and $[D]$ the constitutive matrix.

The order of element stiffness matrix in equation (3.48) is 24×24. In order to obtain this matrix, one needs to perform integration of equation (3.48); however, this process is very tedious and difficult to perform. Therefore, numerical integration is used to obtain the terms of the element stiffness matrix $[\underline{k}]$. This matrix for a 8-noded linear solid isoparametric element can be evaluated by the following Gaussian quadrature rule:

$$\underline{k} = \sum_{i=1}^{n} \underline{B^T}(\zeta_i, \eta_i, z_i')\underline{DB}(\zeta_i, \eta_i, z_i')|J(\zeta_i, \eta_i, z_i')|W_i W_j W_k \tag{3.50}$$

where n is the number of integration points and W_i, W_j, W_k are the associated weights. The number of integration points considered in the ABAQUS finite element package software for 8-noded element and reduced integration element are 2×2×2, and 1×1×1, respectively. In case of 8 Gaussian points integration, the weights $W_i = W_j = W_k = 1$. Once the element stiffness matrix is computed, global stiffness matrix is obtained by applying superposition principle and nodal displacements are calculated from the known value of stiffness matrix and load (including traction and body forces). The crack tip stress at the intensity factors are calculated based on stress, strain and displacement

fields developed crack tip by using the contour integral described earlier in section 2.6.12.

3.7 The Near Crack Tip Nodal Force in Node Release Technique

Node release technique is used to simulate plane crack propagation in a body. A finite element model near the crack tip for a problem having elastodynamic symmetry about the crack plane is shown in Figure 3.5. Here crack-tip trajectory is made to coincide with the symmetric axis of the model. In node release technique, crack tip moves after a time interval by passing the location of node *A* and proceeding to the location of the neighborhood node *B* in the finite element model. In this case, the restraint force of node A, F, decays from the magnitude F_0, which is computed at the instant prior to the release of node *A*, to zero. The variation of the restraining force (from F_0 to zero) is taken differently by different researchers.

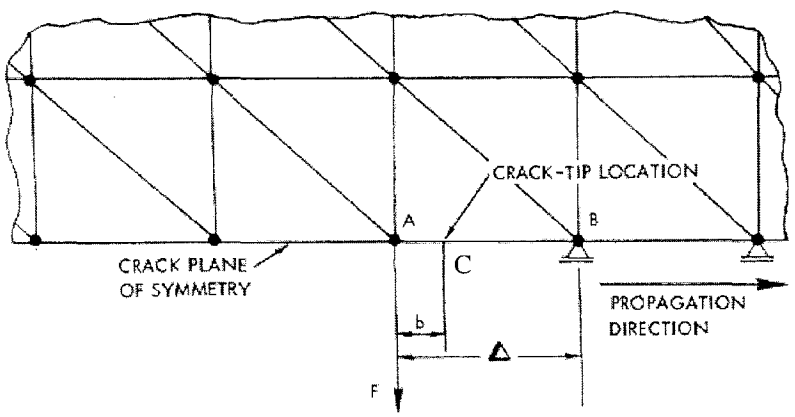

Figure 3.5: Crack tip neighborhood of finite-element model

Two types of algorithms were discussed by Malluck and King (1980). One was proposed by Malluck and King and named *MK* and other by Rydholm, Fredriksson, and Nilsson

and named *RFN*. *MK* used the following relationship between restraining force F, which decayed gradually and the reaction force F_0 based on some assumptions. They assumed a constant stress-intensity factor when crack tip moves from one node to the other and a linearly varying displacement between the nodes.

$$\frac{F}{F_0} = \left[1 - \frac{b}{\Delta}\right]^{3/2} \tag{3.51}$$

where b is the distance from node A to the crack tip and Δ the distance between the nodes. F is the virtual-work-consistent nodal force appropriate to a singular external traction field travelling in advance of the crack tip.

In *RFN*'s formulation F is allowed to decay in such a way that energy-release rate is kept constant in the finite element model when the quasi-static crack tip travel between nodes A and B, while prescribed remote loads or displacements are held constant. According to *RFN* algorithm the variation of F is written as,

$$\frac{F}{F_0} = \left[1 - \frac{b}{\Delta}\right]^{1/2} \tag{3.52}$$

Figure 3.6 shows the variations of nodal force with crack-tip location for MK and RFN algorithm. It is seen that in *MK*'s formulation the force decays more rapidly at the beginning of the interval of extension and the other decays more rapidly at the end of the interval. In the present study, ABAQUS finite element software is used to determine integration point stresses in local directions and mode I stress intensity factor as crack propagated dynamically in the slate block during impact splitting. It appears from ABAQUS analysis results that variation of released force with respect to time (at the relaxed node just before the crack tip node) follows a straight line as crack tip moves.

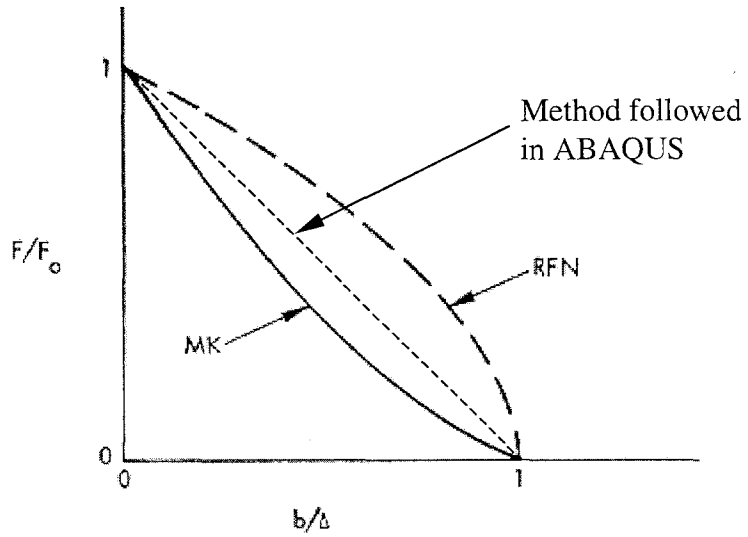

Figure 3.6: Variation of nodal force with crack-tip location

3.8 Summary

At the beginning of this chapter, relevant material characterization (required for slate material) and constitutive equations are reviewed. Effective modulus theory and the fundamentals of the analysis of the physical system having interior cracks have been discussed. Basic finite element method with the formulation of eight-noded isoparametric plane strain elements and eight-noded 3D isoparametric brick elements have been reviewed for isotropic materials as well as for transversely isotropic materials. Node release technique that is used to simulate dynamic crack propagation in a plane or three-dimensional transversely isotropic material has also been discussed to illustrate the load transferring mechanism from released node to crack tip node.

Chapter 4

Experimental Determination of Properties and Splitting Forces of Slate Rock

4.1 General

The experimental investigations described in this chapter were carried out to determine different material properties and splitting forces of naturally bedded layered slate rock, required to validate the results of subsequent numerical analyses. A full-fledged experimental program would require an extensive test program, using variable sizes and shapes of specimens from a very small scale to a large scale. In this study, an optimum number of small scale test specimens were tested, as suggested by ASTM (American Society for Testing and Materials) D 3148 – 80, D 2930 – 78, C 120 – 52, C 170 – 50, C 406 – 58, C 1327 – 99, C 1421 – 99, E 384 – 99 and E 140 – 97, 2000 and ISRM [International Society for Rock Mechanics - Fracture toughness suggested methods (1988)]. Most of the tests were conducted following the specifications established by ASTM and ISRM.

4.2 Outline of the Experiments

The entire test program was divided into five separate groups based on their similarity in test procedures. Determination of modulus of elasticity, Poisson's ratio, compressive and

tensile strengths, hardness and coefficient of friction were taken as group # 1. Fracture toughness test was considered as group # 2. Group # 3 considered the measurement of crack propagation velocities in plane strain and non-plane strain specimens during impact splitting. Microscopic investigations to determine grain sizes, intergranular characteristics (microcrack at the grain boundaries), discontinuities in the material/layer, layer thickness and homogeneity of layer were taken as group # 4. Splitting tests, which were the main focus of this research, were considered to be part of group # 5. Specimen preparation, test set up, testing procedures, plotting and interpretation of results are given in sections 4.5 and 4.6.

Determination of fracture toughness of slate material was one of the most important tests carried out in this investigation. Fracture propagation criterion was established based on the results obtained from this test. Special care had to be taken at every stage of this test, from the preparation of specimen to the completion of the test program, including instrumentation set up, loading rate, calibration of instruments, data acquisition, plotting and interpretation of test results. Beam bending (three/four point bending) experiments were carried out to determine the fracture toughness of slate material and details of specimen preparation and testing procedures are given in section 4.7.

Crack propagation velocities were measured using strain gauge sensors attached to the test specimens at very close intervals along the direction of the crack propagation and perpendicular to the crack. Details of this test program are given in section 4.8.

The physical properties, which could not be determined from macroscopic investigations of the material, such as mineral contents, grain size, texture and micro crack were

determined through a micro-photographic study of the material. Thin sections were carefully prepared to carry out these studies. Scanning Electron Microscope (SEM) was used for this purpose. Test procedure, analysis of microscopic sections and results obtained from this study are reported in section 4.9.

Impact splitting of regular sized slate blocks for plane strain and non plane strain (typical three dimensional slate blocks) tests were carried out to determine the breaking loads of slate blocks. These results were used for validating the results of numerical studies carried out on finite sized slate blocks for the subsequent parametric study. Instrumentation, test set up, data acquisition, analysis systems and discussion of test results are given in section 4.10.

4.3 Experimental Equipment

To carry out all of the laboratory tests mentioned above, except the microscopic investigation, one needs to apply forces on the test specimen and measure the resultant displacements and/or strains at requisite locations. A *servo-controlled (electro-hydraulic) testing machine (either a universal testing machine or a hydraulic actuator with servo control system)* was used to apply force to the specimens. *Strain gauges and LPDTs* (Linear Potentiometer Displacement Transducer) were used to measure strains and displacements. In the servo-controlled testing machine, experimental outputs were given as functions of time. A *strain gauge based load cell transducer* placed in series with the test specimen was used to record the force obtained during the test program. Before obtaining the results the load cell had to be calibrated using a standard calibration method provided by the manufacturing company. A *wedge shape indentor* (shown later in Figure 4.19 (a))

was used to carry out impact splitting tests on different sizes of slate blocks. *LabView data acquisition and analysis software* (1999) was used to acquire results from the experiment in a usable format after applying relevant conversion factors to the voltage signals obtained from electrical sensors or transducers. Thereafter, results were stored in a *computer* for further analyses and plotting.

4.4 Instrument Calibration

Before using any instrument one should make sure whether it works accurately or not, and hence one needs to calibrate all the equipment used in the study prior to performing the tests. LPDT, strain gauges and load cell (strain gauge based) transducers were used to gather results from the tests through LabView data acquisition software. The calibration procedure used in the present study for these instruments are given in the subsequent sections.

4.4.1 Strain Gauges

Strain gauges were used to measure velocities of dynamic crack propagation during the splitting tests on slate blocks. It was also used to determine the elastic moduli, Poisson ratio, and fracture toughness of the test material. Four different types of axial strain gauges were used in the present test program. They were referenced as the number C6-1161-B, CEA-06-500UW-120, EA-15-500BH-120 and EA-06-240LZ-120. The first three gauges were used to determine the velocity of the crack while the last type was used to determine the mechanical properties of slate. All types of gauges were made by Micro-Measurement Division of Measurements Group, Inc., USA. The data related to the properties of gauges are given in Table 4.1, in which gauge factor is defined as,

$F = \frac{\Delta R / R}{\Delta L / L}$, where R = initial resistance, ΔR = change in resistance, L = original length, ΔL = change in length.

Table 4.1: Properties of strain gauges used at 24^0C

Gauge Type	Gauge length	Resistance	Gauge Factor	Transverse Sensitivity
C6-1161-B	Not available	120±0.2%	2.060±0.5%	Not available
CEA-06-500UW-120	6 mm	120±0.3%	2.045±0.5%	-0.4%
EA-15-500BH-120	15 mm	120±0.15%	2.115±0.5%	0.0%
EA-06-240LZ-120	6 mm	120±0.3%	2.060±0.5%	(+0.2±0.2)%

4.4.2 LPDT, Strain Gauge and Load Cell Calibration

LPDTs (as a substitute for LVDT), strain gauges and the load cell were calibrated according to standard calibration procedures supplied by the manufacturing company. Since all of these sensors and transducers were electronic devices, the data obtained from those instruments consisted of readings in voltages units; this voltage value had to be converted to the physically measured values by appropriate conversion factors. The acquired voltage unit was converted to some relevant engineering unit such as, mm or inch (displacement), micro strain (strain) and lbs or N (load) by multiplying it with the conversion factor, obtained through calibration procedures. To obtain the conversion factor for *LPDT* (linear potentiometer displacement transducer) in the data acquisition system, the *LPDT* was connected to the data acquisition board and its core was moved

through a defined displacement and the distance travelled was measured by a slide caliper having micrometer reading device. The voltage change developed by the LPDT due to the movement of core was then correlated to the measured displacement. Linear relationship was observed to exist within a displacement range of – 0.025 (0.635 mm) to 0.025 inch (0.635 mm). A curve was plotted using the data obtained from slide calipers reading and the corresponding voltage change; the slope and intercept of the curve were determined and used as conversion factors. A 2.5 mm movement of *LPDT* core caused a change in voltage signal 1 volt. Therefore, a factor 2.5 was considered as a conversion factor for *LPDT* reading.

Change of voltage signal to the corresponding microstrain (for the specific strain gauge) was accomplished by using a conversion factor in the Labview data acquisition software. The factor used in this case was 5milli-volt = 1000 micro-strain (user manual, LabView 5.4). In order to prove this a digital strain gauge calibrator was used. After connecting the two output ends of the strain gauge with the Labview data acquisition board, the positive and negative ends of the strain gauge calibrator were connected to the strain gauge terminal. The calibrator showed 1000 micro strains in the data acquisition system for a 5 milli-volt potential difference.

All strain gauge load cells were calibrated using a Universal Testing Machine (UTM) that was calibrated by the National Bureau of Calibration, Canada. This machine (UTM) is usually calibrated once a year. Before testing, a calibration chart was made by making comparison of values obtained from the load cell and UTM. It was observed that load - voltage curve showed a linear relationship up to certain portion of the applied load. On

the basis of this linearity a conversion factor was obtained and used in LabView data acquisition software to compute the equivalent load of voltage signal.

A conversion factor of 1000 lbf (4448.2 N) = 1 volt for the 10 kips load cell [and 2200 lbf (9786 N) = 1 volt for 22 kips (97.86 kN) load cell] was applied to the data acquisition system to obtain the applied load (in lbs) from the tests. In order to make sure that the measured load was correct, the load cell was connected to an MTS 407 controller and load was applied on the load cell through the controller. It was observed that the loads acquired through the load cell using data acquisition system showed exactly the same load as applied by the controller.

4.5 Experimental Investigations on Various Mechanical Properties of Slate

The experimental procedures outlined in this section were used to determine the characteristic mechanical properties of slate rock, mentioned as group # 1 in section 4.2. Specimen preparation, experimental setup, testing procedures, data acquisition, analysis methodology and interpretation of test results are given below. Most of these tests were carried out in the Strength Laboratory, Faculty of Engineering and Applied Science, Memorial University of Newfoundland.

4.5.1 Preparation of the Test Specimen

Test specimens to measure the various mechanical properties of the slate material were made from large-sized irregular blocks of slate bought from Carew Services, Portugal Cove, St. John's, and regular-sized blocks supplied by Hurleys Slateworks Company (free samples supplied), Manuels, St. John's, NL, Canada. The initially trimmed samples

were stored at the laboratory in a container, filled with water to ensure that the slate remained moist till the time of testing. Specimens were then cut using water-cooled diamond bladed circular saw to various sizes and again stored in water until they were tested. The following sub-sections give the procedures used in the preparation of specimens for individual test programs.

4.5.2 Tests for Elastic Constants

The mechanical properties such as elastic moduli and Poisson's ratio of slate rock were determined by using rectangular prismatic specimens (compression tests); they were cut from a large block of slate approximately 12″ × 12″ × 4.5″ (0.305 m × 0.305 m × 0.305 m) in size. The prismatic specimens were sawed perpendicular and parallel to the three planes of symmetry. Prismatic cross sectional specimens, with a length to width ratio 2.0 to 2.5 and a width of not less than 2 inches were prepared for these tests. Six specimens of size 2″ × 2″ × 4.5″ (0.051 m × 0.051 m × 0.114 m) were tested to determine elastic moduli parallel to the layer. However, elastic moduli perpendicular to the layer was determined using cylindrical core specimens of size 1.375 inch (0.035 m) in diameter and 2.8 inch (0.071 m) in length (length to diameter ratio of 2.0 to2.5 as suggested by ASTM D 3148 – 80). All surfaces of the experimental specimens were properly finished using water-cooled grinders. Finishing of the specimen ends is very important, since ridges and hollows at the specimen ends would form points of stress concentration that could cause failure of specimens at relatively low loads. Finishing of edges is also important for proper attaching of strain gauges. Therefore, special care was taken during grinding of edges and the ends of the specimens. Stiff rubber pads (almost of the same size as the specimen) were used at the top and the bottom ends of the specimen during the test to

properly distribute the load over the area (Vutukuri, et. al. 1974, Vol. 1, page-22). Totally eighteen specimens were prepared, twelve specimens were tested for determining in-plane elastic constants and six were tested for measuring elastic properties perpendicular to the bedding plane.

The test method recommended by ASTM standard D 3148-80 (1984), for the elastic moduli of intact rock core specimens under uniaxial compression, was followed to determine the elastic constants of slate. Tests were carried out in three mutually perpendicular directions to see whether slate was a transversely isotropic or orthotropic material. Due to some fabrication difficulties (cylindrical core could not be made by drilling rock in a direction parallel to the layer), rectangular prisms were used instead of cylindrical cores. Four strain gauges were glued at the mid height of the front and back faces of each specimen (to avoid stress concentration, i.e., high stress gradients near the specimen ends in uniaxial compression tests), parallel and perpendicular to the axis of loading. Of the four, two strain gauges were glued in the direction parallel to the axis of loading and the other two were glued in the direction perpendicular to the axis of loading. At first a Lepage-12, 5 minute epoxy syringe glue was spread as a thin film on the surfaces of the slate to position the gauges. Thereafter, it was allowed to dry for 24 hours. After glue had dried, a smooth surface was generated by polishing the glued surface with fine grit sandpaper. M-Prep Conditioner A and M-Prep Neutralizer 5 (by M-Line) were then applied successively to the polished surface. The strain gauge was then taped and placed in position where it had to be fixed on the polished surface. Thereafter, the tape was lifted up and M-Bond 200 adhesive was applied to the surface of the slate and 200 Catalyst was applied to the back surface of the strain gauge; after 30 seconds the back

surface of strain gauge got air dried completely. The gauge was then re-taped to the surface of the specimen and external pressure was applied using the thumb (finger) for approximately 1 minute to allow the adhesive to set. After a few minutes the tape was taken away and wires were soldered to the gauge. A multimeter was used to check the resistance of the strain gauge to see whether it is the same as the listed resistance of the strain gauge; in addition it also verifies the continuity of wires in gauge. For proper bonding strain gauge resistance before and after making the connections should show the same values. The gauge wires were then connected to the data acquisition board that was already connected to the computer.

The strain gauged slate specimen was then fixed in between the two compression platens of the compression testing machine (shown in Figure 4.1) and care was taken to see that the sample was aligned centrally in the machine. As mentioned early, thin and stiff rubber strips were placed on the top and bottom loading surfaces (to eliminate stress concentration locations), before load was applied through the machine. The magnitude of the load was obtained from the computer by connecting the calibrated load cell/UTM to the data acquisition board and the computer. Load was applied at a constant rate of 100 lbs/sec. Young's modulus of elasticity (E) and Poisson's ratio (ν) were determined from the stress-strain curve obtained from this test. Axial stress was determined by dividing the load by the cross sectional area of the prism and strain was obtained from the reading of the longitudinal and transverse strain gauge sensors. Young's modulus of elasticity in the direction of the applied load was determined from the slope of the axial stress vs axial strain curve. This slope was determined by linear regression analysis. Since the variation of stress and strain didn't appear to be perfectly linear up to the maximum load value

(a)

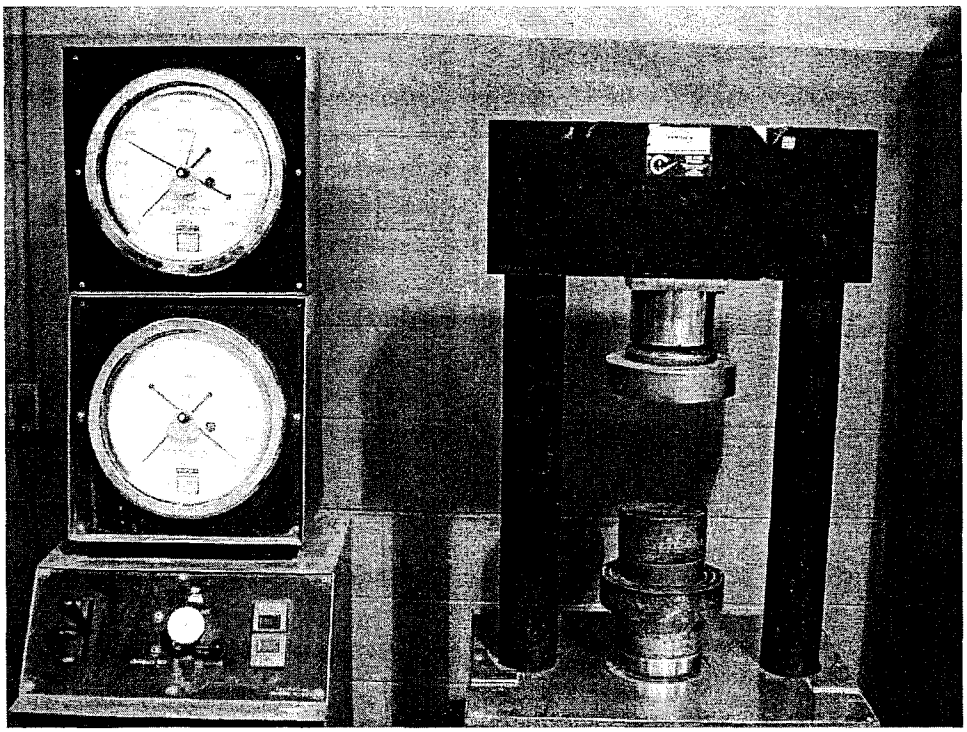

(b)

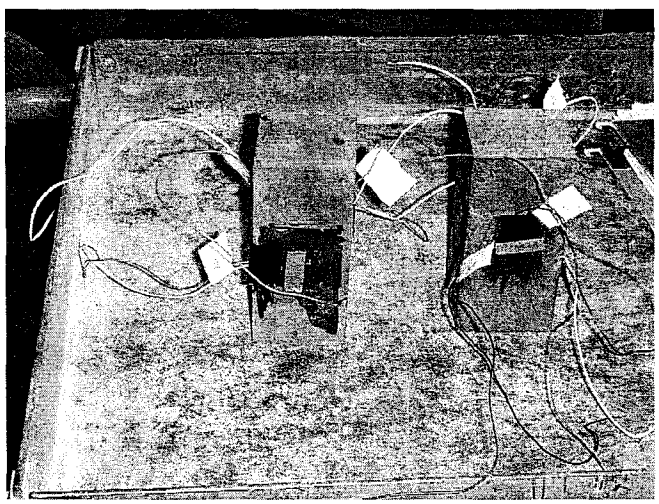

(c)

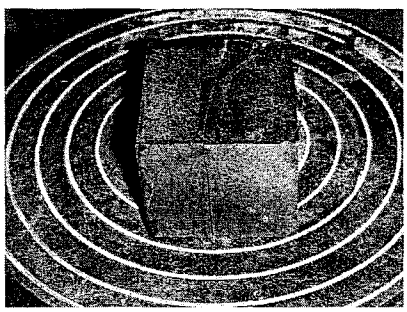

Figure 4.1: (a) Experimental setup for elastic moduli, Poisson's ratio and compressive strength test; (b) slate blocks ready for elastic moduli test; and (c) a block after breaking by compressive load.

(shown in Figures C-1 to C-4), the average slope of the linear portion of the curve (as suggested by ASTM D 3148-80) was taken into consideration to determine the Young's modulus. Young's modulus for a specific test sample was determined by averaging the results obtained from the two axial strain gauges of two sides of test specimen.

Poisson's ratio (ν) was determined by following the guidelines mentioned in ASTM standard D 3148-80. Since it is affected greatly by the nonlinearities present in the specimen at low stress levels, Poisson's ratio was calculated by using the following formula suggested by ASTM standard:

$$\nu = -\text{ slope of axial curve / slope of lateral curve}$$

$$= -E / \text{slope of lateral curve} \qquad (4.1)$$

where, the slope of the lateral curve was obtained along with the Young's modulus of elasticity.

4.5.3 Tensile Strength

Rocks are known to be brittle materials and very weak in tension than compression. Even rock failure under compression occurs due to the developed tensile stresses within the body. The tensile strength of rock is usually determined through direct pull tests on cylindrical specimen. However, indirect tests have also been suggested to determine tensile strength of rock when difficulties arise in gripping the specimens during direct pull tests. The commonly used indirect tests are modulus-of-rupture tests on beam specimens (flexure test) and splitting tests on cylindrical discs (Brazilian test) or rectangular blocks. Direct pull tests, splitting tests on rectangular blocks for indirect tensile strength and flexure tests were carried out in the present study to obtain the tensile strength

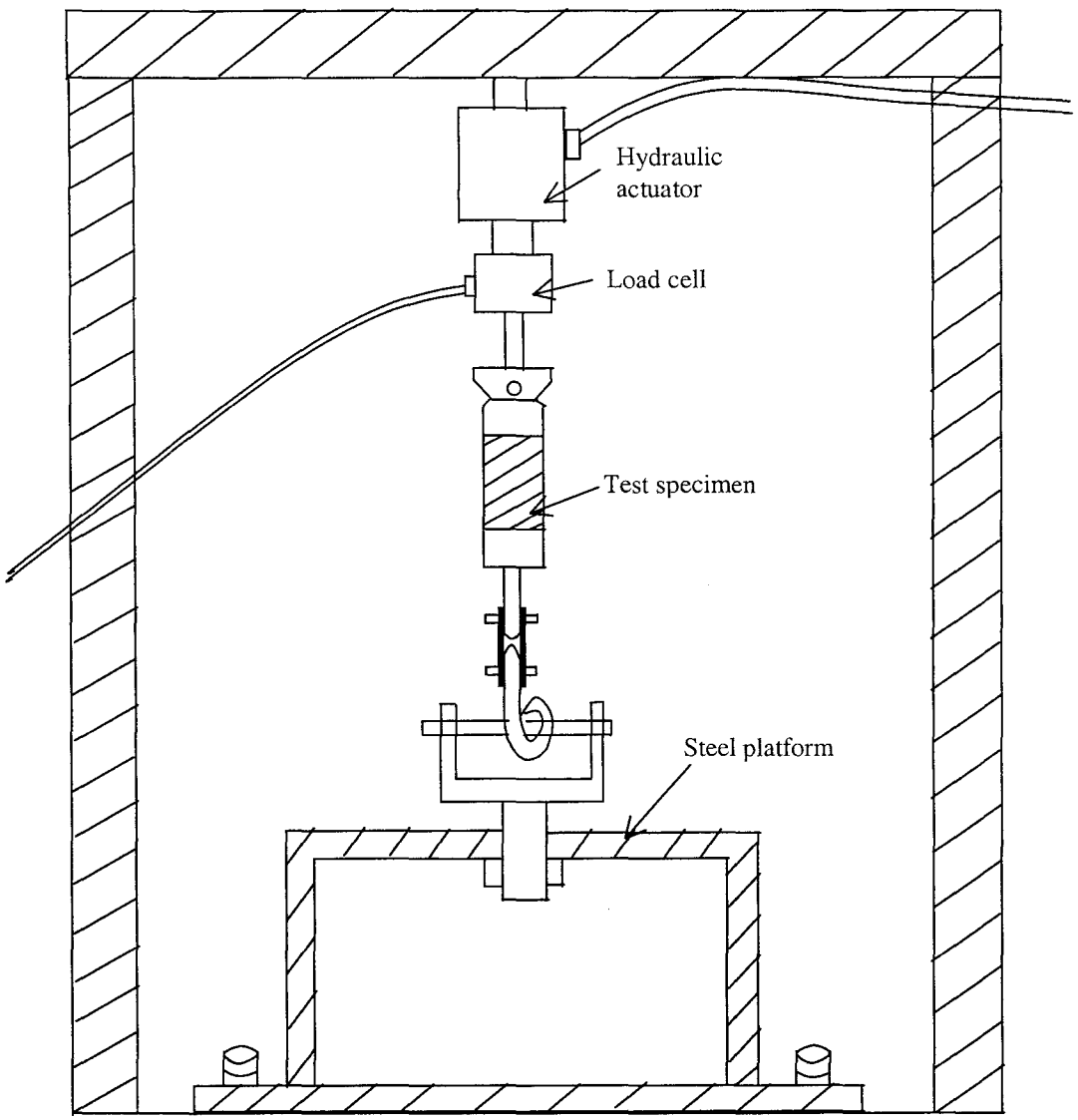

Figure 4.2: Test setup for direct tensile strength of slate rock (Mazur, 1985)

of slate rock. Specimen preparation and testing procedures for these tests are given below.

4.5.4 Direct Tensile Strength Test

This test was carried out based on ASTM standard test D 2936-78. A right circular cylindrical specimen having a height to diameter (*h/d*) ratio of 2.0 to 2.5 was made using high speed cylindrical drill bits (of outside diameter 1.4 inch) on a large slate block. Specimen diameter was obtained as 1.375 inch and height was determined by keeping the *h/d* ratio 2.0. The minimum diameter (2 inches) specified by ASTM code couldn't be maintained due to the nonavailability of longer diameter drill bits. However, the standard *h/d* ratio was maintained. Special care was taken while using the drill for cutting out the cylindrical specimen so that no incidental crack occurred. This test measured the force required to fail the specimens in tension. Load was applied slowly at an approximately constant rate by making sure that test specimens did not fail in less than 5 minutes or greater than 15 minutes. Specimen was cemented by M-bond 200 adhesive and 200 Catalyst to two steel rectangular blocks (at top and bottom of the specimen) whose size was a little greater than the specimen size; the steel blocks were gripped by the tension grips of the loading rig. To prevent the occurrence of bending moments (that could arise while applying tensile load to the specimen) the tensile loading rig was designed to allow lateral motion. Load was applied slowly and gradually until the failure of the specimen under a tensile load occurred. Experimental setup for this test has been shown in Figure 4.2.

4.5.5 Indirect Tensile Strength

This test was carried out on rectangular slate specimens based on the test procedures reported by Davies and Stagg (1970) using test setup shown in Figure 4.1. Specimen

preparation and testing procedures were clearly outlined in their report. Prismatic specimens having a side of 6 inch square and 4 inch deep were made to carry out this test. Machine grinding of four faces was done before testing the specimen. Test specimen was placed centrally on a steel rod having ½ inch square cross section and length equal to the thickness of the specimen. Another similar steel rod was also placed on the top of the specimen along the same vertical line. Thereafter, loading plates of UTM were brought to bear very slowly on the top of the steel rod. Load was applied through UTM until the block broke into two parts. Breaking load was recorded and tensile strength was calculated using the same procedure suggested by Davies and Stagg (1970). Four specimens were tested.

4.5.6 Flexure Testing of Slate

When a bending load is applied to the beam either through a 3-point bending or 4-point bending arrangement (as shown in Figure 4.3), compressive, tensile and shear stresses are developed in the beam. When a portion of the beam is in under pure bending moments only, tensile stresses are developed on the convex side of the beam and compressive stresses on the concave side. The extreme fiber tensile stress at failure is considered as the tensile strength (also called modulus of rupture) and is written based on pure bending beam assumptions as,

$$\sigma_t = \frac{Mc}{I} \tag{4.2}$$

where, σ_t = tensile strength, M = Maximum bending moment, c = extreme fiber distance from the neutral axis of the beam cross section and I = moment of inertia of the beam cross section.

Since rock doesn't have the same stress-strain behaviour both in compression and tension, therefore the neutral axis does not lie at the middle of the beam section. To overcome this problem Duckworth (1951) has given a formula to calculate the tensile strength of rock for a rectangular beam having different Young's modulus of elasticity in tension and compression in the following form:

$$\sigma_t = -\frac{3M(\varepsilon_1 + \varepsilon_2)}{bd^2\varepsilon_1} \tag{4.3}$$

where, ε_1 and ε_2 are the strains at the top and bottom most outer fibers of the beam, b & d are the width and thickness of the beam cross section.

In order to carry out this test in the laboratory, slate block was split to a thickness of approximately 1 ¼ inch and then sawn into strips 12 inch in length by 1-5/8 inch in width (according to the test requirement of ASTM standard test method C 120 – 52 (1981)). Twelve specimens were prepared out of which half the specimens were cut with the length parallel to the grain and other half with the length perpendicular to the grain. Specimens were planed or ground down the 12 by 1 ½ inch faces to a thickness of approximately 12 by 1 inch. Grinding was applied to make surfaces as nearly parallel as possible. Load was applied at a rate of 15 lbf/sec through a three-point bending loading until the specimen failed completely. The breaking load was recorded and the modulus of rupture was calculated using the formula given in ASTM standard code C 120 – 52 (1981).

$$R = \frac{3Wl}{2bd^2} \tag{4.4}$$

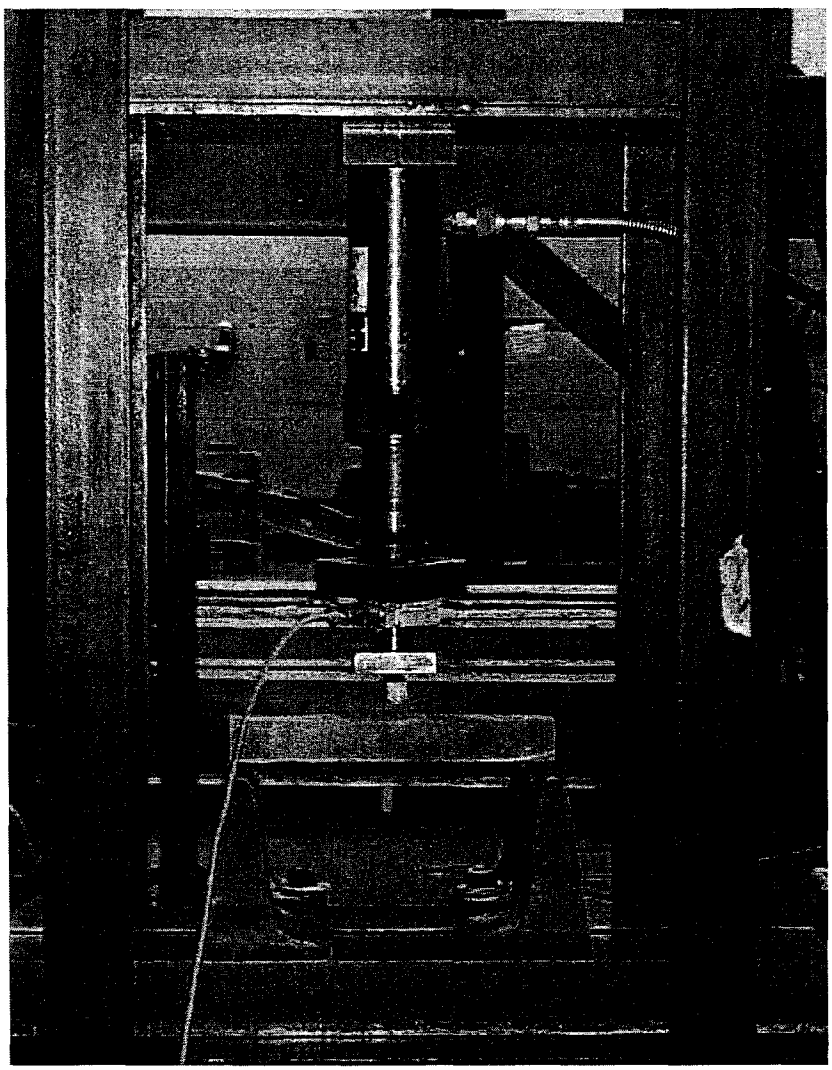

Figure 4.3: Experimental setup for flexure test of slate rock

where, R = modulus of rupture (or tensile strength) in *psi* (or *MPa*), W = breaking load in *lbf* or (*N*), l = span length between supports (in ft or m), and b & d = the width and the depth of the specimen (in ft or m), respectively.

4.5.7 Compressive Strength Test

Compressive strength test was carried out mainly to determine the strength of intact rock and to assist in the characterization of rock masses. It measures the uniaxial compressive strength of rock sample in the form of specimens of regular geometry. Test has been conducted based on ASTM standard C170 – 50 (1981) specifications and testing procedures. Square prisms were cut from the slate sample by a circular disk diamond saw. The lateral dimension was maintained not less than 2 inches and the ratio of height to lateral dimension was kept not less than 1:1. Twelve specimens were prepared for compressive strength tests in directions perpendicular and parallel to the layer, under surface dry conditions. Load bearing surfaces were finished by grinding as nearly true parallel planes as possible, in order to distribute the load uniformly over the bearing surfaces. Grinding was continued until they were perpendicular to the vertical sides as gauged by a try square. Grinding was completed by rubbing the ends on a smooth machine-planed surface of a cast iron plate with No. 80 emery and water. A machine which is suitable and sufficient to apply the load described in the test specification ASTM standard C170 – 50 (1981) to the slate specimens was used. Load was applied slowly at a rate not more than 100 psi/s. Two stiff and thin rubber pads, one at the bottom and the other at the top of the specimen, were used to distribute the load uniformly on the bearing surfaces. Compressive strength of the test specimens was calculated by using the following relationship:

$$\sigma_c = \frac{W}{A} \tag{4.5}$$

where, σ_c = compressive strength in *psi* (or *MPa*), W = total load in *lbf* (or *N*) applied on the specimen at failure, and A = calculated area of the bearing surface in in^2 (or mm^2). Experimental setup for this test has been shown in Figure 4.1.

4.5.8 Hardness

Hardness is the resistance of the material to penetration by a hard indenting spherical ball or other prismatic profiles. It shows a characteristic behaviour of material that depends on the type, quantity and quality of the various mineral constituents of the material and the bond strength that exists between them. Hardness index of rock is important since it would influence greatly the consequent & interactive wear and subsequent damage of rock excavating machines & cutting tools (Whittaker, et. al. 1992) - in the present case the impact indenter. It may also be used to measure the fracture behavior of rock through its relationship to fracture toughness. This factor alone may influence the rate of tool and cutter wear together with the energy required to cause continuous rock disintegration. Micro-hardness testers are used to measure hardness of the individual rock minerals or layers, which subsequently could be used as measure to compute the ultimate tensile strength of the layers of the rock. The layer strengths could then be used in the analysis of the splitting behavior of natural layered rocks such as slate. And it can also show whether individual layer material is isotropic or anisotropic by measuring the two diagonals of Vickers micro indenter that should show equal in size for isotropic materials. The present study of hardness was carried out on layered slate rock using Vickers micro-hardness tester to determine the Vickers/Shore hardness number of the material and to examine

whether individual layer is isotropic or anisotropic. This test was performed following the procedure described by ASTM standard test method (ASTM E 384 – 99 and ASTM C 1327 - 99) for microindentation hardness of materials and the Instruction Manual of MICROMET microhardness tester shown in Fig. 4.4 (Vickers type).

4.5.8.1 Preparation of the Test Specimen for Hardness Test

Test specimens were prepared according to ASTM specification E 384 – 99 and ASTM C 1327 - 99 (2000). Four small pieces of rock, approximately 1″ × 1″ × 0.5″ (25.4 × 25.4 × 12.7 mm) in size were cut using a circular disk type diamond saw. Thereafter, grinding was carried out in the presence of a water coolant to make the surface smooth. In order to make surface perfectly smooth and shiny, polishing the surfaces of the specimen was carried out using different grades of sand papers fixed on a rotating machine, rotating with a reasonable speed. When the hardness test of one layer was completed, a new layer was exposed again after removing the tested layer from the specimen and then the layer was smoothed and polished. The procedure was repeated several times to obtain the hardness values of several layers.

4.5.8.2 Testing Procedure

The test specimen was fixed tightly on the platform of the micro-hardness tester and leveled using the clamping screw. Micro-hardness tester was located in a zone which was free from any kinds of shock or vibration. Thereafter, weight was placed on the weight pan. A weight of 100 gm was chosen to get a clear impression of the indentor on the test surface. The specimen was placed under the lens and viewed by turning the stage elevating handle. Test area was located using the micrometer screws and the light

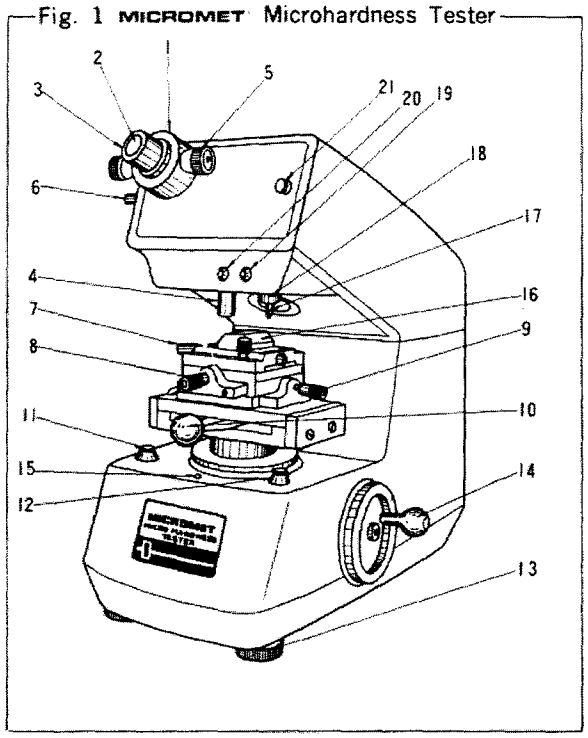

1. Measuring Microscope
2. Measuring Eyepiece (15x)
3. Scale Adjusting Knob
4. Objectives (40x or 6x)
5. Micrometer Measuring Knob
6. Viewing Light Intensity Adjustment Knob
7. Vise Tighteni ng knob
8. Micrometer Screw for Carriage (Front and Rear)
9. Micrometer Screw for Carriage (Right and Left)
10. Carriage Shifting Lever
11. Main Switch
12. Switch for Automatic Load Application
13. Leveling Feet (3)
14. Handle for Elevating Stage
15. Level
16. Vise
17. Diamond Indentor
18. Indentor Holder
19. Green Indication Bulb
20. Red Indication Bulb
21. Weight Chamber Cover

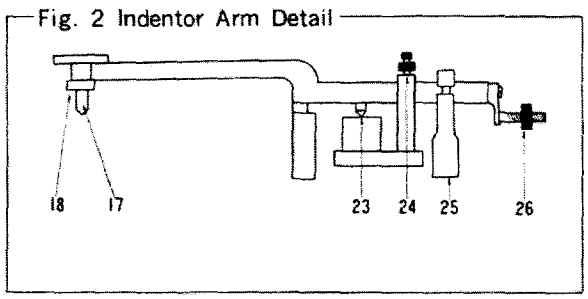

17. Diamond Indentor
18. Indentor Holder
23. Pivot Point
24. Clamping Screw
25. Counter-balance Weight
26. Fine Counter-balance Weight

Figure 4.4: MICROMET micro hardness tester

intensity was adjusted to a comfortable level by turning the light intensity knob. Thereafter the specimen was placed under the diamond indentor and the load was applied on the specimen by pressing the automatic load application switch. After completing the indenting load cycle the diamond indentor was restored back to its initial position. The specimen was then shifted to the viewing lens position and the indented impression was viewed using the stage elevating handle. The length of the two diagonals were measured by using the graduations marked on the eyepiece. A 3D view of MICROMET micro-hardness tester is given in Figure 4.4.

4.5.9 Coefficient of Friction Test

The objective of this test was to determine the coefficient of friction between naturally bedded layered slate rock and steel plate. The need for this test was observed during the splitting of slate blocks using a wedge shaped steel indenter. Since the wedge moves inside the slate block during splitting by transferring force through friction and bearing on the contact surfaces between them, it was essential to determine this force experimentally. The mathematical representation for the coefficient of friction is, $\mu = \frac{F}{W}$, where W = the normal weight of one body acting on another body and F = the force required to slide one body over the other body.

4.5.9.1 Specimen Preparation, Experimental Setup and Testing Procedure

Before carrying out the test, contact and loading sides of rectangular slate block were made uniform and parallel by grinding them to make full contact with the steel plate. The surface of the steel plate (AISI 4340 steel) was also made uniform and parallel by

polishing the steel surface using different graded sandpapers. Thereafter, steel plate was fixed to a wooden table and leveled; the slate block was then placed at the middle over the steel plate. The test was carried out by sliding the slate block over the steel plate. Various weights ranging from 500 to 2500 grams were placed subsequently on the slate block to carry out a number of repetitive tests for various normal forces applied to the steel surface by the slate. A string was glued to the top surface of the slate block and extended over a small pulley (by making sure that the top of the specimen and the top of the pulley were in the same level) and attaching to a cup-shaped loading pan to which sand particles were added slowly to apply a transverse load on the string. The entire test setup is shown in Figure 4.5. At the beginning of the test, empty cup-shaped loading pan and test specimen were weighed and the normal weight applied to the specimen was recorded. To carry out the test, sand particles were added slowly to the pan until the slate block started to move. Thereafter, the pan with sand particles was weighed. The weight of the sand and pan applied to the string, was taken as the tangential force, and the added weight on the sample and its own self weight taken as the normal force. The coefficient of friction was determined by dividing tangential force by the normal force. The summarized results are given in Table 4.2. The coefficient of friction obtained from this measurement, using Figure 4.6, varied from 0.55 to 0.57.

4.6 Test Results

The results obtained during experimental investigation of different mechanical properties of slate material such as, elastic moduli, Poisson's ratio, compressive and tensile strengths, fracture toughness, hardness, and friction coefficient are discussed in subsequent sections.

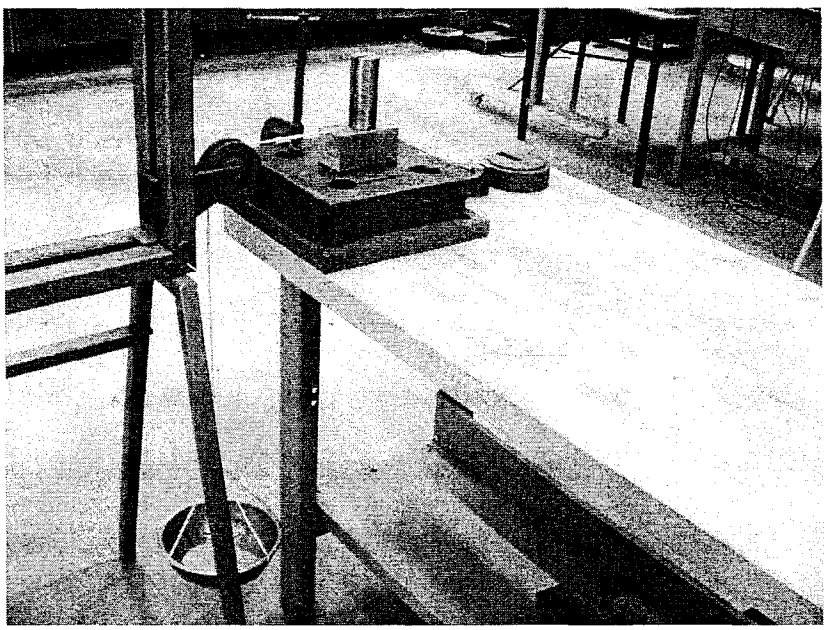

Figure 4.5: Instrument setup for coefficient of friction test

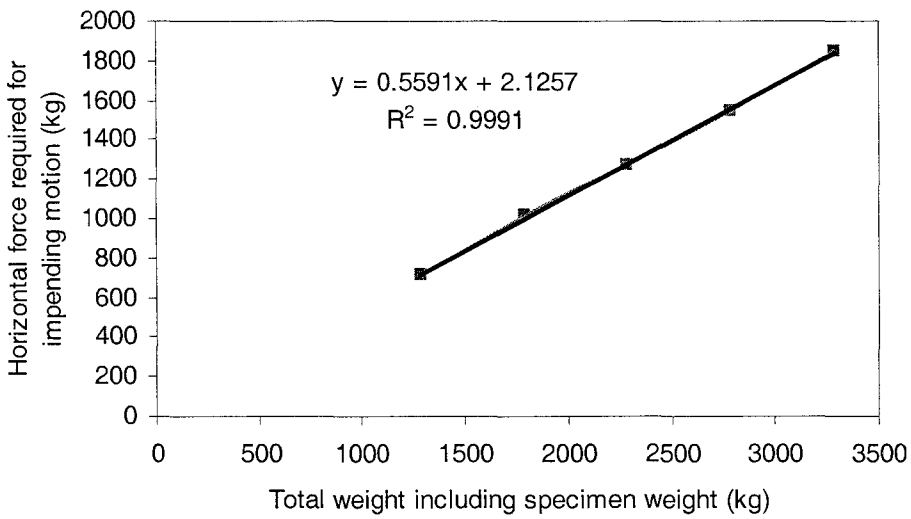

Figure 4.6: Coefficient of Friction between Slate and Steel

Table 4.2: Coefficient of Friction between Slate and Steel

Test Number	Coefficient of Friction (μ)
1	0.55406
2	0.57115
3	0.55772
4	0.55524
5	0.56205
Mean	0.56004
Standard Deviation	$\pm$ 0.003703

4.6.1 Young's Modulus of Elasticity and Poisson's Ratio (Group #1)

Perkins and Krech (1968) reported that the elastic moduli of rock are in general not independent of the stress level at which it is determined, particularly at low compressive stresses and tensile stresses. The variation of elastic modulus of rock is seen due to the presence of internal cracks and voids, which could close under high compressive stresses, yet remain open at low compressive and tensile stresses. For competent (low porosity, low density of micro-cracks) rocks the difference between the compressive and tensile moduli could be lesser than the porous rocks and highly micro-cracked rocks. Modulus properties of rocks are influenced more by their bedding planes and joints. Higher modulus values are experienced when rock is loaded parallel to the bedding planes or joints than when stressed at right angles to them (Lama and Vutukuri, 1978).

The elastic properties (Modulus of elasticity and Poisson's ratio) of slate in three perpendicular directions (shown in Figure 4.7) are given in Table 4.3 and 4.5.

Compressive loads in three perpendicular directions (two in-plane directions i.e. 11 and 22 and one perpendicular to the in-plane direction, 33), were applied through the universal testing machine. Specimen preparation, testing and analysis procedures were described in detail earlier in section 4.5.2. Table 4.3 shows the results of the modulus of elasticity in three different directions obtained for a number of specimens. Twelve specimens were tested by applying load parallel to the layering and four specimens were tested applying load perpendicular to the layering. These test results were also compared with those obtained from Vutukuri et. al. (1974), as shown in Table 4.4. As seen from Tables 4.3 & 4.5, the values are highly variable, depending on the slate type and fabric characteristics.

Probable reason for the existence of different properties in different slate mines could be the geological process of the formation of slate rock; the nature and distribution of grains and mineral along with its microstructure contribute to these variations. The existence of different colors of slates indicates the existence of different percentages of mineral contents. In the present study all tests were conducted on slate samples obtained from Hurleys Slate Works Company and Carew Service, Portugal Cove, St. John's, Newfoundland, Canada.

It is seen from Table 4.3 that the modulus of elasticity varies significantly along and perpendicular to the layer (see Fig. 4.7 for orientation of axes). Modulus of elasticity along the layer direction was greater than that obtained perpendicular to the layer; this indicates the existence of planar isotropy along the bedding planes. Comparing with the results shown in Table 4.3 the Newfoundland slate seems to be closer to the mean values

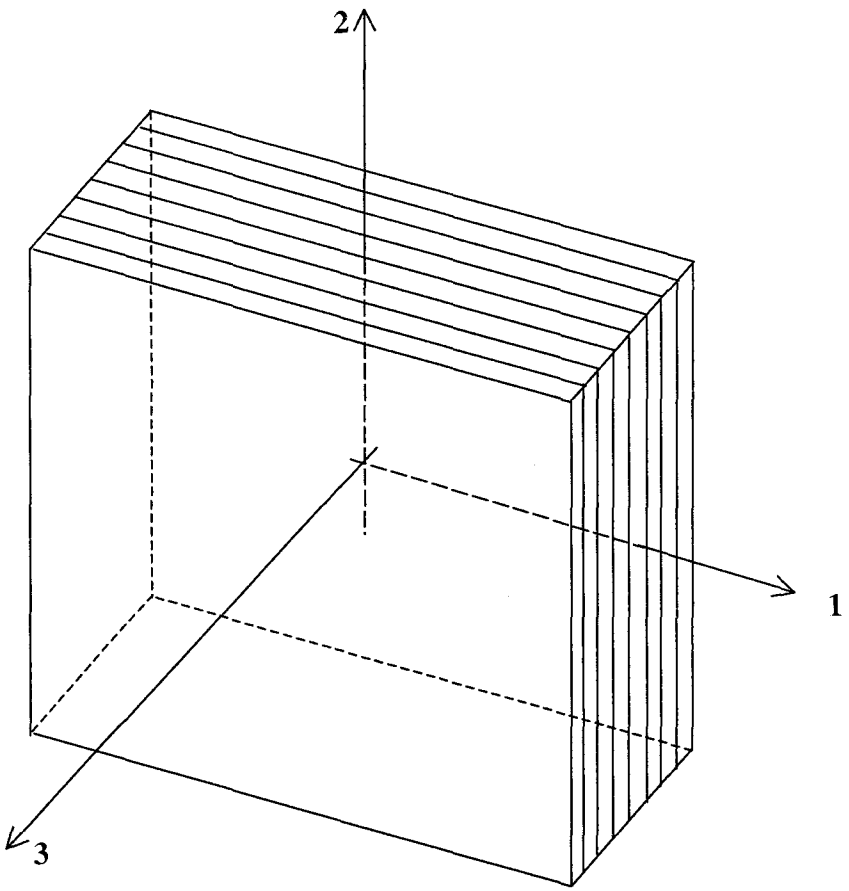

Figure 4.7: Typical slate block with layers' orientation and Cartesian co-ordinate system.

Table 4.3: Young's modulus of elasticity for slate

(In the three material directions)

Test Number	E_{11} (Direction 1)		E_{22} (Direction 2)		E_{33} (Direction 3)	
	psi	GPa	psi	GPa	psi	GPa
1	9.5×10^6	65.5	9.0×10^6	62.05	6×10^6	41.37
2	10×10^6	68.95	15×10^6	88.42	5×10^6	34.474
3	10×10^6	68.95	9.5×10^6	65.5	5.5×10^6	37.92
4	9×10^6	62.05	10×10^6	68.95	6.5×10^6	44.816
5	10×10^6	68.95	10×10^6	68.95	-	-
6	15×10^6	88.42	15×10^6	88.42	-	-
Mean value	10.58×10^6	70.47	11.42×10^6	73.715	5.75	39.645
Standard Deviation	$\pm$ 2.2238	$\pm$ 9.217	$\pm$ 2.5563	$\pm$ 11.674	$\pm$ 0.559	$\pm$ 3.854
Vutukuri, et. al. (1976)	5.05×10^6 to 16.53×10^6	34.8 to 114.0	6.39×10^6 to 16.53×10^6	44.1 to 114.0	1.13×10^6 to 11.91×10^6	7.8 to 82.1

Table 4.4: Slate properties determined earlier by other researchers (Vutukuri, et. al. 1976)

Material	Fabric description	Symmetry	Test method	Test sample size (mm)	GPa						ν_{12} (ν_{21})	ν_{13} (ν_{31})	ν_{23} (ν_{32})	Reference
					E_1	E_2	E_3	G_{23}	G_{13}	G_{12}				
Slate	Laminations parallel to plane 12	"n" fold axis parallel to axis 3	Longitudinal and shear wave velocities on cube samples		114.0	114.0	53.0	19.8	19.8	53.5	0.067	0.328	0.328	ALEXANDROV et al. (1969)
Slate	Axis 3 is normal to the plane of foliation	Orthorhombic	Uniaxial compression and tension tests together with torsion tests. Strain gauges attached to samples		71.5	63.0	82.1	26.9	27.9	24.9	0.218	0.380	0.284	NISHIMATSU (1970)
Hard Blue Pehrhyn Slate	Slaty cleavage associated with preferred orientation of micaceous and chloritic components in the rock. "Planes of elastic and velocity symmetry are coincident with the planes of fabric and tectonic symmetry."	Orthorhombic Stiffest along axis 1 | direction of cleavage dip and max. fabric extension	Ultrasonic longitudinal and shear waves	5, 10, 15 x 64 x 90	46.3	44.1	30.1	10.6	15.4	16.0	0.426	0.426	0.439	ATTEWELL (1970)
Green Pehrhyn Slate		least stiff along axis 3 | normal to planar features and direction of max. fabric shortening			40.5		23.9	8.1	8.1	13.9	0.469		0.462	
Chloritic Slate	Direction of bedding coincides with maximum wave velocity, minimum velocity perpendicular to bedding (i.e. axis 3)	"n" fold axis perpendicular to bedding?	Laboratory tests – longitudinal and shear wave velocities	50 dia. x 120 long	130.0		81.0		35.0	49.0	0.33	0.28 (0.17)		STORIKOVA (1965)
Very Altered Slate	Axis 3 is normal to the plane of foliation	Orthorhombic?	Laboratory tests – oriented samples loaded to 9.8 MPa. Strains recorded by bonded strain gauges. Results quoted are secant moduli	50 x 50 x 150 Prisms	34.8	55.4	7.8							RODRIGUES (1970)
Little Altered Slate					63.8	54.1	11.3							
Sound Slate					85.2	90.7	30.4							

Table 4.5: Poisson's ratio for slate

(In the three material directions)

Test Number	Poisson's ratio ν_{12}	Poisson's ratio ν_{13}	Poisson's ratio ν_{23}	Poisson's ratio ν_{31} or ν_{32}
1	0.25	0.1462	0.200	0.2000
2	0.20	0.1820	0.167	0.2000
3	0.20	0.1820	0.192	0.1833
4	0.20	0.1636	0.200	0.1857
5	-	-	0.146	-
6	0.33	0.1818	0.084	-
Mean value	0.236	0.171	0.165	0.19225
Standard deviation	± 0.085	± 0.01434	± 0.041	± 0.0078
Vutukuri, et. al. (1976)	0.067-0.469	0.280-0.426	0.328-0.462	-

given by Vutukuri, et. al. (1976). From Table 4.4 it could be seen that these mean values are very close to the properties of a sound slate. Younathan (1970) also obtained similar results after an extensive investigation of the physical properties of slate rock having a planar anisotropy. He concluded that in general the physical properties vary less along the plane of layer than perpendicular to the layer.

The stress versus strain curves of some tested specimens were plotted to show the deformation behavior of slate rock. Some of these curves are shown in Figures C-1 to C-4 of Appendix C. A non-linear stress-strain relationships was observed at low and high stress levels. Average slope of the more-or-less straight-line portions of the stress-strain curve was used to determine modulus of elasticity. The existence of nonlinearity at low stress level may perhaps be due to the closing of the numerous micro-cracks within the body. The reason for non-linearity close to the maximum load was due to the extension of the micro-cracks leading to failure of slate block.

Table 4.5 shows the Poisson's ratios of slate calculated based on the procedure described at section 4.5.2. It is seen that the in-plane Poisson's ratios (1-2 direction) are greater than the Poisson's ratios obtained for directions (1-3 and 2-3) perpendicular to the plane.

4.6.2 Dynamic Elastic Moduli

Dynamic elastic moduli were not determined in the present study. It has been observed from earlier studies (Table 4.6) that the magnitude of dynamic elastic moduli was around 1.03 to 1.07 times greater than the static elastic moduli for sedimentary or layered materials such as Sandstone, Gabbro and Dunite.

4.6.3 Compressive and Tensile Strengths (Group #1)

The results obtained from these tests are given in Tables 4.7 to 4.10. It is seen that the compressive strength varies significantly depending on the direction of the applied load. When load was applied parallel to the direction of the bedding plane (1-2 plane in Figure 4.7), the compressive strength was found to be 50% to 60% less than those obtained when load was applied perpendicular to the direction of the layering. Variation of compressive strengths seem to agree with the results given by earlier researchers in Table 4.11. Low tensile strength of the slate block, perpendicular to the layer direction, reported in Tables 4.8 and 4.9, could be attributed to this difference. Tensile strengths of slate, in a direction perpendicular to the layer, were determined by direct tension tests and indirect tension tests. A large variation in strengths for both test procedures was observed from the earlier published results, as shown in Table 4.11.

The results obtained from flexural tests are given in Table 4.10. It is seen that the test results are higher than the minimum value specified by ASTM specification C 406-58 (1981). The minimum modulus of rupture across the grain provided by the ASTM specification for slate is 9000 psi (62.08 MPa).

4.6.4 Hardness (Group #1)

The indentation length of diagonal in μm (Vickers micro indenter, having a square-based pyramidal-shaped diamond indenter with face angles 136^0) obtained from micro-hardness tester was used to determine the Vickers hardness number (HV) using conversion tables available in ASTM E 384-99. Shore Scleroscope hardness number was obtained from HV values using conversion table of ASTM standard E 140-97. Both results are given in

Table 4.6: Static and dynamic elastic properties of some rocks
(after Rzhevsky and Novik, 1971)

Rock	Static modulus of elasticity E_{st}, GPa	Dynamic modulus of elasticity E_{dyn}, GPa	Ratio $\frac{E_{dyn}}{E_{st}}$	Bulk modulus K, GPa	Rigidity or shear modulus G, GPa
Sandstone with chalcedonic cement	73.0	77.8	1.07	23.0	32.0
Equigranular dolomite	50.5	53.1	1.05	52.1	18.8
Limestone	18.8	24.2	1.29	43.5	6.6
Calcareous dolomite	34.9	47.2	1.35	37.0	13.0
Fine-grained detrital limestone	47.7	57.1	1.20	46.0	18.0
Granite	66.0	71.0	1.08	47.3	26.0
Gabbro*	71.0	75.0	1.06	57.0	36.0
Dunite*	149.0	164.0	1.03	107.3	59.0
Syenite	74.0	81.0	1.10	54.0	29.0

* Structure very close to slate having either a sedimentary or layered characteristic

Table 4.7: Compressive Strength of Slate

Test Number	Compressive strength (σ_{11})		Compressive strength (σ_{33})	
	ksi	MPa	ksi	MPa
1	15.182	104.674	25.451	175.485
2	14.665	101.113	21.580	148.789
3	14.586	100.568	25.514	175.915
4	15.686	108.154	27.771	191.478
5	15.802	108.955	-	-
6	18.526	127.735	-	-
7	15.436	106.432	-	-
Mean	15.697	108.233	25.079	172.917
Standard deviation	± 1.2333	± 8.5033	± 2.2258	± 15.346
Solenhofen (2003)	14.50 - 29.00	100 - 200	14.50 - 29.00	100 - 200

Table 4.8: Direct Tensile Strength of Slate

Test Number	Direct tensile strength (σ_{33})	
	psi	KPa
1	119.000	820.505
2	152.203	1049.436
3	112.009	772.297
4	94.826	653.827
5	138.235	953.130
6	124.650	859.462
7	106.800	736.386
8	104.800	722.596
Mean	119.065	820.955
Standard Deviation	± 17.635	± 121.5948
Solenhofen (2003)	580.15 - 3625.92	7000 - 20000

Table 4.9: Indirect Tensile Strength of Slate

Specimen Size	Breaking load (lbf)	Tensile Strength	
		psi	kPa
4.00″ × 4.750″ × 6.0″	5360	139.28	960.33
4.20″ × 4.000″ × 6.0″	2675	69.51	479.27
4.10″ × 4.200″ × 5.0″	5100	155.15	1069.75
4.00″ × 4.500″ × 5.8″	12550	337.36	2326.06
4.75″ × 4.125″ × 6.0″	5650	142.37	981.61
Mean	6267	168.73	1163.40
Standard Deviation	± 3314.93	± 89.47	± 616.91
Solenhofen (2003)		580.15 - 3625.92	7000-20000

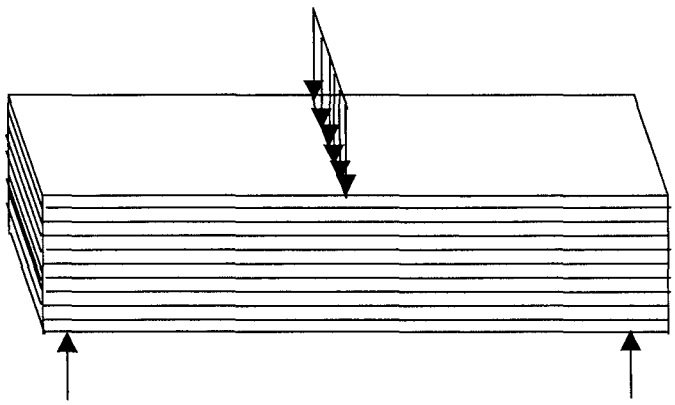

Table 4.10: Flexural Strength of Slate

Test Number	Modulus of Rupture (across the grain)	
	ksi	MPa
1	14.981	103.29
2	14.000	96.53
3	13.674	94.28
4	11.858	81.76
5	16.584	114.34
Mean	14.219	98.04
Standard deviation	± 1.555	± 10.72
ASTM C 406 – 58 value (1981)	9.000	62.08

Table 4.11: Strength properties of different layered rocks (Solenhofen, 2003)

Rock types	Compressive strength (MPa)	Tensile strength (MPa)	Shear strength (MPa)
Slate	100-200	7-20	15-30
Sandstone	20-170	4-25	8-40
Limestone	30-250	5-25	10-50

Table 4.12. During conversion of hardness numbers, a correlation equation was made using available conversion numbers of Vickers and Shore scleroscope to obtain Shore scleroscope hardness number corresponding to the small values of Vickers hardness numbers. From the experimental results given in Table 4.12, it is seen that the average value of Shore scleroscope hardness number is approximately 41. The Shore hardness numbers given by Bureau of Mines, United States Department of the Interior (Windes, 1949) for Michigan slate and Pennsylvania slate were 46 and 56, respectively. In comparison to the results supplied by the above reference, the test result obtained in the present study seems to be reasonable for slates obtained from Hurley's Mines, Newfoundland, Canada.

4.7 Fracture Toughness Test (Group # 2)

Three types of specimens (arrester, divider and short transverse) suggested by Schmidt (1976), based on the specimens' layer orientations, were used to determine the fracture toughness of slate material. The geometry of each type is given in Figure 4.8.

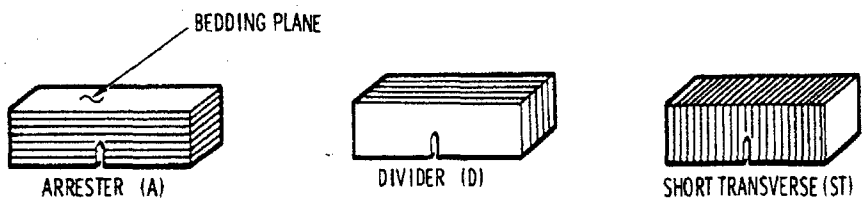

Figure 4.8: Geometry of arrester, divider and short transverse specimen of slate rock for fracture toughness test (Schmidt, 1976).

Before cutting the specimens from the initially trimmed slate block (lumped slate block), geological planes were examined by visual observation. A size little higher than the size

Table 4.12: Vicker's Micro Hardness Test Results

Prism (square) diagonal distance (micro meter)	Vickers hardness number	Shore hardness number
27.50	245.00	34.166
30.20	203.00	29.166
32.00	181.00	26.750
35.10	151.00	22.000
30.00	206.00	29.800
20.00	464.00	62.060
28.00	237.00	33.429
33.00	170.00	25.000
20.50	441.00	59.133
30.60	198.00	28.000
35.70	146.00	21.000
20.20	454.00	60.870
14.00	946.00	-
21.00	420.00	57.330
25.00	297.00	41.556
22.00	383.00	52.000
18.00	572.00	70.844
23.00	351.00	48.100
27.00	254.00	36.125
20.10	459.00	61.470
29.90	207.00	30.000
17.00	642.00	77.162
28.40	230.00	33.000
33.70	163.00	24.000
15.25	797.50	87.880
10.00	1854.00	-
24.00	322.00	45.333
Mean	407.17	40.636
Windes (1949)	-	46 - 56

required for the test was cut from the larger block using circular saw with a water-cooled diamond tip blade for specimens having rectangular cross section. Due to the existence of layers in slate rock it was very difficult to prepare rectangular specimen having a plane face perpendicular to the centroidal plane of the beam specimen; consequently cylindrical core specimens were chosen to determine the fracture toughness of slate instead of rectangular ones. This specimen was prepared by inserting a hollow drill bit, having a diameter of 1.4″ (35.84 mm) and a length of 6″ (152.40 mm), fixed to a drilling machine and drilling into the slate block at a constant speed.

This shape of test specimens was found to be more advantageous over rectangular shape for not requiring grinding to make specimen smooth. However, it was easier to cut rectangular specimens in a direction parallel to the layer. Specimens were then marked with chalk/marker according to their orientation and block numbers. Both shapes of specimens were prepared according to ISRM: Fracture toughness suggested method (1988). During the preparation of the test samples water (as a cooling agent) was used constantly. The nominal size of the rectangular specimens was 6.5″×1.0″×1.5″ (165.4 × 25.4 × 38.1 mm) with a variable initial crack. Cylindrical specimens were 5.5″ (139.70 mm) long and 1.375″ (34.93 mm) in diameter, with a variable initial crack. The initial crack was introduced using manual hex saw having a blade thickness of approximately 0.5 mm. The use of this saw was important because of the difficulty of introducing an initial fatigue crack in the slate specimens. For fracture toughness tests, different depths of straight through cracks of size 0.36, 0.375, 0.44, 0.5 and 0.6 times the thickness or diameter of the specimens were cut using the above saw; the crack width was kept less than 1 mm. Seven rectangular prism specimens were tested under four-point bending

loads and seven cylindrical core specimens were tested under three-point bending loads. The test was carried out under displacement controlled mode at a constant rate 0.1 mm/min. Strain gauge sensors capable of measuring micro strains were used to measure strains for four point bending test. An *LPDT* was used to measure crack mouth opening displacements in the case of three-point bending tests.

Test specimens were prepared and tested by following procedures described by both ASTM C 1421 – 99 (1999) and ISRM standard (1988). Two types of loading systems shown in Figures 4.9 and 4.10 (three-point-bending [3PB] and four-point-bending [4PB]) were used to apply the load externally to the test specimens. The fracture toughness obtained in this test was considered as apparent fracture toughness.

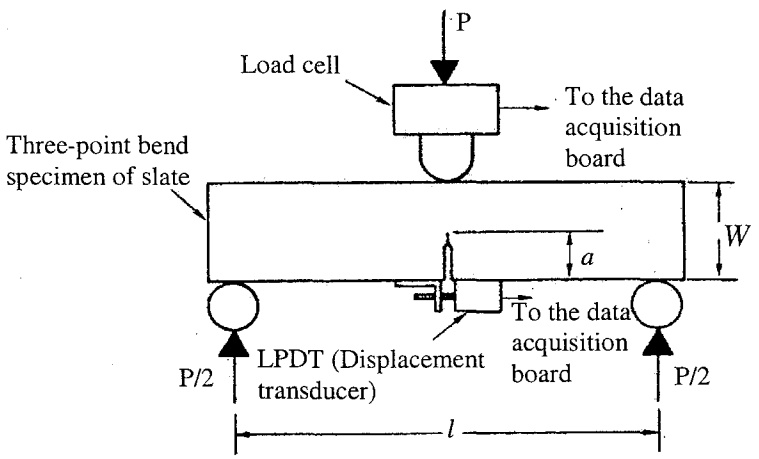

Figure 4.9: Schematic of three-point-bend specimen and experimental setup (Schmidt, 1976)

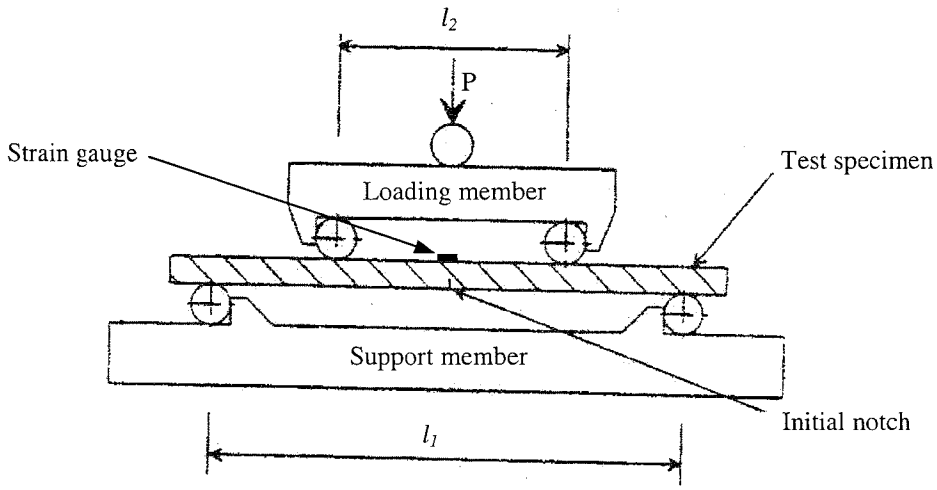

Fig. 4.10: Schematic of four-point-bend specimen and experimental setup (C 1421 – 99, ASTM, 1999)

4.7.1 Testing Procedure

Before the start of the test, specimens were removed from the container and kept in a dry place for 24 hours to evaporate the moisture from their external surfaces. Thereafter, a *LPDT* and a short piece of aluminum plate of thickness approximately 0.5 inch (12.7 mm) were glued at the bottom face of the specimens across the mouth of the notch for three-point-bending test. For four-point-bending test, strain gauge was glued at the back face opposite to the notch of the specimen following the procedure mentioned earlier in section 4.5.2. The *LPDT* and strain gauge were connected to the data acquisition board and initial readings were checked from the Lab view data acquisition software and made to be zero. After that the test specimen was placed in the test rig and the loading ram was brought in contact with the specimen by using the MTS 407 controller; the controller was connected to the data acquisition board. The initial reading obtained from the computer was also verified with those obtained from the controller. Before applying the load it was ensured that all the readings shown by the controller and computer were zero and that it

should also show the same load (both controller and computer) at all stages of loading. Once specimens were placed under the loading devices properly, the computer and MTS 407 controller were brought on line and the data acquisition begun. Displacement was controlled by MTS 410 digital function generator connected externally to the MTS 407 controller. A displacement rate 0.1mm/min was applied to the test specimen until failure of the specimen. Each test sample was examined to check whether the crack has propagated along the notch or not. Load displacement curve was plotted for each test specimen and maximum breaking load was determined. This load was used to calculate the apparent fracture toughness of slate. Similar procedures were applied in case of four point bending loading. Peak load was obtained from load vs. strain plots of test results.

4.7.2 Empirical Determination of Fracture Toughness

Two different geometric test specimens described in the previous section have been used to determine the fracture toughness of slate. The geometry described for three-point bending has been generalized for rock by ISRM (1988). The ISRM suggested dimensions are shown in Table 4.13 below.

Table 4.13: Specimen dimensions suggested by ISRM (1988)

Geometry parameter	Value	Tolerance
Specimen diameter	D	$>(10)$(*grain size*)
Specimen length, L	$4D$	$>3.5D$
Loading span, l	$3.33D$	$\pm 0.1D$
Notch width, t	$\leq$ the greatest of 0.03D and 1 mm	
$\alpha = a/D$, the dimensionless crack length ($0 \leq \alpha \leq 0.6$) where 'a' is the crack depth		

The expression for the stress intensity factor K_I provided by Bush (1976) and Ouchterlony (1980c) for three-point bending was,

$$K_I^S = \frac{P}{D^{3/2}} \times Y_k^S \text{ for } 0 \le \alpha \le 0.6 \tag{4.6}$$

where,

$$Y_k^S = \frac{l}{8D} \sqrt{\frac{1}{\sqrt{\alpha - \alpha^2}} \frac{\partial \left(Y_\lambda^S\right)}{\partial \alpha}} \tag{4.7}$$

Ouchterlony (1980) has given the following value of Y_k^S as,

$$Y_k^S = \frac{l}{4D} \times \frac{12.75\sqrt{\alpha}\sqrt{1+19.646\alpha^{4.5}}}{(1-\alpha)^{0.25}} \tag{4.8}$$

The other geometry used for four-point loading was the rectangular prism of depth W, width B and span l_1. Four-point loading system was chosen to eliminate the effect of shear stress on the cross section of the specimen which leads to pure bending. The stress intensity factor has been given by Srawley and Gross (1976) for four-point loading. According to their findings stress intensity factor can be written as:

$$K_I = \frac{P(l_1 - l_2)\sqrt{a}}{BW^2} \times \frac{3}{2\left(1-\frac{a}{W}\right)^{3/2}} \times \left\{ 1.989 - 1.33\frac{a}{W} - \frac{\left[3.49 - 0.68\frac{a}{W} + 1.35\left(\frac{a}{W}\right)^2\right]\frac{a}{W}\left(1-\frac{a}{W}\right)}{\left(1+\frac{a}{W}\right)^2} \right\} \tag{4.9}$$

for $0 \le a/W \le 0.6$ and $l/W = 4$, where l_1 & l_2 are the center to center support length of the test specimen and the loading member, respectively, shown in Figures 4.10; a is the crack depth.

4.7.3 Test Results

The results obtained from this test are given in Tables 4.14 and 4.15 for different crack lengths and specimen geometries. Table 4.14 gives the test results for three-point bending and Table 4.15 gives the test results for four-point bending. The variation of load with crack mouth opening displacement (three-point bending) and back face strain (four-point bending) obtained during fracture toughness test are shown in Figures C-5 to C-10 in Appendix C. From these figures it is seen that the magnitude of the maximum load varies with the depth of crack and the direction of layering. When load was applied perpendicular to the layer, the maximum load was obtained to be nearly ten times greater than those obtained for the load applied parallel to the layering. From these results it could be stated that the interlayer resistant force (so called cohesive force) is much less than the resistant force along the layer.

From these plots, it is also seen that material behaves non linearly at the beginning of the applied load and then it behaves linearly up to the maximum load and then decreases suddenly. The reason could be the development and coalescence of micro-cracks (so-called fracture process zone) at the tip of the crack before extending along the plane. Another reason could be the bluntness of crack tip that was created during making of the initial crack by manual hex saw. The post failure curve was nonlinear with a certain amount of plastic strain for three-point-bending. This nonlinearity was due to the presence of shear forces in addition to the bending moment along the crack plane during the application of load. Although nonlinearity exists very close to the maximum values of the load, the fracture toughness is calculated by using maximum load. It is seen that when the load reaches its maximum value, test specimen begins to lose its resistance very fast.

Table 4.14: Fracture Toughness of Slate

Load Parallel to the Bedding Plane (Three Point Bending Loading)

Cylindrical Specimen having Diameter =1.375″ (0.035 m) and Length = 5.5″ (0.14 m)

[Using equations (4.6) to (4.8)]

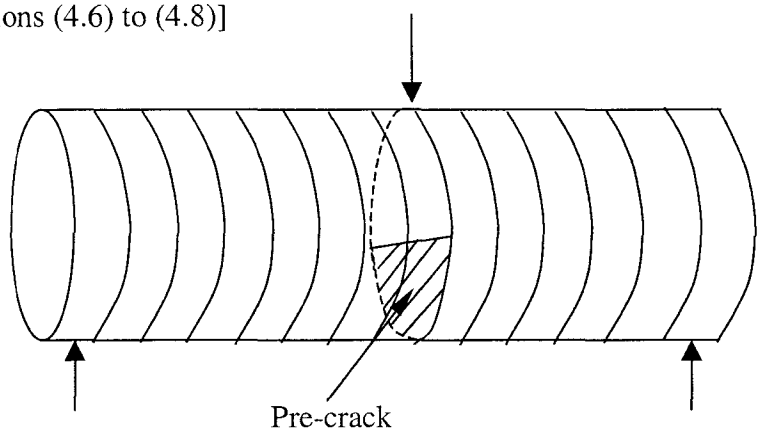

Crack depth (inch)	Maximum load (lbs)	K_{IC} [as per Bush (1976) and Ouchterlony (1980)]		K_{IC} from FE analysis of present tests
		psi.in$^{1/2}$	MPa.m$^{1/2}$	MPa.m$^{1/2}$
0.4375	73.8711	318.651	0.350	0.2414
0.5000	80.6289	393.856	0.433	0.2974
0.5625	72.6833	405.977	0.446	0.2871
0.5000	94.3555	460.907	0.506	0.3481
0.5625	84.0566	469.503	0.516	0.3319
0.5625	60.8000	339.602	0.373	0.2401
0.6400	61.6904	414.349	0.455	0.2979
Mean	75.4408	400.730	0.440	0.2920
Standard Deviation	± 11.1638 (± 14.80%)	± 52.277 (± 12.62%)	± 0.0574 (± 12.62%)	± 0.03795 (± 13.00%)
As per Bear and Bar (1977)	-	98.28 ± 27.30	0.108 ± 0.03	-

Table 4.15: Fracture Toughness of Slate

Load Perpendicular to the Bedding Plane (Four Point Bending Loading)

Rectangular Specimen having Sizes, Depth =1.5″ (0.38 m), Width = 1.0″ (25.4 mm) and Length = 6.5″ (0.165 m)

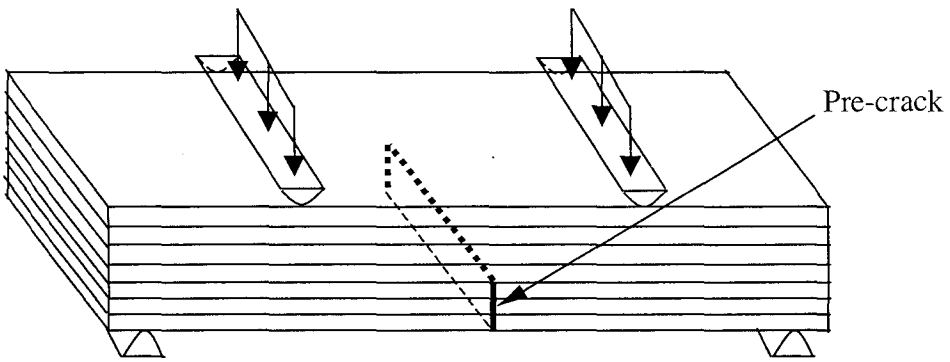

Test No.	Crack depth (inch)	Maximum load (lbs)	K_{IC} [as per Srawley and Gross (1976)]		K_{IC} from FE analysis of present tests
			psi.in$^{1/2}$	MPa.m$^{1/2}$	MPa.m$^{1/2}$
1	0.6720	659.74	2382.03	2.6175	0.31 (0.29*)
2	0.6563	710.34	2491.04	2.7073	0.35 (0.32*)
3	0.71875	559.05	2208.68	2.4270	0.22 (0.20*)
4	0.6875	986.99	3670.49	4.0333	0.44 (0.41*)
5	0.71875	876.99	3464.78	3.8073	0.35 (0.32*)
6	0.672	702.95	2538.05	2.7889	0.33 (0.37*)
	Mean	749.34	2794.64	3.0685	0.33 (0.31*)
	Standard Deviation	± 141.82 (± 18.93%)	± 561.38 (± 18.89%)	± 0.6164 (± 20.00%)	± 0.064 (± 19.40%)
	As per Bear and Barr (1977)	-	204.76 ± 16.38	0.225 ± 0.018	-

* - Values obtained from plane-strain finite element analysis of slate like material having isotropic properties

Therefore, the failure behaviour of slate could be considered as brittle and crack extension as stable crack extension. The crack extension profiles, obtained for some test specimens after carrying out fracture toughness test, are shown in Figures 4.11 (a) - (c).

The test results given in Tables 4.14 and 4.15 show that fracture toughness values of slate rock in mode I loading varies from 0.35 MPa.$m^{1/2}$ to 0.52 MPa.$m^{1/2}$ (mean value 0.44 ± 0.057 MPa.$m^{1/2}$) when load was applied parallel to the bedding plane and from 2.43 MPa.$m^{1/2}$ to 4.03 MPa.$m^{1/2}$ (mean value 3.07 ± 0.62 MPa.$m^{1/2}$) when load was applied perpendicular to the bedding plane. These values were computed by using the empirical formulae given by Bush (1976) and Ouchterlony (1980) for three-point bending load and by Srawley and Gross (1976) for single edge straight-through cracked rectangular beam under four-point bending loads. Test results were compared with those given by Bear and Barr (1977). Bear and Barr used CNRBEL test (circumferentially notched round bar specimen subjected to an eccentric longitudinal load) to determine the fracture toughness of slate. The values obtained by Bear and Barr were K_{IC} = 0.225 ± 0.018 MPa.$m^{1/2}$ for specimens drilled parallel to the bedding plane and K_{IC} = 0.108 ± 0.03 MPa.$m^{1/2}$ for specimens drilled perpendicularly to the bedding plane. Present test results [obtained using the empirical equations of Srawley and Gross (1976) and Bush (1976) and Ouchterlony (1980)] seem to give values quite different from those given by Bear and Barr (1977).

In order to overcome these inconsistencies, detailed plane strain and 3D finite element analyses (for a transversely isotropic material) were also carried out using the experimental values of slate properties and applied loads for three-point and four-point

bending fracture toughness tests; in addition finite element analysis (FEA) was also carried out for a simulated isotropic slate like material considering experimentally obtained in-plane properties (E = 76.0 GPa and ν = 0.20) as the system properties of isotropic material. The results of the plane strain FEA were found to be higher by less than 1% from those obtained from the three-dimensional finite element analysis using 20-noded isoparametric brick elements with reduced integration. Therefore, only plane strain FE analysis results are provided here for four-point bending tests. Moreover, 3D finite element analysis using 8-noded brick elements was also carried out for three-point bending tests of cylindrical specimens. Fracture toughness values obtained from the finite element analyses were compared with those obtained from the experimental studies. It was observed that the experimentally computed fracture toughness values [using the empirical equations of Bush (1976), Ouchterlony (1980) and Srawley and Gross (1976)] were much higher than numerically computed values (for the actual transversely isotropic slate); even for an artificially simulated isotropic slate, the fracture toughness values were only slightly different from those for the transversely isotropic slate. Hence the finite element analysis given values are taken to be the correct fracture toughness of slate. Thus the equations given by Bush (1976) and Ouchterlony (1980) for three-point bending load and Srawley and Gross (1976) for four-point-bending load seem to overestimate the actual fracture toughness of slate.

4.8 Dynamic Crack Propagation Velocities (Group #3)

Crack propagation velocity is an important parameter that has a great influence on the dynamic fracture toughness and needs to be considered properly to simulate the splitting phenomenon using a dynamic load. Bilek (1980) mentioned that dynamic fracture

(a)

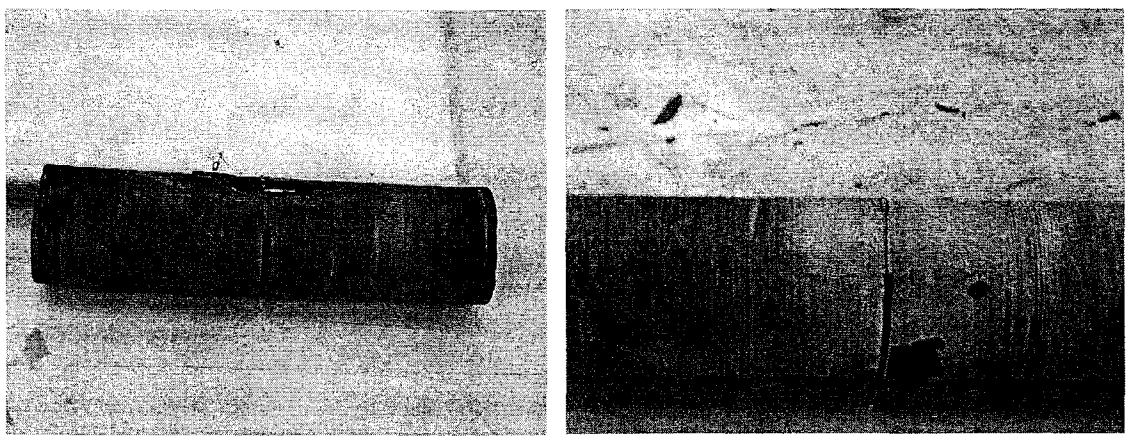

(b)

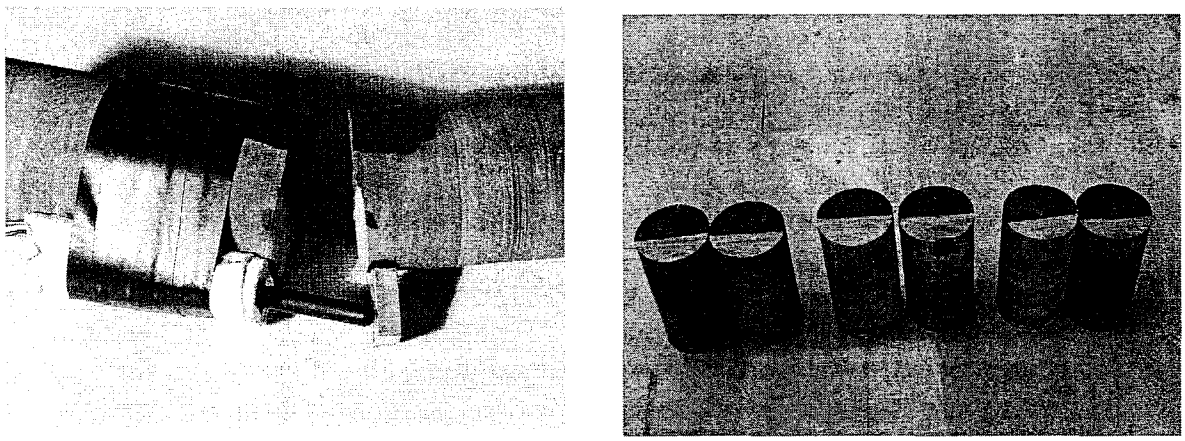

(c)

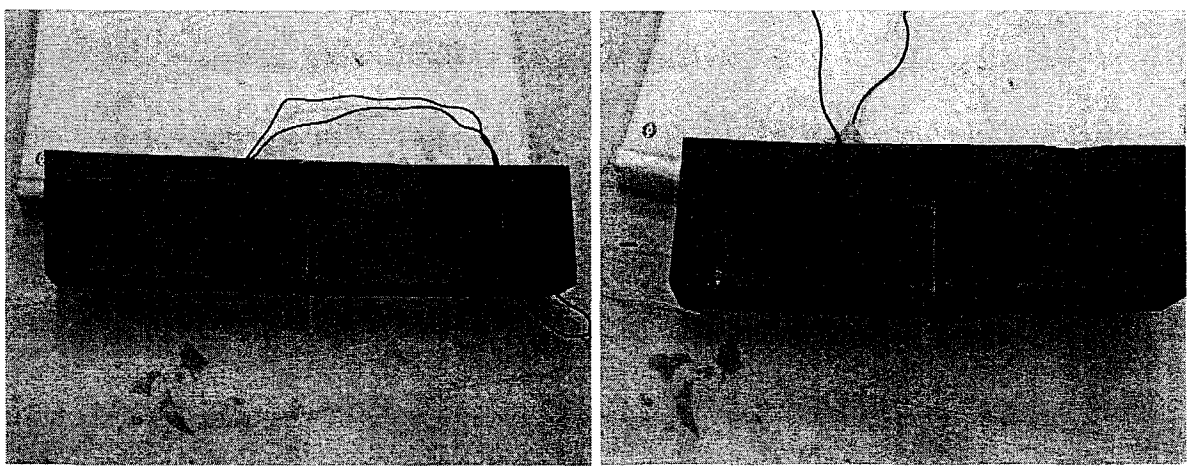

Figure 4.11: Post failure crack patterns: (a) and (b) cylindrical specimens; and (c) rectangular specimens

toughness for a running crack in SAE 4340 steel under quenched-and-tempered condition increased slowly up to a crack velocity of 100 m/s, and thereafter increased sharply up to and beyond a velocity of 1000 m/s. He mentioned that the crack velocity starts at a constant rate and varies continuously throughout the test, and it decreases as the crack length increases. He used rapidly wedged DCB (double cantilever beam) specimens to produce a stable crack propagation with a crack velocity < 150 m/s. Chow and Barns (1980) pointed out that slow crack velocities are typical of the rapidly wedged DCB tests. They carried out their investigation on low carbon steels at various temperatures ranging from -196^0 C to 0^0 C, to obtain relationship between dynamic critical stress intensity factor (K_{Id}) and crack velocity. They mentioned that K_{Id} decreases as crack velocity increases up to 50 m/s and reaches a minimum value in the range of 50 to 80 m/s; thereafter it increases slowly for velocities higher than 80 m/s, at a temperature -196^0 C (brittle behaviour of steel).

The commonly used experimental methods to determine the velocity of the dynamic crack propagation have been discussed earlier in Chapter 2. In this study, crack propagation velocities were measured using strain gauge sensors attached perpendicular to the plane of splitting of slate blocks. Strain gauges were fixed along the depth of the specimen to obtain strain signals during crack propagation. Gauges were glued on the surfaces of the specimens by following the same procedures as used in the pasting of strain gauges on the specimen surface for the tests for elastic moduli. The travel time of crack from one strain gauge to the other was obtained by analyzing the strain signal vs. time curve. When crack went beyond the strain gauge location, the strain increased to its maximum capacity (shown in Figures C-11 to C-20 in Appendix C). The time difference

between two successive jumps obtained from two strain gauges was calculated. Thereafter, the velocity of the crack propagation was obtained by dividing the distance by the time. The variations of strain signals with time are shown in Figure C-11 to C-20.

4.8.1 Results

The velocity computed from experimental measurement was an average velocity over the distance between the two strain gauges. The velocity was considered as the velocity at the middle position between the two gauge positions and plotted as a function of crack length to check whether their variations were linear (increase/decrease), constant or nonlinear (increase/decrease) or random. In order to obtain better representation of the variation of velocities one would require instantaneous measurement of velocity by fixing strain gauges very close to each other or by using crack gauges.

The crack propagation velocities and their variations with crack length obtained from different splitting tests (plane strain and non plane strain specimen) are shown in Figures 4.12 and C-21 to C-25 of Appendix C. It is seen that the velocities of crack propagation varied irregularly when crack started to propagate from the impact point to the bottom of the specimen (complete failure of specimen). Irregularities in crack propagation velocity are seen more in plane strain impact splitting blocks (Figure 4.12, C-22 & C-24 of Appendix C) than those obtained in non plane strain impact splitting blocks (C-21, C23 & C-25) of Appendix C). However in some cases the variation of velocities in plane strain and non plane strain blocks were obtained to be a nonlinearly decreasing one (Figures 4.12 and C-25).

Figure 4.12: Crack propagation velocity during impact splitting of slate blocks

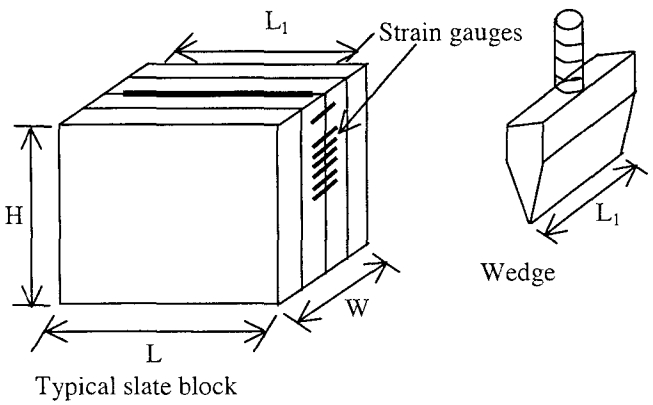

Specimen dimensions, L = 4.33 inch (110.0 mm), W = 4.0 inch (101.6 mm) and H = 5.12 inch (130.05 mm), wedge length, L_1 = 4 inch (101.6 mm), clear height between wedge and specimen = 1.5 inch (38.1 mm), wedge penetration depth = 0.394 inch (10.0 mm).

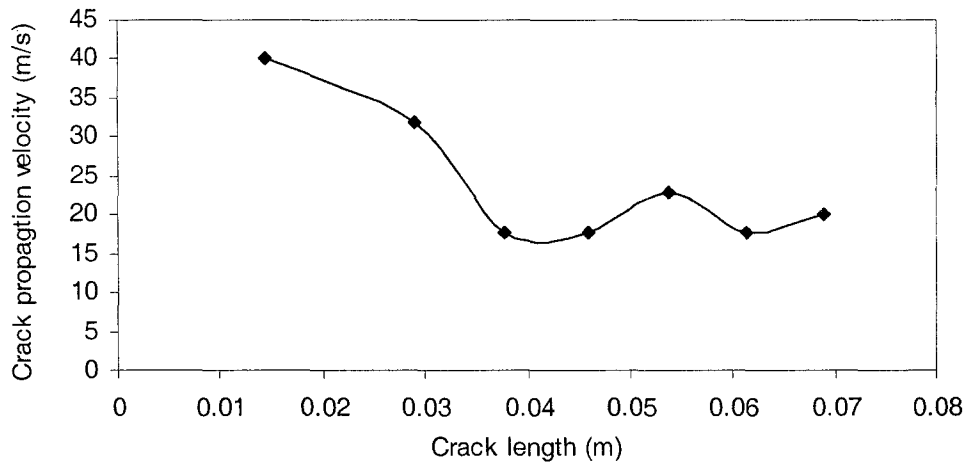

Table 4.16: Crack propagation velocity during impact splitting of slate blocks

Crack length (m)	Crack velocity (m/s)	Average velocity (m/s)
0.014	40	
0.029	32	
0.038	17.78	
0.046	17.78	24.03
0.054	22.86	
0.061	17.78	
0.069	20	

The crack propagation velocities obtained from this study varied from 2 m/s to 120 m/s approximately; if the lower velocities were neglected then it varies 30 to 120 m/s. This large variation of velocities probably occurred due to pre-existing flaws in the cracked plane or other flaws such as, material discontinuity, flattening of grain particles along the layer boundaries, etc., in the specimen. This was also observed during the impact splitting of slate as seen from split surfaces shown in Figures 4.20 (a) – (d). It is seen that some parts of the split surfaces were not joined together or bonded (Figures 4.20 (b) & (d)) under intact conditions

4.9 Microscopic Test (Group # 4)

4.9.1 Specimen Preparation and Testing Procedures

Four small pieces of rectangular slate rock blocks, of size approximately $1'' \times 1'' \times 0.5''$ ($25.4 \times 25.4 \times 12.7$ mm), were cut from the available slate material. Two blocks were cut parallel to the bedding plane and two were cut perpendicular to the bedding plane. All four blocks were machined first by using the grinder with water; thereafter, a very smooth polishing was done to obtain a shining surface. A very thin layer of gold coating was applied on the surface to be scanned. Gold coating was applied according to the requirement of Scanning Electron Microscope (SEM) [Gabriel (SEM user manual), 1985].

At first the specimen was fixed properly on a circular plate and kept under the microscope in the chamber of SEM. After choosing the proper resolution and magnification of the microscope a microphotograph of a location was taken for observing the composition of the material. At least 2 scanning pictures at different resolutions and magnifications were taken for the same location. Ten different locations on the same

surface were also chosen to obtain information related to the grain sizes and the distribution of the particles. The same procedure was repeated for new layers after removal of the old layers. In case of specimens where layer direction was parallel to the microscopic axis, microscope was focused at different locations parallel to the layering to obtain individual layer thickness. The SEM microphotographs were stored in a computer for further analyses such as measuring grain sizes, grain distribution and layer thickness.

4.9.2 Results and Discussions

The SEM microphotographs obtained from this test are shown in Figures 4.13 to 4.16. Figures 4.13 (a) - (d) show the in-plane (layer) material micro characteristics. Microphotographs were also taken in a direction perpendicular to the layering. Figures 4.14 (a) and (b) show discontinuity of the layer on the layer surface. Figures 4.15 and 4.16 show the layer thickness and the irregular characteristics of interlayer boundaries. All the SEM observations were varied from a scale of 200 μm to 10 μm. After a detailed study of the scanning electronic microscopic pictures, it was found that the sizes of grains in a layer varied approximately from 1 to 30 micrometers and grains seemed to be flattened and smooth. The existence of discontinuities at the boundary of the grains was observed when magnification was increased from 100 μm to 10 μm. From this observation it could be concluded that large discontinuities exist along the grain boundaries and its size is so small that it is almost invisible in a micro level observation. It is also seen that their distributions are random in nature. The cracks considered in this study are macro level cracks, which ignored the grain boundary discontinuities or cracks by assuming that grains are bound together by intermolecular forces within a layer and discontinuities are developed only at the layer's boundary. Layers seem to be not well

(a) (b)

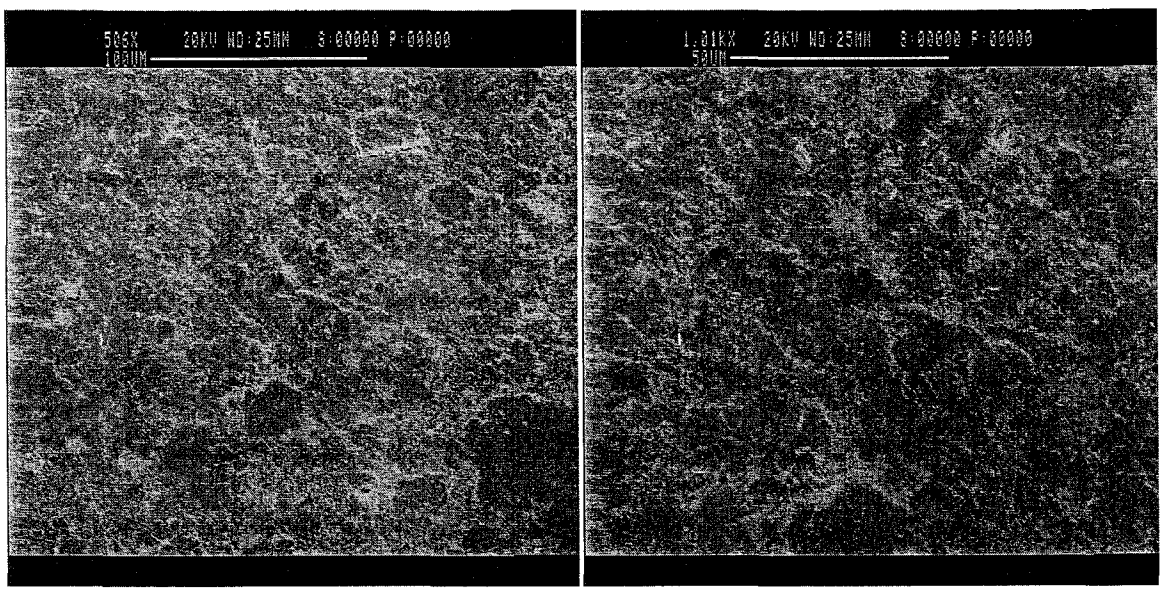

(c) (d)

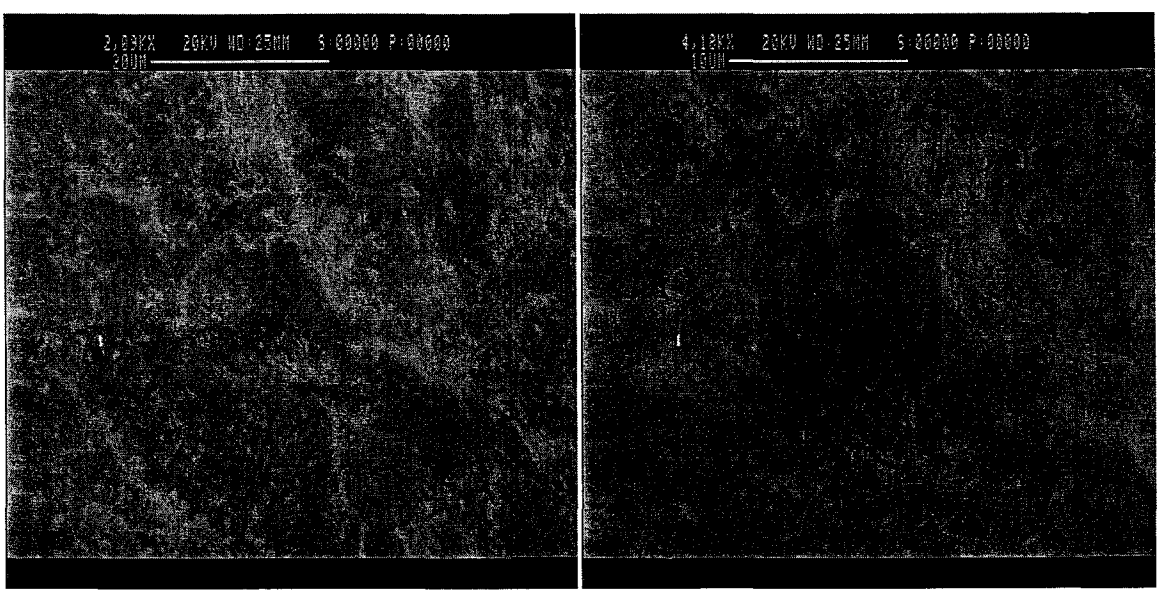

Figure 4.13: In plane microphotograph showing grain size and grain boundary at different micro scales: (a) 100 μm; (b) 50 μm; (c) 20 μm; and (d) 10 μm.

(a) (b)

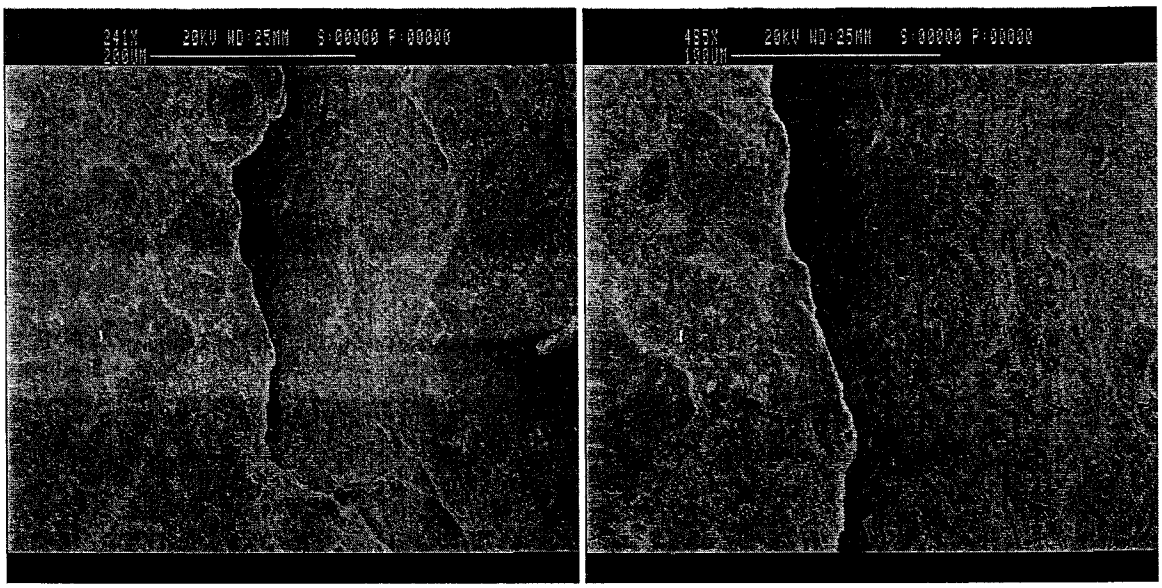

Figure 4.14: Microphotographs showing the layer discontinuity at scales of: (a) 200 μm; and (b) 100 μm

(a) (b)

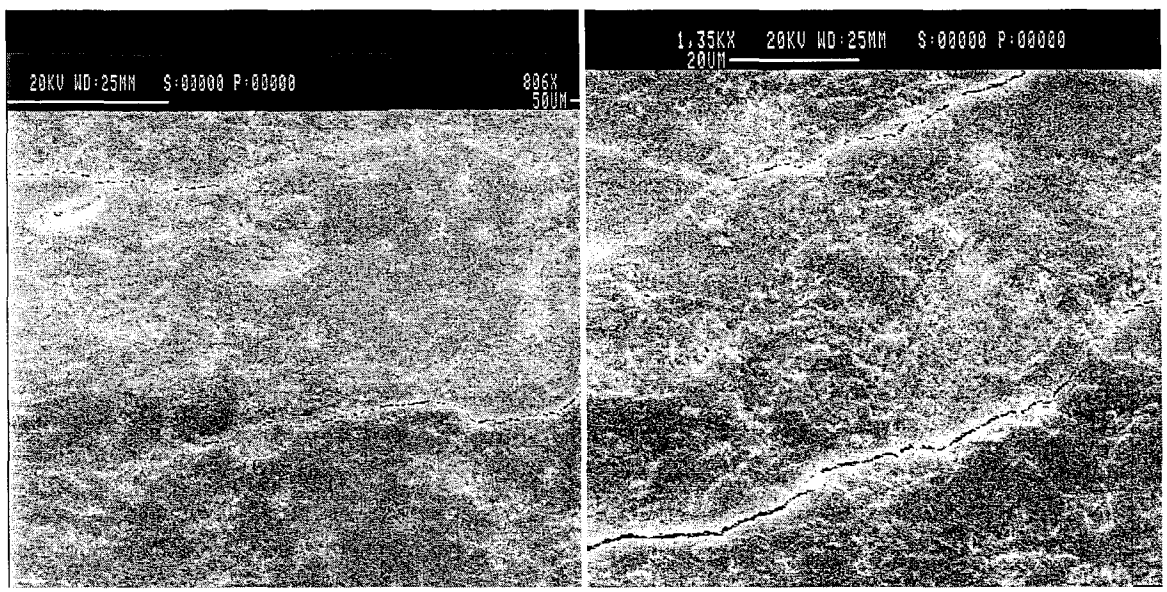

(c) (d)

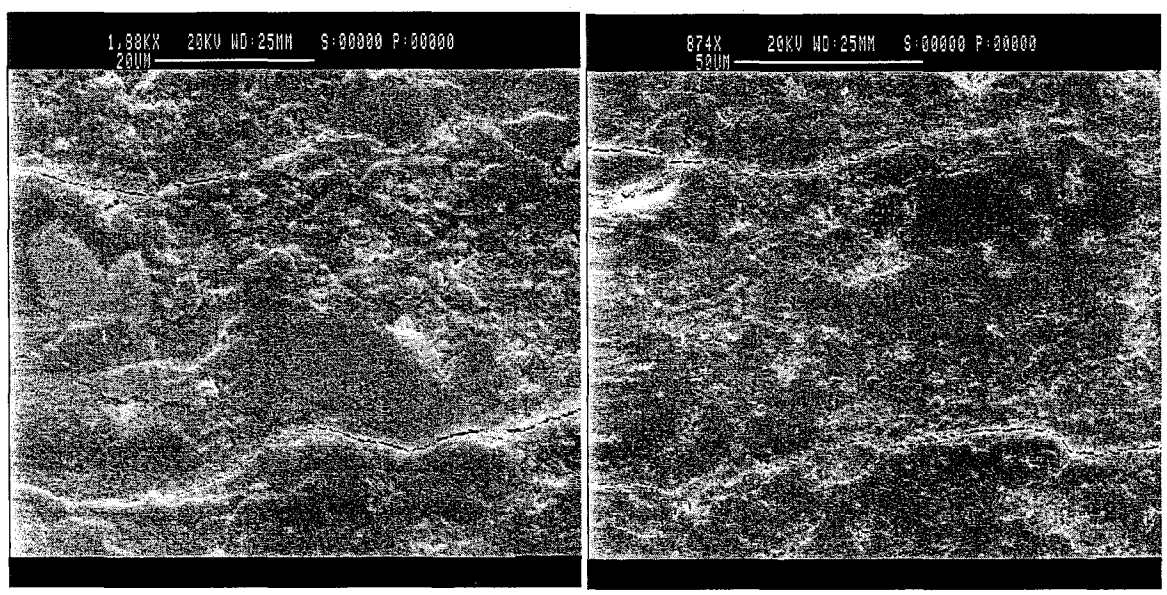

Figure 4.15: Microphotographs of layer thickness and orientation at a scale of: (a) 50 μm; (b) 20 μm; (c) 20 μm; and (d) 50 μm

(a) (b)

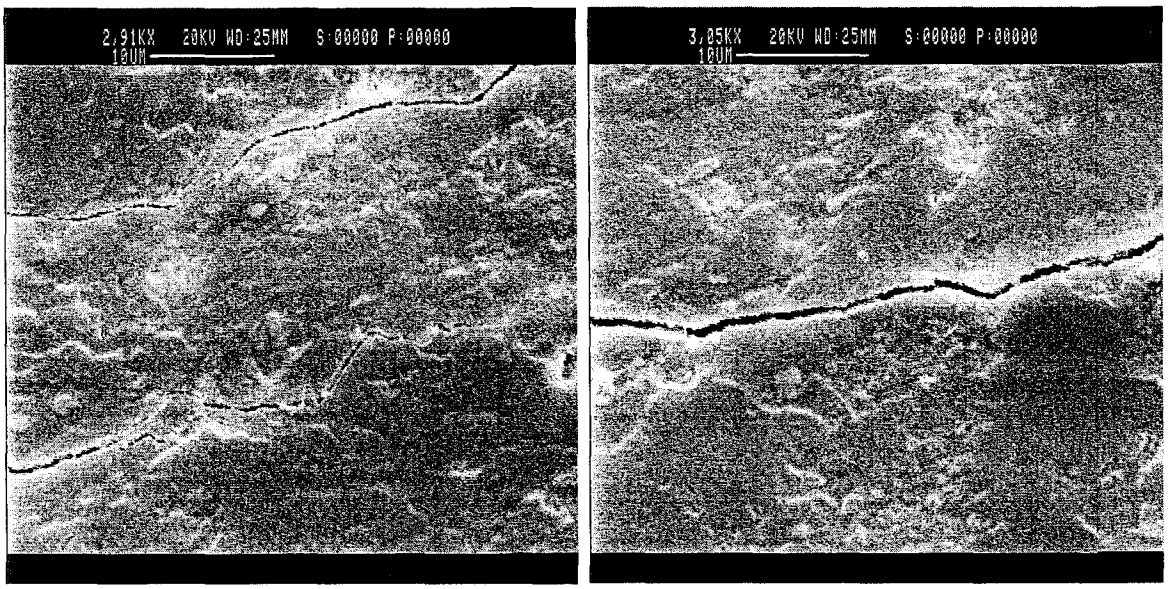

Figure 4.16: Microphotographs of layer boundaries at scales of: (a) 10 μm; and (b) 10 μm

defined. Discontinuity of layers is the common phenomena (Figure 4.14 (a) and (b)). After examining the interlayer boundaries at 10μm scale level it was observed that a gap of approximate width 500 nanometer occurred between two layers (Figure 4.16 (b)). However, at macro level it could be assumed that each layer is connected to each other by weak cohesive forces at the layer boundaries. A picture showing the crack at the layer boundary is shown in Figure 4.16 (b). In this study micro layer thickness was obtained to be approximately between 20 to 50 μm.

4.10. Splitting Test of Slate Blocks (Group # 5)

4.10.1 Specimen Preparation and Experimental Setup

Specimens were cut from large sized slate blocks to determine the splitting forces of various sizes of slate blocks in the same manner as those for elastic properties test. Specimens were taken out from the water tank two days before the tests were to be carried out to make them air dry and for fixing the strain gauges. Strain gauges were fixed on the sides of the specimen using the same procedure described earlier in section 4.5.2.

In order to fabricate the setup for the impact breaking of slate blocks, a load frame was assembled to carry the hydraulic actuator, load cell and the wedge-shaped impact indenter; the swivel end hydraulic actuator was hung vertically on the load frame to apply in-plane loads on slate specimens. A load cell rated for 22 kips (97.86 kN) [10 kips (44.48 kN) for small blocks] was fixed to the lower part of the actuator. A fabricated wedge shaped impact indenter (shown in Figure 4.18) was attached to the bottom of the load cell. This device applied the impact force directly to the slate specimen using a MTS load test frame through the hydraulic actuator. The movement of the ram of the hydraulic actuator was controlled by a MTS 407 controller. This controller had the capability to control both load and displacement, independently. A displacement controlled square pulse impact force was applied to the sample through a 410 digital function generator connected externally to the MTS 407 controller. The actuator used in this test is designed to allow a total movement of the ram up to 6 inches (152.4 mm); this means that the actuator ram can move only 3.0 inches (76.2 mm) in a certain direction either up or down from its central position. Test specimens were placed on a heavy steel platform that was fixed to a 3.0 feet (0.914 m)

thick concrete floor slab. In order to keep the specimen stationary on the platform, lateral supports were provided. Two L-shaped lateral supports, made of wooden planks, were fixed slightly away [approximately 0.5 inch (12.7 mm) on both sides] from the sample using heavy steel clamps. A cable was connected between MTS 407 controller and data acquisition system to transfer load signals from the controller to the computer via the data acquisition board. This signal was converted to load using proper conversion factor. The voltage signals obtained from strain gauges were passed through the data acquisition board to the computer. Commercially available LabView data acquisition software was used to acquire data from load cell and strain gauges and stored for further analysis. Basically, hydraulic actuator, strain gauges, load cell transducers and data acquisition system were required to set the system up. Flow chart and laboratory instrumental setups for the experimental study of splitting of slate block are given in Figures 4.17 and 4.18

4.10.2 Hydraulic Actuator and Controller

The hydraulic actuator used in this test provided the driving force required for applying impact force on the test specimen. A hydraulic pump was connected to the actuator. Before applying load to the system hydraulic pump was started by using the MTS 407-controller system. This controller is a single channel, digitally-supervised, proportional, integral, derivative, feed-forward servo controller that provided a complete control of one servohydraulic channel/station in a MTS testing system. The controller included AC and DC transducer conditioning, basic function generation (with the capability to accept externally generated command signals), servo-valve drive signal generation, and hydraulic pressure control. Actuator was connected to the MTS 407.05 pump interface and pump interface was connected to the controller. Input displacement/load signal is

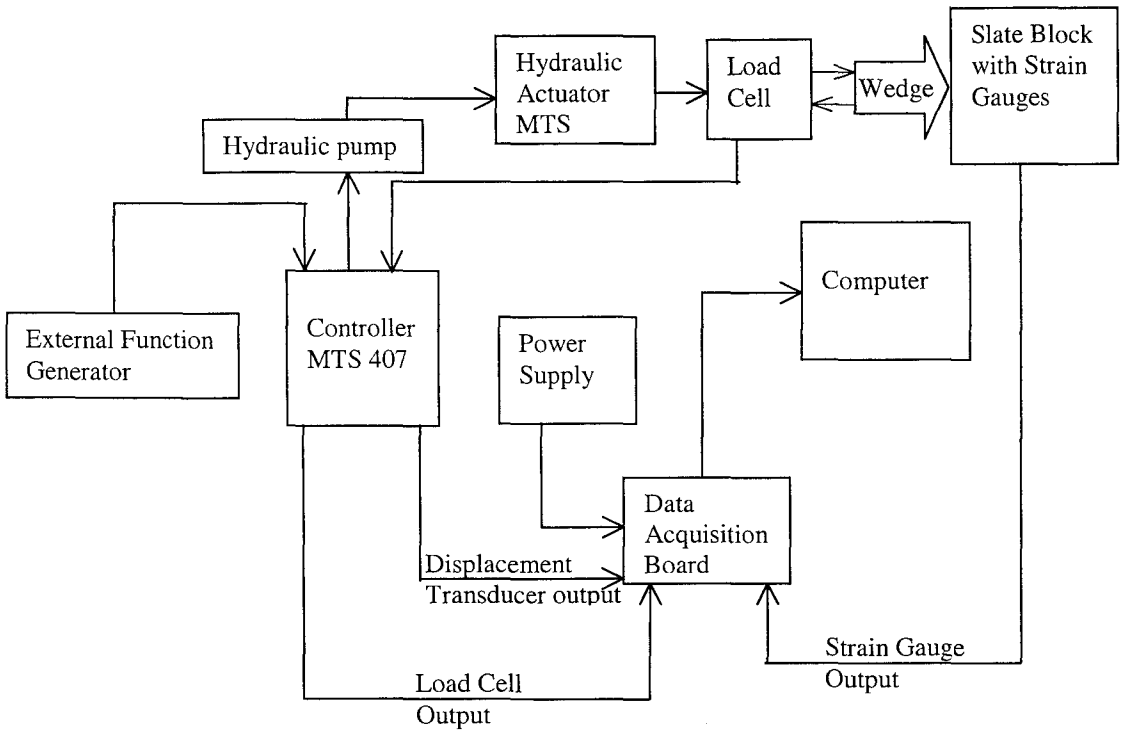

Figure 4.17: Flow chart for experimental setup of splitting test on slate block

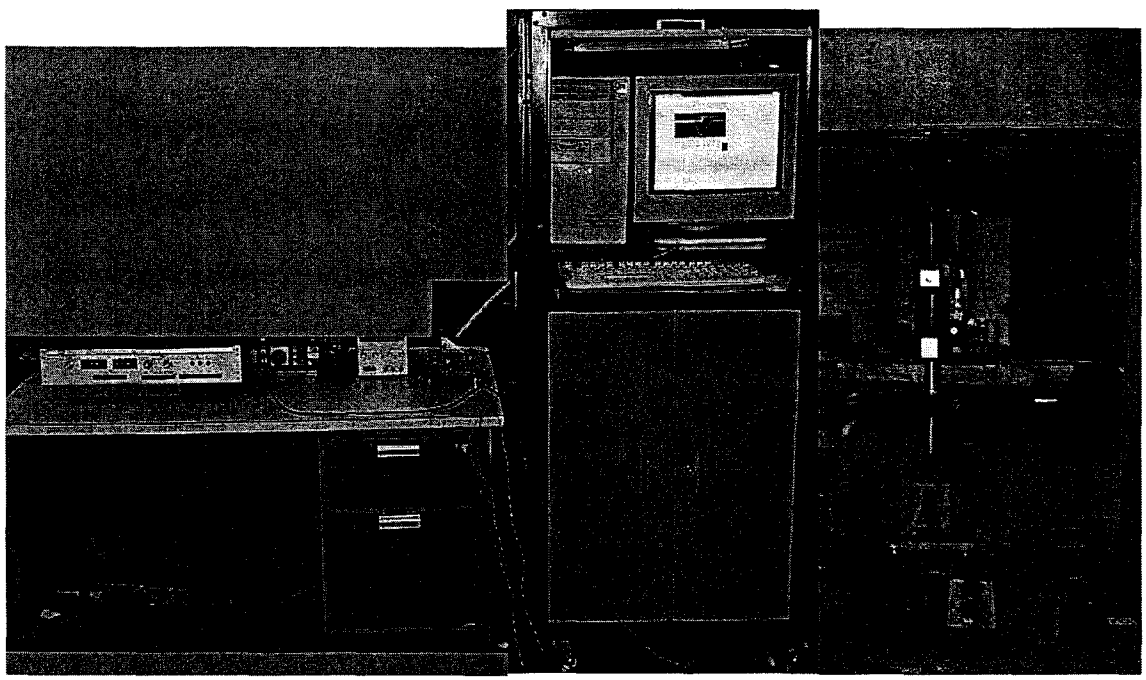

Figure 4.18: Instrument set up for impact splitting test on slate block.

passed to the actuator through the hydraulic pump from the function generator of the MTS controller. Hydraulic actuator [Model number: 244.22, Serial number: 637, Assembly number: 367715-11, Force: 22 kips (100kN), Area: 7.57 in^2 (48.9 cm^2)] made by MTS System Corporation, Minneapolis, Minnesota 55424, USA, was used during the entire test program for applying the impulsive force. It is s double-acting, double-ended, heavy-duty actuator that operated under precision servovalve control in the MTS closed-loop servohydraulic system. The maximum force it can apply on the test specimen is 22 kips (100 kN) and its stroke for the dynamic loading is ± 3.0 inch (± 76.2 mm) and static loading is ± 3.4 inch (± 86.36 mm).

4.10.3 Impact Splitting Test Results

Different sizes of surface dried slate blocks (from 0.1 m × 0.048 m × 0.1 m to 0.3429 m × 0.15 m × 0.3175 m) shown in Figures 4.19 (a) and (b) were split using the hydraulic actuator in the laboratory. Force and strain gauge responses were recorded during the progress of tests. The variation of impact force and strain gauge readings with respect to time for slate blocks having different sizes are shown in Figures C-11 to C-20 in Appendix C.

The entire breaking process may be characterized into two separate physical phenomena: crushing and splitting. Therefore, the measured impact force could be considered to be made up of into two force components; crushing force and splitting force. Crushing force may be defined as the force required to crush the slate material at the beginning of impact at the impact interface on slate (or entrance point of wedge into the specimen) and is calculated based on shear failure criteria. In this part of the analysis, it is assumed that

failure occurs in slate due to shear stress developed in the test specimen just below the initial contact area of wedge, when the applied load is equal to the material shear strength of the crushed volume. It is essential to mention here that crushing of brittle material would be the result of the coalescence of micro cracks (tensile failure) or shearing of a plane of material over the other. Existing cracks in a favourable direction are propagated fast under a fast compressive force and they coalesce and grow within a local region and pulverize the rock. Pulverizing phenomenon usually happens in case of hard rocks and high velocity impact problems. However, for relatively soft rocks (such as slate, schist, and sandstone) and low velocity impacts, shear failure is the commonly observable event. This load was taken as the initial crushing load.

Olofsson, et. al. (1991) studied ice failure mechanism close to the contact area in a series of small scale crushing tests at relatively high indentation velocities. They used an iterative numerical model based on successive shear failure to predict the crushing behaviour. They mentioned that the ratio of shear strength to contact pressure controls the fractal behaviour of ice crushing. They pointed out that shear strength and contact pressure are related to the velocity of the indentor. Their ratio (shear strength and contact pressure) decreases as the indentation rate increases and finer fragmentation of crushed ice is produced.

In a similar manner, after the initial crushing penetration of the specimen, the indenter starts to apply force normal to the penetrating face of the indenter on the slate specimen. This force acts on the penetrated specimen face as a normal-to-the-face compressive force. Force applied in addition to the initial crushing force attempts to split the slate

block. Splitting force is calculated based on either the normal stress failure criteria or mode I fracture toughness of the material by assuming that mode I stress intensity factor, for a particular length of crack and applied loading, is equal to the material fracture toughness. Normal stress failure criterion is applied at the starting of splitting process by assuming that the maximum principal stress developed due to applied load is equal to the tensile strength of the material over the split area. Since splitting is an indirect effect of applied load on the specimen, it is assumed to start when the applied force reaches its peak value in plane strain splitting tests. For this reason, the peak value of load-time curve represents the critical impact load required for plane strain splitting tests [specimen length (0.1 m) was the same as the length of wedge (0.1 m)].

Wedge was assumed to enter 10 mm inside the specimen during splitting; it was 37 mm above the specimen before impacting the specimen surface. Therefore, the full length of crack propagated from top to bottom during the splitting process. The post peak part (separating and falling) of breaking force vs. time curve represents resistance of slate block at different stages of crack propagation. When crack starts to propagate, opening of the split surfaces increases and the area of the uncracked ligament (i.e. resisting area) decreases gradually. Consequently, resistance of the block also decreases. This phenomenon has been shown by plotting the load cell and strain gauge responses together after making a time shift. The shifting of time was needed to synchronize the force and strain gauge reading to describe the splitting process of slate block. It was done by considering starting time of crushing failure as the zero time for strain gauge readings. Another time shifting of strain gauge readings was required to include the time delay of load cell response as its output depends on the resistance of the material and the length of

the interposed steel cylinder placed between load cell and test specimen. Since strain gauges were on the test specimen and an indenter and a 8 inch long, 2 inch outer diameter hollow threaded steel rod were placed between the specimen and the load cell (for varying the distance between actuator ram and the slate specimen for testing different sizes of slate blocks from a fixed bottom platform), the strain gauges' responses reached the data acquisition system a little earlier than the load cell response. The load cell reading was shifted by a time equal to that needed for a propagating longitudinal wave pulse to reach the load cell. The time taken to propagate the longitudinal load pulse to the load cell depended on the slate properties and intensity of striking force (indentation rate). The velocity of longitudinal wave propagation pulse for isotropic steel material was calculated using the formula $v_L = \sqrt{\frac{E}{\rho}}$. The travel time needed for the longitudinal wave from wedge tip to reach the load cell was increased to twice its value due to the low velocity impact force and damping of the medium (since the wave propagation velocity decreases by half for a damping of 5%-7%). When the impact load reached its peak value, crack started to propagate at speeds of 30 - 120 m/s (approximately, neglecting lower values of propagation velocities) as detected by the strain gages used.

In Figure C-11 (in Appendix C), the first strain gauge was fixed 3.4 mm away (along the depth of the specimen) from the impacting point of wedge, the 2nd strain gauge was fixed 22 mm away from the first gauge and other gauges were fixed along the depth of the specimen at equal intervals of 8 mm. In Figures C-12 and C-13 (Appendix C) first strain gauge was fixed very close to the impacting point (4 mm and 2 mm, respectively). In C-12 the 2nd strain gauge was 35 mm below the impacting point and other gauges were

fixed at equal intervals of 7 mm. In Figure C-13, the distance between 1^{st} –2^{nd} was 35 mm, 2^{nd} – 3^{rd} was 15 mm, 3^{rd} – 4^{th} was 12 mm and the rest of the gauges were 10 mm apart.

In Figure C-14, it is seen that crack starts in the specimen before reaching the peak load. This load-strain interaction curve was obtained during the splitting of a non-plane strain specimen having length of block greater than the length of indentor. Wedge was kept 58 mm above the specimen before impacting the specimen and it was observed to enter 12.5 mm inside the specimen before the slab split apart. First strain gauge was fixed 7 mm away from the impacting edge, 2^{nd} strain gauge was fixed 45 mm away from the first strain gauge and the subsequent strain gauges were fixed at intervals of 38 mm, 36 mm, 36 mm, 34.5 mm and 19.5 mm, respectively. Strain gauge positions for Figure C-15 were not the same as Figure C-14. First strain gauge was 4 mm below the top surface of the specimen and the others were fixed sequentially at 20 mm, 13.55 mm, 14.33 mm, 20 mm, 14.2 mm, 15 mm and 13.63 mm, beyond the preceding one, respectively. In both cases crack starts first under the wedge tip and grows horizontally and vertically downward; more energy is required to propagate the crack transversely, to the edge of the specimen. The peak value of applied load develops after the crack advances to a certain distance (horizontally) from the initial wedge impact locations. If the load vs. strain interaction diagram is plotted after shifting time it is seen that load reaches the peak value when crack reaches the strain gauge fixed at a distance 140 mm away from the center line of the block. Thereafter, it starts to decrease.

The load vs. strain interaction diagram shown in Figure C-16 shows the results for a

block where strain gauges were fixed on both parallel edges of slate specimens at the same height along the depth. The first strain gauge was fixed at a depth equal to 71 mm below the top surface and others were fixed 89 mm apart. Strain gauge readings were not coincident with one other due to the fact that the crack did not propagate symmetrically on either side of the specimen. A small time delay was observed. Crack reached the face 1 faster than the face 2 in an inclined manner. Unsymmetric application of impacting load and the unsymmetric distribution of the pre-existing cracks inside the specimen could have contributed to this nonsymmetric nature of crack growth. Similar cracking scenarios were observed in Figures C-17 to C-20. In all these cases strain gauges were fixed at the same height on parallel edges by fixing the first gauge at 51 mm below the top surface and the subsequent gauges at 64 mm below the other. The maximum loads obtained during splitting of different sizes of slate blocks are given in Tables 4.17 to 4.19.

Some of the blocks, split in the laboratory, are shown in Figures 4.20 – 4.22. In all cases, slate blocks were impacted by the indenting wedge at the center of the top surface. A crushing zone that developed during splitting has also been shown (marked by rectangular box) on the splitting surfaces [see Figures 4.20(a), 4.20(c), 4.20(d) and 4.21]. In Figures 4.20 (a), (b) and (d) it is seen that a part of slate block along the splitting plane seems to be separate initially itself and does not seem to offer any resisting forces. Therefore, breaking load obtained was much less than those obtained from the same size block where entire breaking plane was active in resisting the splitting force [Figures 4.20 (c) and 4.21]. Split surface texture of load resisting parts of splitting surface is different from those of unresisting parts [as could be seen in Figures 4.20 (a) and (b)]. Resisting parts of splitting surfaces seem to be smooth whereas the unresisting parts seem to be

Table 4.17: Impact breaking load of different sizes of slate block using wedge having a 63.5 mm transverse length (Three-dimensional impact splitting).

Specimen size ($L \times W \times D$) in 'm'	Breaking force	
	lbf	kN
$0.095 \times 0.042 \times 0.171$	1348.00	5.996
$0.108 \times 0.042 \times 0.124$	1670.00	7.428
$0.108 \times 0.048 \times 0.102$	1100.00	4.893
$0.108 \times 0.051 \times 0.102$	1060.00	4.715
$0.110 \times 0.057 \times 0.113$	1245.00	5.538
$0.111 \times 0.059 \times 0.109$	1865.00	8.296
$0.113 \times 0.065 \times 0.113$	1611.00	7.166
$0.111 \times 0.067 \times 0.121$	1763.00	7.842
$0.108 \times 0.067 \times 0.111$	1733.00	7.709
$0.116 \times 0.071 \times 0.113$	1425.00	6.339
$0.113 \times 0.074 \times 0.122$	1387.00	6.170
$0.140 \times 0.051 \times 0.143$	1665.00	7.406
$0.163 \times 0.061 \times 0.160$	2266.00	10.079
$0.160 \times 0.075 \times 0.168$	3140.00	13.967
$0.168 \times 0.071 \times 0.162$	2246.00	9.990
$0.152 \times 0.078 \times 0.162$	3020.00	13.433
$0.162 \times 0.083 \times 0.159$	2770.00	12.321
$0.160 \times 0.083 \times 0.170$	2200.00	9.786
$0.159 \times 0.092 \times 0.165$	2832.50	12.599
$0.163 \times 0.092 \times 0.171$	2400.00	10.675

L = Length, W = Width and D = Depth

Table 4.18: Impact breaking force of plane strain slate block using wedge having a 0.1016 m (4 inch) transverse length (plane strain impact splitting).

Specimen size ($L \times W \times D$) in 'm'	Breaking force	
	lbf	kN
$0.102 \times 0.051 \times 0.102$	977.00	4.345 *
$0.102 \times 0.076 \times 0.102$	1100.00	4.893 *
$0.102 \times 0.102 \times 0.102$	1236.46	5.500 *
$0.102 \times 0.127 \times 0.102$	1618.63	7.200 *
$0.102 \times 0.102 \times 0.127$	1300.53	5.785
$0.102 \times 0.102 \times 0.152$	1503.53	6.688 *
$0.102 \times 0.102 \times 0.178$	1627.85	7.241
$0.102 \times 0.102 \times 0.203$	1813.77	8.068 *

* - Indicates average value of two blocks
L = Length, W = Width and D = Depth

Table 4.19: Impact breaking force of 3D typical slate block using wedge having a 0.1016 m (4 inch) transverse length.

Specimen size ($L \times W \times D$) in 'm'	Breaking force	
	lbf	kN
$0.127 \times 0.152 \times 0.157$	3533.00	15.716
$0.232 \times 0.062 \times 0.156$	3500.00	15.568
$0.239 \times 0.095 \times 0.172$	3706.00	16.485
$0.248 \times 0.080 \times 0.192$	4004.00	17.810
$0.232 \times 0.124 \times 0.156$	4300.00	19.130
$0.235 \times 0.076 \times 0.156$	6300.00	28.024
$0.243 \times 0.081 \times 0.163$	4700.00	20.906
$0.250 \times 0.104 \times 0.220$	4941.00	21.980
$0.232 \times 0.124 \times 0.160$	6500.00	28.910
$0.25 \times 0.122 \times 0.200$	7202.00	32.040
$0.254 \times 0.127 \times 0.203$	4725.51	21.020
$0.305 \times 0.086 \times 0.184$	4956.00	22.045
$0.305 \times 0.080 \times 0.175$	4526.00	20.130
$0.305 \times 0.152 \times 0.254$	4985.16	22.175
$0.340 \times 0.100 \times 0.320$	7305.00	32.500
$0.337 \times 0.149 \times 0.254$	2835.75	12.614
$0.368 \times 0.098 \times 0.305$	5933.00	26.391

L = Length, W = Width and D = Depth

splitting across different layers. In Figures 4.20 (a) and (b) it is seen that part of the unresisting slate layer under the initial crushing zone got detached from the original plane of splitting and pushed into the specimen during the splitting process. This is a sign of shear failure under short term high intensity impact loads. This force was generated more at the beginning of low velocity impact force, causing a crack to start under the tip of the indenting wedge; the crack then propagated gradually towards the end of the specimen along the same plane in a non-plane strain cracking.

Some meandering of crack front (away from a straight vertical plane) was observed in some specimens. Non uniform layering in slate could be a reason for this. However, regular splitting and uniformity of layering was a common feature for most of the slate blocks. In order to examine whether the crack propagated symmetrically along the crack plane or not, strain gauges were fixed at the same distance on both sides of the test specimen from the center of the wedge. The variation of strain gauge responses obtained from tests of a typical slate block was given earlier in Figures C-16 to C-20 (Appendix C) where the load was applied in a three-dimensional manner at the center of the transverse width of slate block. It is seen from those figures that crack propagation wasn't exactly symmetrical. The crack propagation plane for plane strain splitting test is shown in Figures 4.22 (b) and (c). It is seen that the block was broken exactly into two pieces and crack plane was almost vertical, and crack front almost horizontal.

In order to obtain the generalized shape of experimental impact splitting force for plane strain and non-plane strain slate blocks normalized splitting force was plotted with respect to normalized time. Normalized splitting force was obtained by dividing the time

(a)

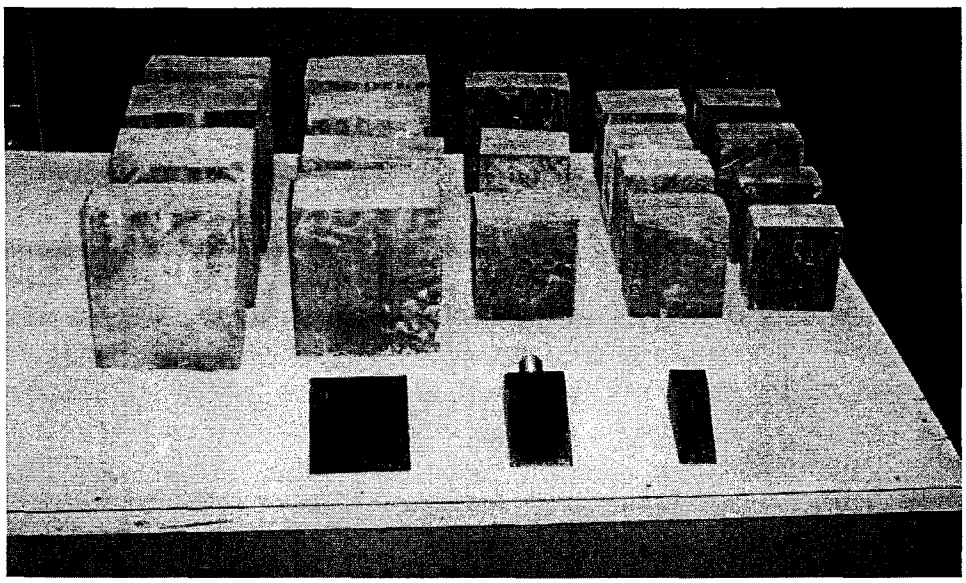

(b)

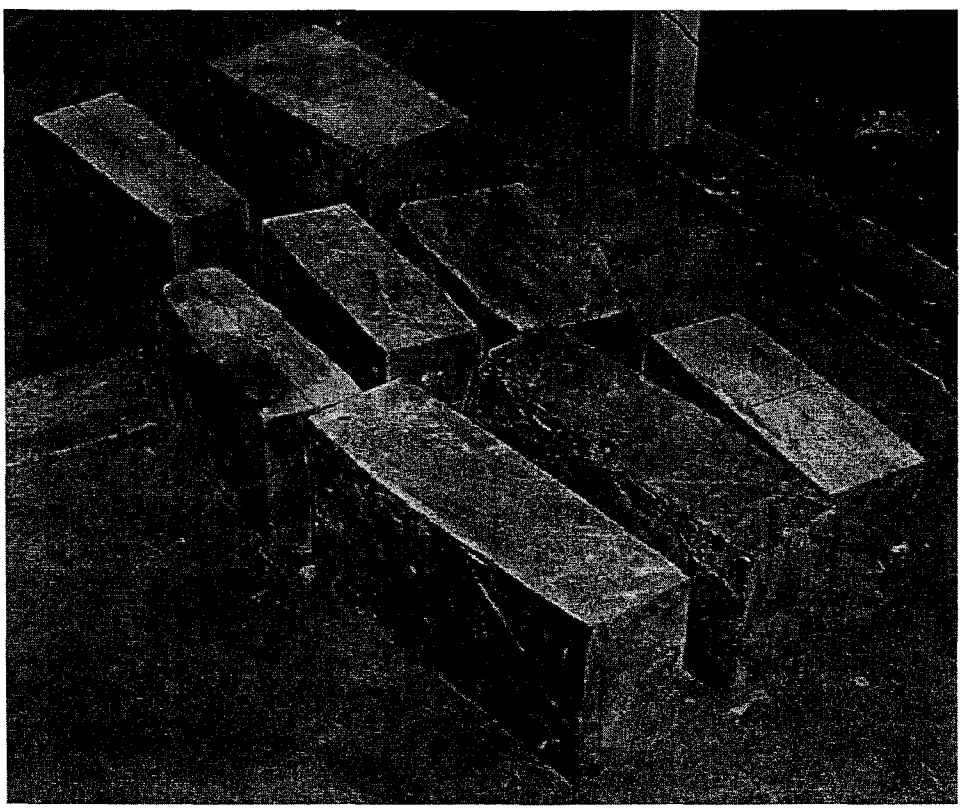

Figure 4.19 (a) and (b): Different sizes of slate block ready for splitting

(a)

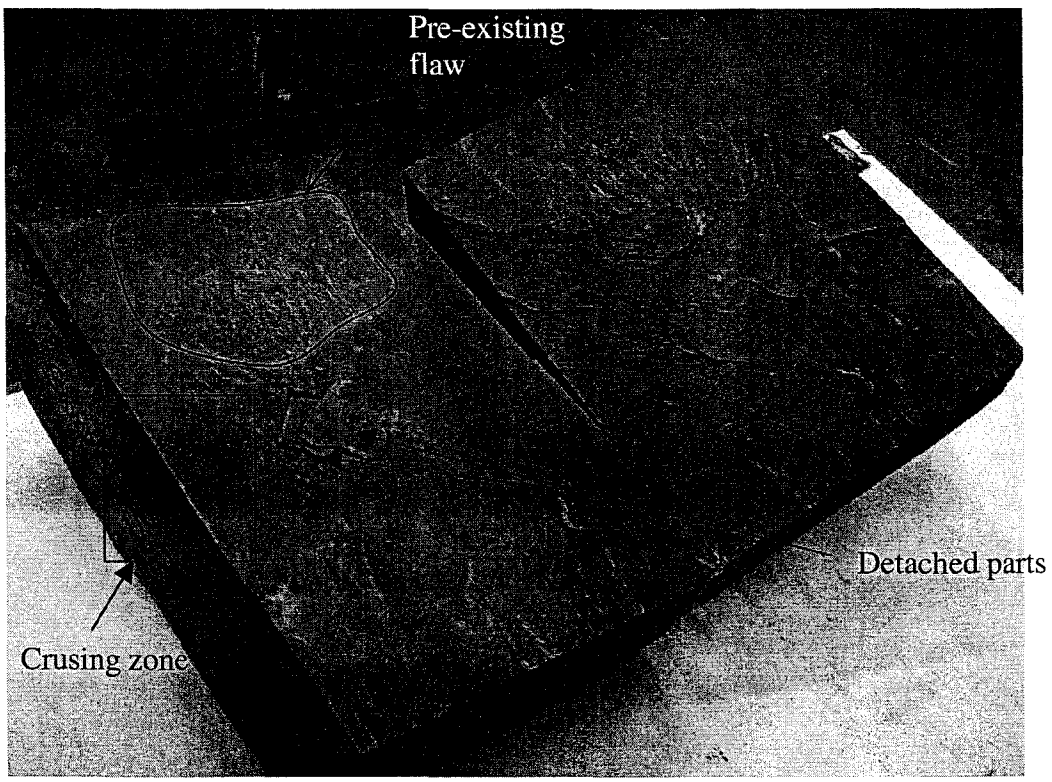
Pre-existing
flaw
Detached parts
Crusing zone

(b)

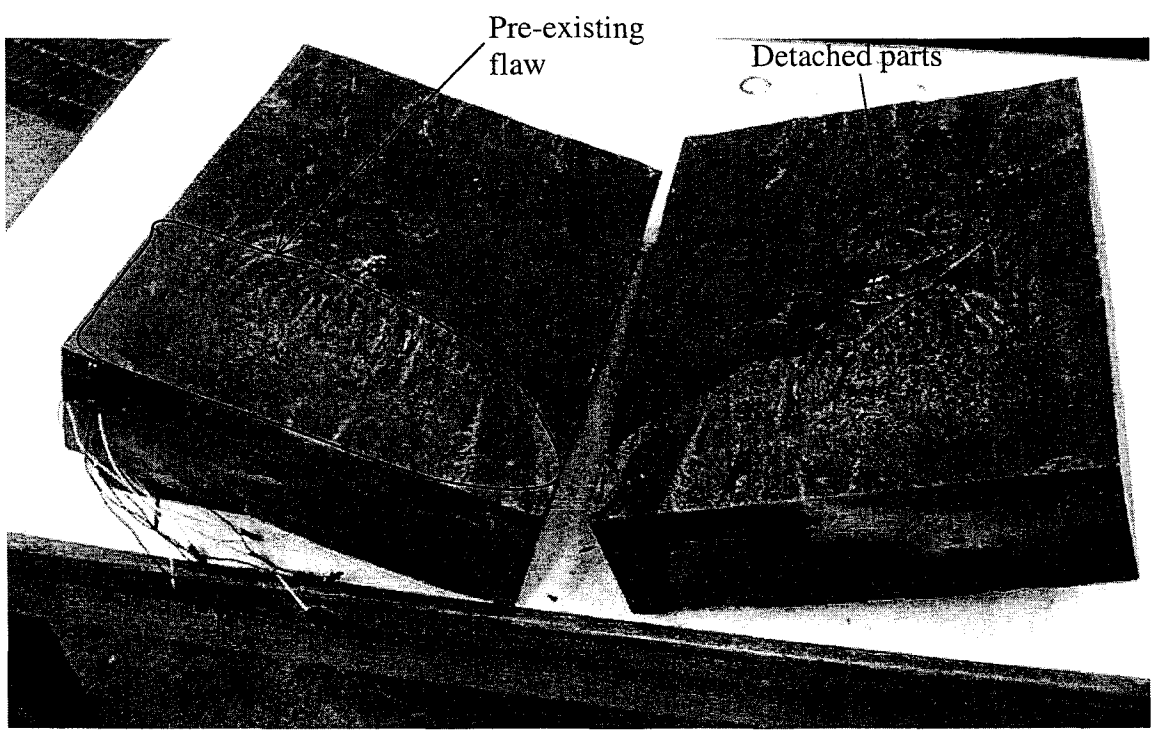
Pre-existing
flaw
Detached parts

(c)

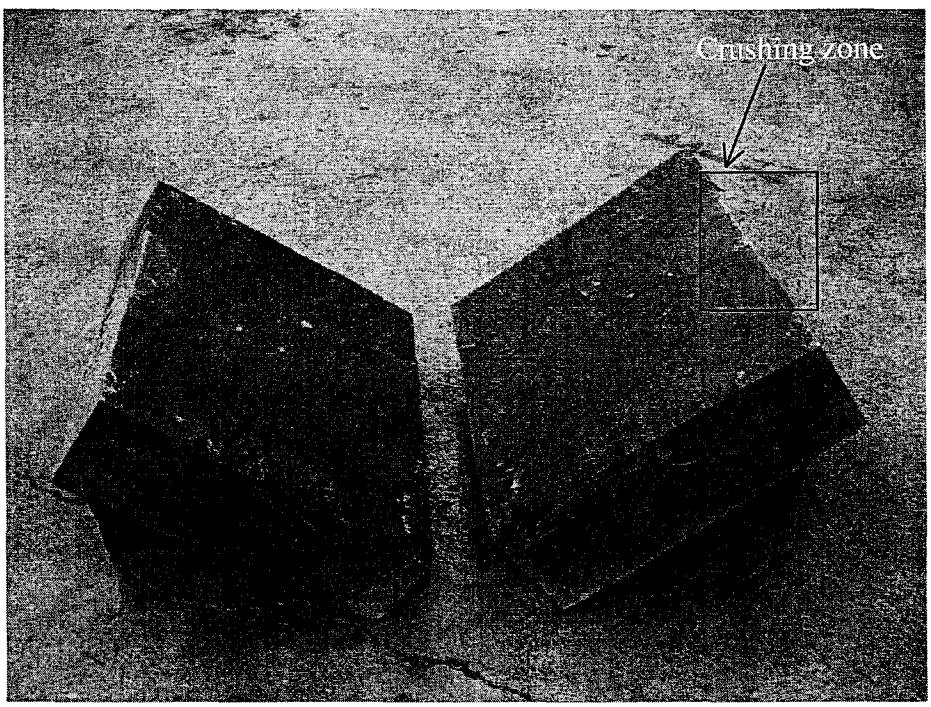

(d)

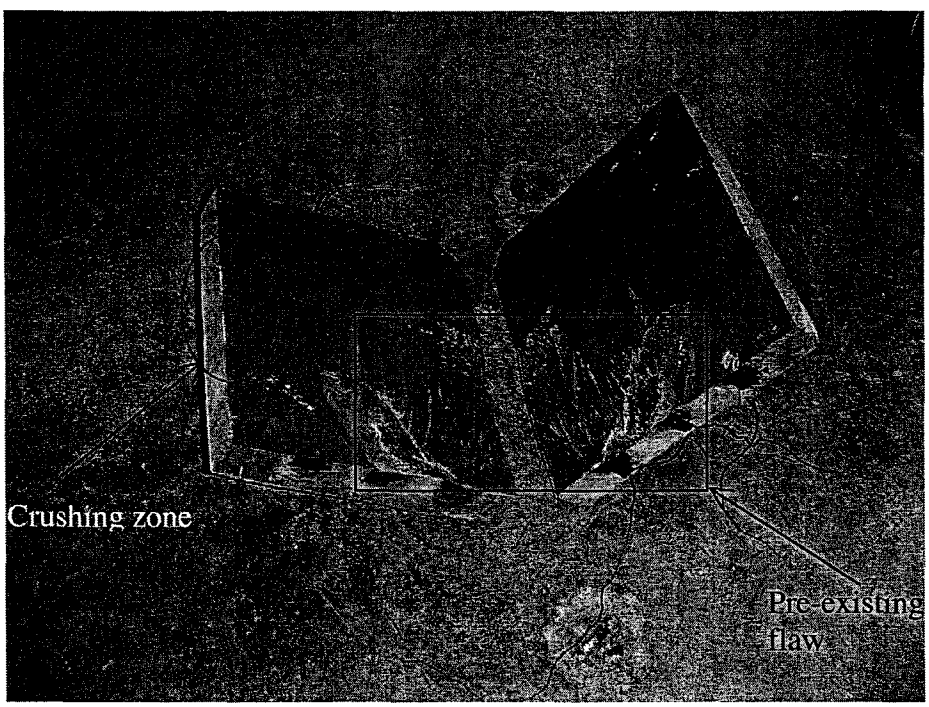

Figure 4.20 (a) – (d): Impact splitting post failure surfaces

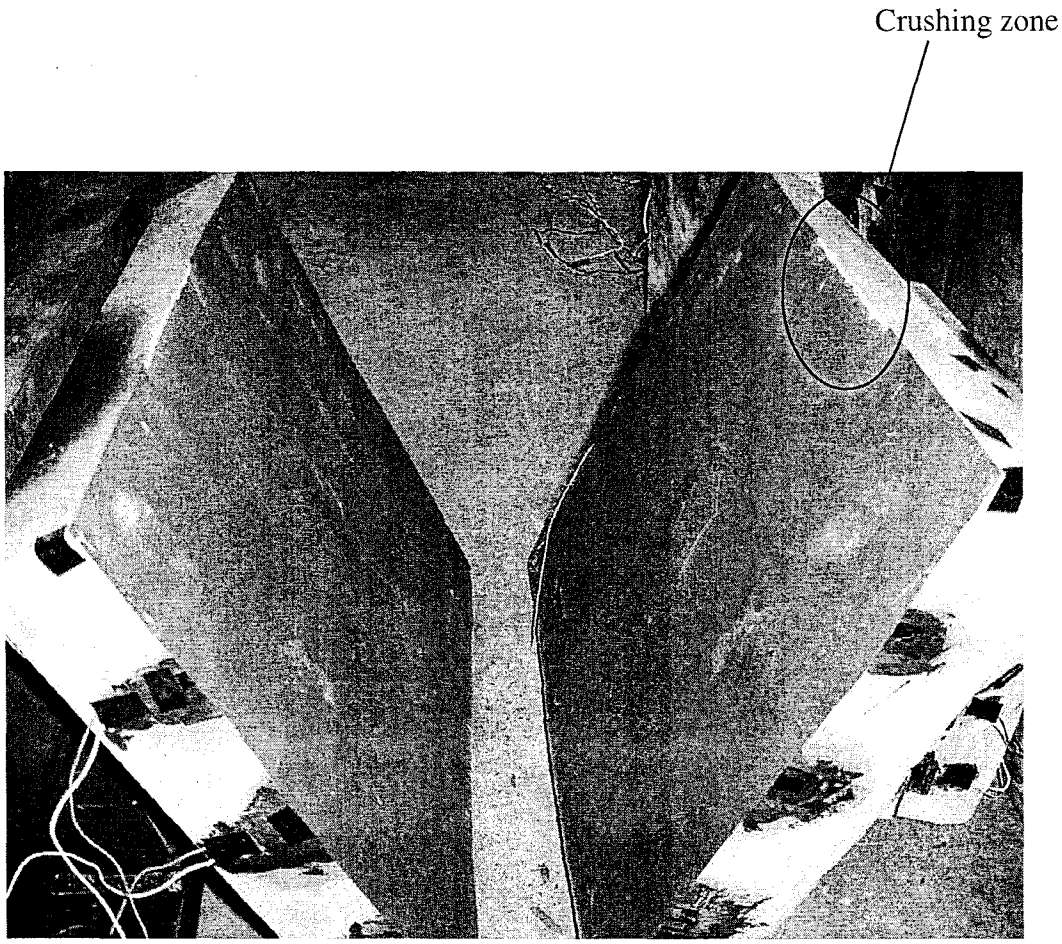

Figure 4.21: Impact splitting failure surfaces indicating crushing zone

(a)

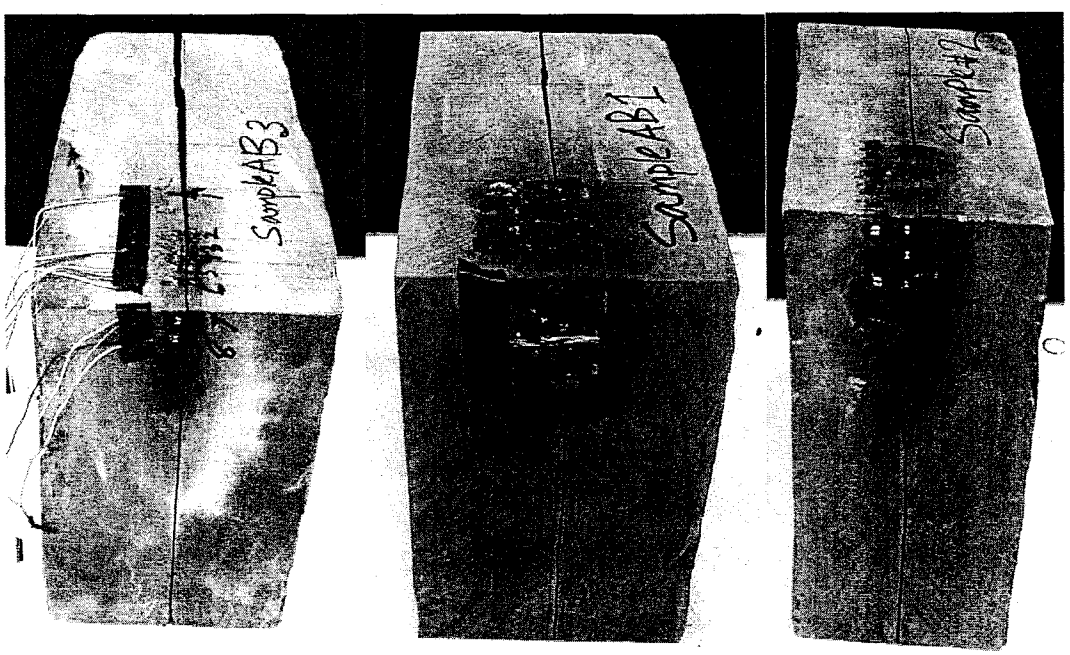

(b)

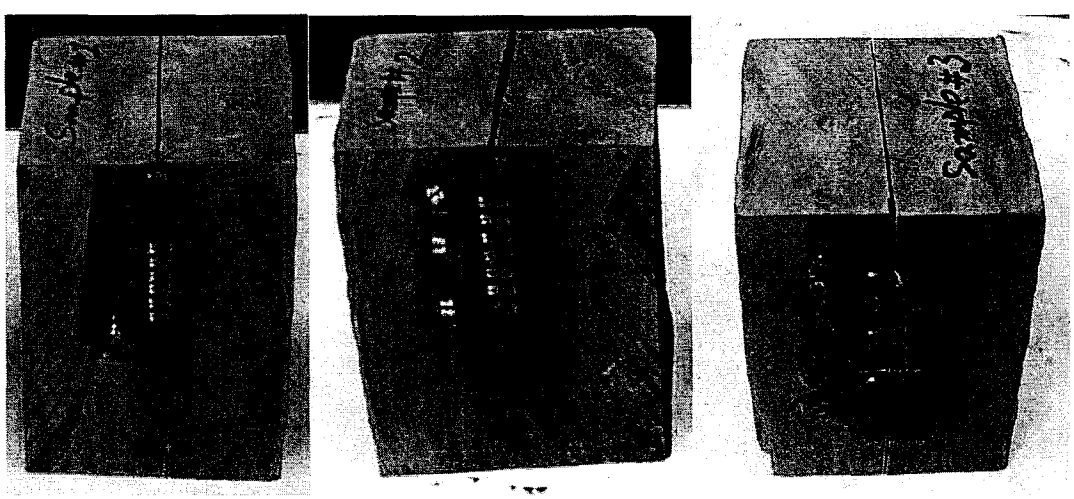

(c)

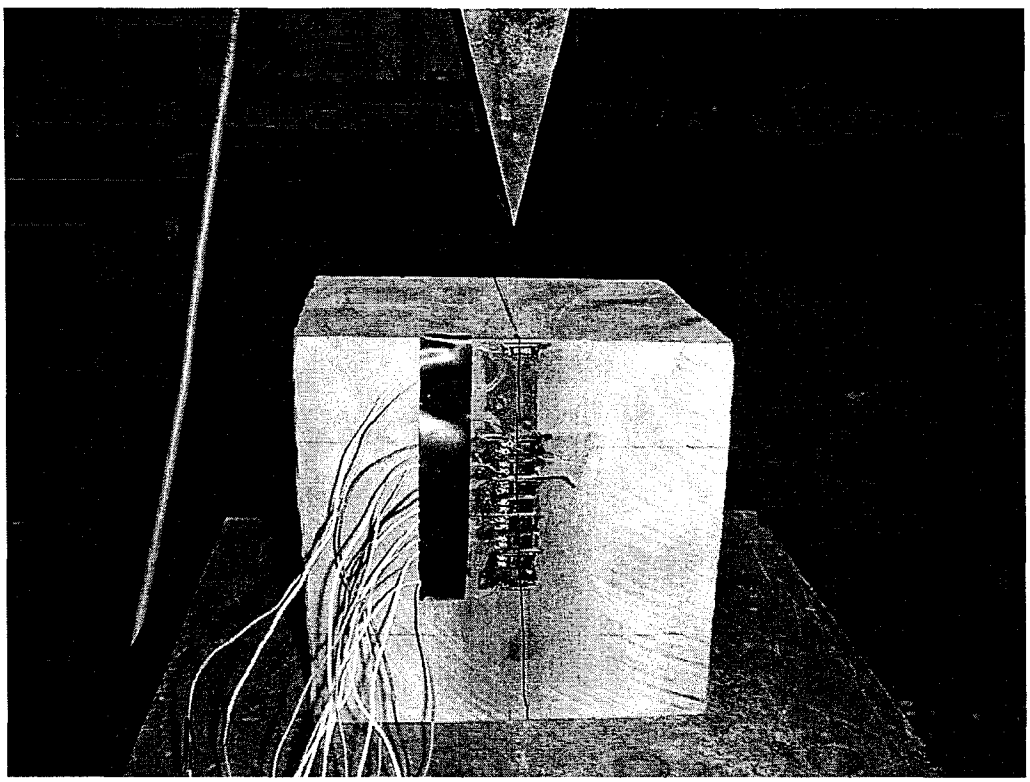

(d)

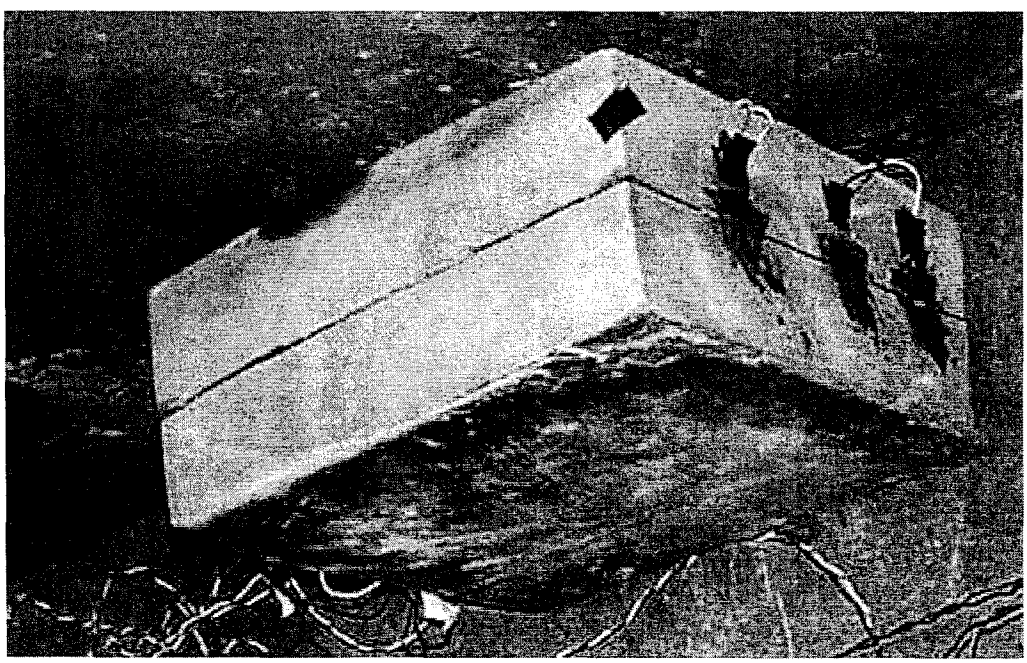

Figure 4.22: Post splitting failure crack patterns: (a) and (d) Non plane strain splitting; (b) and (c) Plane strain splitting.

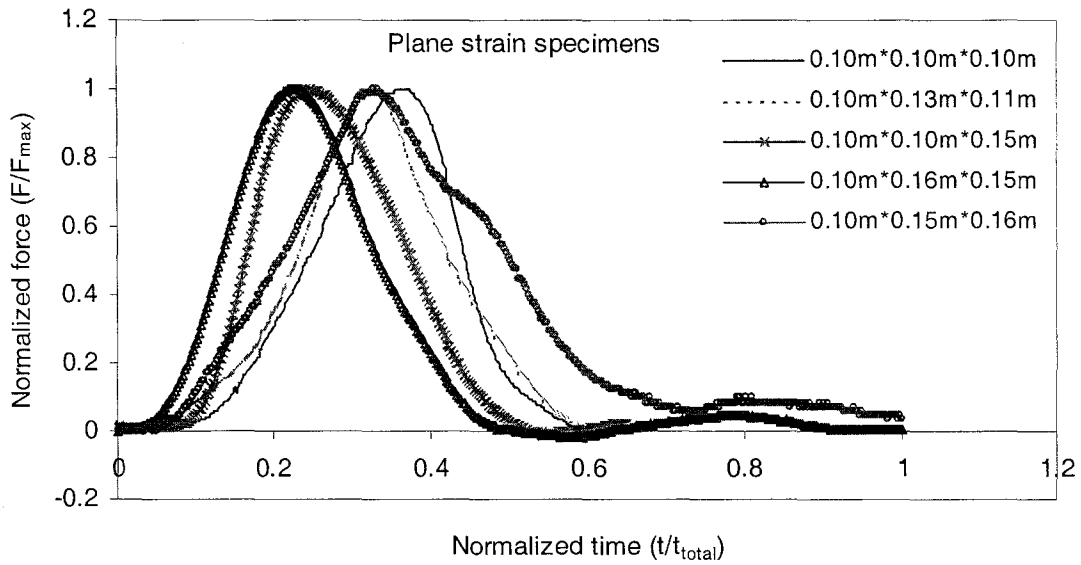

Figure 4.23: Variation of normalized impact splitting force with respect to normalized time for plane strain (indenting transverse wedge length equal to the transverse length of the block) slate blocks having different widths and depths.

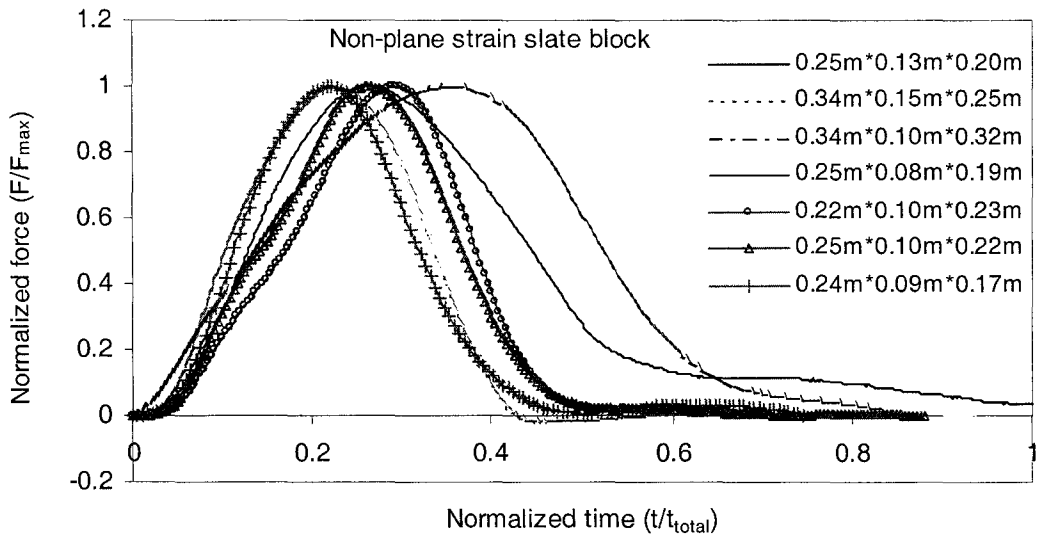

Figure 4.24: Variation of normalized impact splitting force with respect to normalized time for non-plane strain (transverse length of the block greater than the transverse length of the indenting wedge) slate blocks having different sizes.

dependent force by the peak value of the splitting force and normalized time was obtained by dividing the instant time by the total splitting time of the slate block. The variation of normalized splitting force with respect to normalized time for both cases (plane strain and non-plane strain test) of impact splitting are given in Figures 4.23 and 4.24. It is seen that the variation of normalized splitting force with respect to normalized time is almost similar for all plane strain and non plane strain slate blocks. Hakalehto (1970) tested and observed the type of fracture of shale specimen under various pulse amplitudes. He reported that lower amplitude pulse causes a better splitting type of fracture along the bedding planes than the higher amplitude pulse, i.e., if a splitting type of fracture is desired, it is better to increase the duration of the pulse rather than the amplitude. This similarity of normalized impact load vs. time feature was utilized in carrying out numerical analysis for impact splitting of slate blocks.

4.11 Summary

The experimental study reported in this chapter has been divided into five groups for properly understanding the various types of tests carried out in this study. Naturally bedded slate rock was considered in this test program as the test material. Calibration of instruments, instrumentation setup, specimen preparation, testing procedures and interpretation of results for each group of tests have been described separately. It is observed from test results obtained from different properties tests that the present test results, except the tensile strength of slate are almost closer to those found earlier in other published results. In order to confirm the tensile strength test results subsequent studies need to be carried out taking special care for removing bending moment effects that arise during the carrying out of tests. Shear modulus of

rigidity and shear strength tests were not carried out in the present study due to their lesser importance in the analysis of mode I dynamic crack propagation. Fracture toughness tests were carried out for two different types of layering scenarios (arrester and short transverse as per Figures 4.8 and 4.11) where initial cut was parallel and perpendicular to the layering plane. Due to difficulties that arose while making test specimens, two distinct shapes of specimen (cylindrical and rectangular) were considered in this test program. There were no special test procedures available in codes to measure crack propagation velocity in slate block. It was measured during breaking of slate blocks by wedge impact force, using strain gauge sensors. It has been observed that crack propagates comparatively slowly, along an almost single plane and crack propagation velocities vary in an irregular manner. In Scanning Electron Microscopic study of slate material, it is seen: (i) that micro cracks exist at grain boundaries; (ii) discontinuities of layering are common features; and (iii) layer interfaces seem to be well defined incipient crack surfaces. After examination of the load-time plots obtained from the impact splitting tests it could be concluded that peak load occurred at the onset of unstable crack propagation in plane strain specimens. However, crack started before the load reached its peak value for non-plane strain slate blocks. Splitting loads were not consistent (in some cases) with the sizes of blocks. Some of large blocks took lesser load to break than those found in relatively small blocks; the probable reason for this inconsistency could be the existence of a larger number of pre-existing flaws per unit volume in the slate material. A study on the variation of normalized splitting forces for different types of slate blocks (plane strain and non-plane strain) was carried out to establish the general shape of impact splitting forces. The shapes obtained for normalized splitting forces with respect to normalized times were almost similar for all slate blocks considered for the splitting series of tests.

The properties used in the subsequent numerical investigations are given below.

Slate was characterized as a transversely isotropic material having the following elastic properties:

$E_{11} = E_{22} = 75.85$ (GPa)

$E_{33} = 39.65$ GPa

$\nu_{12} = 0.236$

$\nu_{13} = \nu_{23} = 0.170$

Direct tensile strength = 2.33 MPa (highest value obtained)

Hardness of slate rock (Shore hardness number) = 40.64 (used in the choice of material used for indenter)

Fracture toughness of slate rock = 0.292 ($MPa.m^{1/2}$)

Crack propagation velocity variation = 38 to 55 m/s

Coefficient of friction = 0.56 (used in the interface sliding of wedge indenter into slate)

Chapter 5

Numerical Analysis of Impact Splitting of Slate Rock

5.1 Introduction

Theoretical estimation of the required in-plane impact loads, before actually splitting a layered rock, is required to obtain an idea of the maximum load needed to break a specific size of block and the subsequent design of necessary machinery/equipment to apply that load. Once it is possible to estimate the breaking load for a specific size of block, it is also possible to setup a machinery to apply that load on the body. In order to determine the approximate breaking load of any regular sized layered rock block one needs to carry out extensive experimental investigations, using small- and large- scale specimens. However, the experimental investigations on large-scale specimens are almost impossible to be carried out in a medium-sized research laboratory. The other way to do the same is to verify and establish a numerical methodology first from the results of small-scale experimental investigations and thereafter to apply the same numerical procedure to estimate the approximate breaking loads for large rock blocks. From the computed breaking load the field equipment can be designed and fabricated. The present

chapter outlines a finite element based numerical analysis that was carried out based on small-scale experimental test results obtained during the breaking of finite sized square/rectangular slate blocks. Mode I dynamic stress intensity factors were determined for a finite sized slate block using plane strain and 3D finite element analyses; incremental crack growth analysis was carried out and the stress intensity factors obtained through analysis were compared with the plane strain material fracture toughness values obtained from experiments.

5.2 Finite Element Analysis – A numerical approach for simulating dynamic crack growth

5.2.1 General

The use of finite element method as a numerical technique has advanced considerably to analyze very large structural elements as well as highly sophisticated structures. Advances have also been made in materials used earlier for fabricating these structures such as steel and timber, which are now-a-days frequently replaced with composites and ceramic materials. Theoretical basis required for the application of finite element methodology for these cases has been discussed briefly in Chapter 3. Two-dimensional finite element analyses of mode I fast crack propagation in linear elastic isotropic bodies have been carried out during the past three decades and a number of papers and reports have been published (Malluck and King 1980, Mall, et al. 1980, Sun and Hun 2001). Most of the researchers have taken advantage of elastodynamic symmetry about the crack tip trajectory to simulate the rapid crack propagation phenomenon by sequential release of nodes along one side of the finite-element model. This technique has also been used by Jih and Sun (1990) to simulate the crack advancement in running crack problems.

Numerical modeling of dynamic crack propagation in finite bodies was carried out earlier by Nishioka and Atluri (1980) using moving singular elements in finite element approach. In the present study splitting tests were carried out on two separate groups of slate blocks viz., plane strain blocks (transverse length of the test block equal to the transverse length of the wedge) and real three-dimensional (3D) blocks (transverse length of the test block greater than the transverse length of the wedge). Consequently the results of finite element analyses have been presented separately for each group to clarify the relevant issues observed during the analyses. In this chapter, results of the finite element analyses of slate blocks having a transverse length equal to the transverse length of the indenting wedge are presented and discussed (plane strain analysis). Assumptions, simplifications, finite element model discretization, special procedures used, numerical results and discussions are presented herein to highlight dynamic plane strain impact crack propagation from the impact point to the bottom of the specimen, splitting the slate rock specimens exactly into two pieces.

5.2.2 Assumptions and Simplifications

During the experimental splitting tests of slate blocks salient dimensions of test specimens such as thickness, width and length could not be kept constant, due to them being cut out from large irregular sized slate blocks. Crushing depth of slate at the initial impact interface was not measured exactly due to the sequential occurrence of two events (crushing and splitting) during the splitting process. Layer discontinuities and very small irregular layer thicknesses were obtained in microscopic studies reported earlier in section 4.9.2. However, in the numerical analysis this irregular layer thickness could not be implemented due to difficulties experienced in the determination of individual layer

properties having very small layer thicknesses. Experimental crack propagation line was not exactly collinear with the plane of loading. Therefore, it was not possible to simulate the real slate behaviour exactly by the theoretical model. Hence, some assumptions and simplifications became essential to carry out numerical analysis. The following assumptions and simplifications were made for finite element analysis of the impact splitting process of plane strain slate blocks.

- Material was taken to be homogeneous and transversely isotropic (observed from experimental results, reported earlier)
- Thickness of the specimen was assumed to be uniform over the specimen height
- Breaking of block was assumed to be symmetric (exactly into two equal pieces)
- Crack propagation event was also considered symmetric
- Crack was assumed to be a plane crack and propagated along the vertical impact plane by maintaining same depth of penetration in the transverse direction, for each time
- Dynamic impact load was assumed to be distributed uniformly on the indenter, at a height 10 mm above the tip of the indenting wedge
- The initial fracture process zone was assumed to be very small in comparison to other geometric dimensions including crack length/area. Moreover slate was observed to be a brittle material. Therefore, linear elastic fracture mechanics (LEFM) was applied to analyze crack propagation phenomena though it is not valid during the crack initiation process; it is applicable for crack propagation process
- It is assumed that when the wedge penetrates 5 mm deep into the specimen, the crack is assumed to have grown to 23.5% of the specimen depth in both plane strain and

3D-block "equivalent to plane strain" block analyses. Rest of the specimen crack (uncracked part) will grow as wedge moves further inwards

- Damping was considered to be zero for the entire system during the splitting process; this is justified on the basis that the damping plays an insignificant role during the fast crack growth process.
- Some of the components used to apply the sudden impact load, such as, hydraulic actuator and their accessories were not taken into consideration in finite element analysis. The impact load was considered to be applied directly through the wedge indenter (see Fig. 5.1).

5.2.3 Finite Element Model – Description of Elements Used

Finite element model of the entire test procedure for plane strain splitting test was generated using CPE8R, CPE6 and CINPE5R elements shown in Figure 5.2. CPE8R is an eight-noded biquadratic rectangular plane strain solid element with reduced integration, and CPE6 is a six-noded quadratic triangular plane strain solid element, CINPE5R is a five-noded quadratic semi-infinite element used to simulate non-reflecting wave propagation aspect required at the support interface. All nodes of elements have two degrees of freedom denoted by u_x and u_y. The integration points for element CPE8R and CINPE5R (reduced integration) are 4, and 3 for CPE6 (full integration). Except a small part of wedge and concrete floor, the entire system is modelled using CPE8R elements. Both CPE8R and CPE6 elements are used to model wedge indentor. The test specimen was kept on a steel platform (wide flange I-beam) that was fixed to a 3 feet thick reinforced concrete floor. Therefore, the concrete floor was considered as an infinite media of homogeneous isotropic material and modelled using infinite elements (CINPE5R).

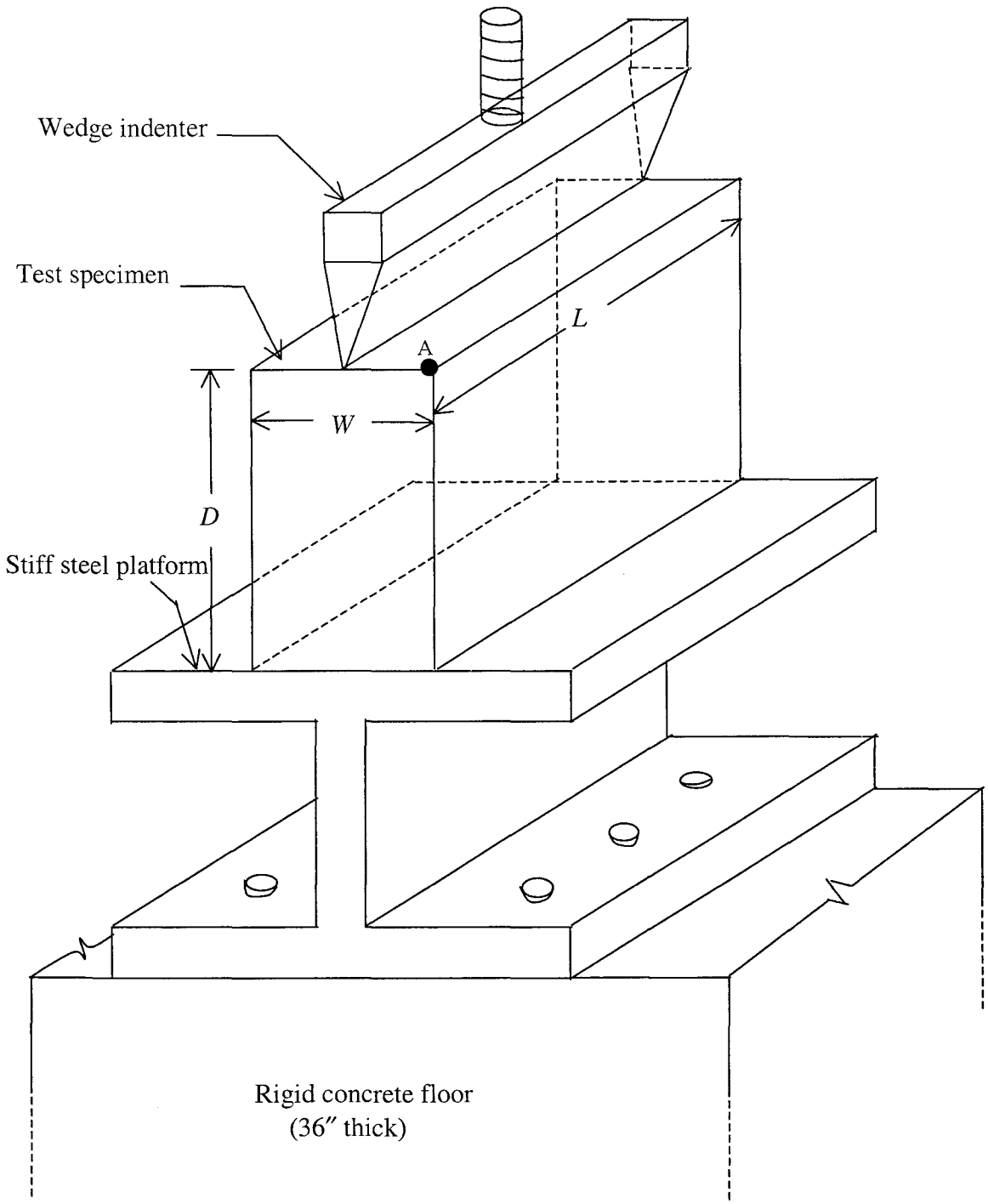

Figure 5.1: Partial experimental setup used for finite element discretization.

Wide flange I-beam was modelled using CPE8R elements. Reduced integration was applied to obtain more accurate results and less computational time (ABAQUS 2002). Finite element model of a regular cubic slate block (0.1 m × 0.1 m × 0.1 m) i.e., 3D model of plane strain splitting analysis was generated using C3D8, C3D6 and CIN3D8 elements. C3D8 is an eight-noded linear brick element and C3D6 is a 6-node linear triangular prism. CIN3D8 is an eight-noded linear 3D infinite element having 8 integration points for determining element stiffness matrix through numerical integration and used to model the concrete floor. Integration points for elements C3D8 and C3D6 are 8 and 2, respectively. All the nodes of elements have 3 displacement degrees of freedom denoted by u_x, u_y and u_z. Test specimen, indenter wedge and wide flange I-beam were modelled using C3D8 and C3D6 elements. Elements and their integration points are shown in Figures 5.2.

5.2.4 Mesh Generation

It is known that finite element model with very fine mesh provides more accurate results than that with a coarse mesh for a specific element type in stress/displacement analysis of a finite body. However, finite element analysis of a body with very fine mesh requires many elements and also more computational time. Therefore, computational time and mesh size are two important factors in finite element analysis and they are inter-dependent on one another. There is a thumb rule in finite element analysis that the computational time increases approximately as the square of the number of degrees of freedom. Therefore increasing the number of elements means increasing the degrees of freedom, and consequently, would require more time to complete the analysis. The effective capacity of computer is also another factor. The use of small sized elements

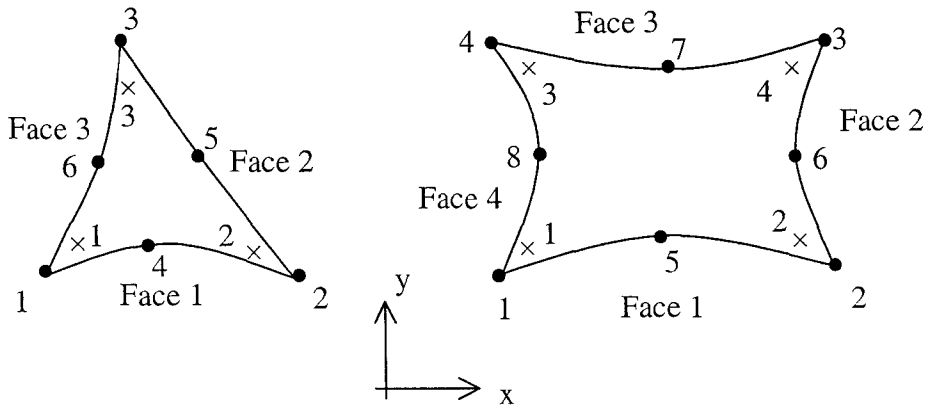

6-node element (CPE6)

8-node reduced integration element (CPE8R)

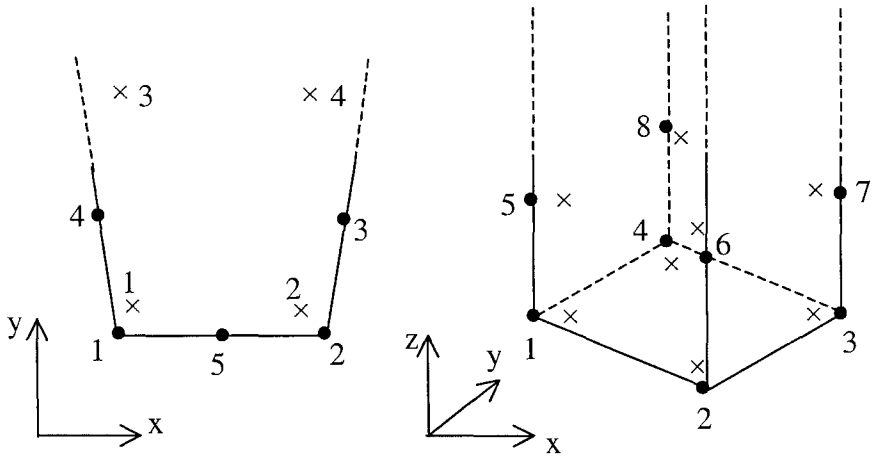

CINPE5R

CIN3D

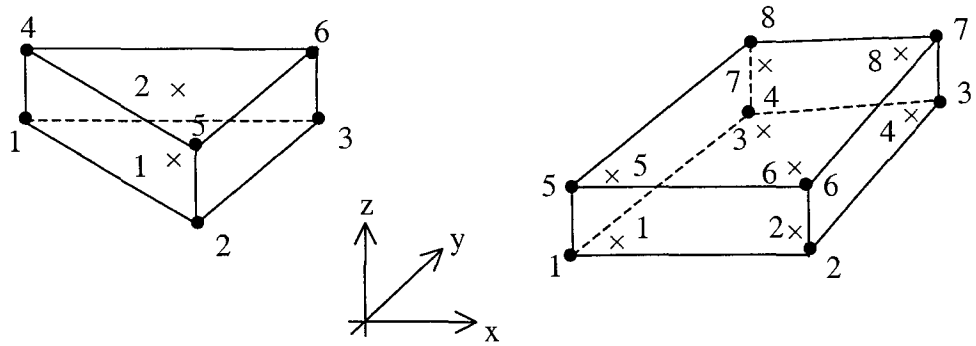

6-node element (C3D6)

8-node element (C3D8)

Figure 5.2: Different types of elements used in discretizing the finite element model of splitting process of slate block

(large number of elements) may sometime exceed the capacity of the computer. Specially in dynamic analysis where a large number of time steps and iterations are required to attain good accuracy of result, one needs a larger memory space to store the data. Hence, one should select mesh size in such a way so that it would give results with sufficient accuracy and be able to analyze within the capability of the computer available for the study, i.e., it requires a reasonable mesh size by careful selection of element sizes and their distribution.

In the present study the discretization of the test specimen has been carried out by dividing it into three zones such as splitting zone, contact zone and less stressed zone. Splitting and contact zones are defined as critical zones. Therefore, they have been discretized using very small elements which are almost square in shape. Coarser meshes have been provided in the less stressed zone. In other words, non-uniform mesh sizes were used by employing very fine meshes (element size 0.75 mm by 0.75 mm) along the crack front and contact planes, and coarse mesh was used away from these critical zones, specially for locations (within a region of interest, slate block) where there were no stress concentrations or sharp variations. The overall slate block size and the representative impact load-time curve used in this part of the numerical study are shown in Figures 5.3 and 5.4. A detailed plane strain finite element mesh of the entire body is shown in Figures 5.5 (a-d). Non-uniform mesh (fine mesh with element size 3 mm by 1.5 mm by 2.5 mm along the crack front and contact planes, and coarse mesh away from these critical zones) was also used in 3D analysis. The finite element mesh for the three-dimensional block is shown in Figures 5.6 (a-d).

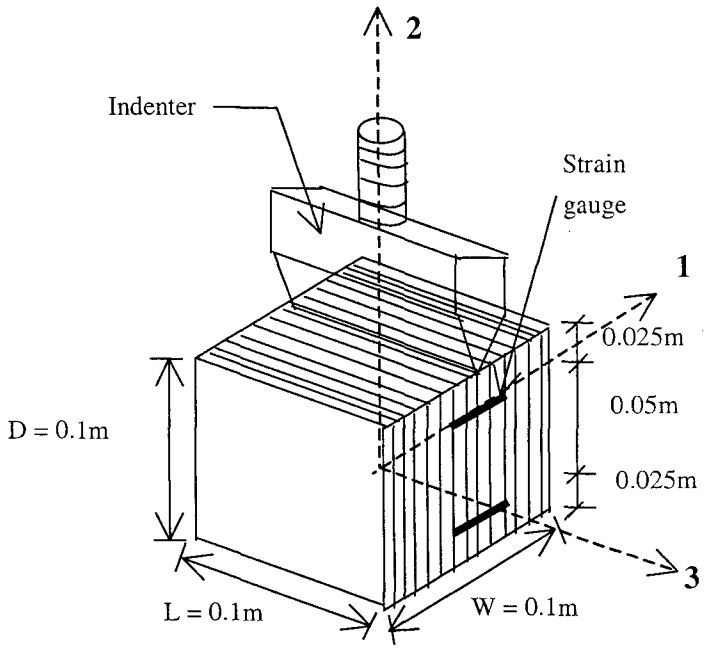

Figure 5.3: Geometry of plane strain slate block used for finite element analysis

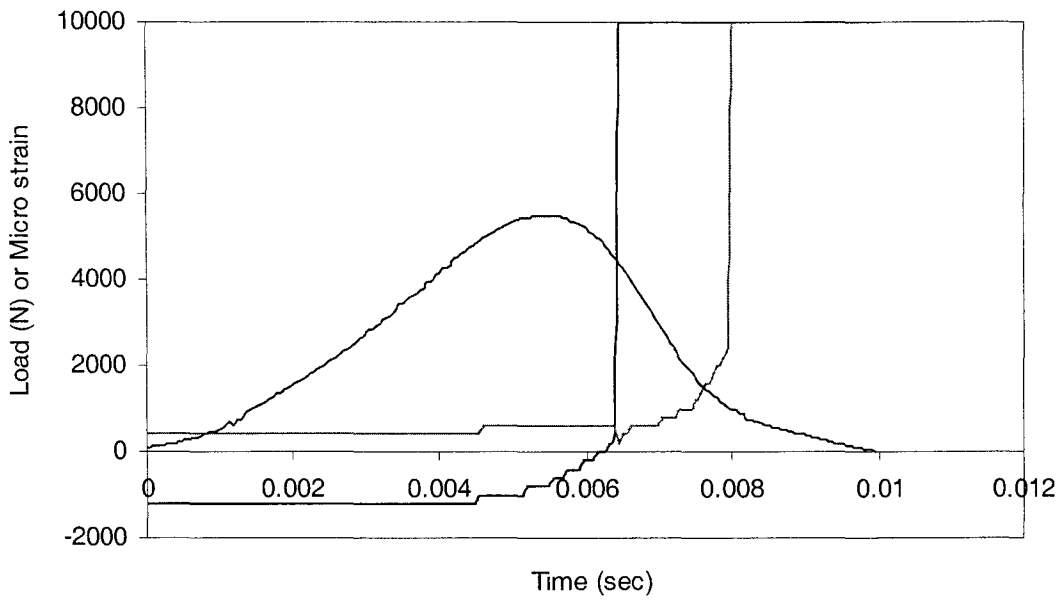

Figure 5.4: Variation of splitting load and strain gauge readings with respect to time obtained from experimental studies of the slate block shown in Figure 5.3.

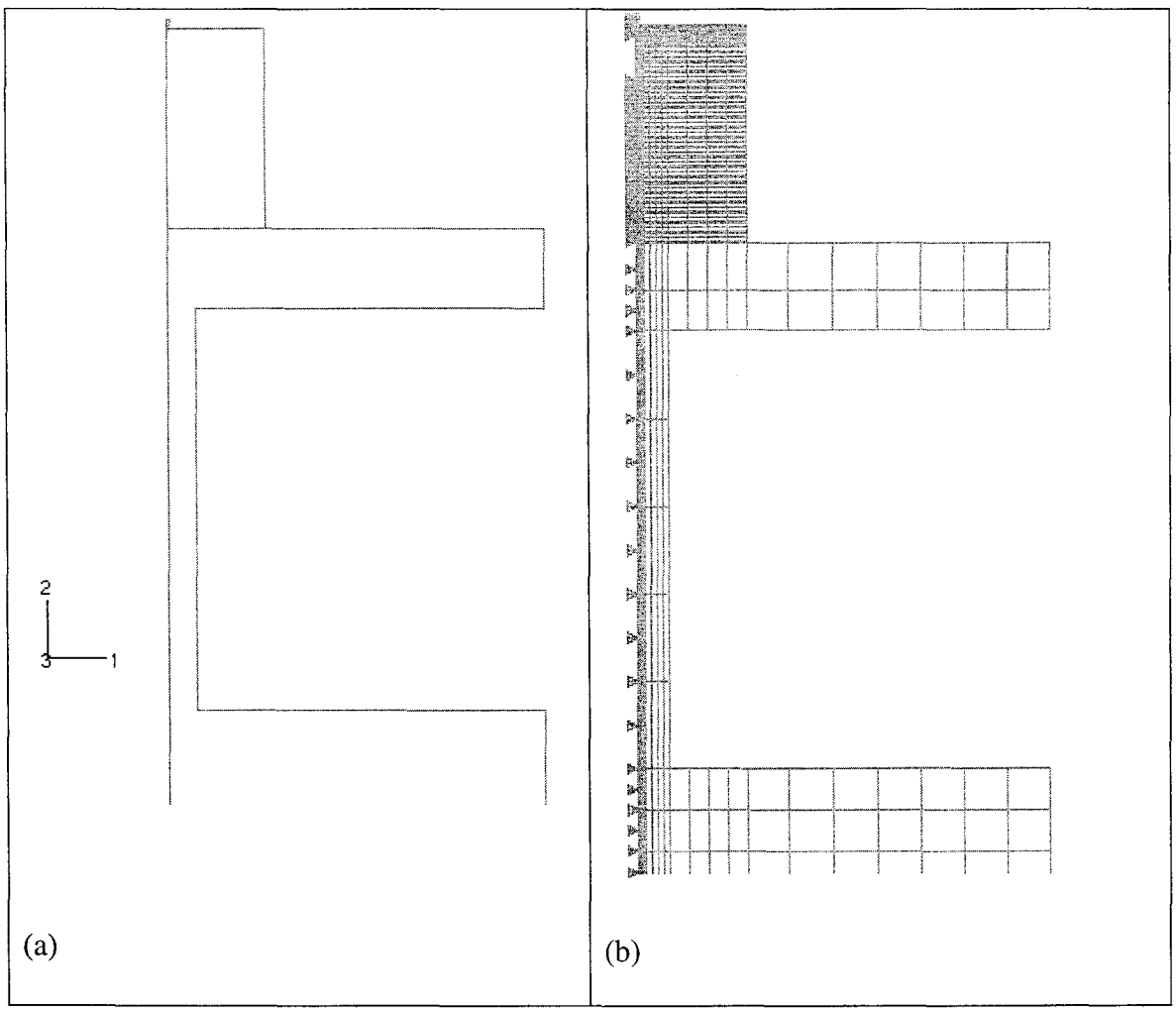
2
3
1
(a)
(b)

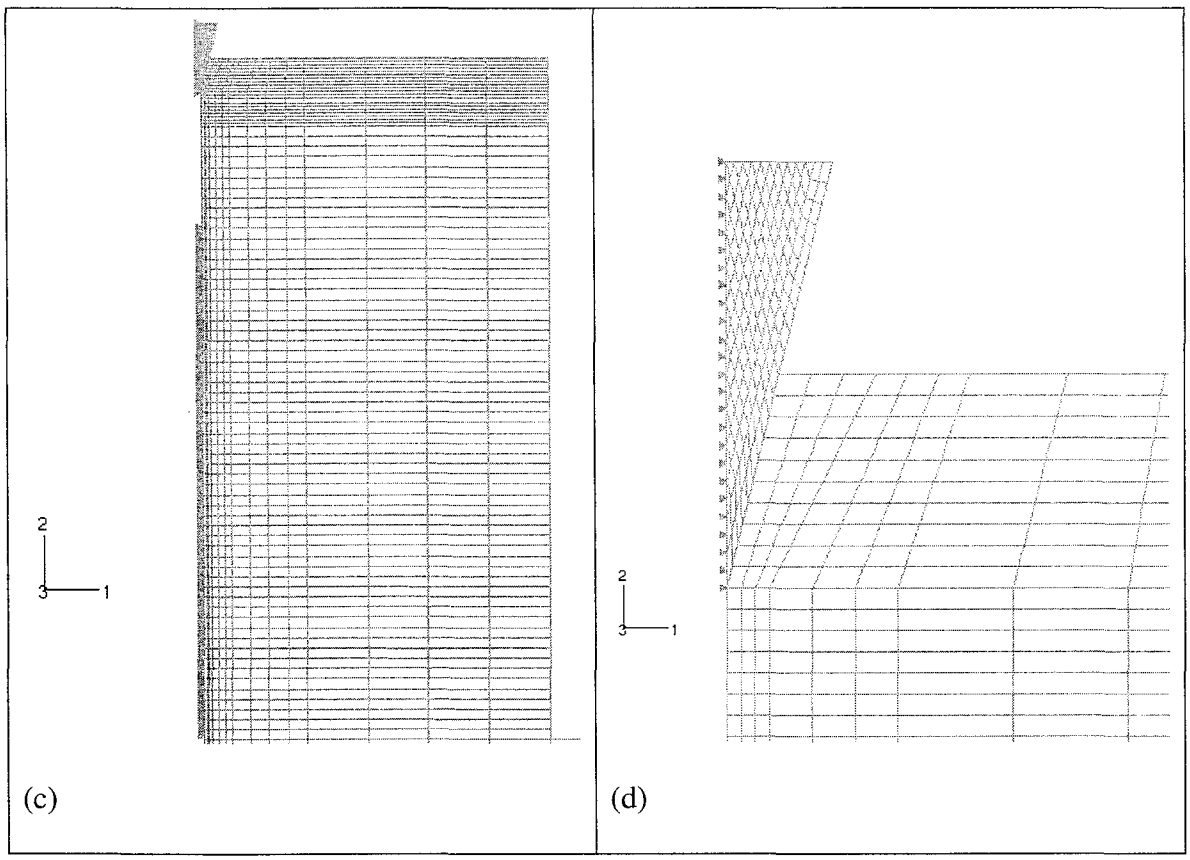

Figure 5.5: Finite element discretization for plane strain analysis: (a) Test specimen on the platform under impacting indenter; (b) Combined mesh used for the slate specimen and the wide flange I-beam; (c) Mesh used for slate specimen only; and (d) Enlarged mesh at the junction of indenting wedge and slate specimen.

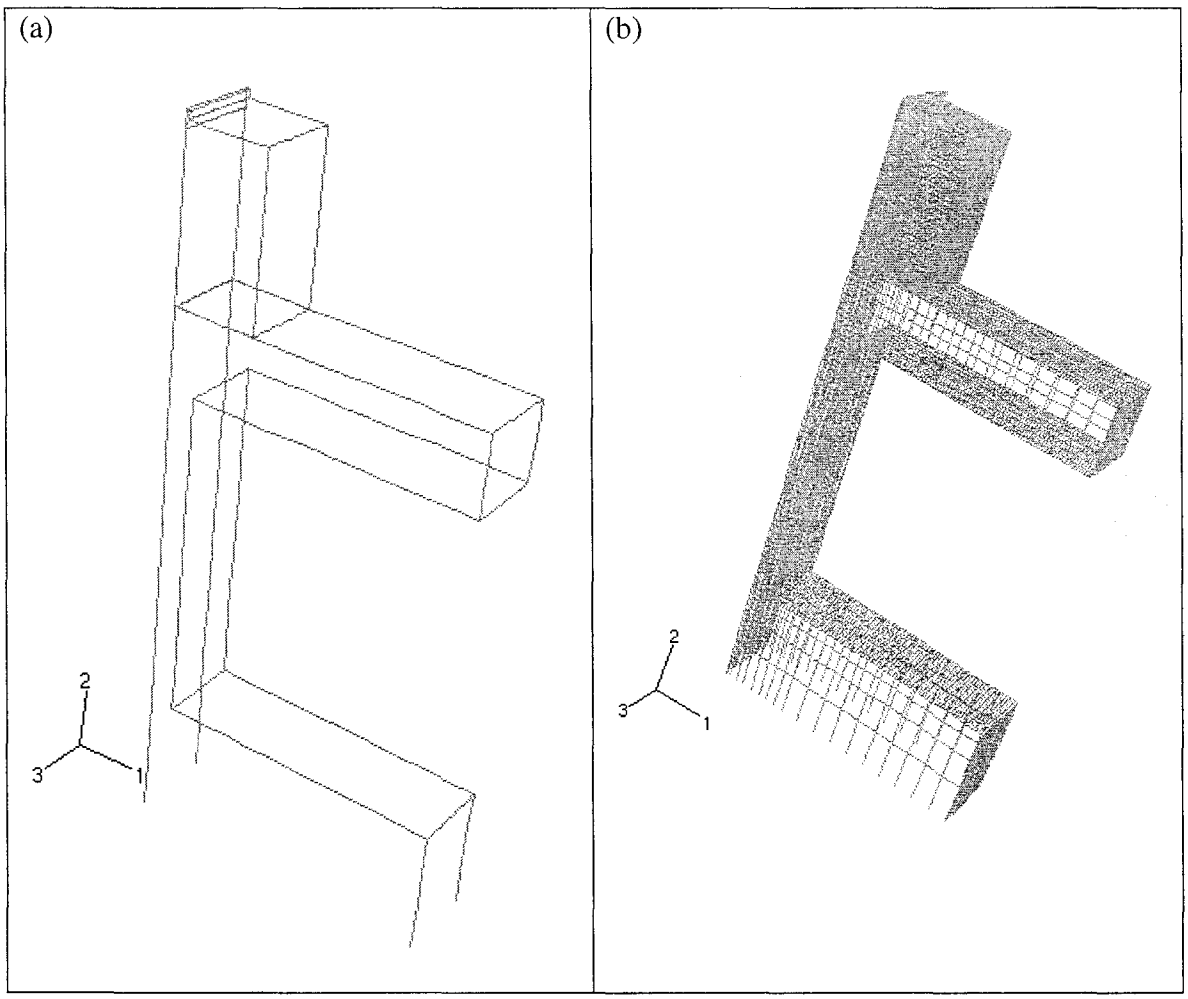
(a)
2
3
1
(b)
2
3
1

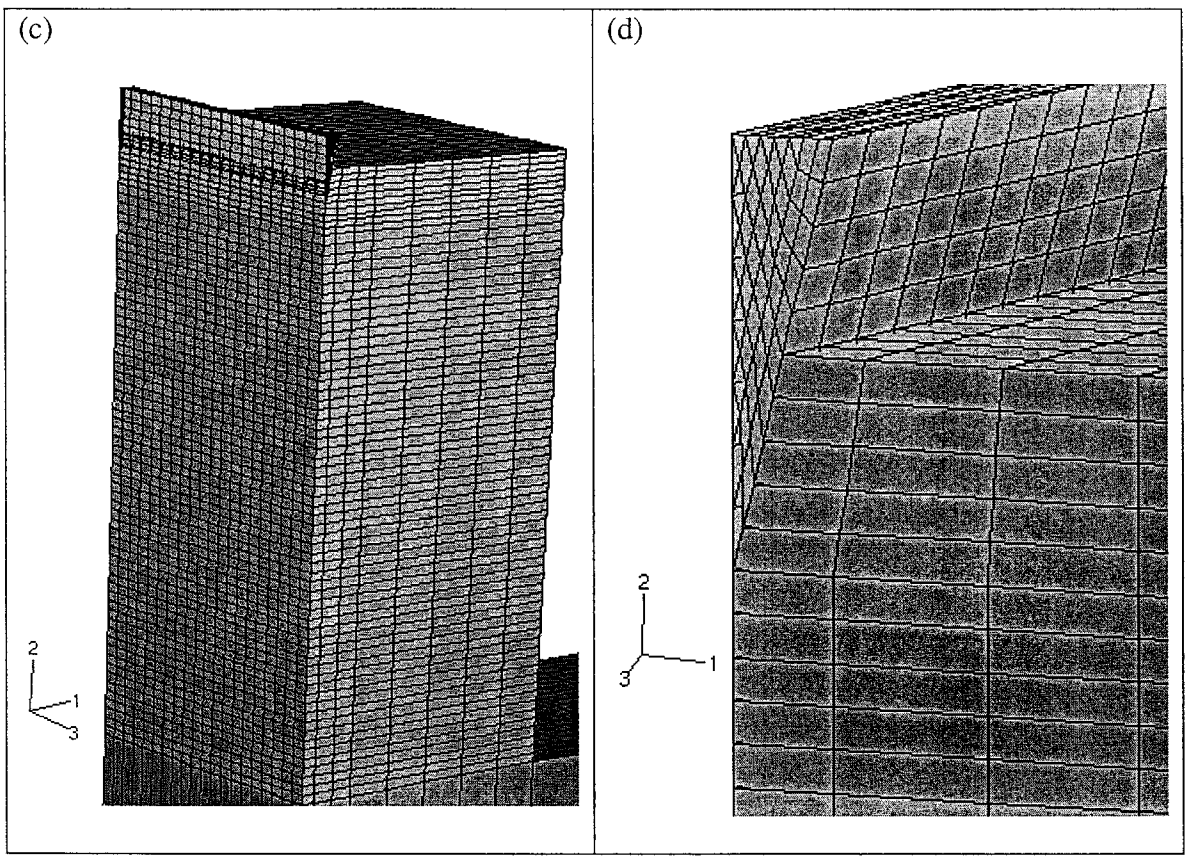

Figure 5.6: Finite element discretization for 3D analysis: (a) Test specimen on the platform under the impact indenter; (b) Combined mesh used for the slate specimen and the wide flange I-beam; (c) Mesh used for slate specimen only; and (d) Enlarged mesh at the junction of indenting wedge and slate specimen

5.2.5 Boundary Condition

Due to the symmetry of the entire test system i.e., geometry (platform, specimen) and loading (see in Figure 5.1 and 5.3) only half of the entire system was modeled in plane strain finite element analysis. Displacement degrees of freedom in direction x or 1 (u_x) of wedge, platform, concrete floor and uncracked part of slate specimen, along the symmetry line, were restrained to obtain elastodynamic symmetry for simulating dynamic crack propagation by sequential node release technique (shown in Figure 5.5 (b)). For 3D analysis, while using symmetry conditions, one-quarter of the entire system was modelled by restraining all the nodal displacement degrees of freedom in direction z or 3 (u_z) of nodes in plane x-y (1-2) and in direction x or 1 (u_x) of nodes in plane y-z (2-3) (except cracked part). Load was considered to act as distributed loads at a distance above the tip of the wedge equal to twice the wedge penetration depth (= 0.005 m). The magnitude of the distributed load was calculated by dividing the load obtained from the impact event by the area of the wedge at a height of 0.01m from the tip of the wedge. Surface-based contact was introduced between: (i) wedge and specimen (near the indenting edge); and (ii) specimen and steel platform. A frictional coefficient 0.56 obtained from experimental studies was provided between all the contact surfaces of slate and steel.

5.2.6 Convergence Test

Finite element analysis of a cracked body is quite complex and time consuming due to the density of the finite element mesh required at or very close to the crack tip. In a running (or progressing) crack problem, mesh density along the predefined crack line would also influence the analysis results. In order to verify the proper sizing of the elements of the model, a convergence test was carried out on plane strain analysis by determining the

displacements at the top upper exterior corner indicated by a solid circular symbol in Figure 5.1. A crack length equal to 23.5% of the total height of the specimen was introduced at the beginning of the analysis. At first 560 eight-noded plane strain elements were used to discretize the specimen by providing 40 elements along the vertical direction. Element dimension along the symmetry line was 0.003 m × 0.003 m for first four columns and beyond that lateral dimension of element was increased. Thereafter 840, 1148, 1414, 1736, 2016 and 2240 elements were used to model the specimen only and element numbers along the vertical direction changed progressively to 60, 80, 100, 120, 140 and 160, respectively. This also changed the subsequent element dimensions. Element dimensions were 0.002 m × 0.002 m, 0.0015 m × 0.0015 m, 0.0012 m × 0.0012 m, 0.001 m × 0.001 m, 0.0009 m × 0.0009 m and 0.00075 m × 0.00075 m, respectively. In all the above cases element type, crack length, boundary conditions and loading remained the same. Displacement at point A (shown in Figure 5.1) is plotted against the number of elements used (only to discretize slate block) and shown in Figure 5.7. It is seen that displacements seem to be constant beyond 2240 elements. Therefore, 2240 elements with an element size 0.00075 m × 0.00075 m along and near to the symmetry line were used to model the test specimen in the present plane strain analysis.

5.2.7 Probable Methods for Finite Element Analysis

There are two different ways by which finite element analysis could be carried out to analyze the impact splitting process. First, ultimate load carrying capacity of the finite size slate block could be obtained by introducing a failure criteria (maximum normal stress criterion, i.e., ultimate tensile stress) in the finite element model. In this case,

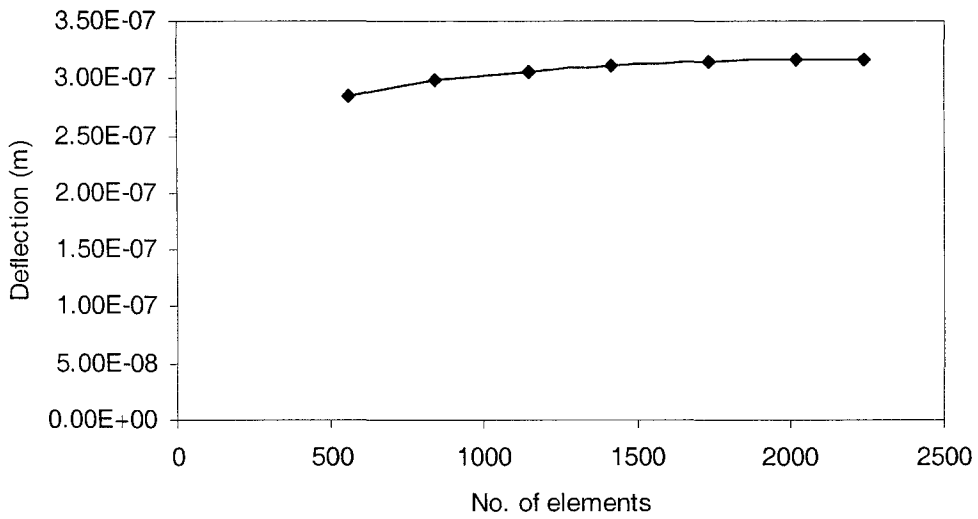

Figure 5.7: Variation of deflection with number of elements

loading is applied incrementally with an iterative non-linear solution technique. Modified Riks method or Newton-Raphson algorithm is generally used in ABAQUS finite element software to determine maximum load. This procedure is good for static analysis to predict unstable, geometrically nonlinear collapse of a structure or postbuckling analysis. This procedure is not followed in the present study because it is not suitable for dynamic analysis of the impact event.

Second method, called fracture mechanics approach, i.e., used the breaking load obtained from an earlier experimental study (considered as the applied load on the body) to compute stress intensity factor for each subsequent crack extension. The cracking load is computed based on the plane strain material fracture toughness value being exceeded by the stress intensity factor for further crack propagation. For complete failure of the body SIF should be constant and equal to or greater than the plane strain fracture toughness

value for various crack lengths. This approach is used in the present study to analyze the impact splitting process numerically.

5.2.8 Process of Results - Plane Strain Analysis

Numerical analysis of this problem was carried out using the commercially available general purpose finite element software ABAQUS 6.3. Procedure for linear elastic fracture mechanics available in ABAQUS was used to analyze the dynamic crack propagation. A post processing procedure was used to generate results directly from ABAQUS. This program automatically determined mode I stress intensity factor (SIF) close to the crack tip through the contour integral evaluation. Since the contribution of inertia to SIF would be almost negligible when the contour integral contours (which were used to calculate SIF) shrink to the crack tip (ABAQUS 1991) and for running crack problems (for constant crack velocity) the inertia forces would remain the same as crack propagates through the body, the effect of inertia on SIF calculation in dynamic analysis was neglected. Basically ABAQUS calculates SIF using contour integral considering various contours around the crack tip. The FE discretization of the real impact test scenario using plane strain elements has been given earlier in Figure 5.5 (a)-(d).

ABAQUS uses implicit time integration to calculate the transient dynamic response in general linear or nonlinear dynamic analysis. It uses Hilber-Hughes-Taylor operator which is an extension of the trapezoidal rule to perform general direct-integration method. This operator is unconditionally stable for linear systems. Therefore, there is no mathematical limit on the size of the time increment (ABAQUS 5.7, Vol. 1). A direct fixed time increment was used by providing 20 increments in each step. Though there

was an initial velocity in the indentation wedge before it impacted the test specimen, no initial conditions was considered in numerical analysis since their magnitude at the hitting point was not determined during the carrying out of test in the laboratory; this velocity effect has been indirectly considered by making the impact load vs. time curve to be the same as the applied force impulse.

For dynamic simulation of impact loading, the load history (Figure 5.4) obtained from the load cell reading was applied to the wedge as distributed load. Mode I stress intensity factor around the crack tip and stresses in local 1- and 2-directions at integration points of crack tip element were calculated for each new crack length and applied load, as both load and crack length changed simultaneously. Since both ABAQUS standard and ABAQUS explicit do not support dynamic crack propagation analysis, a method that applied Mall and Luz (1980) and Sun and Han (2001) procedure to model delamination crack propagation was used to simulate the dynamic crack propagation process. In this procedure crack propagation was simulated by sequentially releasing the constrained degree of freedom on the boundary nodes along the crack propagation path, step by step, according to the calculated time.

Since crack starts (at top of specimen) when load reaches its peak value and the first crack tip was considered at 0.0235 m below the top of the specimen, the applied load on the first crack tip should have been less than the maximum load obtained during the experimental cracking (80% of the maximum load) and this load was taken as the starting load for crack propagation. When crack advanced, the magnitude of the applied load decreased and the time also changed. Since both the loading and the crack propagation

were time-dependent, careful time shifting was taken into consideration in order to synchronize these two variables. Since contour integral is path independent (discussed earlier in section 2.6.4) and ABAQUS calculates stress intensity factor (SIF) from the evaluation of contour integral, the first contour was not included in the computation of SIF [it was located at 0.0001 (approximately) m from the crack tip and was very close to the tip and SIF varied greatly around the first integral]. The variation of SIF with various number of contours are shown in Figure 5.8 for different crack lengths. It is seen that SIF obtained from first and second contours differed by around 2% to 5%. However, the difference in SIF corresponding to 2nd and 3rd contours was less than 1%. Therefore, average SIF corresponding to 2nd and 3rd contours was taken as the correct SIF.

Due to varying values of crack propagation velocities measured during the experimental program, two different cases were investigated to simulate the splitting phenomenon. In case I, SIF was determined along crack growth path by assuming a constant velocity for

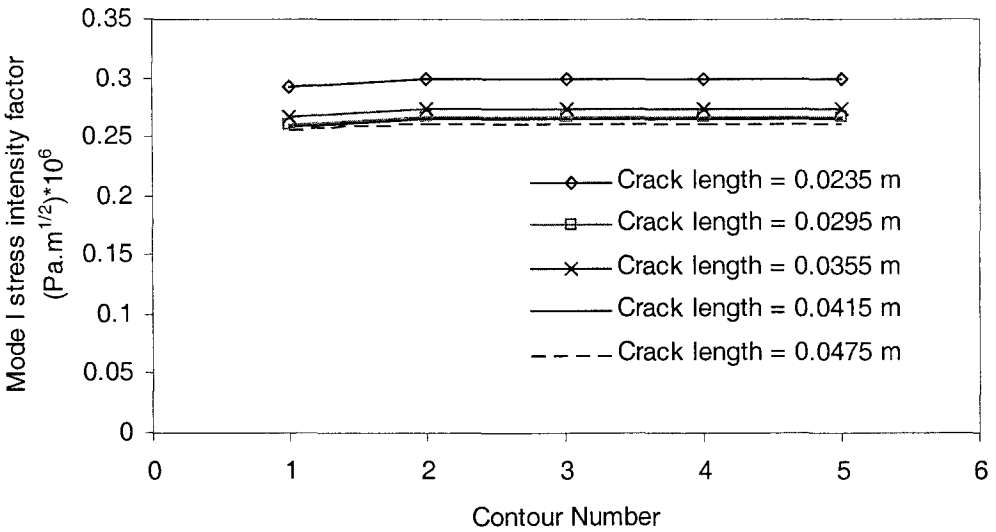

Figure 5.8: Variation of stress intensity factor with the various contours for different crack lengths.

the propagating crack. In case II, crack propagation velocities were assumed to decrease linearly with respect to crack extension. Variation of assumed crack propagation velocity with crack length is shown in Figure 5.9. Since a range of 2 - 120 m/s crack propagation velocity was obtained in the experimental study, a gross variation (55-38 m/s for linearly decreasing crack velocity and the average of these two end velocities, viz., 46.5 m/s for constant crack velocity) that approximately satisfied most of the test results was considered for analysis. In case II, even though the propagation velocity was assumed to be constant over the element length, the crack extension time was varied from element to element owing to the same size of elements. Time of crack extension from one element tip to other was calculated by dividing crack length (or length of the cracking elemental face) by the crack propagation velocity.

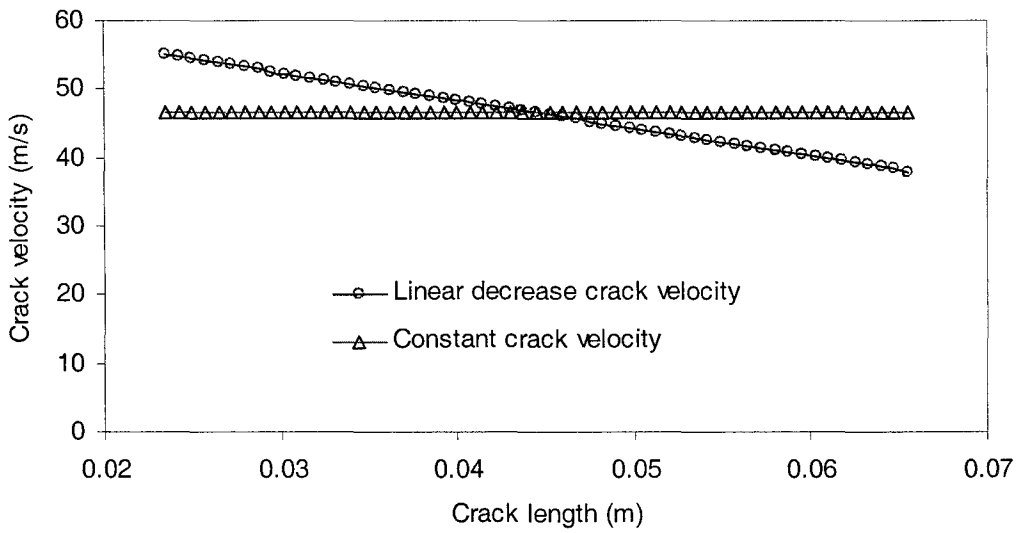

Figure 5.9: Variation of crack propagation velocity with respect to crack length

5.2.9 Results and Discussion

Contour plots of stresses in the local 1-direction for different time-dependent crack lengths are shown in Figures 5.10 (a)-(h). It is seen that stress concentration is developed at the crack tip. As crack tip moves due to propagation of crack along the plane with respect to time, stress concentration points also change their positions with respect to time as seen in Figures 5.10 (a)-(h). Stresses in local 1- and 2- directions along the depth of the specimen were also determined and are shown in Figures 5.11-5.14 for different crack lengths and for two cases of crack velocity variations. It is observed that the variation of stresses in local 1 direction seems to be almost constant for crack lengths between 0.0295-0.0535 m (see Figure 5.11). Also the stresses are very high around the crack tip leading to a progressive crack growth along the crack front.

Due to friction present between contact surfaces of steel and slate material, stress was obtained compressive at the indentation location on the specimen. Compressive stresses in directions 1 and 2 at the bottom of the specimen were developed due to Poisson's effect. At first, a compressive stress develops in direction-2 at the bottom contact surface due to the vertical component of applied load. Then due to Poisson's effect, applied load components in direction 2 will introduce compressive stresses in direction 1. This compressive stress effect in local 1 direction disappears at a distance of approximately 10% of the specimen depth from the bottom of the specimen (see Figures 5.11 and 5.13). Thereafter, stresses increase gradually becoming a maximum at the crack tip and suddenly decreasing thereafter.

(a)

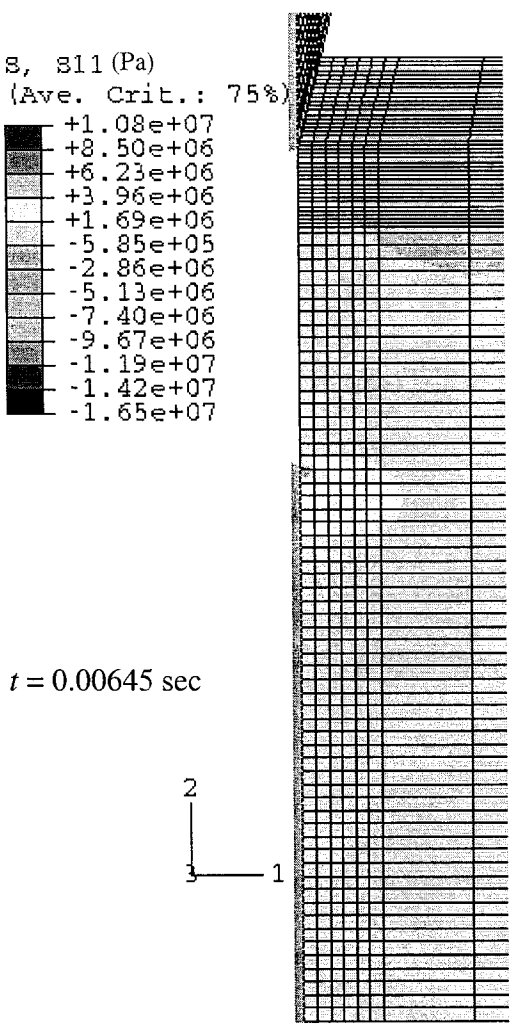

$t = 0.00645$ sec

(b)

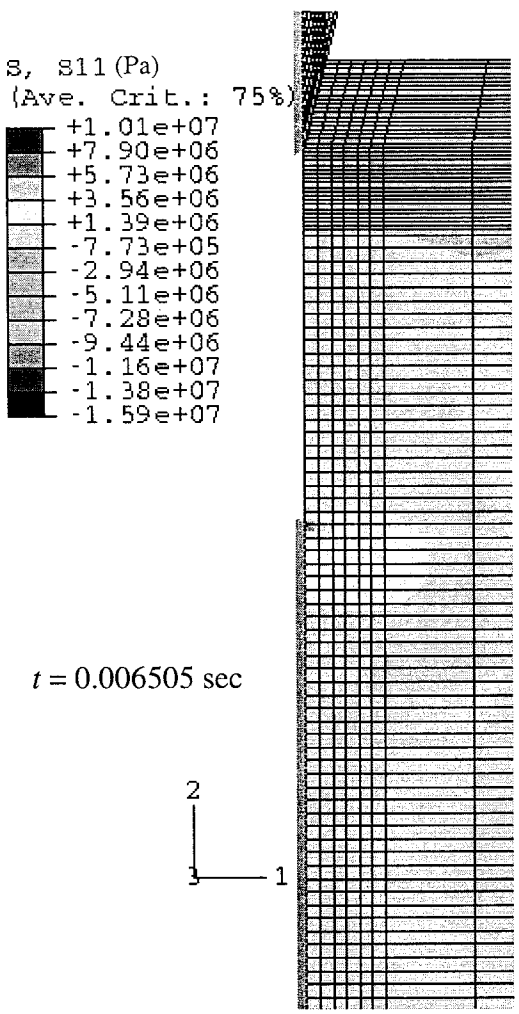

$t = 0.006505$ sec

(c)

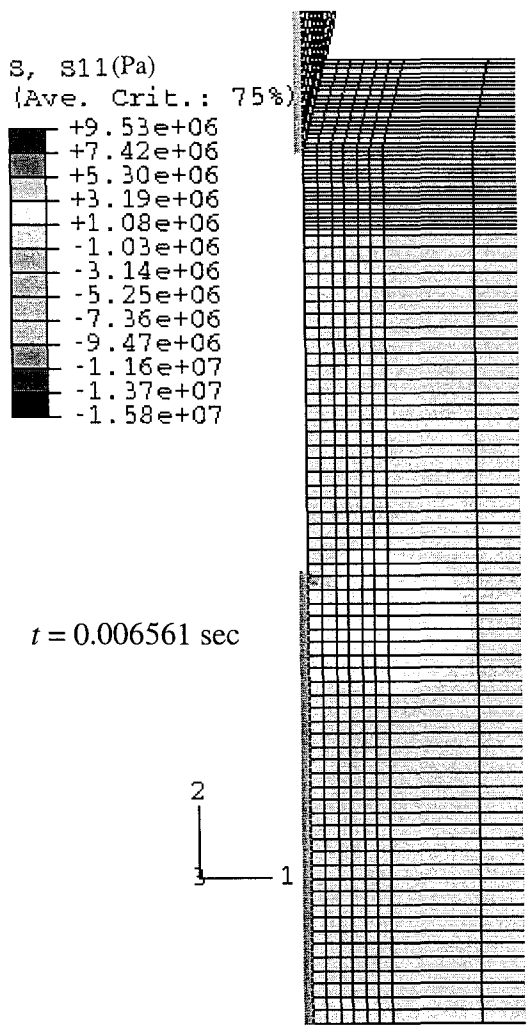

$t = 0.006561$ sec

(d)

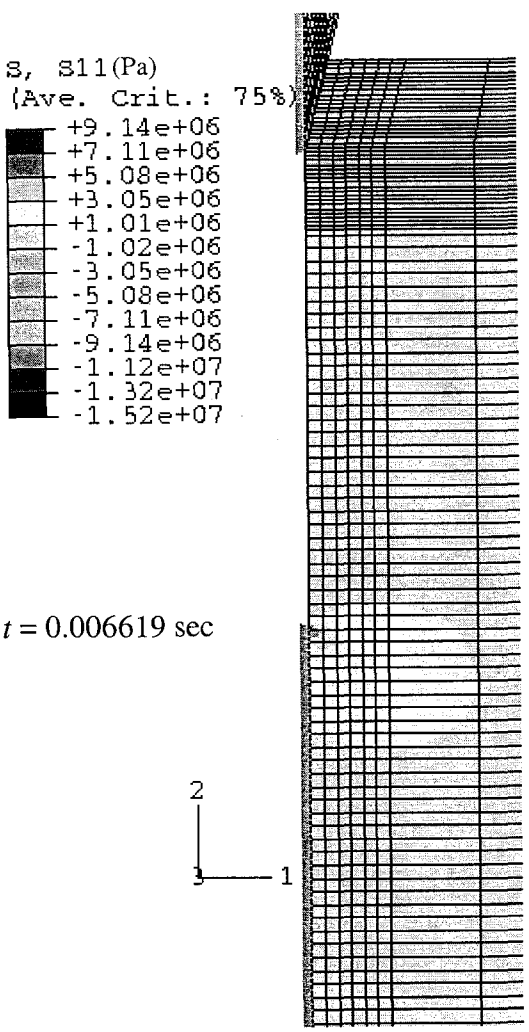

$t = 0.006619$ sec

(e)

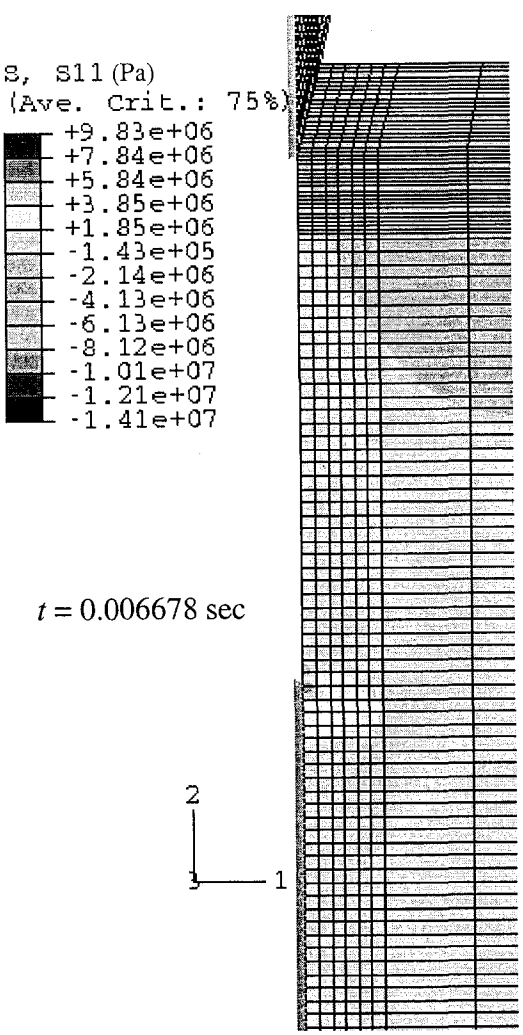

$t = 0.006678$ sec

(f)

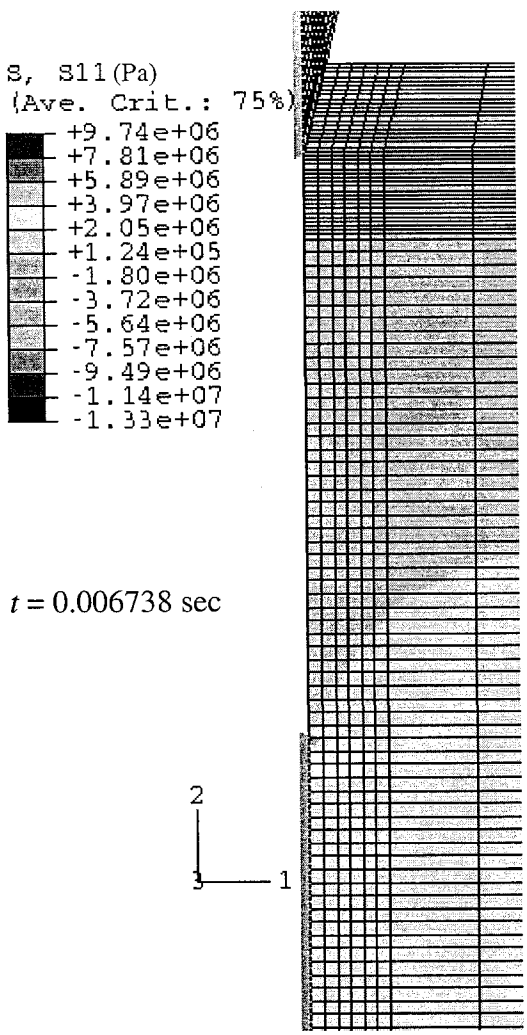

$t = 0.006738$ sec

(g)

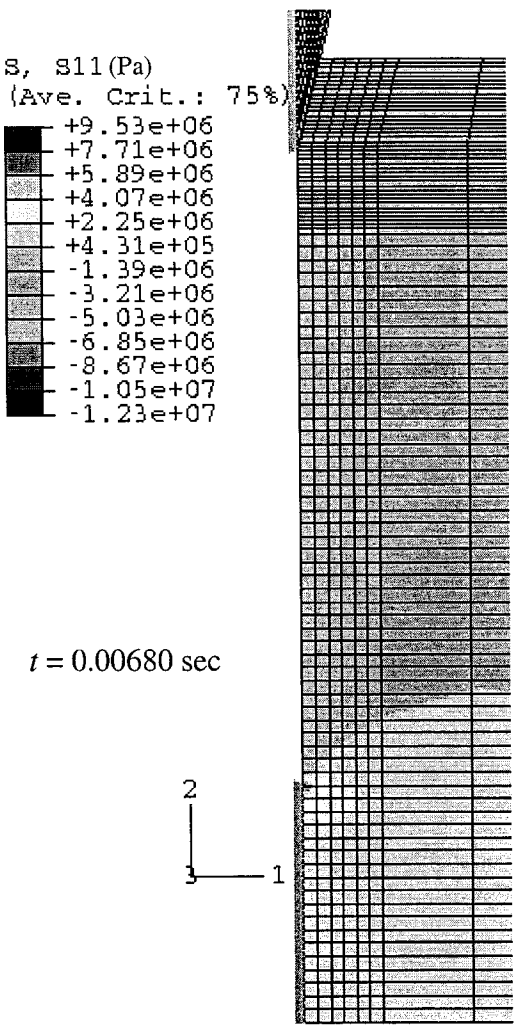

(h)

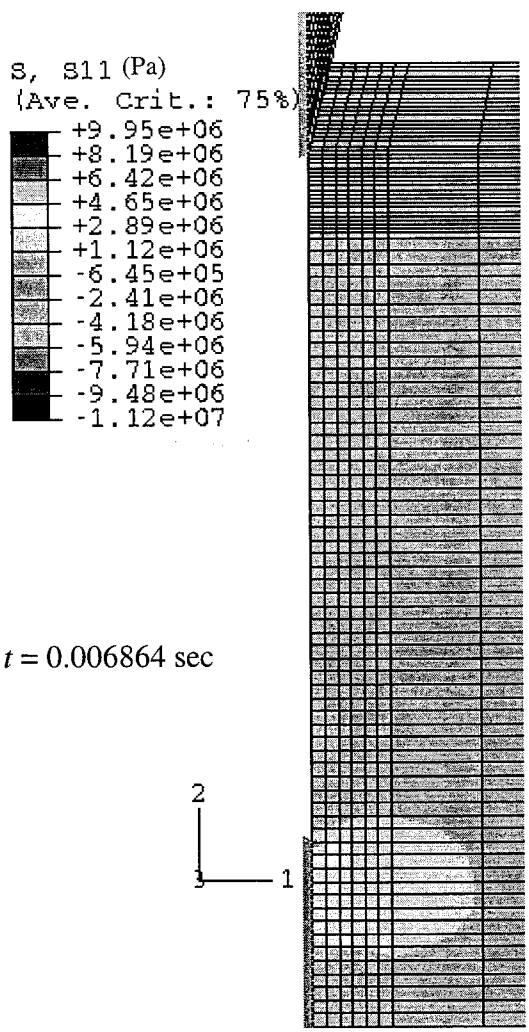

Figure 5.10 (a)-(h): Contour plot of stress in local direction 1 of test specimen for different time dependent crack lengths

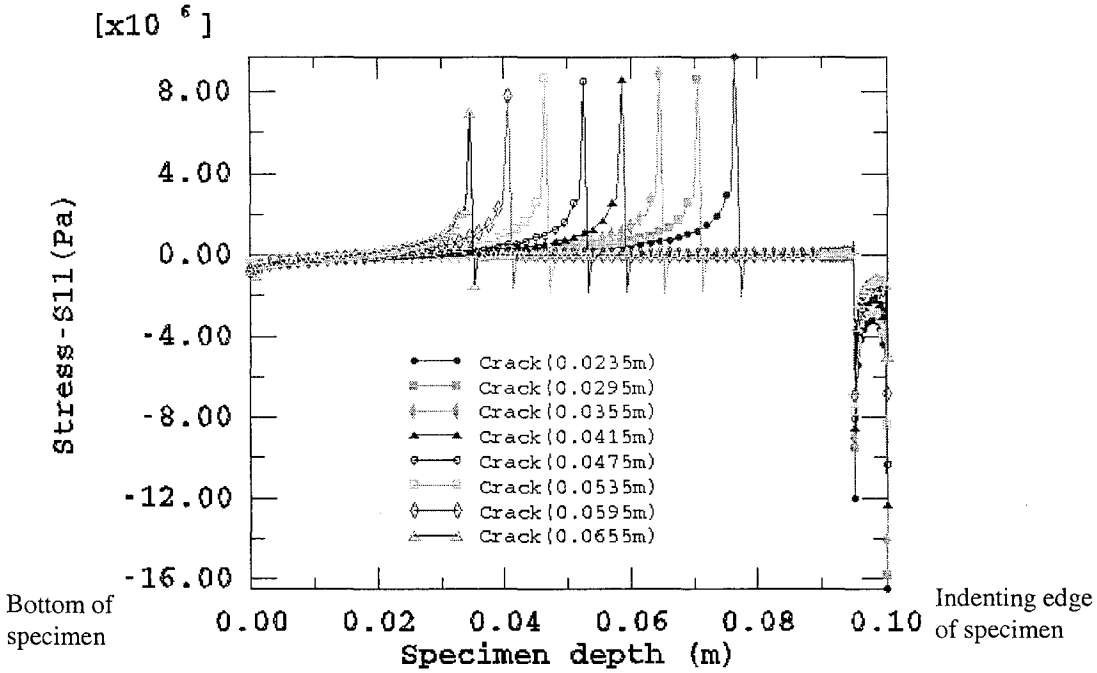

Figure 5.11: Variation of stress in local 1-direction along the depth of the specimen for different crack lengths and linearly decreasing crack propagation velocities.

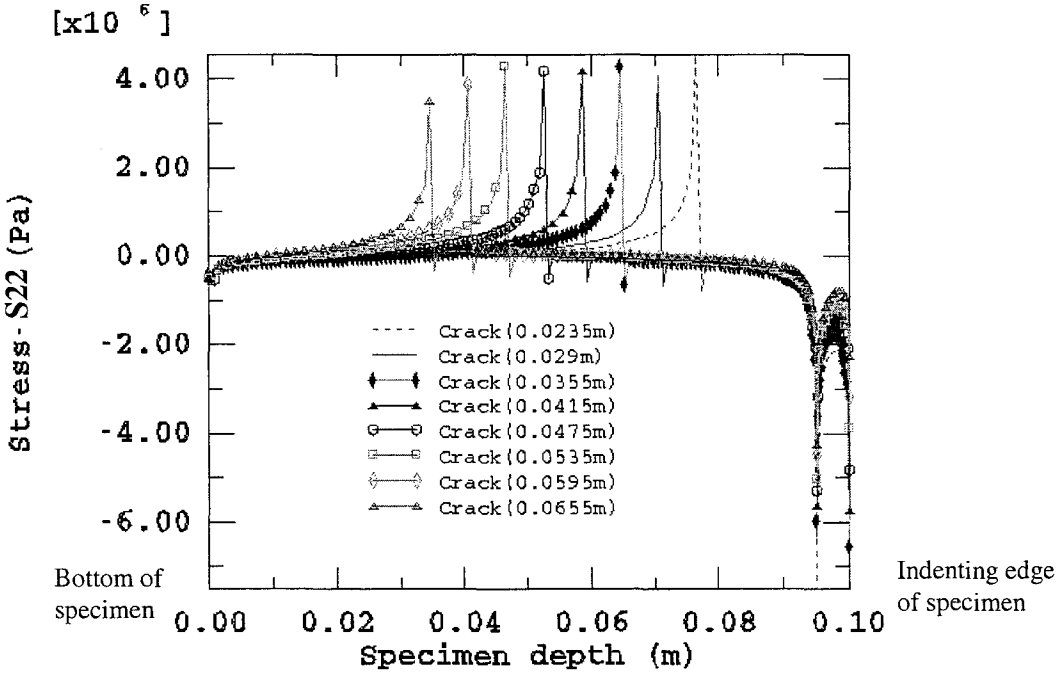

Figure 5.12: Variation of stress in local 2-direction along the depth of the specimen for different crack lengths and linearly decreasing crack propagation velocities

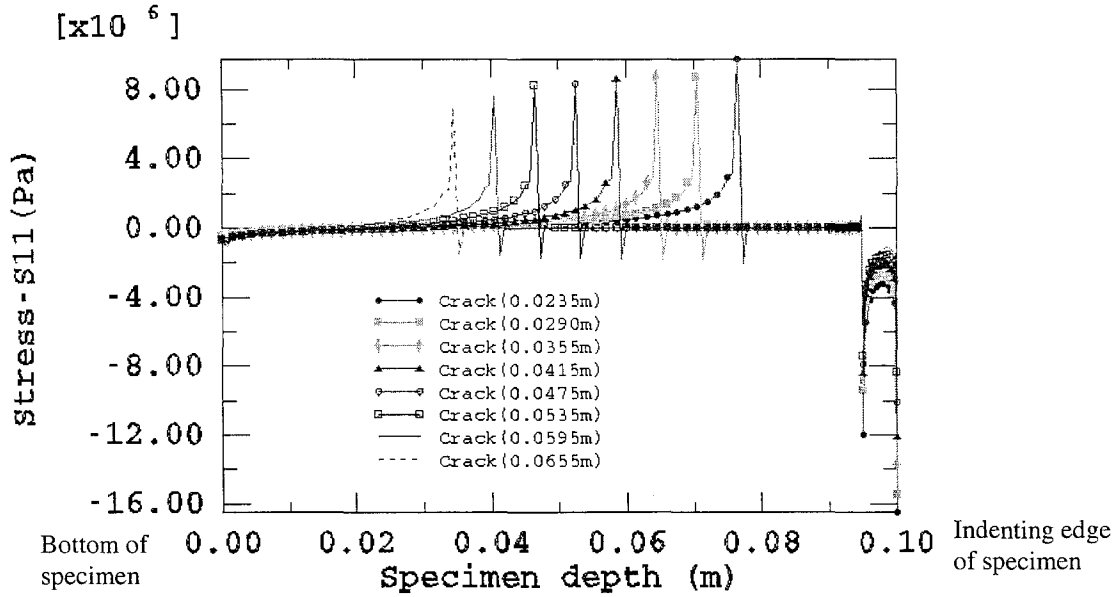

Figure 5.13: Variation of stress in local 1-direction along the depth of the specimen for different crack lengths and constant crack propagation velocities.

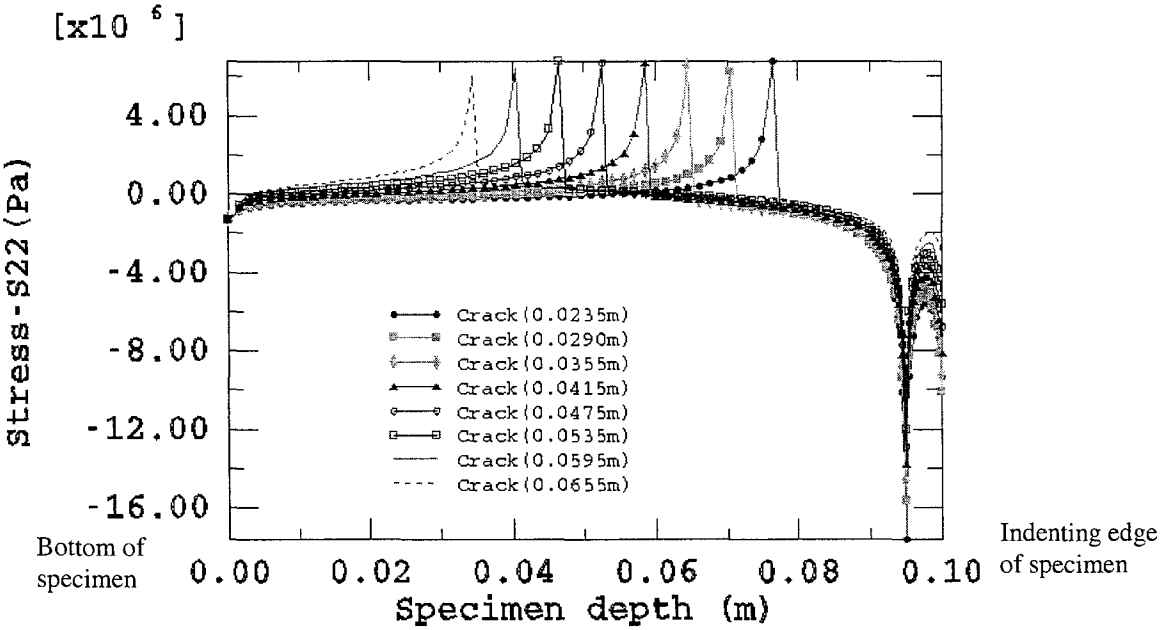

Figure 5.14: Variation of stress in local 2-direction along the depth of the specimen for different crack lengths and constant crack propagation velocities.

Sharp variation of stresses is observed again at the starting of the contact surface between wedge and specimen. Along the contact surface this variation seems to be constant except at the two boundary edges where stress discontinuity is developed. Maximum magnitude of stress components (S_{11} and S_{22}) decreases when crack continues to extend beyond the crack length of 0.0535m.

The variation of mode I dynamic stress intensity factors (at crack tip) along the line of symmetry of the slate block for different crack lengths and for the two modes of crack propagation velocities is shown in Figures 5.15. If plane strain fracture toughness is the material property to be used during crack propagation then crack will propagate only when SIF (obtained from the impact splitting load) is equal to the fracture toughness value obtained earlier from experiments. Therefore, SIF should be constant all along the crack front as the crack grows with a low crack propagation velocity (because dynamic fracture toughness is velocity dependent for high crack propagation velocity problems).

From the finite element analysis it can be seen that when the crack propagation velocity is constant, the SIF decreases gradually from the beginning of crack propagation (23.5%) to 33.5% depth of the body (see Figure 5.15). Almost an identical variation in SIF was also observed for case II, considering linearly decreasing crack propagation velocity. The initial decreasing trend in SIF plots would happen if the impact load (applied from experimental measurements on the theoretical model) was higher than the actual required theoretical value. Thereafter, an oscillatory behavior in the variation of SIFs is observed from a crack length 0.35 to 0.5 specimen depth for constant crack velocities and 0.35 to 0.55 depth for linearly decreasing crack propagation velocities; the differences between

the two curves were less than 5%. SIFs reduced when crack extension crossed 0.50 times the depth of the specimen for constant crack velocities. However, for case II, this occurred when crack extension went beyond 0.55 times the depth of specimen. Regular crack velocities and compressive stresses at the bottom of the specimen may be the reasons for this regular decrease observed in SIF values. When the SIF variation was compared with the static fracture toughness of the slate material for both the cases, the variation of SIF corresponding to the breaking load was very close to the experimental results (0.2242 ± 0.0481 MPa.m$^{1/2}$) obtained from static fracture toughness tests.

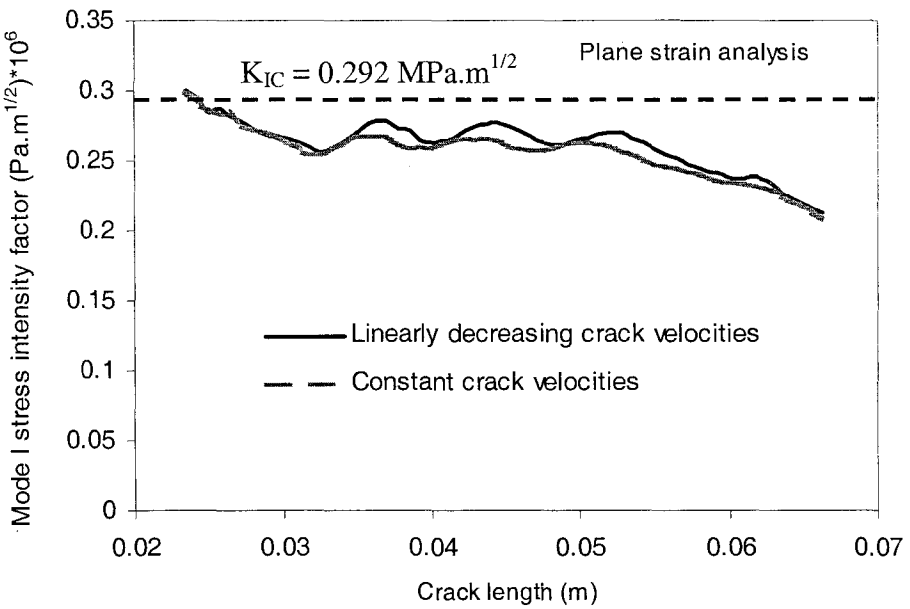

Figure 5.15: Variation of mode I dynamic stress intensity factor with crack length as plane crack propagates in the 0.1m cube slate block during impact splitting for constant and linearly decreasing crack propagation velocities.

5.3 Three-Dimensional (3D) Finite Element Analysis of Impact Splitting of Slate Block

3D finite element analysis of a regular cubic slate block (0.1 m × 0.1 m × 0.1 m) was carried out to compare results obtained from the equivalent plane strain analysis. The assumptions and simplifications mentioned in section 5.2.2 regarding the material, initial crack length, damping and wedge penetration were also used for 3D analysis. The specimen length was kept the same as the length of the wedge during experiment and the test specimen broke along a single vertical plane. Therefore, in numerical simulations, the crack was allowed to propagate in the same plane and crack front nodes were considered at the same horizontal level for each increment of crack length.

Sequential node release technique was also applied to simulate dynamic crack propagation in 3D analysis. All nodes along the crack front were released together at the same time for the next advancement of the crack. Contour plots of stresses in local 1-direction with the increased time and crack length are shown in Figures 5.16 (a)-(h). It is seen that crack front stresses are tensile and their magnitudes are higher than the stresses of other points. Contour plots of contact pressures on the surface of slate block at the contact surface of indenting wedge and slate is also shown in Figure 5.17. It is seen that contact pressures are compressive and their magnitudes are higher at the edges of the contact surfaces. Stresses (at the element integration point) in local 1-, 2- and 3-directions and mode I dynamic stress intensity factor for each node along the crack front were determined for each increment of crack along the vertical plane. The variation of integration point stresses (1- and 2- directions) along the vertical 2-direction through the middle of the symmetry plane 2-3 for different crack lengths (0.0235m, 0.0295m,

0.0355m, 0.0415m, 0.0475m, 0.0535m, 0.0595m and 0.0655m) are shown in Figures 5.18 & 5.19 and 5.22 & 5.23 for both linearly decreasing and constant crack propagation velocities. It is seen that the variation of stresses are similar to those obtained in the plane strain analysis (Figures 5.11 to 5.14). However, magnitude of stresses in local 1- and 2-directions are much less (almost 2.5-3.0 times) than those obtained from plane strain analysis. The reason could be the choice of two different types of elements for the two analyses (plane strain and 3D). Second order elements were used in plane strain analysis and linear elements were used in 3D analysis. Sizes of elements would also be another reason as stress analysis gives good results for very fine meshes. Element size close to the crack plane was 0.00075m square in plane strain analysis and 0.003m $\times$ 0.0025m $\times$ 0.0015m in 3D analysis (4 times larger than plane strain case).

Stresses along the crack front for different crack lengths are shown in Figures 5.20 and 5.21 for linearly decreasing crack propagation velocities and in Figures 5.24 and 5.25 for constant crack propagation velocities. It is seen that stresses are almost constant up to a crack width equal to the 0.5 times the half length of block (0.025 m from the symmetry plane 1-2); thereafter, it decreases gradually toward the boundary by 15-25% in direction 1 and 30-60% in direction 2. Existence of traction free boundary in directions 2 and 3 could be the reason for this. Since all degrees of freedom in local 1-direction of the uncracked part of the specimen were restrained and local 2 and 3 degrees of freedom were made free near the outer edges of the specimen. Therefore, decrease of stress in direction 2 would be more than that in direction 1 since it should become zero at the free boundary. Moreover, since stresses obtained from this analysis are integration point stresses, the stress values do not become zero at free boundaries.

As seen from Figures 5.11 and 5.18 stresses decrease more with the increase of crack length in vertical direction. It has been observed from Figure 5.19 that stresses in local 2-direction at crack tip node is less than the stress obtained for the node just behind the crack tip for 3D analysis. A comparison of results obtained from integration point stresses in local 1- and 2-directions and contact pressure (at the middle line of the contact plane) of plane strain and 3D analysis are shown in Figures 5.26 to 5.28. A large variation of stresses at the crack tip and the boundaries of the contact surfaces are observed between the two analysis procedures. However, variation of the contact pressure at the middle 95% of the contact surface was less than 10% though it was more than 300% at the free boundaries.

(a)

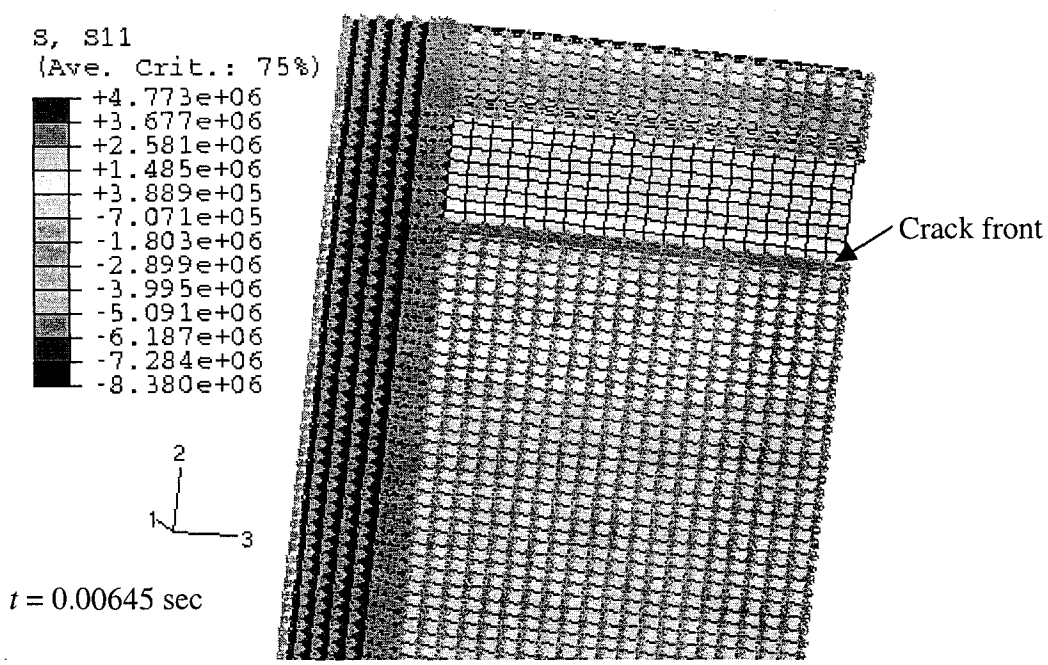

(b)

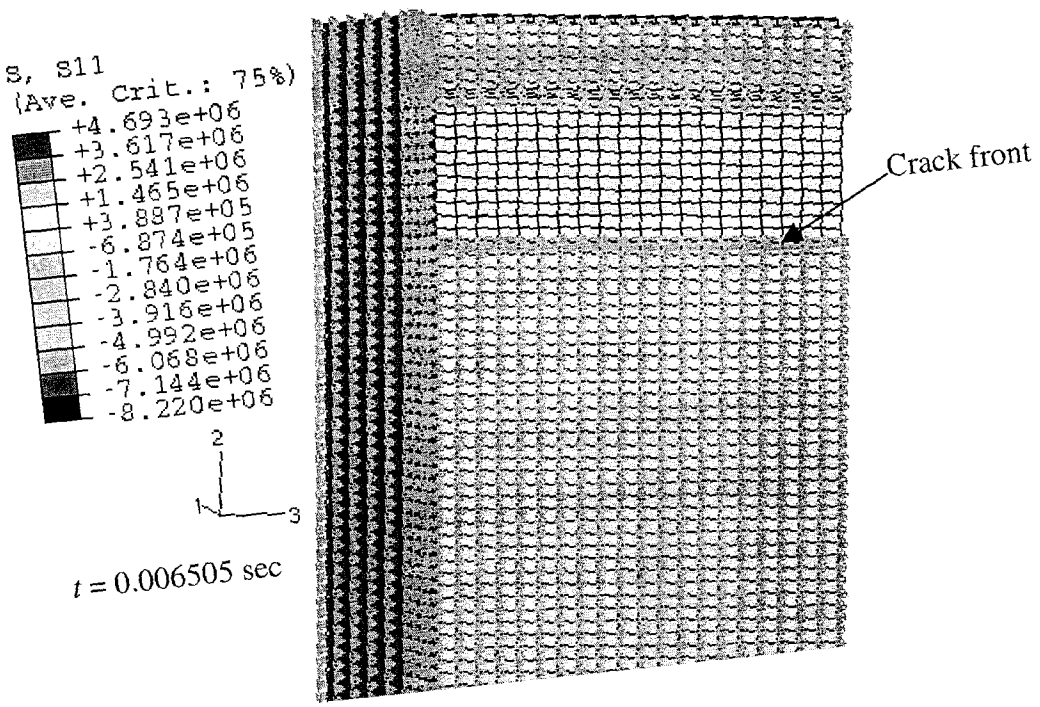

$t = 0.006505$ sec

(c)

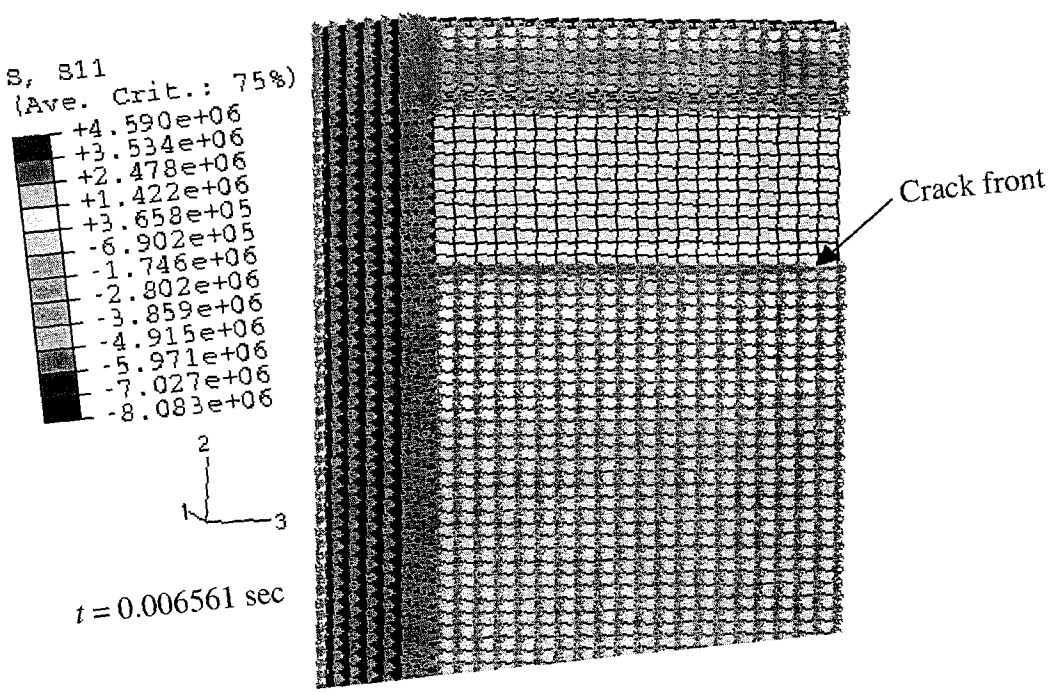

$t = 0.006561$ sec

(d)

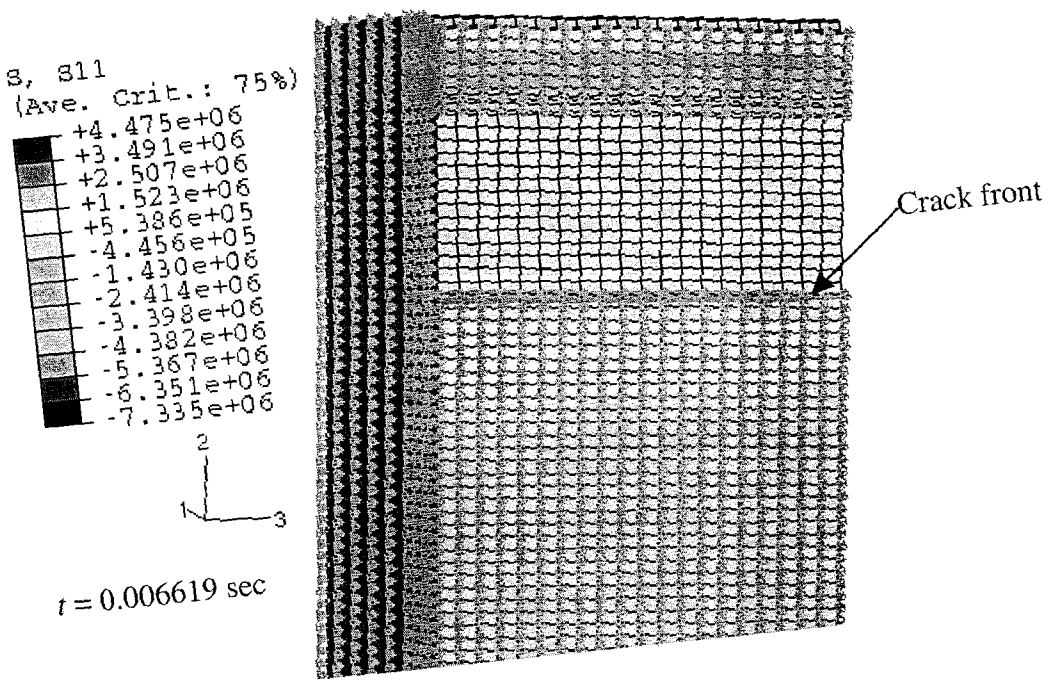

$t = 0.006619$ sec

(e)

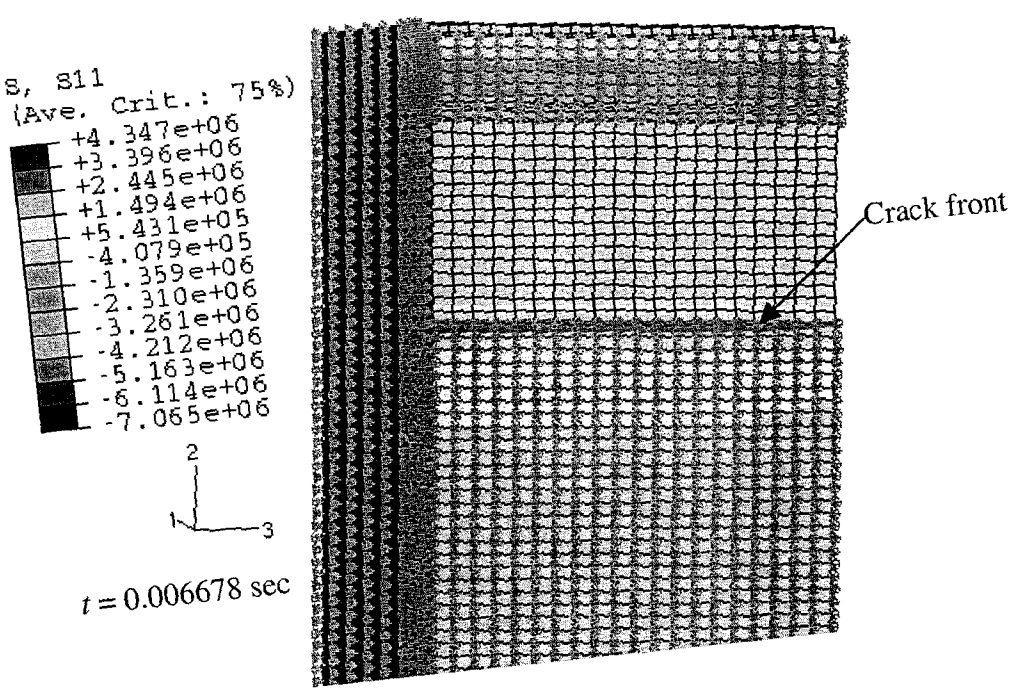

$t = 0.006678$ sec

(f)

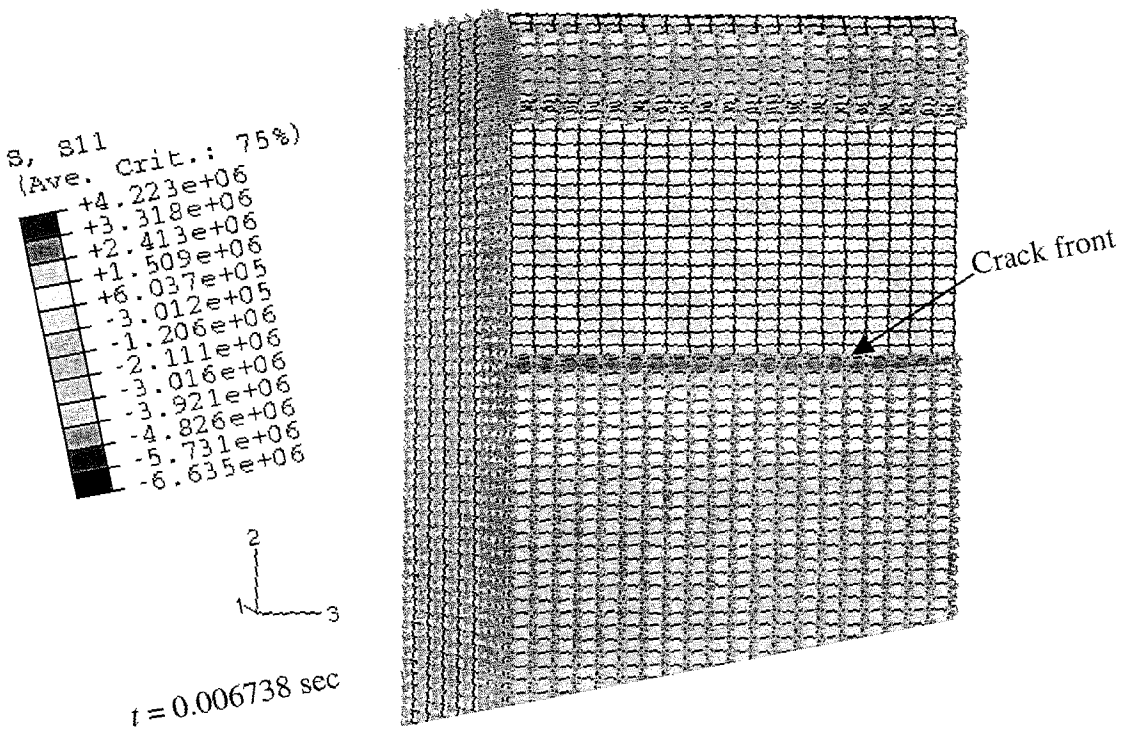

$t = 0.006738$ sec

(g)

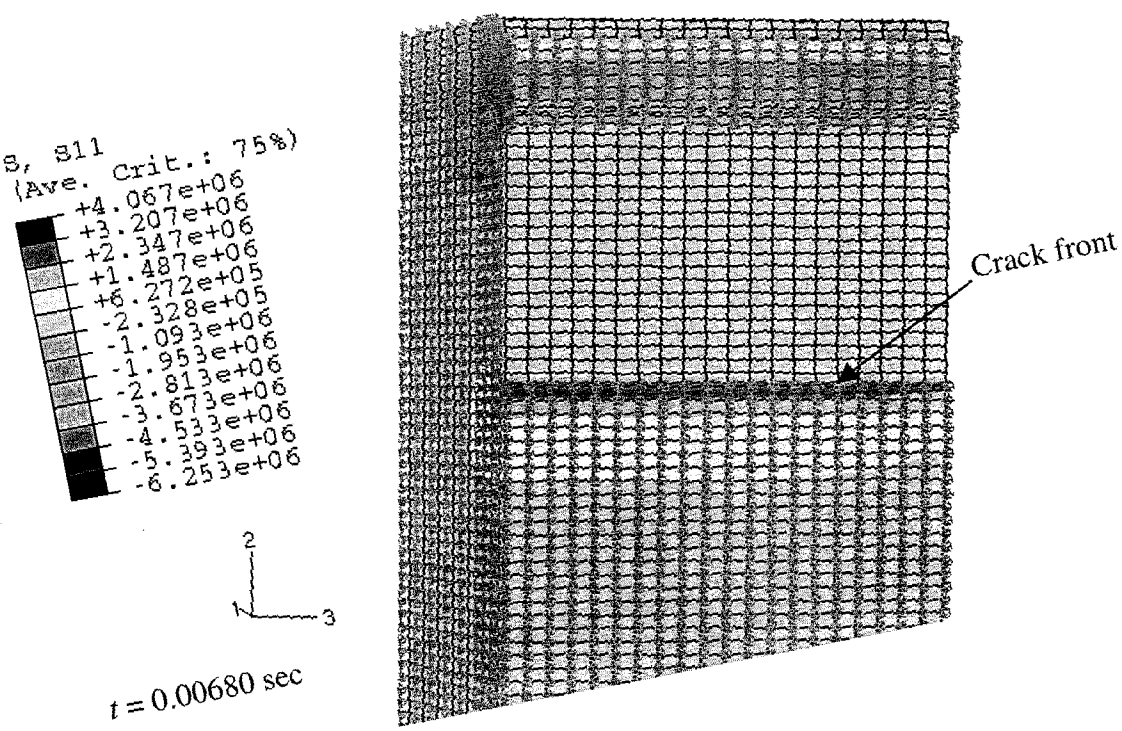

$t = 0.00680$ sec

(h)

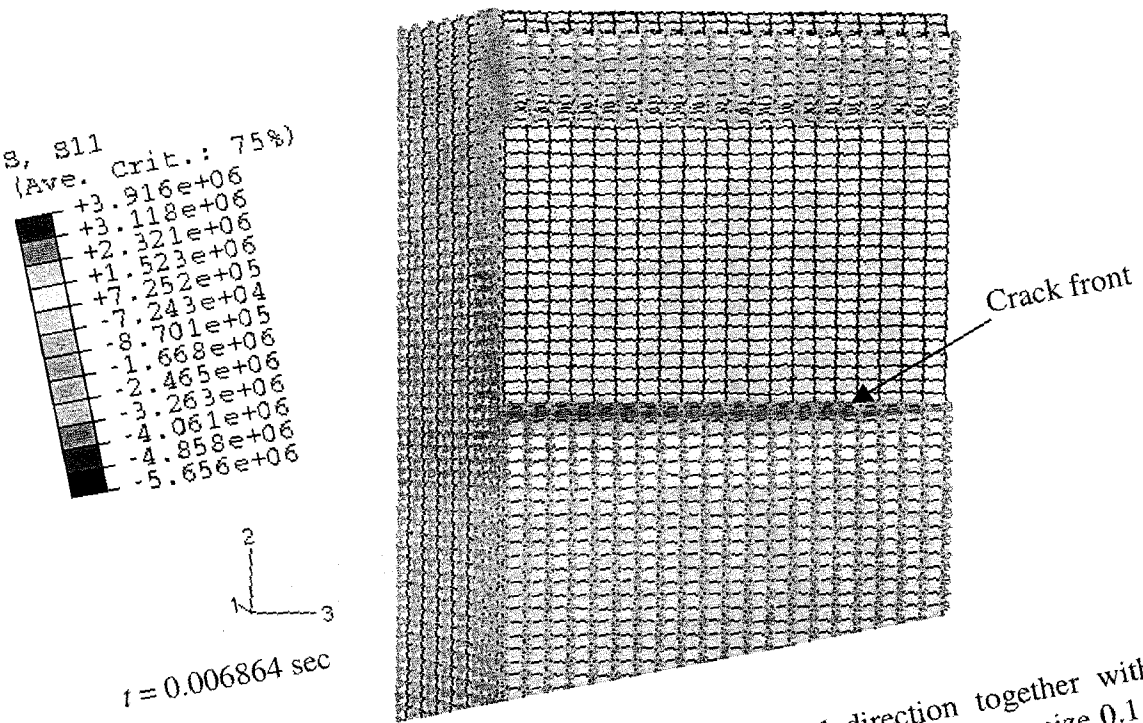

Figure 5.16 (a)-(h): Contour plot of stresses in local 1-direction together with the boundaries required to maintain symmetry condition of slate block having size $0.1 \times 0.1 \times 0.1$ m for different time dependent crack lengths.

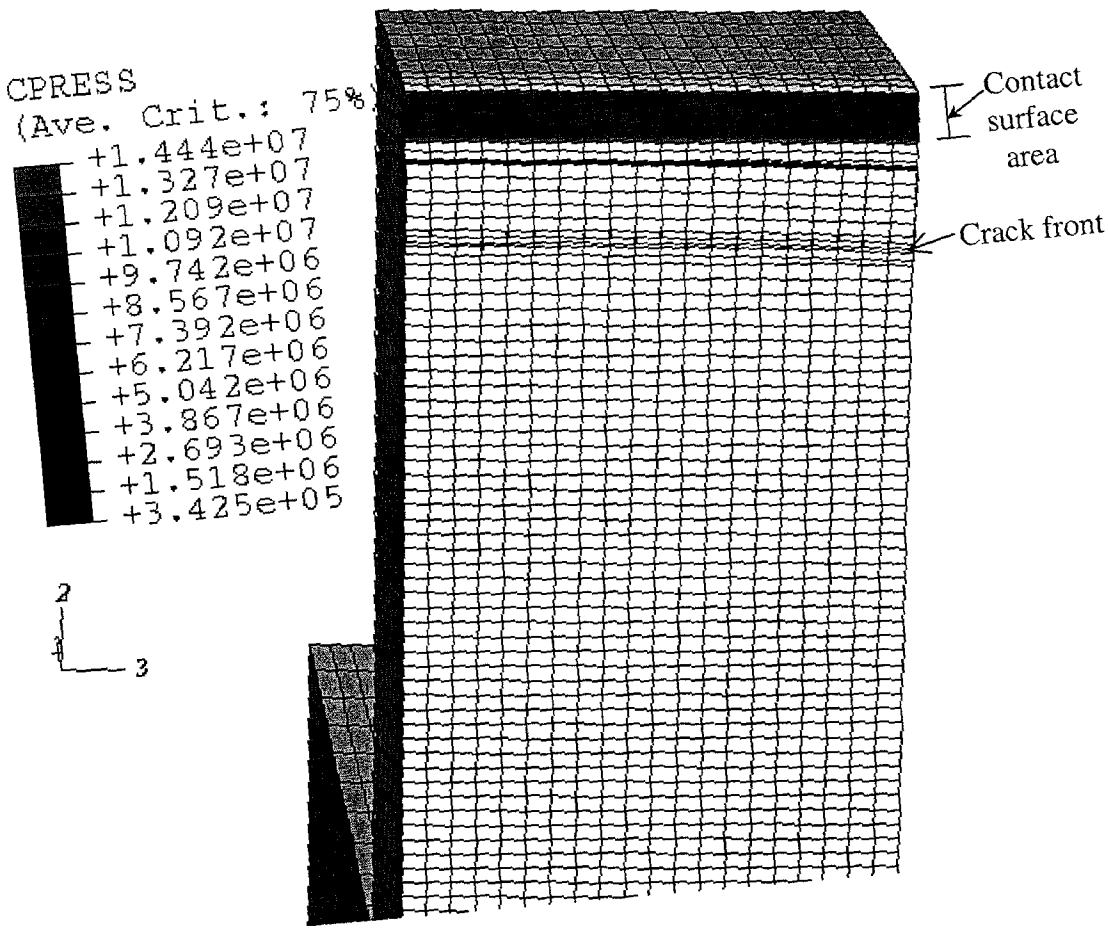

Figure 5.17: Contour plot of contact pressures on the surface of slate block along the contact surfaces of wedge indenter and slate.

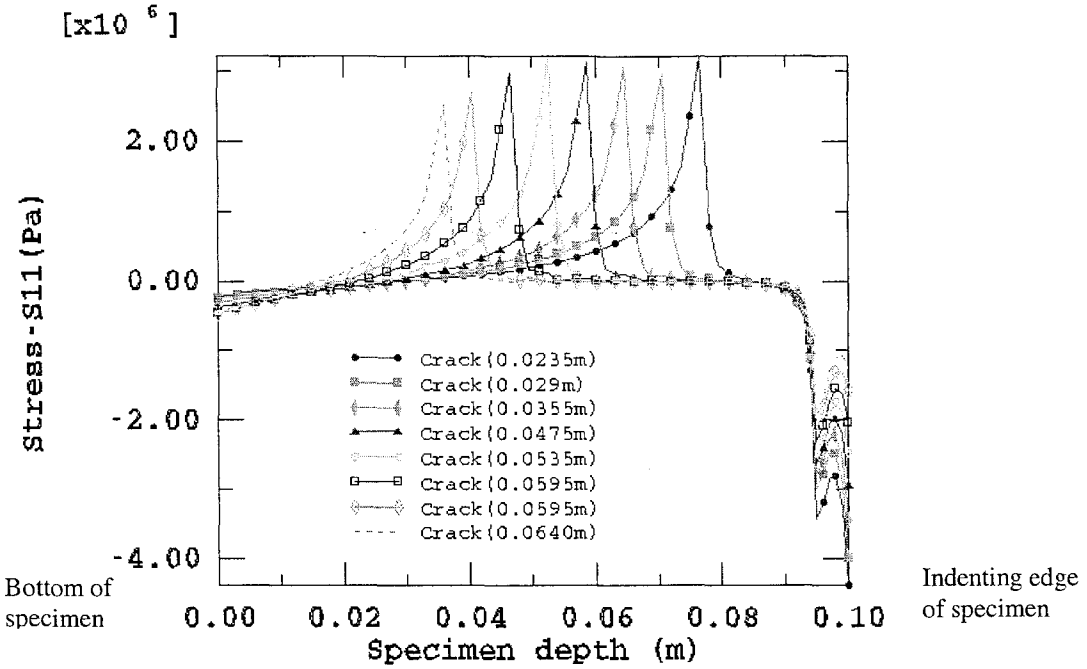

Figure 5.18: Variation of stress in local 1-direction along the depth of the specimen for different crack lengths and linearly decreasing crack propagation velocity

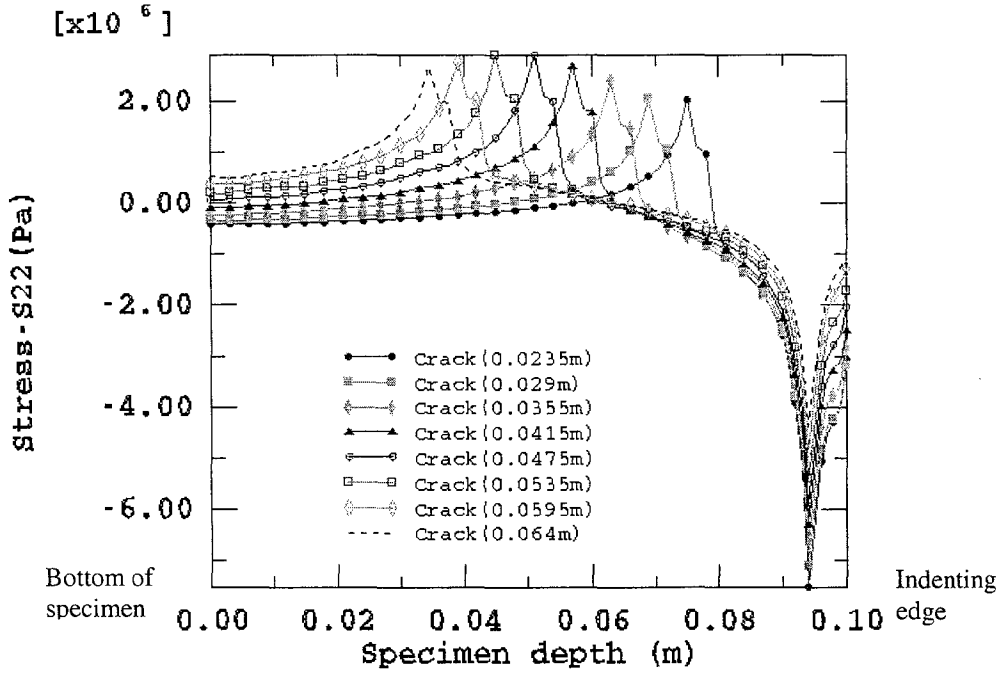

Figure 5.19: Variation of stress in local 2-direction along the depth of the specimen for different crack lengths and linearly decreasing crack propagation velocities.

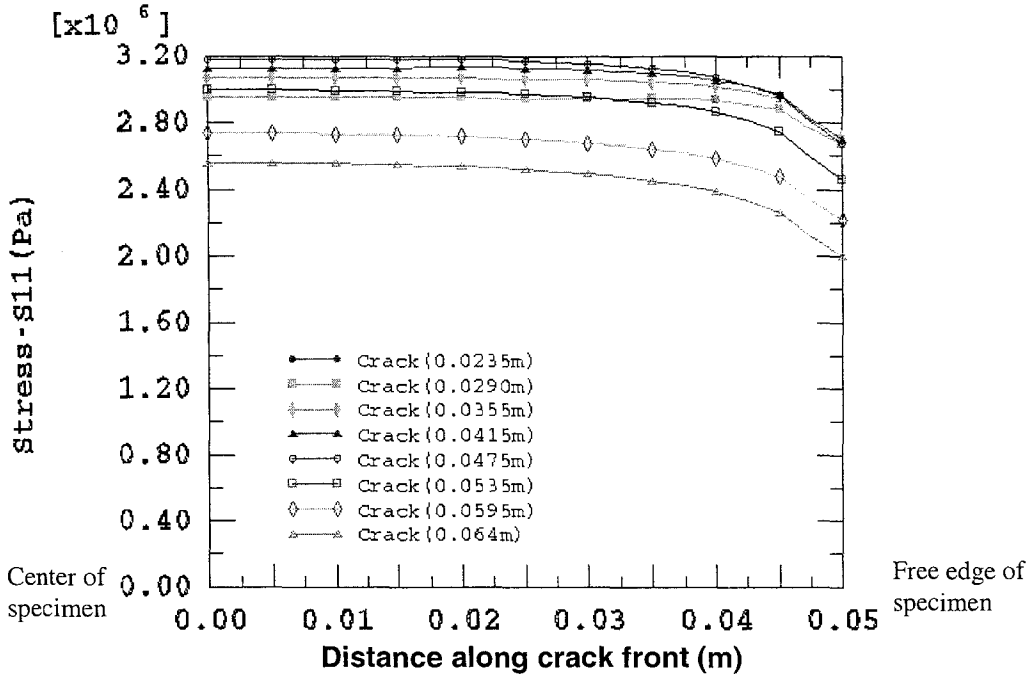

Figure 5.20: Variation of stress in local 1-direction along the crack front of slate block for different crack lengths for linearly varying crack propagation velocities.

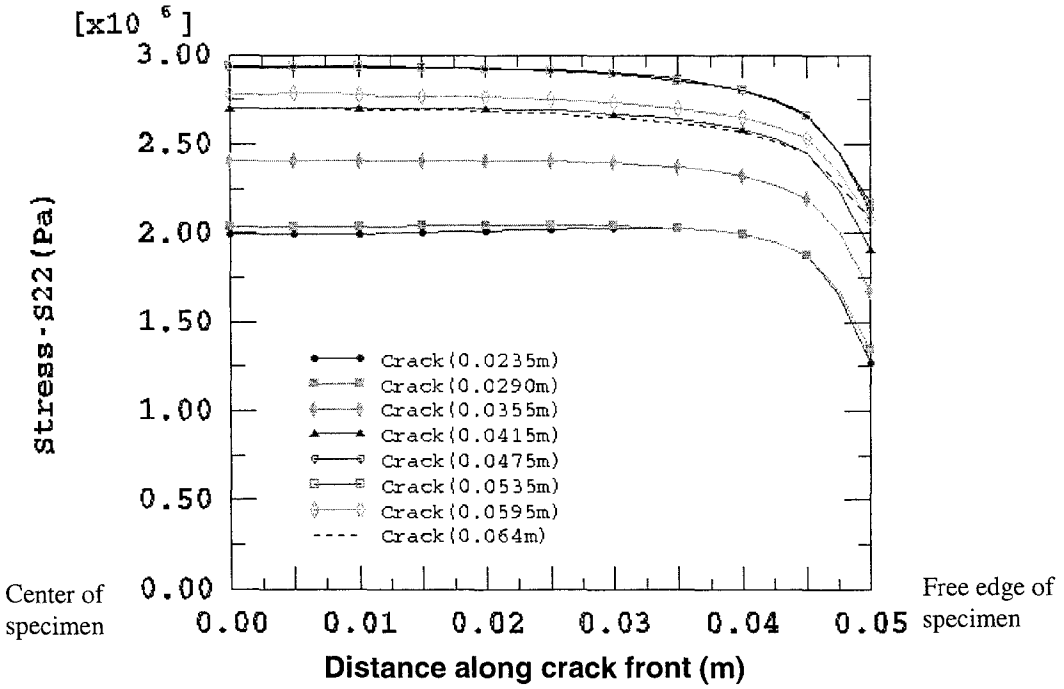

Figure 5.21: Variation of stress in local 2-direction along the crack front of slate block for different crack lengths for linearly varying crack propagation velocities.

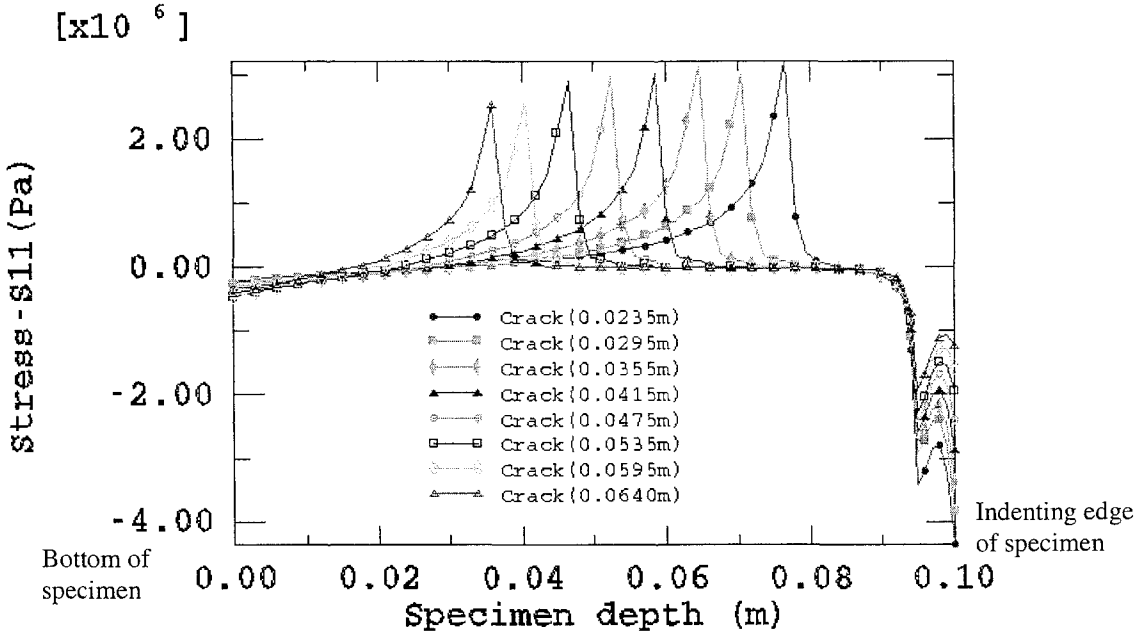

Figure 5.22: Variation of stress in local 1-direction along the depth of the specimen for different crack lengths and constant crack propagation velocities.

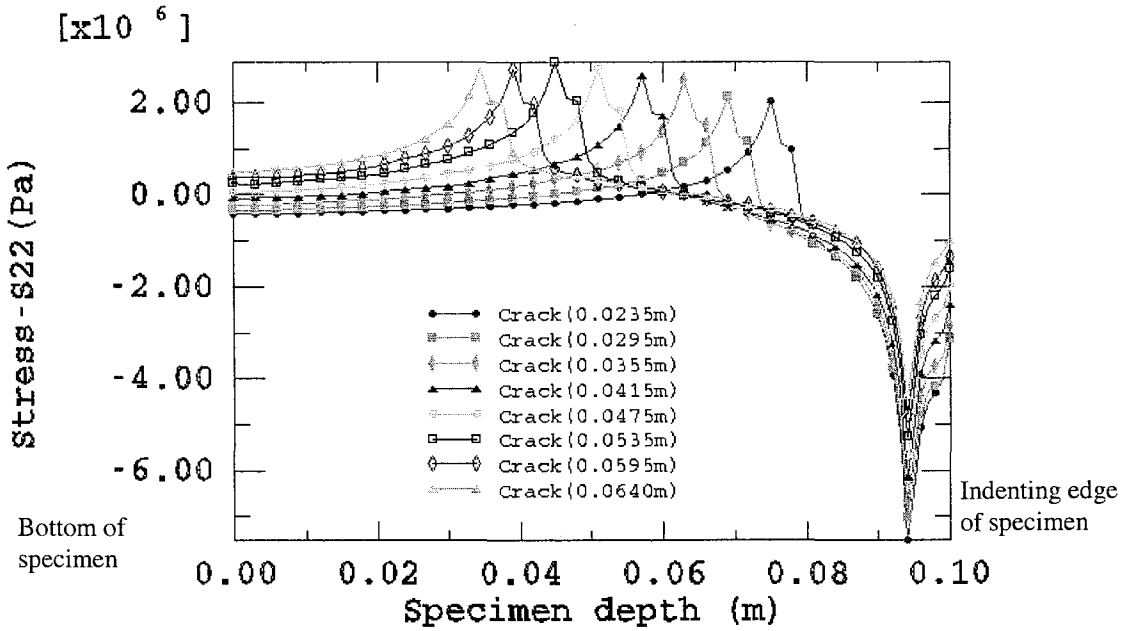

Figure 5.23: Variation of stress in local 2-direction along the depth of the specimen for different crack lengths and constant crack propagation velocities.

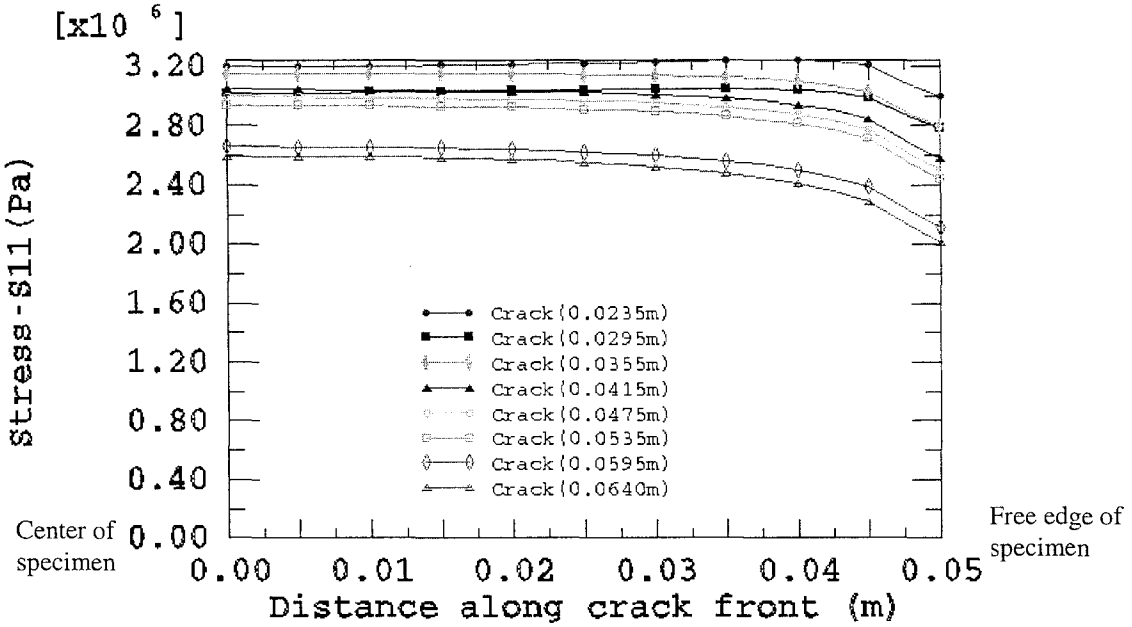

Figure 5.24: Variation of stress in local 1-direction along the crack front of slate block for different crack lengths for constant crack propagation velocities.

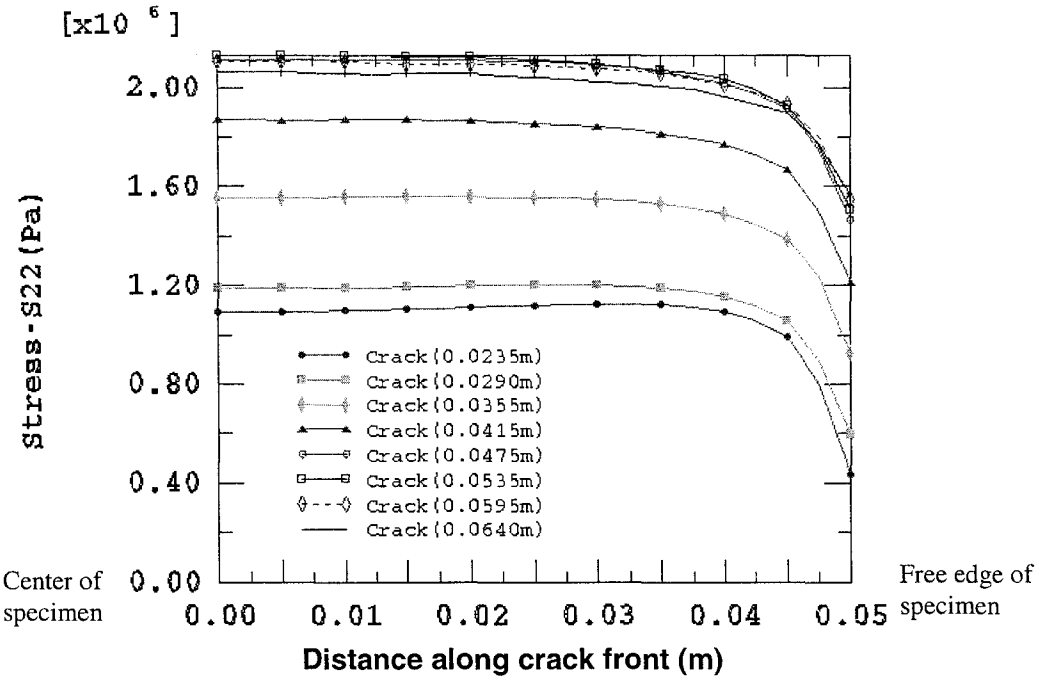

Figure 5.25: Variation of stress in local 2-direction along the crack front of slate block for different crack lengths for constant crack propagation velocities.

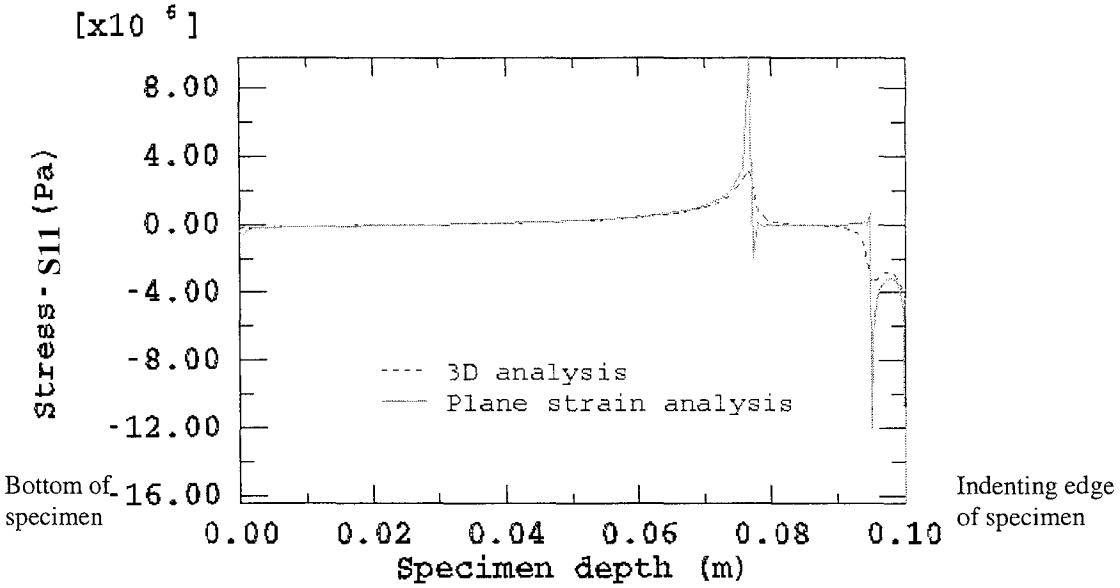

Figure 5.26: Variation of stress in local 1-direction for plane strain analysis and 3D analysis

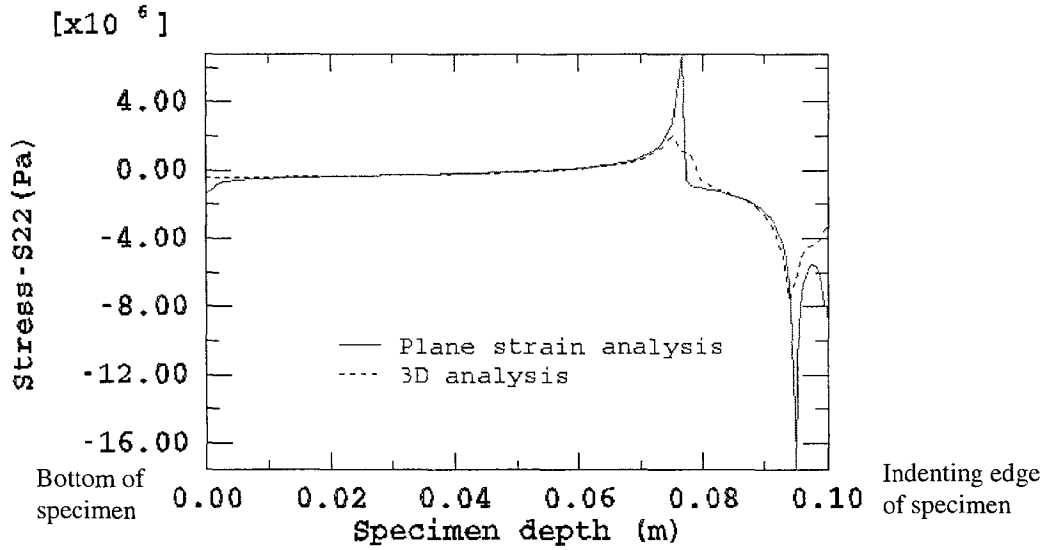

Figure 5.27: Variation of stress in local 2-direction for plane strain analysis and 3D analysis

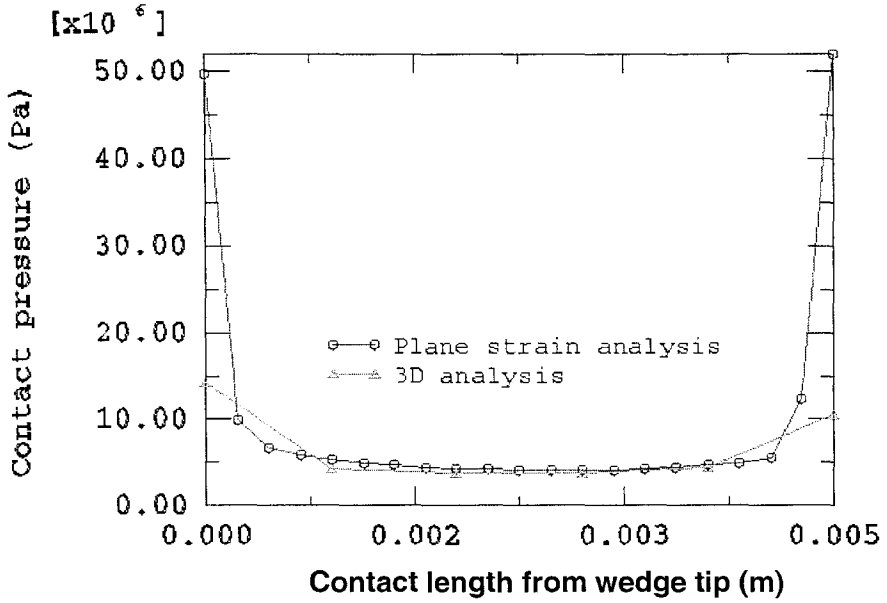

Figure 5.28: Variation of contact pressure along the contact line of wedge and slate block for plane strain analysis and 3D analysis.

The variation of mode I dynamic stress intensity factors (SIF) along the vertical 2-direction at a distance 0.01 m away from the free boundary edge is shown in Figure 5.29 for different crack lengths and constant and linearly decreasing crack propagation velocities. It is seen that variation of SIFs between two cases (constant and linearly decreasing crack propagation velocities) up to a crack length 0.05m from its initial value of 0.0235m is less than 10%. An oscillatory variation is observed for both constant and linearly decreasing crack propagation velocities. This is probably due to the fact that the cracking develops in stages; once a crack front is released, it takes time to build up to the next maximum SIF value since loads are applied in an incremental manner (time-wise). However, SIFs values were slightly higher for linearly decreasing crack propagation velocities than the constant crack velocities, for most of the crack extension period. From these results it could be said that dynamic stress intensity factor is not significantly

influenced by low velocity crack propagation. It is also influenced less by the type of velocity variation whether it is constant or varying linearly. SIF values decrease slowly beyond a crack length equal to 0.05 m. In this region, SIF values are probably influenced by the compressive stresses developed at the bottom of the specimen

A comparison of results (SIFs) between plane strain and 3D analyses are shown in Figures 5.30 and 5.31. It is seen that variation of SIFs is almost similar in both plane strain and 3D analyses. However, SIFs in plane strain analysis were higher by 10% for the crack lengths between 0.0235-0.03 m and greater than 0.05m. For a crack of length in the range of 0.03 m to 0.05 m, SIFs fluctuate. Though stress variation in local 1 direction was observed to be more than 300%, the SIF variation was less than 10%. This seems to be reasonable since SIFs evaluation through contour integral is less affected by the size of elements. The main reason for this difference may be attributed to the coarseness in mesh size used for 3D analyses and the use of linear eight-noded elements used in analysis. As mentioned earlier, the use of dynamic elastic constants (which are higher by 3% to 7%) would also improve the correlation between experiments and analyses.

The variation of SIFs along the transverse crack front of 3D model, for different crack lengths and different propagation velocities, is shown in Figures 5.32 and 5.33. It is seen that SIFs are constant up to a distance equal to 0.9 times the half length along local 3-direction; thereafter it starts to decrease and at the free edge it is 90 percent of the SIFs obtained for the constant variation region. This variation in SIF is due to the free boundary effect.

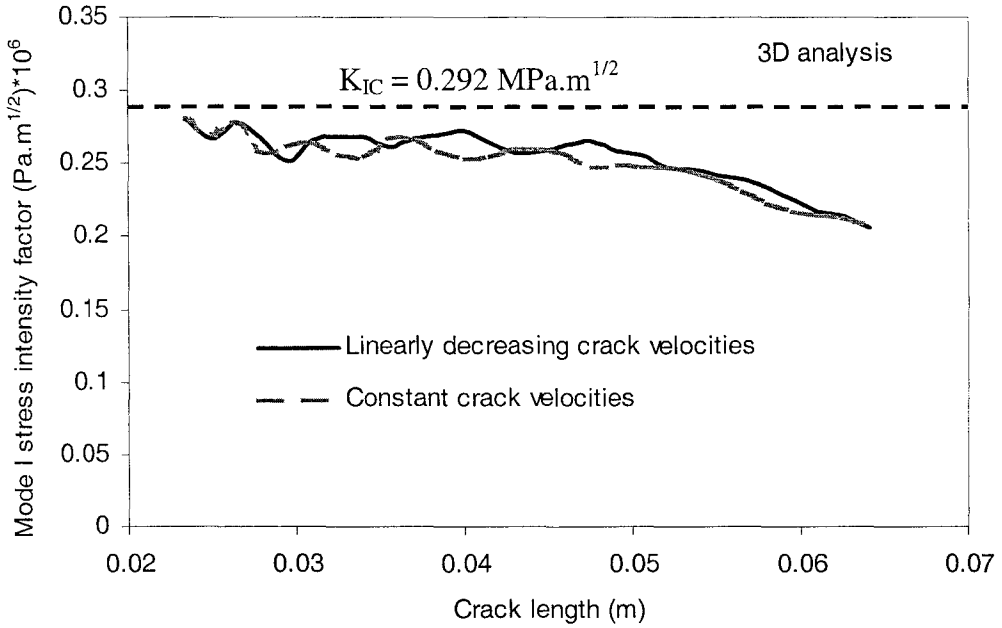

Figure 5.29: Variation of SIFs along the depth of the specimen for different time dependent crack lengths and constant and linearly decreasing crack velocities.

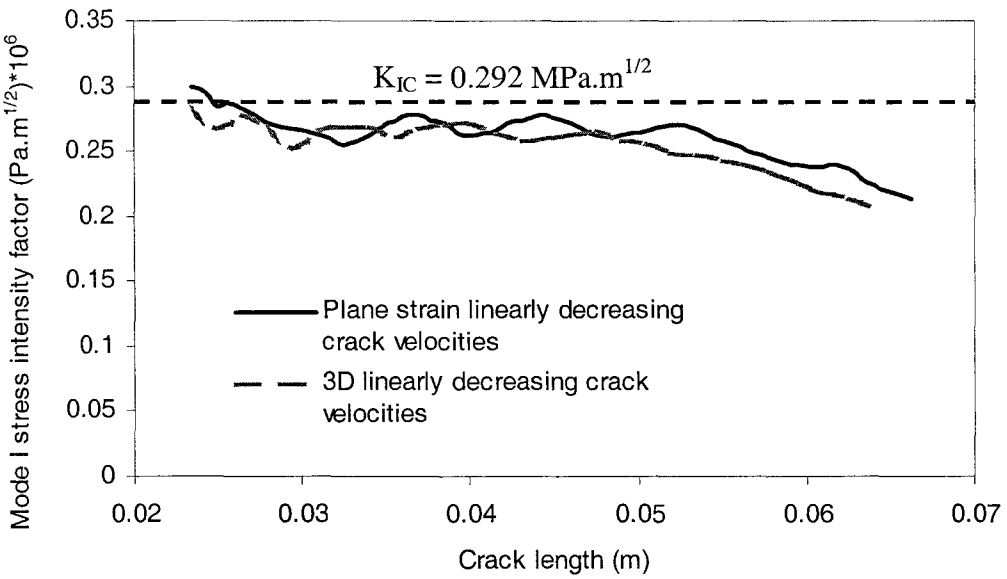

Figure 5.30: Variation of SIFs along the depth of the specimen for different time dependent crack lengths and linearly decreasing crack propagation velocities in plane strain and 3D analyses.

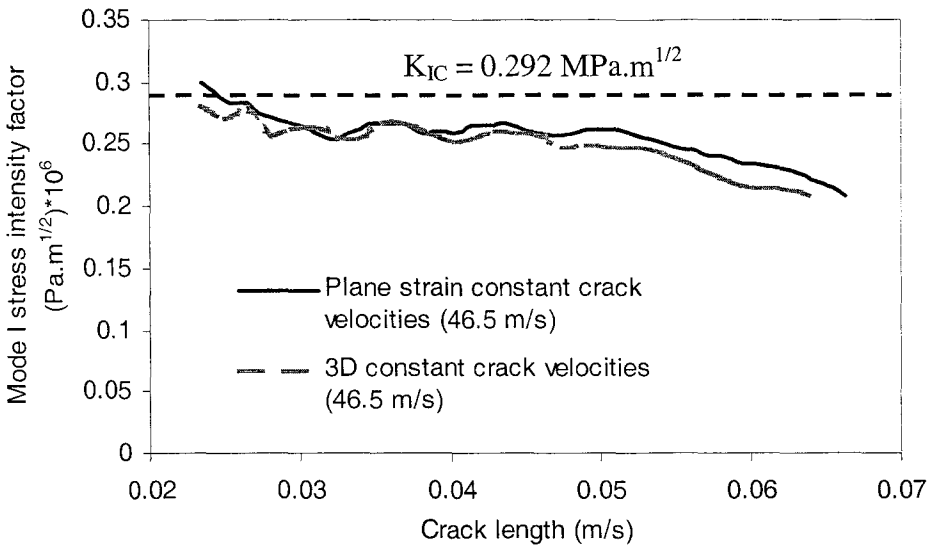

Figure 5.31: Variation of SIFs along the depth of the specimen for different time dependent crack lengths and constant crack propagation velocities in plane strain and 3D analyses.

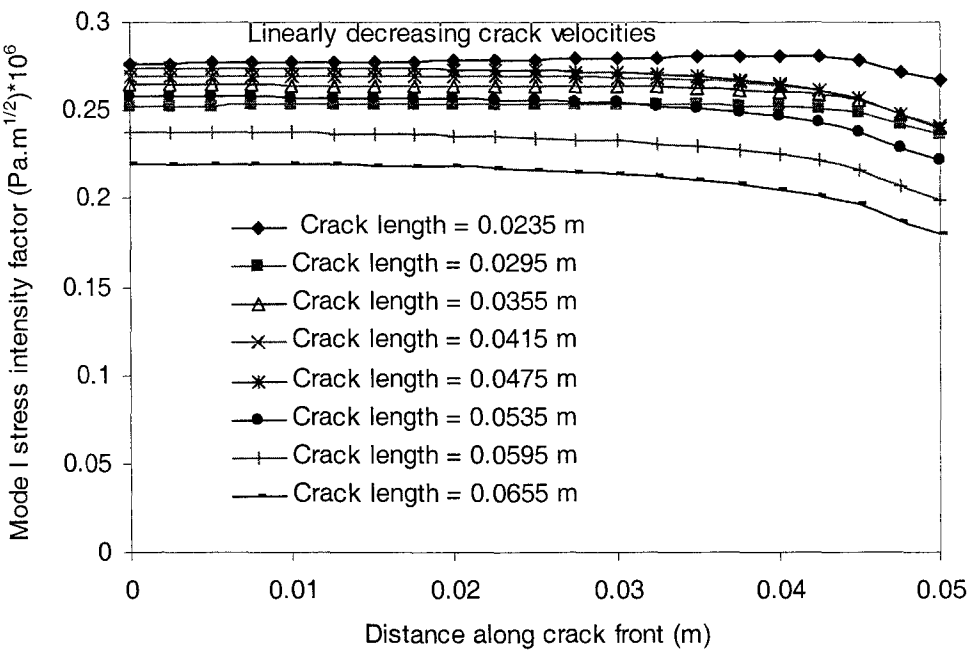

Figure 5.32: Variation of SIFs along the crack front for different time dependent crack lengths and linearly decreasing crack propagation velocities.

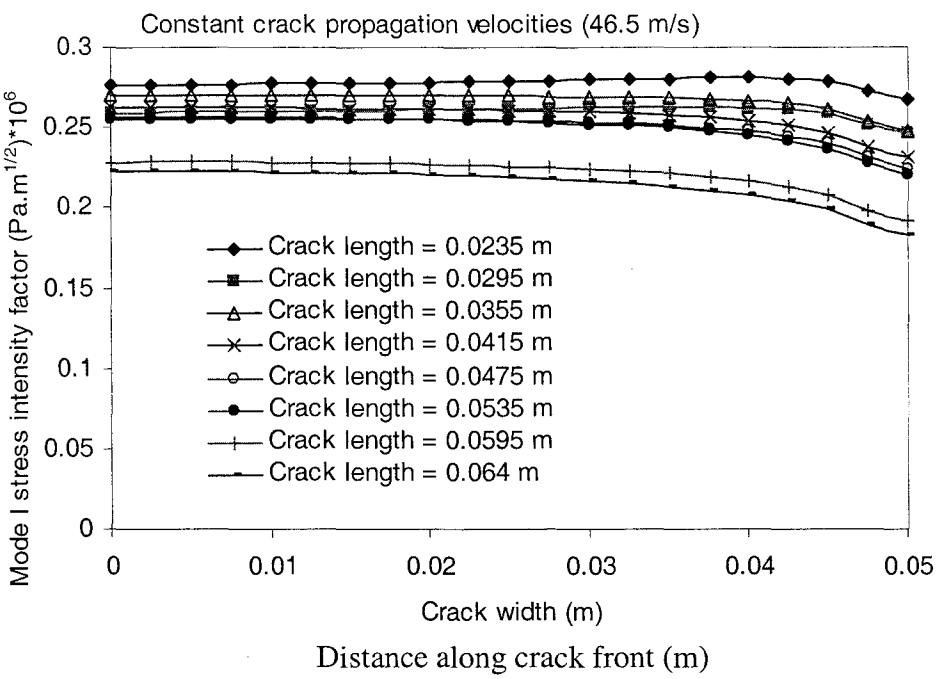

Figure 5.33: Variation of SIFs along the crack front for different time dependent crack lengths and constant crack propagation velocities.

5.4 Effect of Specimen Size on the Mode I Stress Intensity Factor of Slate Rock

Before extrapolating the laboratory experimental results for larger sized slate samples, the effect of test specimen size on the observed mode I stress intensity factor of rock needs to be established. In order to examine whether mode I stress intensity factor varies with the specimen width and depth or not, various widths and depths of slate block were analyzed numerically using ABAQUS. Analysis has been carried out in this study by keeping transverse length of the block constant (which is equal to the transverse length of the wedge) and varying width and depth subsequently. The geometry of slate block is shown in Figure 5.1. A range of widths, viz., w_1 = 0.0508 m, w_2 = 0.076 m, w_3 = 0.1 m, w_4 = 0.127 m and w_5 = 0.1524 m and depths, viz., d_1 = 0.1 m, d_2 = 0.127 m d_3 = 0.1524 m, d_4 = 0.1778 m and d_5 = 0.2 m were considered in this study. The block sizes analyzed in this study are given in Table 5.1

Table 5.1: Size of the slate blocks considered for numerical analysis

Block No.	Block Size ($L \times W \times D$)
#1	0.102 m × 0.051 m × 0.102 m
#2	0.102 m × 0.076 m × 0.102 m
#3	0.102 m × 0.102 m × 0.102 m
#4	0.102 m × 0.127 m × 0.102 m
#5	0.102 m × 0.152 m × 0.102 m
#6	0.102 m × 0.102 m × 0.127 m
#7	0.102 m × 0.102 m × 0.152 m
#8	0.102 m × 0.102 m × 0.178 m
#9	0.102 m × 0.102 m × 0.203 m

Initial crack length and element sizes were kept constant for all blocks. In all cases analyses (dynamic) were carried out by considering plane strain conditions since differences of results (mode I stress intensity factors) between plane strain and 3D analyses were within the acceptable ranges (<10%). Since depth of the specimen was assumed to be constant for variable width cases, it was found necessary to keep element dimensions constant for elements located near the crack path - 4 columns of elements in the vertical direction for each specimen. However, element numbers and dimensions were varied along the width of the specimen. The mode I stress intensity factor was determined for each increment of a crack length (0.00075 m) with a starting crack length 0.0235 m. Crack was extended up to a specimen depth 0.0655 m for each independent width of specimen. The splitting load obtained for a slate block of size 0.1 m × 0.1 m × 0.1 m was taken as the applied load for all observations.

The SIFs obtained from dynamic analysis for different crack lengths and various specimen widths, are shown in Figures 5.34 and 5.35 for a coefficient of friction equal to 0.56 and also for two different modes of crack propagation velocities (constant and linear decrease). It is seen that the variation of SIFs is not linear. It decreases nonlinearly as width increases. For a width smaller than 0.1 m, the SIF was larger than that for a width greater than 0.1 m. Since SIF is related to the splitting force linearly and also is a function of crack length and specimen geometry, it could be concluded from these observations that smaller splitting forces are required to split small width specimens; on the other hand larger splitting forces are required when widths of the specimen are increased. Also it is observed that when the width of specimen increases beyond 0.127 m, the SIF value tends to show very small increases; this indicates that to produce larger widths of slate

specimens, the required impact splitting load becomes almost a constant. During the experimental study a similar phenomena was observed in that the splitting forces increased, as width of the specimens increased, and wider samples took greater breaking loads (see Table 4.18).

The mode I dynamic stress intensity factors were also computed for various depths of specimens having same width (0.1 m) and length (0.1 m). The specimen size equal to 0.1 m $\times$ 0.1 m $\times$ 0.1 m and its breaking load were considered as a reference for the comparison of results with other sized specimens having various depths and same length and width. To maintain same element length (0.00075 m along the crack path) for all specimens, the number of elements was increased in proportion to the depth of the specimen. A crack length equal to 0.0235 m was assumed as the initial crack length for all specimens to keep similarity between the results. The variation of mode I stress intensity factors (SIF) for dynamic analyses with respect to different crack lengths, for different specimen depths, are shown in Figures 5.36 and 5.37 (coefficient of friction equal to 0.56) for two different modes of crack propagation velocities. It is seen that the trend of variation is similar for all cases and SIFs decrease is marginal as depth of the specimen increases. This indicates that the breaking load will not be greatly influenced by the depths of the rock specimens.

Some slate blocks having larger widths and depths than the reference block, were analyzed in a similar manner as plane strain analysis to determine the mode I dynamic stress intensity factor for the breaking load of 0.10m cubic block (reference block). The block sizes considered for this study were 0.10 m $\times$ 0.127 m $\times$ 0.1778 m, 0.10 m $\times$ 0.1524 m

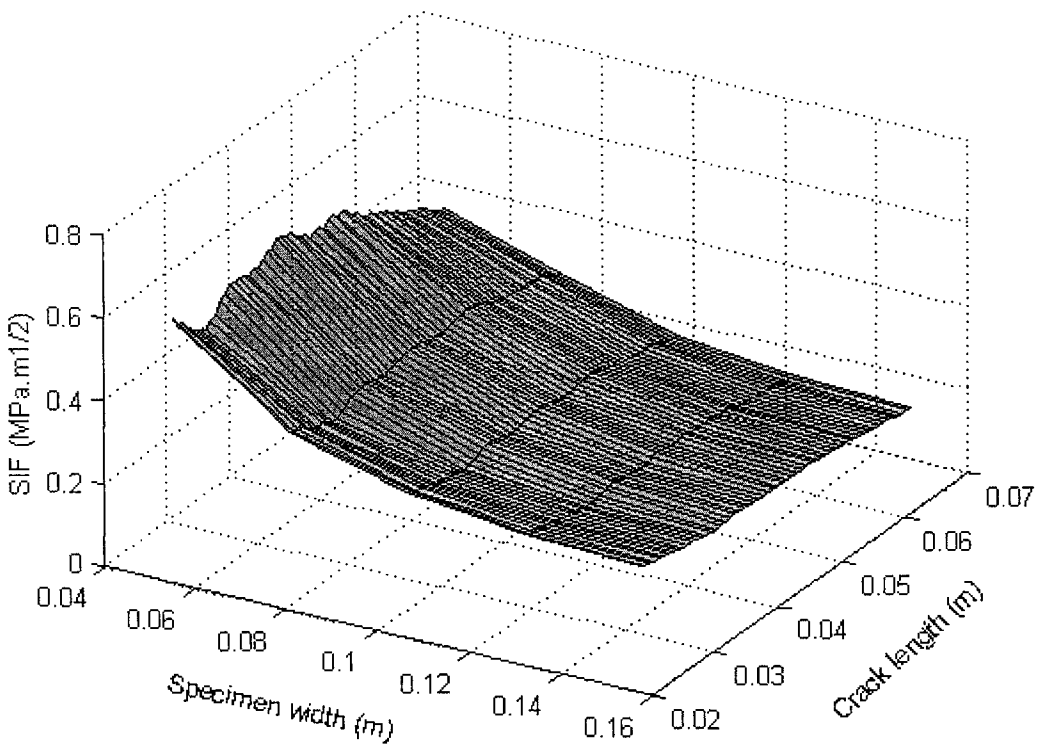

Figure 5.34: Variation of SIF with specimen widths and different crack lengths for crack propagation velocities having a linear decrease.

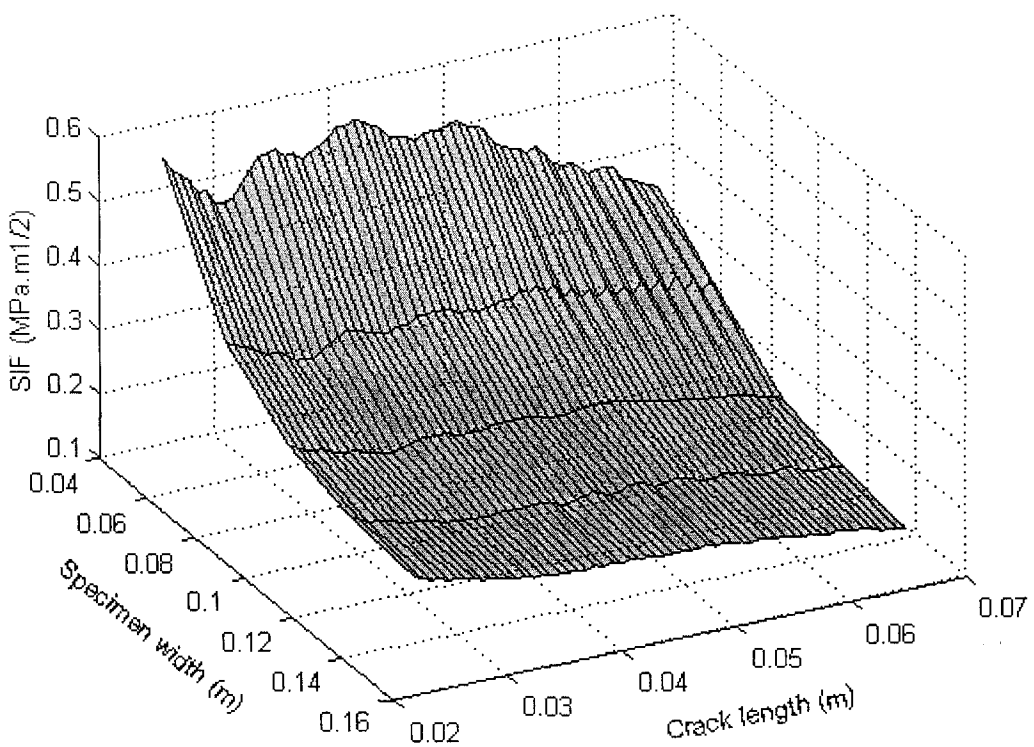

Figure 5.35: Variation of SIF with specimen widths and different crack lengths for crack propagation velocities having a constant value

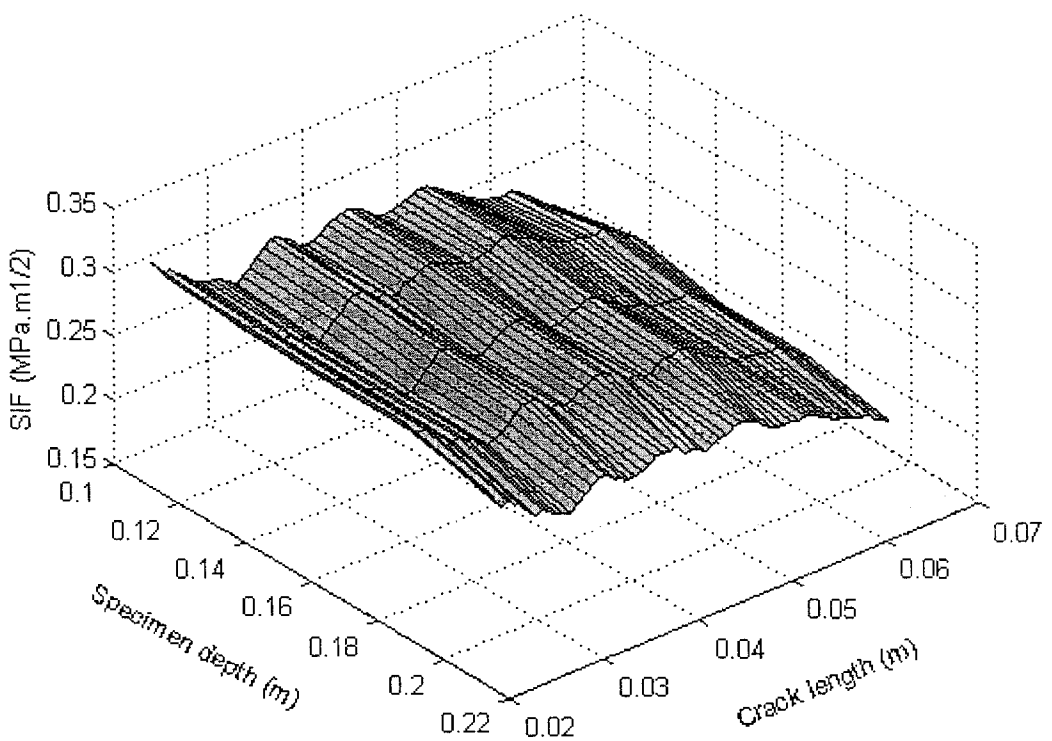

Figure 5.36: Variation of SIF with specimen depths and different crack lengths for crack propagation velocities having a linear decrease.

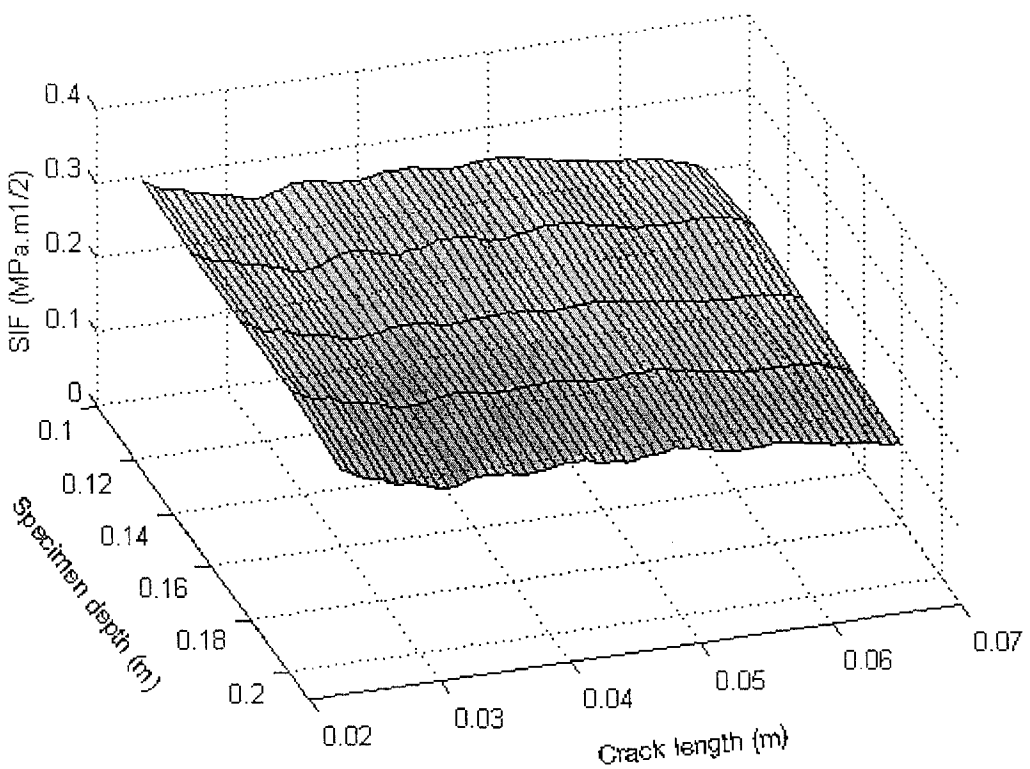

Figure 5.37: Variation of SIF with specimen depths and different crack lengths for a crack propagation velocities having a constant value

× 0.1778 m, 0.10 m × 0.127 m × 0.2032 m and 0.10 m × 0.1524 m × 0.2032 m. Width and depth were changed together from the standard 0.10 m cubic slate block (see Figure 5.3). Plane strain analysis was carried out by taking into consideration all assumptions stated earlier in this chapter. Element aspect ratio was kept constant along and near the crack propagation line (symmetry line) by increasing number of elements along the width and depth directions. Mode I stress intensity factors were determined for each block up to a crack length 0.0655 m and shown in Figures 5.38 and 5.39 for two different types of crack propagation velocities (linearly decreasing and constant). It is seen that SIFs obtained from greater blocks are less than those obtained from reference block (0.10 m × 0.10 m × 0.10 m) due to the lower impact load applied. Variation of SIFs was also not linear. As size of the slate blocks increased (> 0.1 m cube block) variation of SIF between them decreased. From this observation it could be said that SIFs vary only within a certain limit of depth and width, beyond which SIFs do not vary even though a larger and wider specimen is analyzed.

From Figures 5.38 to 5.43 it is seen that oscillation of SIFs occurred as crack extended from a crack length 0.03m to 0.054m for both constant and linearly varying crack propagation velocities. This is observed to be more in slate blocks having comparatively smaller widths (Figures 5.38 and 5.39). As widths increase this oscillation disappears gradually. It has also been observed that lesser oscillations are present in constant crack propagation cases (Figures 5.40 and 5.41) than decreasing velocity cases. Instability of the solution generally results in larger oscillations in the output variable; this was observed when the ratio of width and depth of slate blocks was less than or equal to 1.

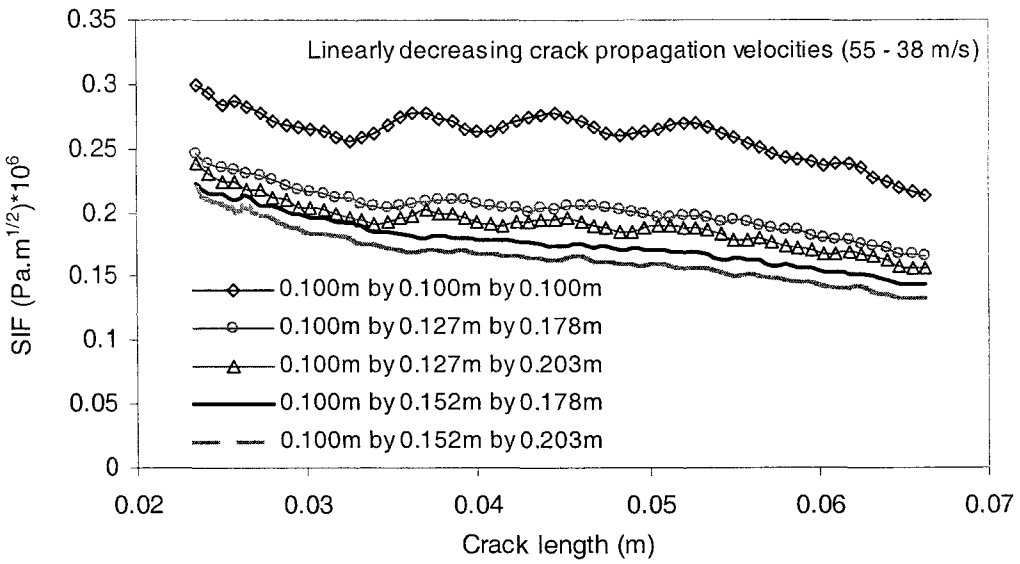

Figure 5.38: Variation of SIFs with different crack length for slate blocks having size greater than the reference slate block of size 1 cubic meter.

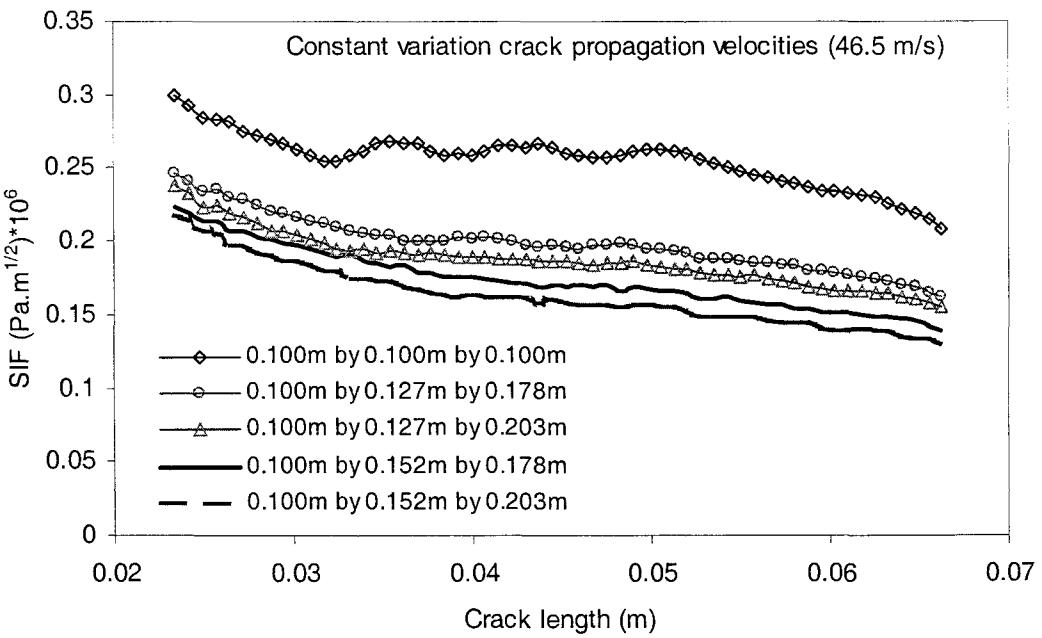

Figure 5.39: Variation of SIFs with different crack length for slate blocks having size greater than the reference slate block of size 1 cubic meter.

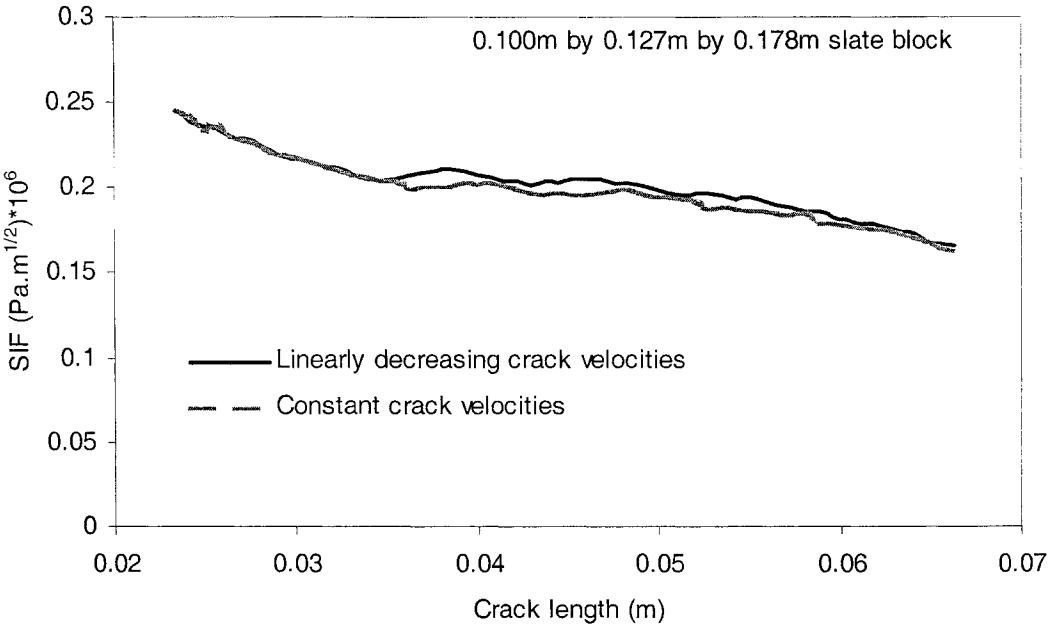

Figure 5.40: Variation of SIFs with different crack lengths for a slate block having a size 0.100m × 0.127m × 0.178m for different variations of crack propagation velocities in plane strain analyses.

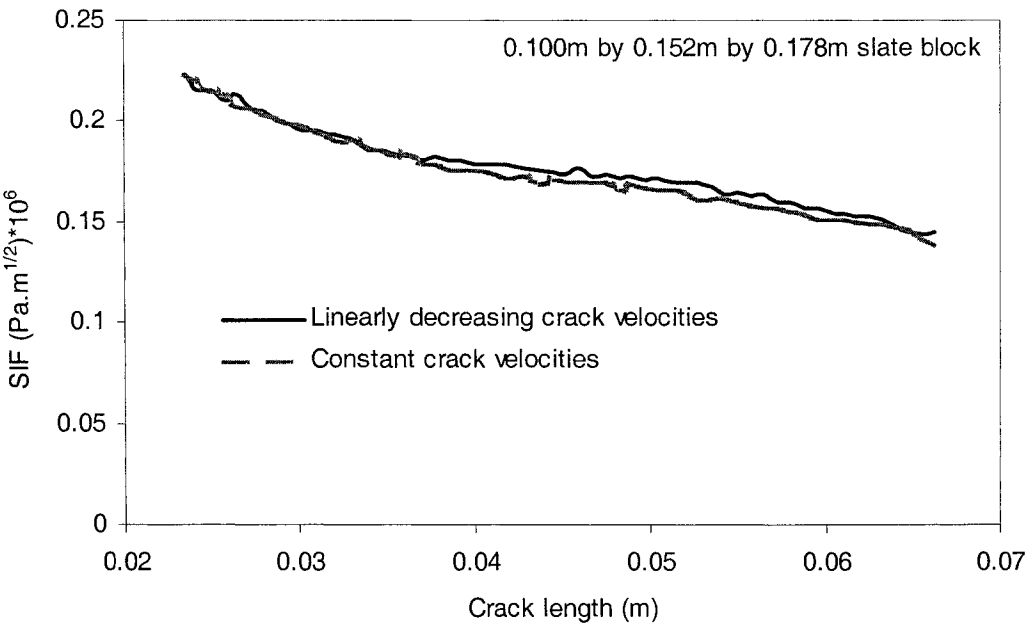

Figure 5.41: Variation of SIFs with different crack lengths for a slate block having a size 0.100m × 0.152m × 0.178m for different variations of crack propagation velocities in plane strain analyses.

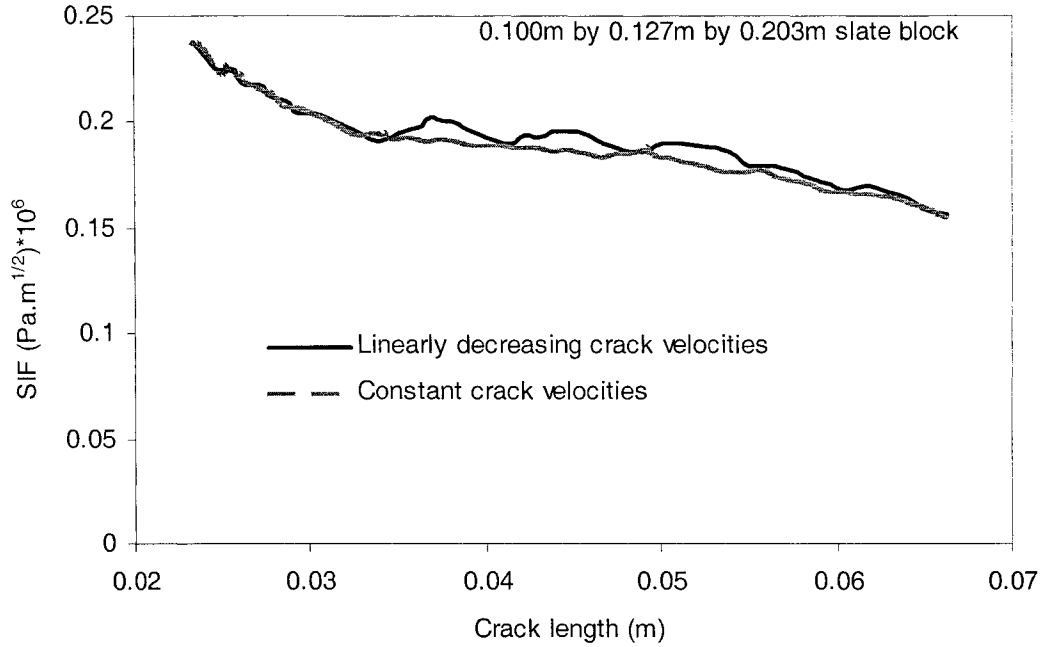

Figure 5.42: Variation of SIFs with different crack lengths for a slate block having a size 0.100m × 0.127m × 0.203m for different variations of crack propagation velocities in plane strain analyses.

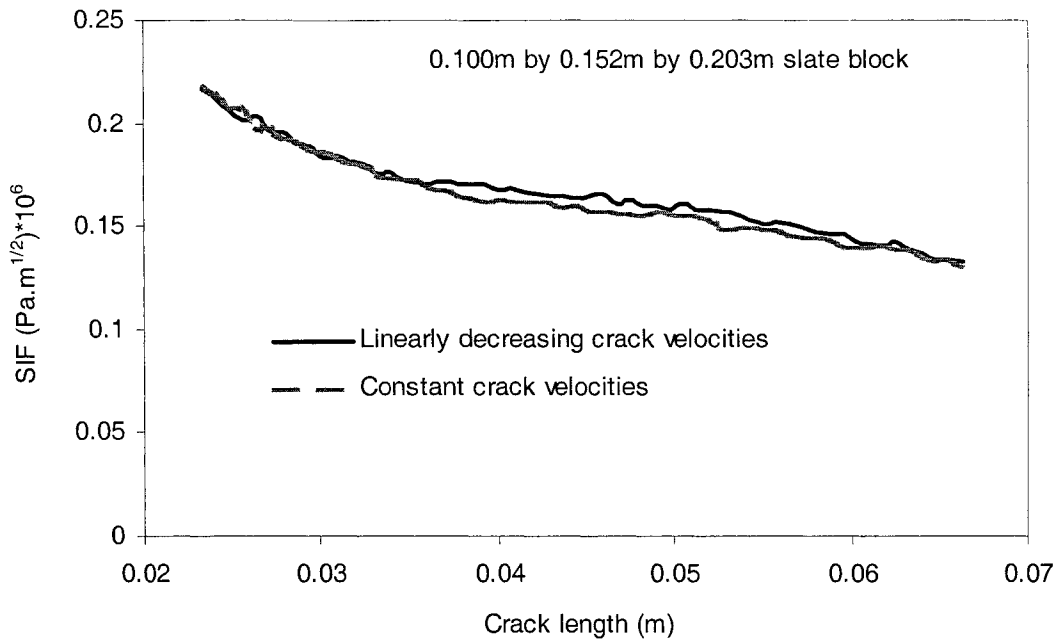

Figure 5.43: Variation of SIFs with different crack lengths for a slate block having a size 0.100m × 0.127m × 0.203m for different variations of crack propagation velocities in plane strain analyses.

5.5 Summary

In this chapter numerical analyses results based on plane strain and 3D finite element methods, were presented for a slate block having a size of 0.10 m × 0.10 m × 0.10 m and broken under a plane strain loading condition. A comparison of obtained results (stresses and mode I dynamic stress intensity factors) between plane strain analysis and 3D analysis was made. It is observed that the stresses in local 1- and 2-directions of 3D finite element analysis were much lower than those in plane strain finite element analysis; however, the SIFs were in very good agreement (<10% difference). The mode I stress intensity factors of 0.10 m cubic slate block, in the range of propagated crack lengths of 0.0325-0.0550 m seemed to agree very well with the experimentally measured static fracture toughness (0.2242 ± 0.0481 MPa.$m^{1/2}$) for both the modes of crack propagation velocities. Investigation of size effect on the mode I dynamic stress intensity factor was also carried out by analyzing different sizes of plane strain slate blocks. Results obtained for various sized slate blocks were compared with those obtained from the reference slate block (0.10 m × 0.10 m × 0.10 m).

It was observed that higher SIFs were obtained for specimens having a width less than the width of the reference slate block and lower SIFs were obtained for specimens having width greater than the width of the reference block. SIFs obtained were double (approximately) when the width of the test block decreased to half the size of reference block. SIFs also varied with the depth of the specimens but the variation was much less than the width. Variation of SIFs was less than 7.8% when depth of the block was increased to twice that of the reference block by keeping other dimensions constant. SIF

values were higher by 10% for linearly decreasing crack propagation velocities than those for constant crack propagation velocities for both plane strain and 3D analyses.

Chapter 6

Numerical Analysis of 3D Slate Block having a Transverse Length greater than the Transverse Length of the Indenting Wedge

6.1 General

Plane strain and 3D finite element analyses of slate blocks, broken experimentally under plane strain conditions (transverse length of the block was equal to the transverse length of the wedge), were analyzed in the previous Chapter 5. However, the prevalence of plane strain conditions for rock breaking process is rather a rare event. In reality, different sizes of slate blocks would be generated during the impact splitting procedure and in most of the cases, sizes of slate blocks would be greater than the transverse length of the impacting wedge. Also the loading area or extend of line load would be much smaller than the length of slate rock over which the impact load is applied. This leads to a three-dimension loading condition. Therefore, it is necessary to analyze large slate blocks numerically as well. In the present chapter, numerical analysis of slate rocks that have larger transverse lengths than the indenting wedge was carried out for simulating the experimental splitting process.

6.2 Modelling and Prediction of Crack Growth in 3D Structures

When a plane crack propagates along the vertical impact plane by maintaining same depth of penetration in the transverse direction for each time, it is comparatively easier to model the crack propagation in finite element analysis. However, when crack propagates both in horizontal and vertical directions in the same plane from the starting point, it is difficult to model the crack growth in a simple manner, since it is hard to trace the locations of crack trajectory inside the body with respect to time and find the shape of crack growth. Many researchers have modelled crack propagation in 3D structures using different techniques. Popelar (1980) developed a simple one-dimensional mathematical model for rapid fracture and crack arrest in a double-torsion fracture specimen. Mikkola, et. al. (1990) proposed an easy implementation procedure and the consequent results by developing a fracture assessment program including automatic fracture analysis for structures using three dimensional (3D) finite element models. Krueger (1999) developed a shell/3D modelling technique to simulate delaminations in composite laminates, by using 3D solid finite element in the local region in the vicinity of the delamination front (extending to a minimum of about three specimen thickness in front of and behind the delamination front) and shell or plate finite elements for the global structural model. He used multi-point constraints to provide a kinematically compatible interface between the local 3D model and the global structure modelled by shell/plate elements. He computed mixed mode energy release rate across the width using nonlinear finite element analyses using virtual crack closure technique for a simple double cantilever beam; the fixed end was notched. He used both shell/3D elements in his modelling procedure and compared

his results with a full 3D analysis to examine the accuracy of the developed procedure. He obtained very good agreement with full 3D analysis results.

The prediction of crack growth for 3D models under various modes of loading has been made in many studies for a number of years (Martha, et. al. 1990, Cook, et. al. 1990, Remzi, et. al. 1990, Shephard, et. al. 1985). In most of the above cases the prediction techniques were limited to crack growth within a small region of a model. Very few researchers have analyzed large scale crack growth in a real body. Browning, et. al. (2001) predicted large scale crack growth in 3D finite element models. They presented a new method for automatically predicting large scale crack growth in a 3D finite element model by allowing the crack front to move through the model. They analyzed the spinning test of a cracked compressor disc of a turbine engine with a single edge notch crack, which was quarter circular shaped at the corner. During the spin test analysis they also included the presence of a high level of plasticity and the effect of crack closure. They used Timbrell, et. al. (1994) concept to insert a crack into a 3D model for fatigue crack growth analysis using ABAQUS finite element software; the crack was modelled to grow in a quarter-circular manner. Timbrell et. al. carried out their job using the joint application of ABAQUS and ZENCRACK commercial software. They used ZENCRACK as an interface to ABAQUS. At first they generated the finite element mesh in ABAQUS format for the uncracked component.

The mesh plot and properties for their analysis were generated properly, containing the necessary loading data, boundary conditions and material specification. This was done using conventional methods. They stated that the mesh could consist of any element type,

but must also contain 20 noded brick elements in the region(s) which holds the crack(s). To generate the crack front(s), they replaced one or more of these brick elements by 'crack-blocks'. They reported that these crack-blocks were meshes of brick elements which were mapped onto the original element space and properly joined with the surrounding mesh. Their technique had several advantages. One of the advantages was that the user can directly control the initial crack orientation and size. Timbrell et. al. transferred boundary conditions and loads to the crack-block elements and a modified J-INTEGRAL option was generated (presently contour integral option is used to obtain desired outputs such as J-integral, stress intensity factor, etc.). They mentioned that, if required, this updating procedure can be used to apply pressure loading in the crack region, including the crack face. After completing the mesh, the analysis was done by ABAQUS. However, they processed results of the modified J-INTEGRAL evaluations by ZENCRACK and a new crack front position was calculated based on user defined crack growth criteria. The mesh was automatically modified to contain this new crack position and a further ABAQUS analysis was carried out. They continued this procedure until user specified limits on crack growth was reached. The entire procedure is shown in Figure 6.1. This technique was not used in the present study due to unavailability of ZENCRACK software in the available workstation. The method (node release technique) used to model dynamic crack propagation in the earlier plane strain and the associated 3D analyses was also used to simulate dynamic crack propagation in the present case.

The distribution of maximum energy release rate and SIF along the crack fronts having various shapes such as circular, semi-elliptical and elliptical have been determined in many earlier studies. Timbrell (1994) showed that the maximum energy release rate along

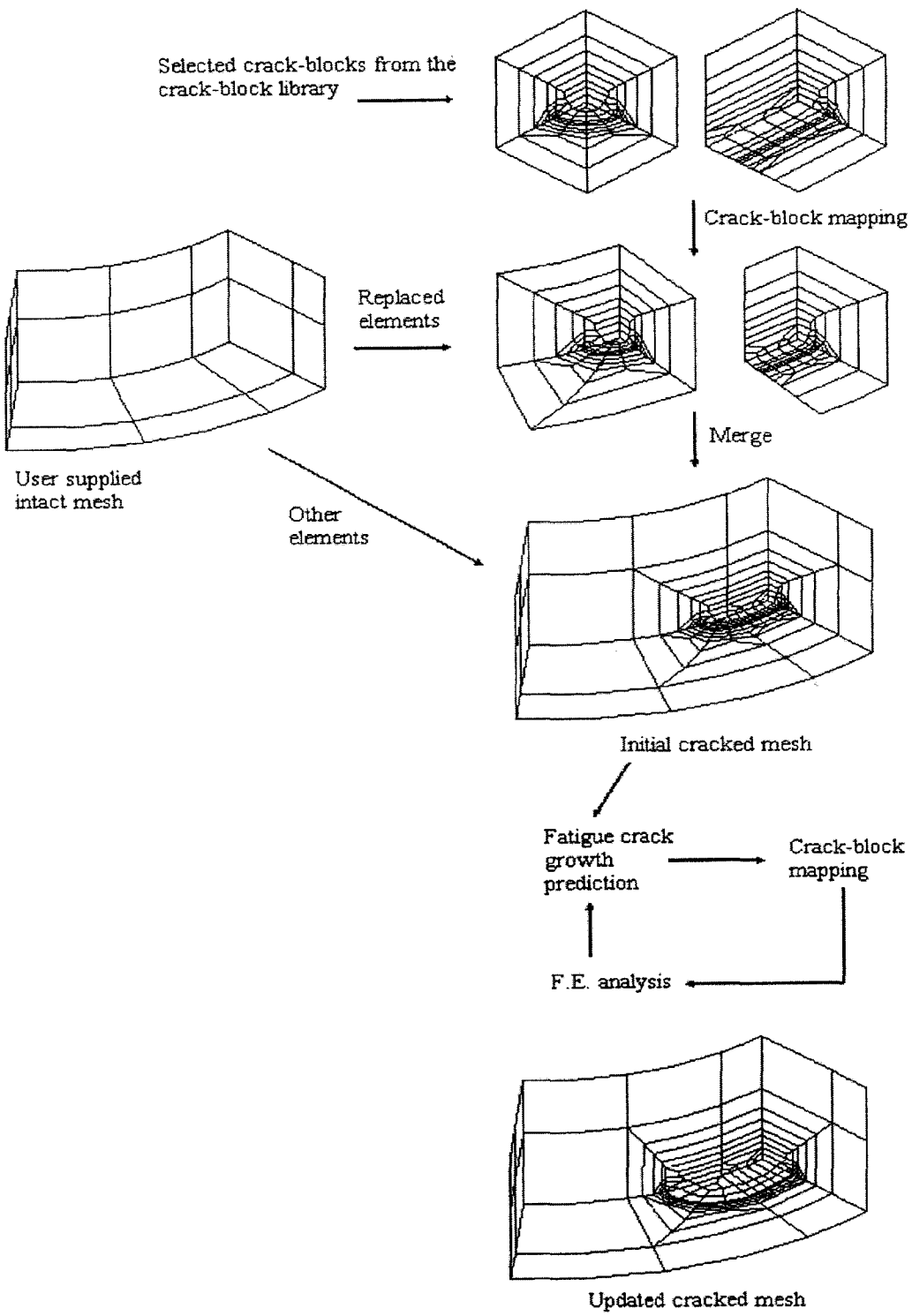

Figure 6.1: Summary of crack insertion and mesh updating procedure (Timbrell, et. al. 1994)

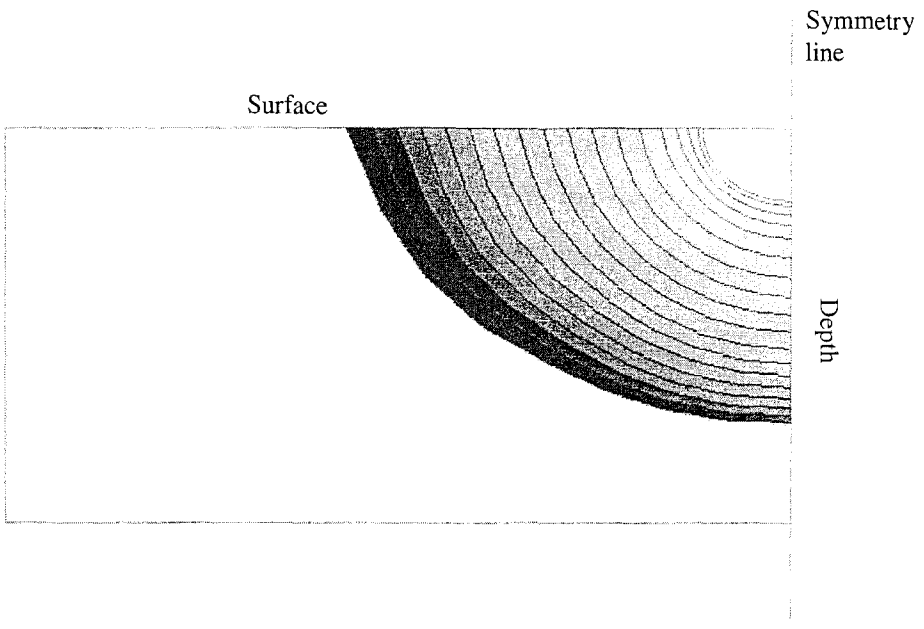

Figure 6.2: Planar crack growth pattern for an initial semi-elliptical defect in a bar under uni-axial tension. (Timbrell, et. al. 1994)

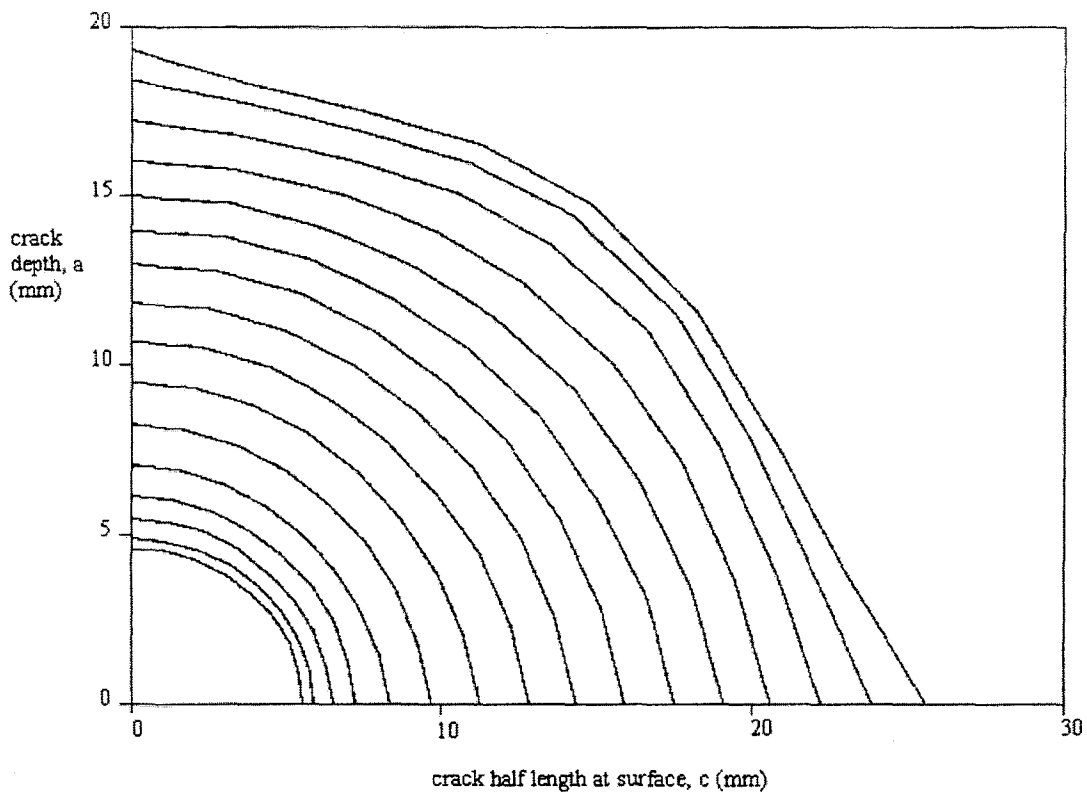

Figure 6.3: Fatigue crack growth development of an elliptical crack (Cook, et. al. 1990)

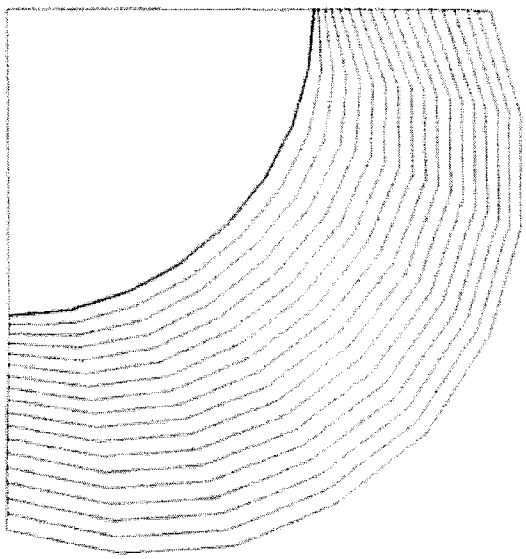

Figure 6.4: Plastic crack growth ring starting from a quarter circular corner crack in spin test (Browning, et. al. 2001).

the crack front will be a maximum at 0^0 and 90^0 and will be minimum at 45^0 (angles were measured around the crack front) for a quarter circle crack front. He also gave the planar crack growth pattern for an initial semi-elliptical defect in a bar under uni-axial tension (Fig. 6.2). Cook, et. al. (1990) used the semi-elliptical fatigue crack growth pattern (Fig. 6.3). Browning, et. al. (2001) used a quarter-circular plastic crack growth ring starting from the quarter circular corner crack in a spin test (Fig. 6.4).

In the present study, neither quarter circular nor elliptical shaped starting crack showed equal mode I stress intensity factor along the crack front under wedge loading. Therefore a starting crack having parabolic shape was considered to model dynamic crack growth under wedge impact loads.

6.3 Finite Element Modelling and Processing of Results

Finite element analysis was carried out to investigate the splitting process of a typical slate block having the size of 0.330 m × 0.254 m × 0.147 m as shown in Figures 6.5 (a) & (b). This block was first split in the laboratory applying impact force through the wedge shape indenter [whose transverse length (0.1 m) was less than the transverse length of the specimen]. The responses (force and crack propagation velocities) obtained from the laboratory test were used to calculate the numerical responses (such as, stresses and stress intensity factors) using the finite element procedure. The assumptions concerning the material, damping and wedge penetration used for plane strain and 3D analyses of slate blocks in Chapter 5 (section 5.2.2) were taken to be the same for this case also. Due to symmetry in structural geometry and loading conditions with respect to the planes 1-2 and 2-3 (shown in Figs. 6.5 (a) & (b)), only one quarter of the entire system was modeled. Even though crack propagation was not always obtained exactly symmetrical with respect to the wedge impacting position in plane 2-3 (see Figures C-16 to C-20 in Appendix C) for most of the experimental splitting cases of slate blocks, it was assumed in analyses that the crack propagated along a parabolic (approximately) crack front in a symmetric manner under the wedge edge PQ [see Figure 6.5 (a)].

The entire body was discretized using eight-noded linear brick elements and six-noded wedge elements. Although these elements are only linear and not singular (second order 20-noded elements would be better for crack tip singularity), it would be shown to provide acceptable results because of the small sizes of elements used and due to the use of path independent contour integrals for SIF computation. A non-uniform mesh was introduced by employing relatively fine mesh along the crack front and contact planes,

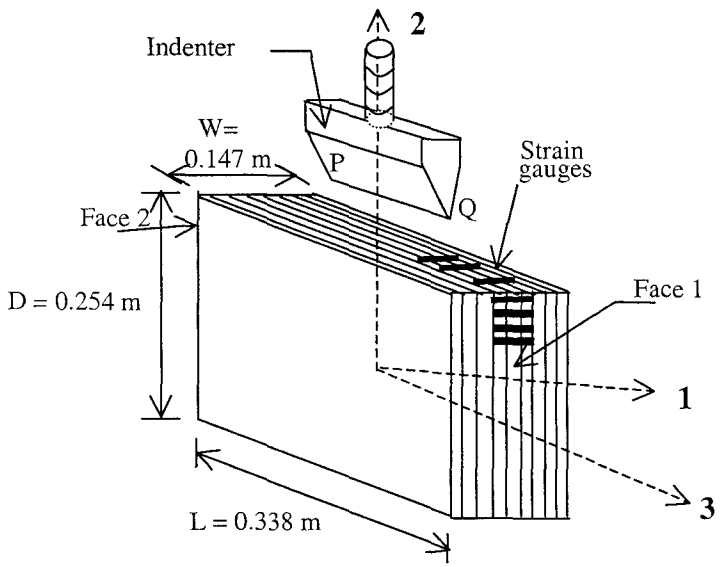

Figure 6.5 (a): Typical slate block with impacting wedge and strain gauges.

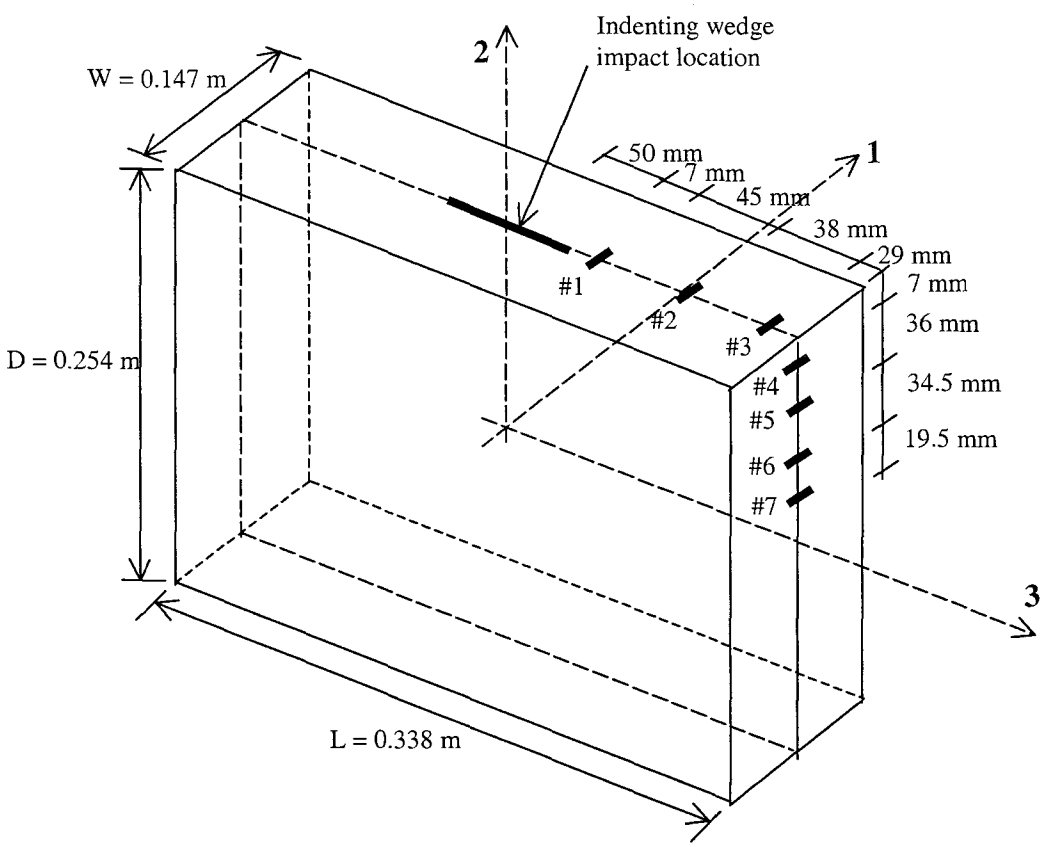

Figure 6.5 (b): Details strain gauges layout on slate block

and a coarse mesh away from these critical zones. Wedge penetration was assumed to be 0.005 m in the beginning of the analysis.

Initially, a 2D parabolic plane crack of length equal to 0.080 m along the local 3-direction and 0.0514 m along the local 2-direction was considered to be present in the body (the shape of the crack surface was the sector of a parabola in 2-3 plane). To obtain the desire shaped of crack front of propagating crack, three different shapes of crack front such as quarter circular, semi-elliptical and parabolic were taken into consideration for obtaining the variation of mode I stress intensity factor along the crack front. Parabolic shaped crack front with aspect ratios (between minor and major axes) of 0.64 to 0.76 showed almost equal variation of SIFs along the crack front. The assumed crack propagation path and the number of elements used are shown in Figures 6.6 and 6.7.

Since all the experimental test specimens broke almost in a vertical plane, the crack was set to propagate along the same vertical plane during the numerical simulation. Finite element discretization was done by following the crack propagation path in a sequential manner. The finite element mesh of one-quarter of the slate block along with wedge indenter is shown in Figures 6.8 (a) & (b) and 6.9 (a) & (b). Load was considered to be acting as distribute loads at a height equal to double the wedge penetration depth above the tip of the wedge. The intensity of the distributed load was determined by dividing the load obtained from the earlier experiment (shown in Figure 6.10) by the area of the wedge present at a height 0.010 m from the tip of the wedge.

During the experimental studies crushing of material was observed at the beginning of wedge penetration, due to very high contact pressure developed at the contact surface (between the wedge tip and slate block) within a very short time (of impact), a crushing width equal to 2.50 mm (1.250 mm on either side of the symmetry plane) was introduced at the wedge location. That width was reduced gradually to a point within a distance 6.0 mm from the vertical edge of the wedge (shown by AB on Figure 6.9 (b)). Crack front was considered to vary a parabolic manner and all crack front nodes were defined along that path. For each step of the extension of the crack along the splitting plane a new line of crack front was obtained and similar parabolic variation of crack front was considered. However, the variation of parabola was gradually changed to a straight line at the bottom of the specimen (shown in Figure 6.8 (b)).

When wedge impacted on the specimen, the material directly under the wedge started to crush first and then split the entire block gradually through the crack growth. The load measured through data acquisition system was the total load required for the complete

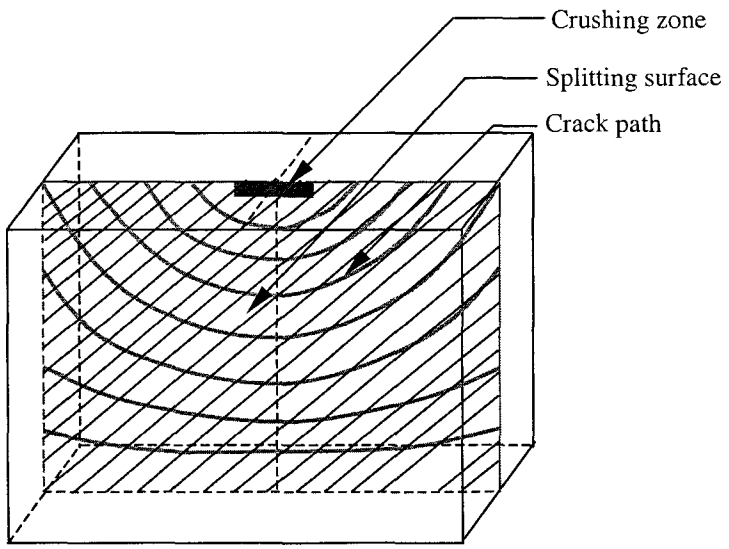

Figure 6.6: Assumed crack propagation pattern (during 3D finite element analysis) in the typical slate block during impact splitting of slate block.

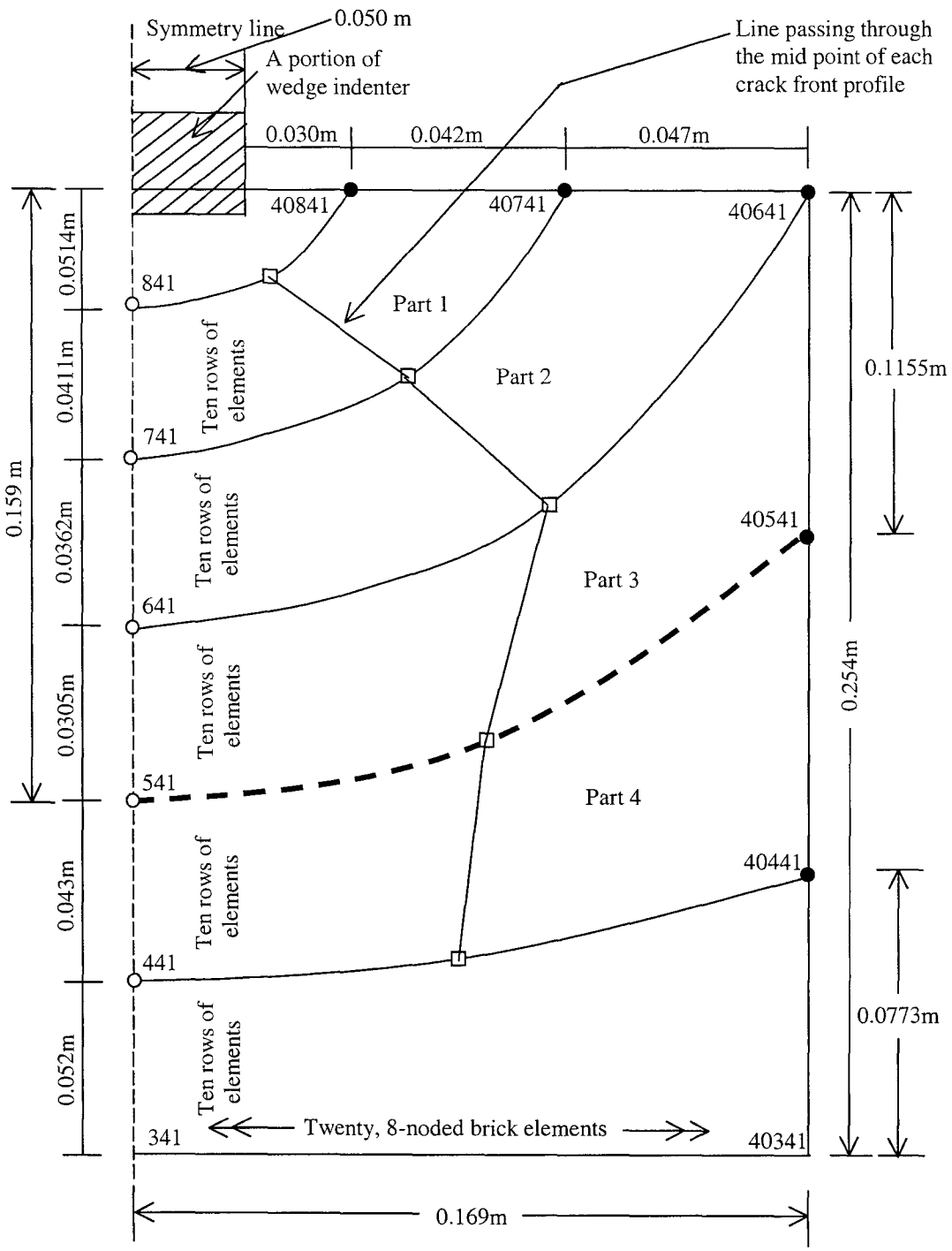

Figure 6.7: Subdivision of crack plane (and its geometric dimensions) into a number of regions suitable for mesh generation

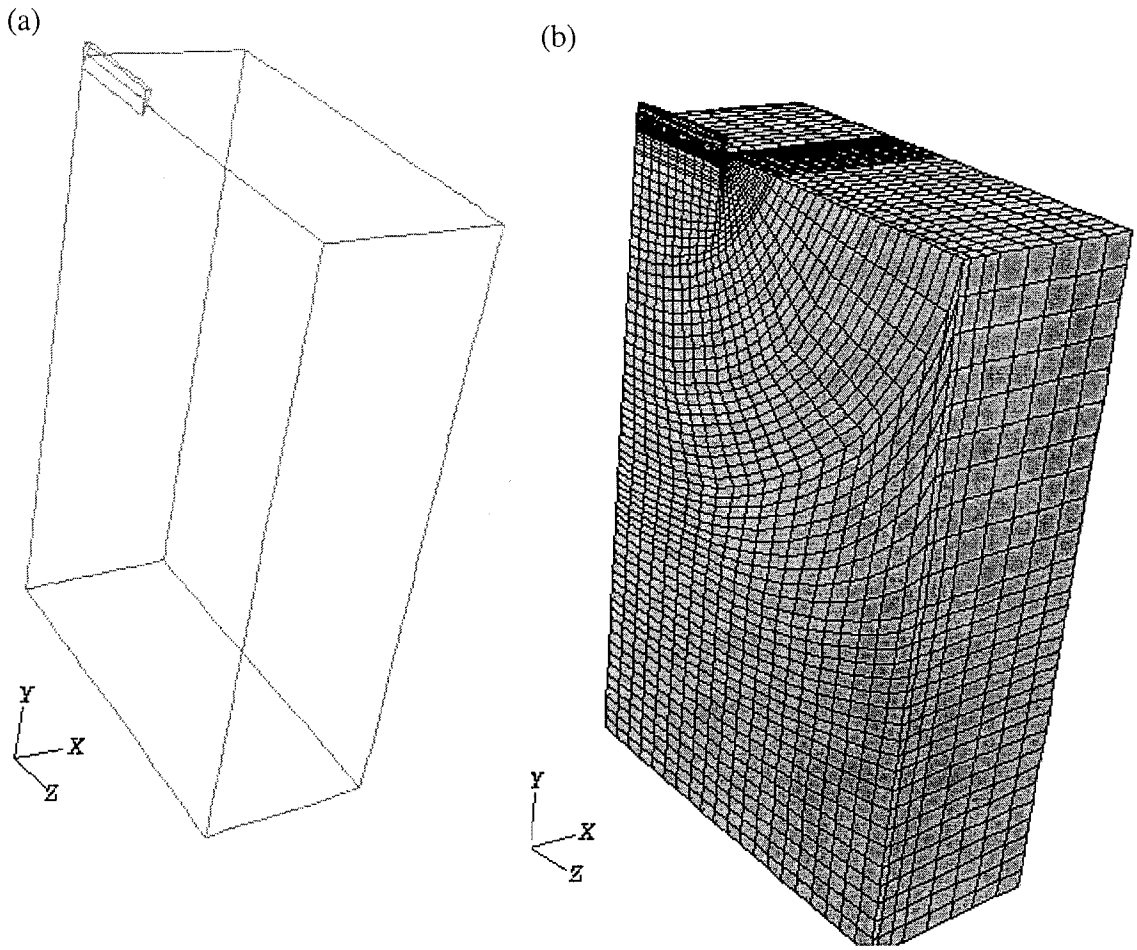

Figure 6.8: (a) One-quarter of the slate block; (b) Finite element discretization of the same block shown in Figure (a), using eight-noded brick elements and six-noded wedge elements.

(a)

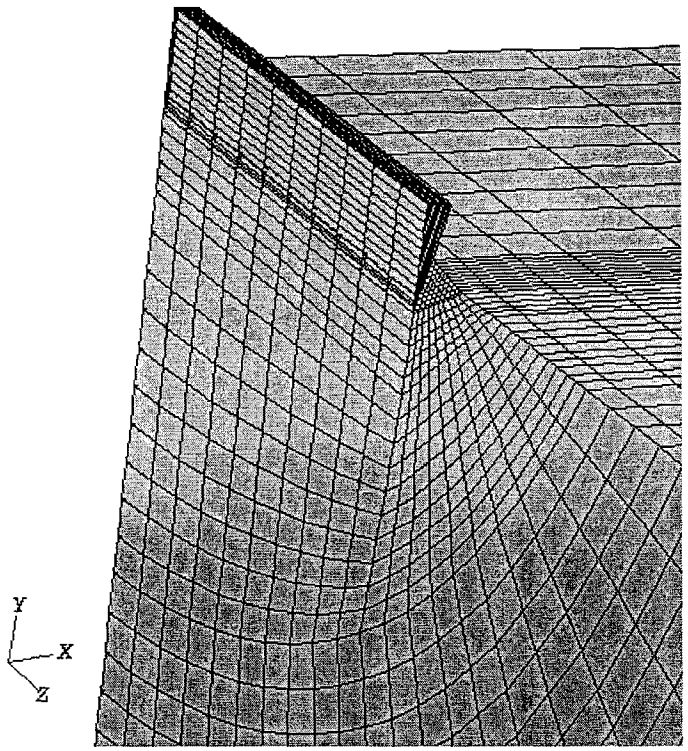

(b)

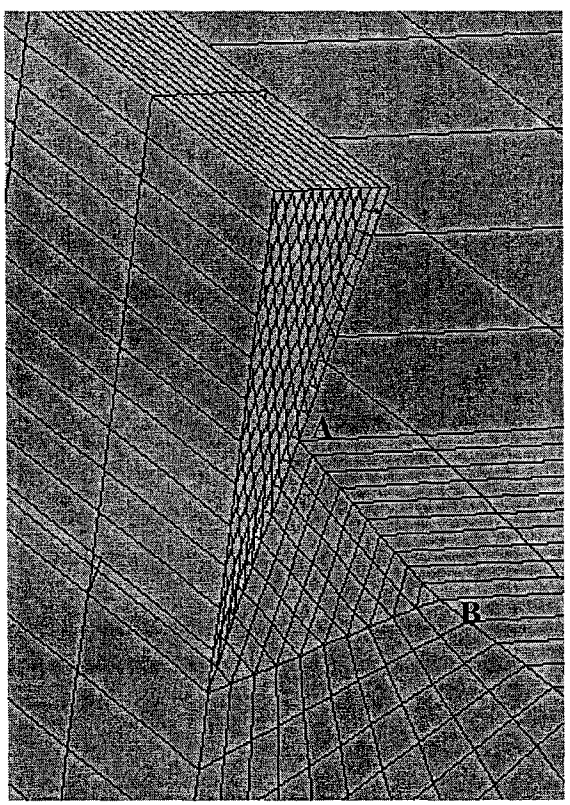

Figure 6.9: Finite element mesh: (a) closer to the interface of slate block and wedge; and (b) at the contact surface of wedge and slate block.

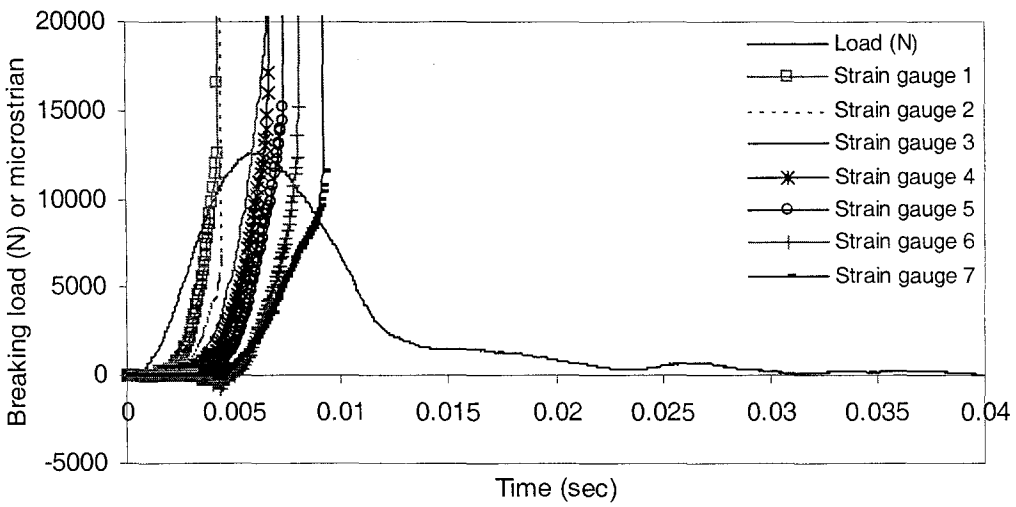

Figure 6.10: Variation of breaking load and microstrain with respect to time during impact splitting of a slate block having the dimensions, L = 0.338 m, H = 0.254 m and W = 0.147 m considered for finite element analysis.

breakdown of the specimen. It included the load that was needed to crush the impact interface of the specimen as well as the load required to propagate the crack through the specimen. The magnitudes of the splitting load required to reach the crack location at various strain gauge points attached to the specimen were obtained from the measured load-strain gauge readings shown in Figure 6.10. First crack tip (on the impacting surface) was considered at a distance equal to 22 mm ahead of the second strain gauge point (2^{nd} strain gauge was fixed at 52 mm away from the vertical edge of the wedge) since the first strain gauge was located very close to the impacting location which could be a point of stress concentration. The magnitude of the load at the location of the 2^{nd} gauge was obtained as 95% of the maximum load, ahead of the peak value (see Fig. 6.11). Initial crack tip load was determined after extrapolating the load from the load obtained at the 2^{nd} gauge location. A load equal to 0.90 times the peak value was considered as the initial crack tip load. From the load vs. strain gauge readings variation

diagram (Figure 6.10) it is observed that peak value of the load was attained after the propagating crack reached the third strain gauge which was fixed at 29 mm ahead of the right upper corner of the splitting block.

For crack propagation velocity it was assumed that the peak value of the load occurred at the junction of the horizontal and vertical exterior surface planes. A relatively slow crack propagation velocity having a piecewise constant variation over the strain gauge intervals was assumed before and after the peak load as shown in Fig.6.12. Velocity variation with respect to crack length on the horizontal surface and on the vertical edge (up to the region of analysis shown by the dotted line in Figure 6.7) is shown in Figure 6.12. It is seen that when crack tip travels along the outer surface on the vertical plane, to a vertical depth equal to 0.1155 m, it also travels 0.15925 m along the symmetry line in the vertical 2-direction (see Figure 6.7). At this crack front, crack has already propagated to more than half the available crack plane area of the slate rock. The load acting on this crack front (30^{th} crack front) obtained from the measured load vs. strain gauge results, shown in Fig. 6.11, is 64% of the peak load.

Though it was easy to determine crack propagation velocities on the outer surface of the specimen, the initial crack length, profile and crack propagation velocity in the interior of the body were assumed based on the almost constant variation of stresses and mode I stress intensity factors along the crack front. Trial method was used for this purpose. Trial was continued by considering different ratios of horizontal to vertical lengths of parabolic crack front (with an applied static load) until a uniform variation of SIF was obtained along the crack front. A limiting aspect ratio between 0.64 to 0.76 for different positions

of crack front showed the variation of SIFs along the crack front to be less than 20%. Therefore, crack front parabolas were introduced in the model with an aspect ratio varying between 0.64 –0.76.

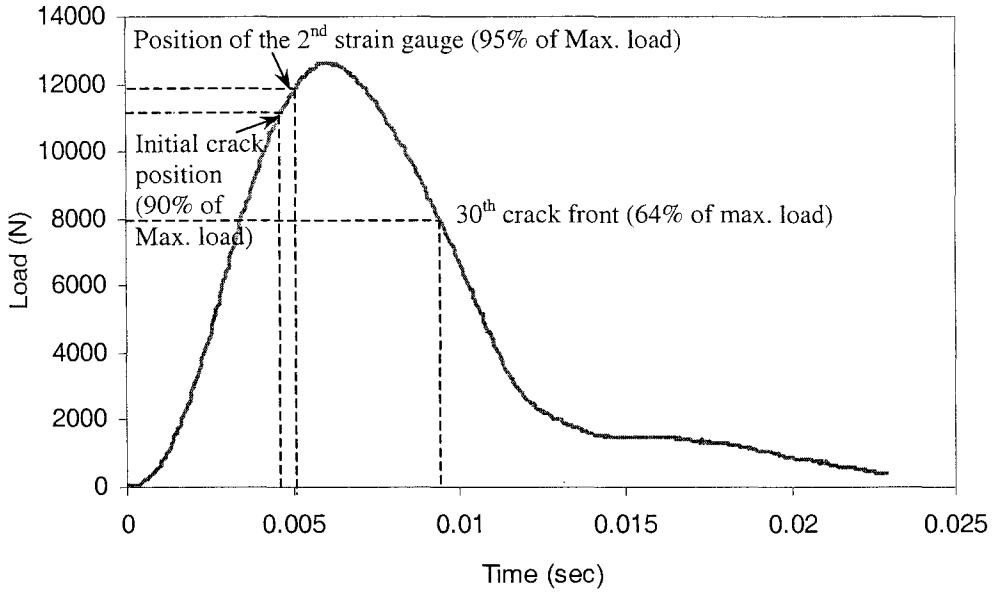

Figure 6.11: Variation of impact splitting load with respect to time

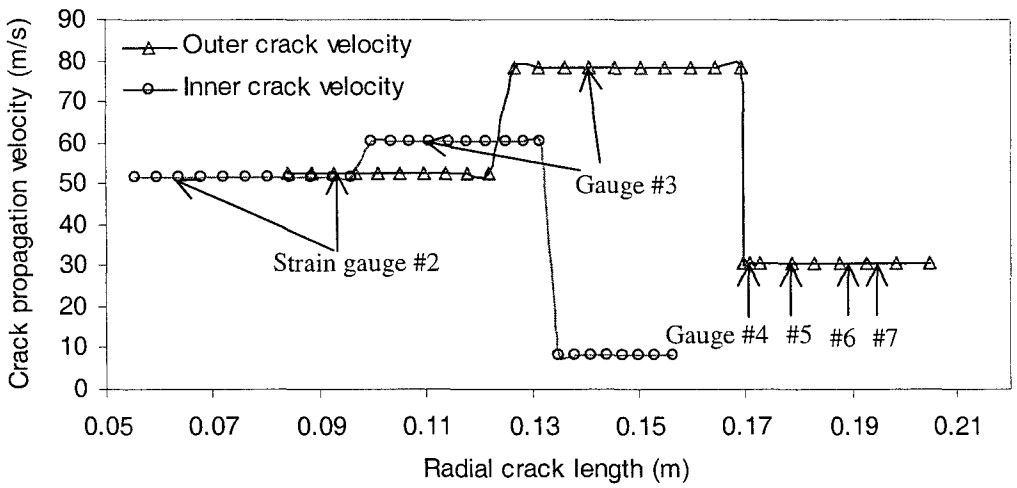

Figure 6.12: Variation of assumed crack propagation velocity with radial crack length

Due to the restriction of internal processing memory of ABAQUS software and the large number of degrees of freedom used to discretize the slate block, test platform and base of the platform (concrete floor) were not taken into consideration in the three-dimensional finite element model. The extent of the model was reduced by restraining all vertical 2-axis direction degrees of freedom, and allowing all the horizontal displacements at all nodes on the bottom surface of the specimen.

Proper constraints were applied to represent the symmetry conditions assumed. In order to do this all the local degrees of freedom in direction-3 or z [perpendicular to the plane 1-2 (x-y) in Figures 6.5 (a) and (b)] for all nodes on plane 1-2 were restrained. In addition, all the local degrees of freedom in direction-1 of all nodes that exist in the plane of symmetry 2-3 (or y-z) (except those above the crack front) were also restrained. Sequential node release technique was applied to simulate in-plane dynamic crack propagation. All nodes along the crack front were released together at the same time for the next advancement of the crack.

Contour plots of stresses in local 1-direction (along with the used boundary conditions) at every five intervals of crack extension are shown in Figures 6.13 – 6.16. It is seen that the maximum tensile stress in local 1-direction develops along the crack front as the 2D plane crack propagates with respect to time on the crack plane 2-3. The crack (with a parabolic variation) propagates from the center of the block to the outer periphery of the block and tries to maintain equal SIF values along the crack front as it travels through the depth of the block. It was assumed to have the same SIF value for all nodes along the crack front even after propagating through the entire distance along both the horizontal

and vertical directions. Therefore, outer surface crack tip is assumed to have propagated faster than the interior radial one (see Figure 6.12). Velocity also varied along the crack front by giving higher velocities at the outer surface and lower velocities at the interior points. This velocity variation was obtained due to different sizes of elements along the crack front. The initial crack velocity at a location very close to the wedge (30.0 mm away from the vertical edge of the indenting wedge) on the outside top surface of the block was computed as 52.5 m/s. However, velocity at the first crack tip element at the interior point of the block was 51.0 m/s. The velocity variation of crack propagation along the interior vertical 2-direction and outer periphery were shown earlier in Figure 6.12. This variation was maintained at the exterior and interior of the regions of interest. In the present analysis the region of interest (shown in Figure 6.7) was more than 50% of the total vertical splitting plane area from the beginning of the split. The total region of interest was divided into 3 parts. Each part consisted of 10 rows of elements having equal row width. Each row also consisted of 21 elements. Therefore, over a part of the region of interest, element width (inside as well as the outside of the block) was kept constant. At the outer face of the block, element widths were varied from 0.0042 to 0.0115m and at the interior of the block it varied from 0.003 to 0.0043m.

From the earlier analysis of the slate block under in plane strain and 3D conditions, it was observed that stress intensity factors were influenced very less by the choice of linearly decreasing or constant velocity condition. For this reason, in the present problem, splitting analysis was carried out only for piecewise constant velocities (assumed) for crack propagation in the slate block (see Fig. 6.12).

Mode I stress intensity factors were computed using ABAQUS finite element software and ABAQUS calculates it through CONTOUR INTEGRAL option along the crack front nodes. In order to verify the tension force at the crack tip node, mode II stress intensity factors and sign of mode I stress intensity factor were examined. Mode II stress intensity factors were obtained as zero and mode I stress intensity factor were obtained as + ve for each step of crack growth.

Local stresses in 1- and 2- directions of all nodes along the crack front were also determined (shown in Figures 6.17 and 6.18) and magnitudes were also compared. Since the applied load had two components, viz., in directions 1 and 2, its effect in direction-1 was tension (due to bending) and in direction 2 was due to the combined effect of bending and compression. Therefore, it was expected to develop similar stresses along the crack tip nodes in local direction 1 (tension) and tension & compression in direction 2. This variation is seen in the stress plot in local 1- and 2- directions along the crack front for different crack locations (see in Figures 6.17 & 6.18).

It is observed that along the horizontal plane on the top of the specimen, stresses (local 1-direction) increased gradually along successive crack fronts (but was less than the interior point) up to the corner where vertical and horizontal planes intersected. Stresses in local 1-direction on the outer surface of the vertical plane increased up to a certain depth and then decreased again. Applied load and crack length increased gradually from the beginning of crack propagation till the right upper corner of the block was reached; thereafter the load decreased and crack length growth increased. Once crack started to propagate along the vertical plane the crack propagation direction was not normal to the crack front (along which the maximum velocity occurred). For this reason the rate of crack growth started to decrease again. At the

interior of the crack plane (along the symmetric line) the variation of stresses in local 1-direction was less than 20%.

Crack front nodal stresses in directions 2 and 3 were the resultant effect of loading components and Poisson's effect. It could be either tension or compression or a combination of these along the crack front. The variation of stresses in local 2-direction is shown in Figure 6.18. It is seen that the stress increased gradually in the interior of the specimen as crack propagated. However, stresses in direction-2 were obtained to be almost zero for a crack extension up to the upper right corner due to the absence of traction force in local 2-direction along the horizontal boundary. Thereafter, compressive stresses dominated at the outer vertical edge of the specimen.

Stresses in local 1- and 2- directions along the symmetry line and the outer periphery for different crack extensions are shown in Figures 6.19 to 6.22. A consistent variation of crack tip stresses is seen in Figures 6.19 & 6.20. However, inconsistent variation of stresses is seen in Figures 6.21 & 6.22. This is due to boundary and sudden change of outer crack tip position after 21^{st} increment of crack.

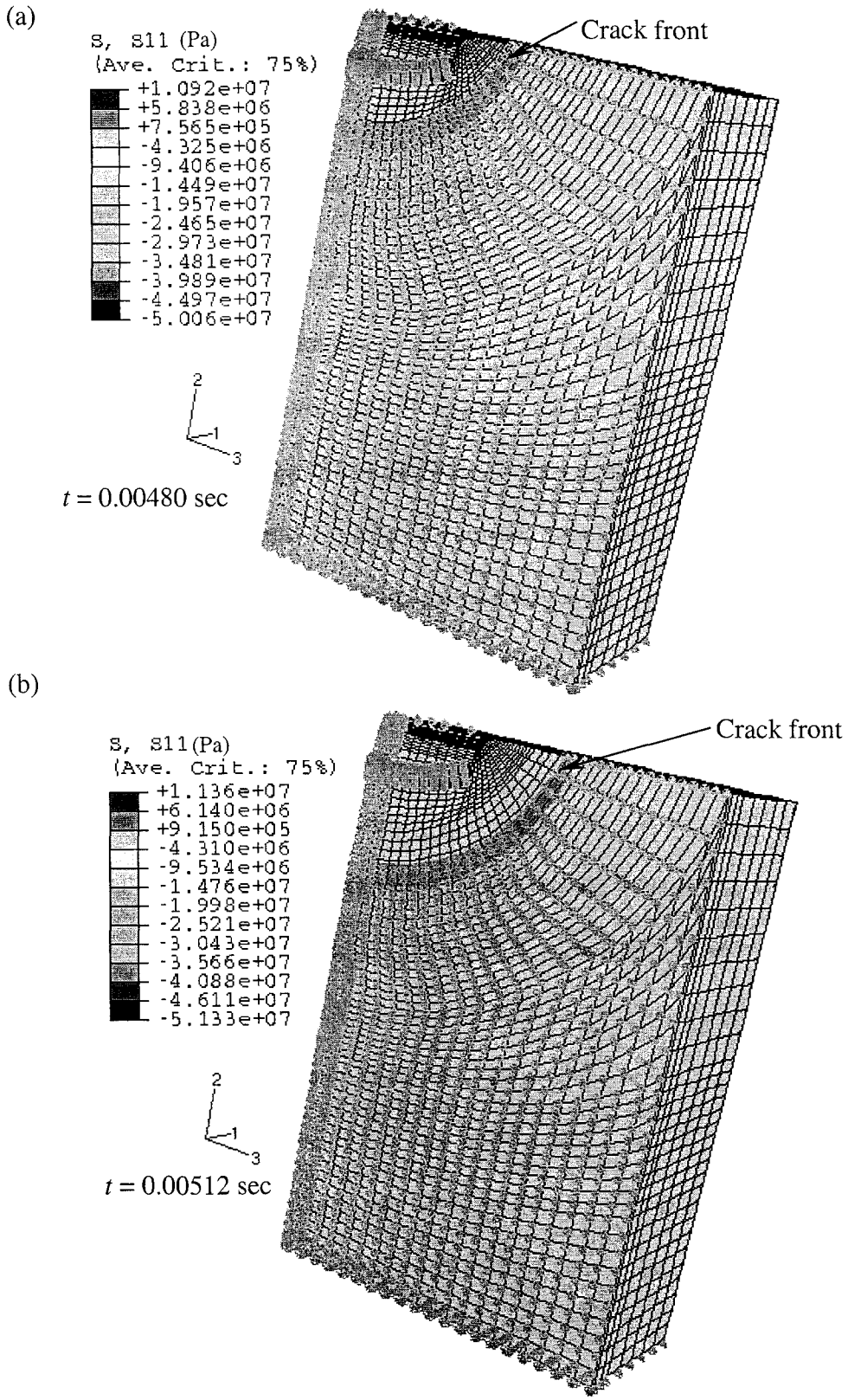

Figure 6.13: Distribution of stresses (in Pa) in local 1-direction at: (a) 1st crack front; and (b) 5th crack front.

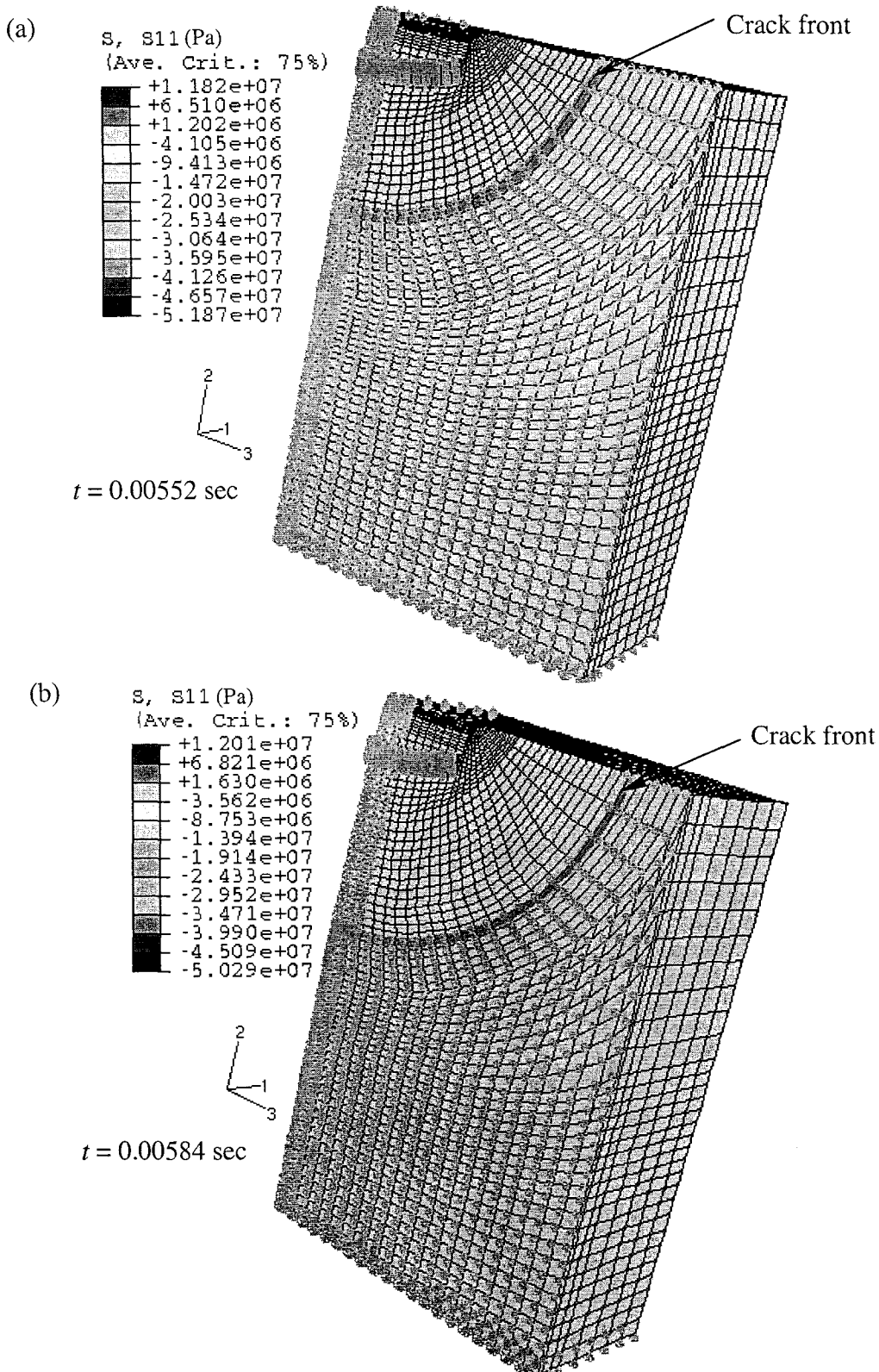

Figure 6.14: Distribution of stresses (in Pa) in local 1-direction: (a) 10th crack front; and (b) 15th crack front.

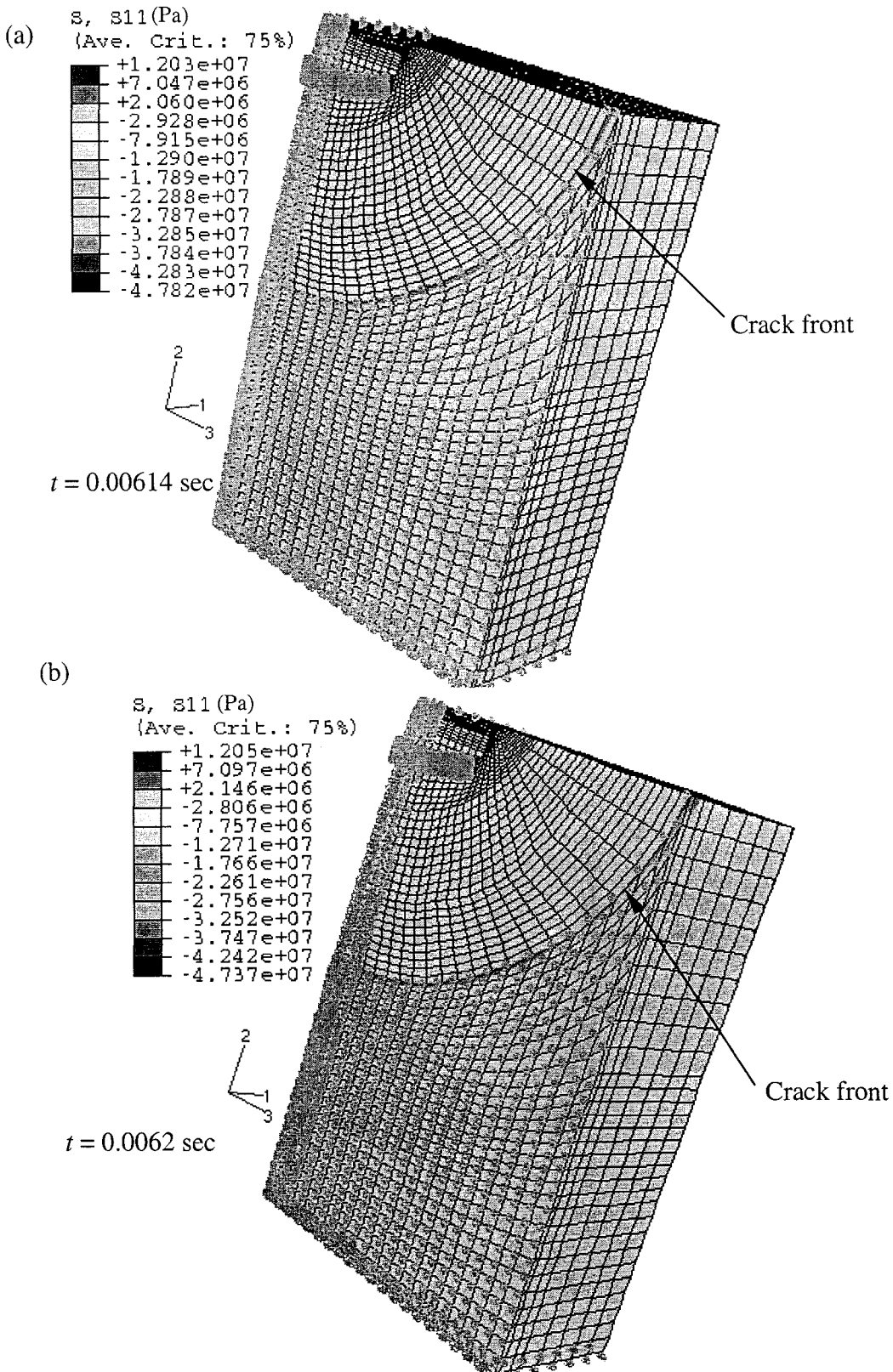

Figure 6.15: Distribution of stresses (in Pa) in local 1-direction at: (a) 20th crack front; and (b) 21st crack front.

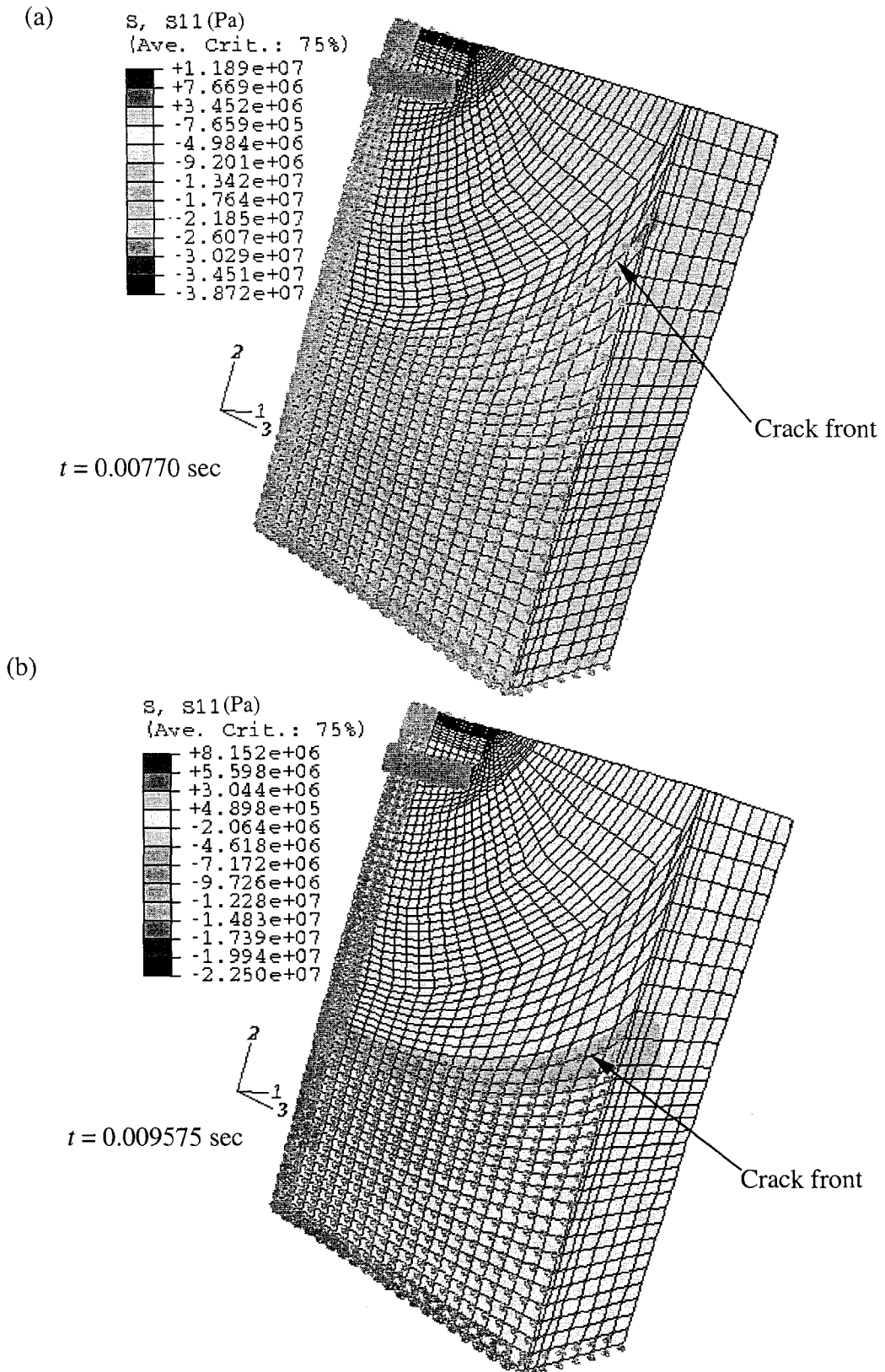

Figure 6.16: Distribution of stresses (in Pa) in local 1-direction at: (a) 25th crack front; and (b) 30th crack front.

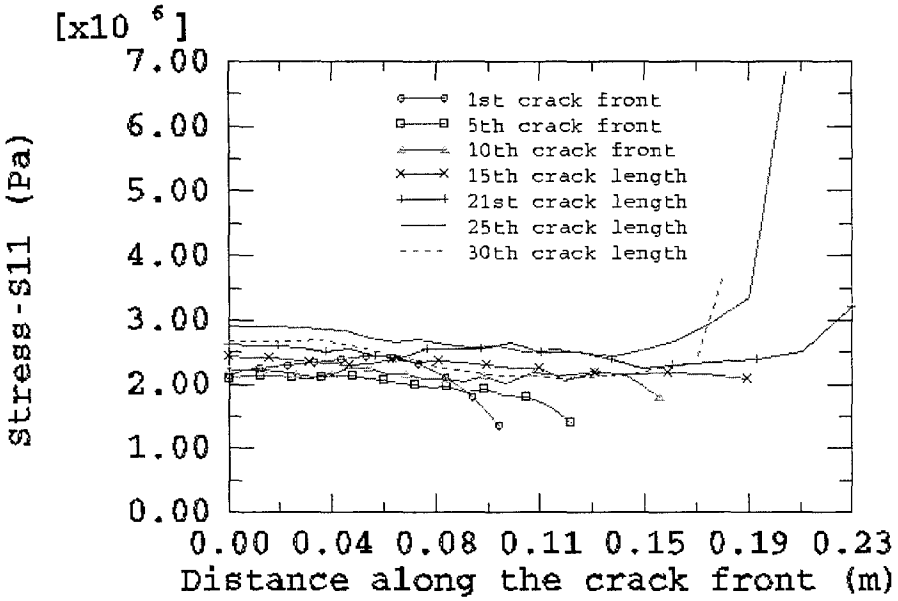

Figure 6.17: Variation of stress in local 1-direction along the crack front for various lengths of crack as plane crack propagated along symmetry plane.

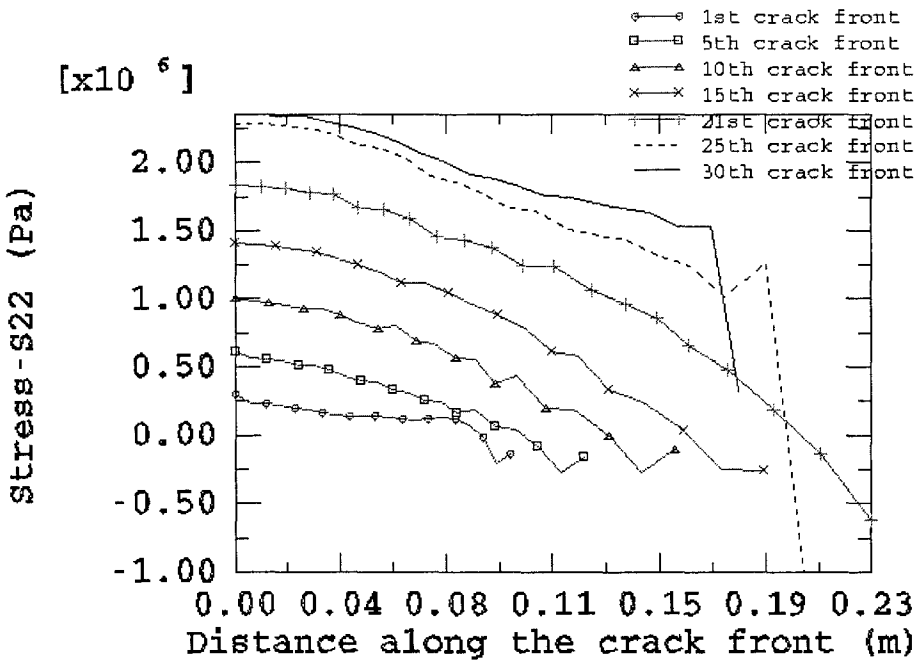

Figure 6.18: Variation of stress in local 2-direction along the crack front for various lengths of crack as plane crack propagated along symmetry plane.

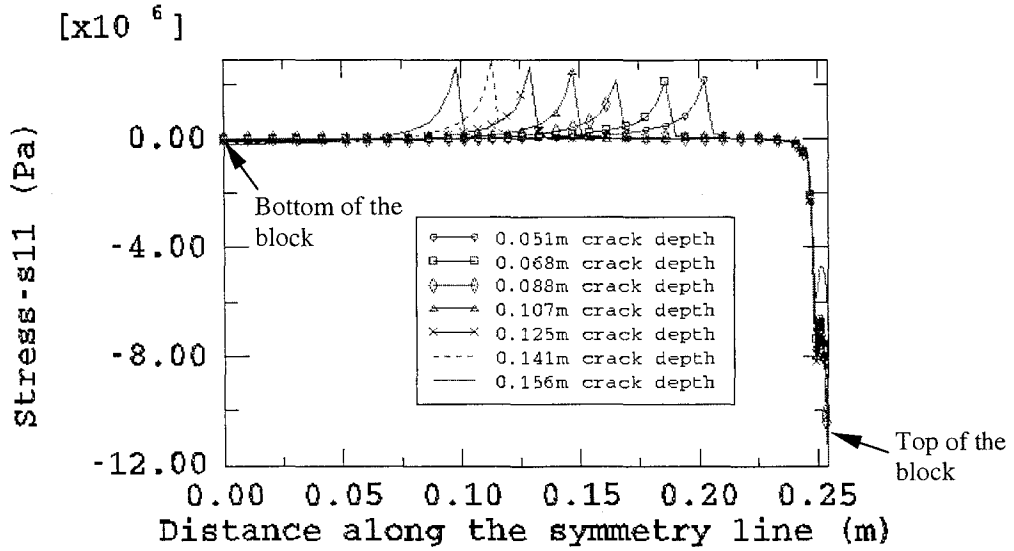

Figure 6.19: Variation of stress in local 1-direction along the symmetry line of the specimen in the vertical direction (along the interior boundary).

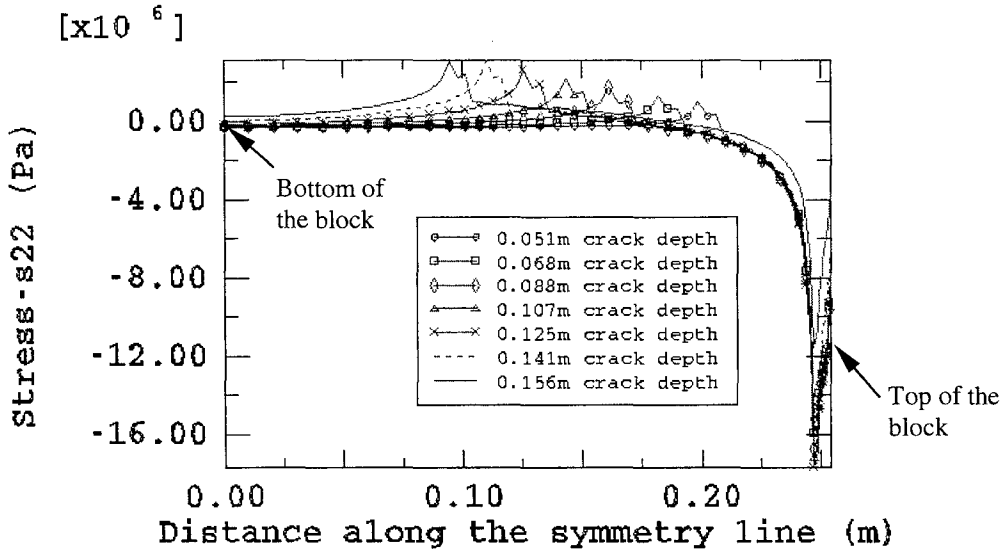

Figure 6.20: Variation of stress in local 2-direction along the symmetry line of the specimen in the vertical direction (along the interior boundary).

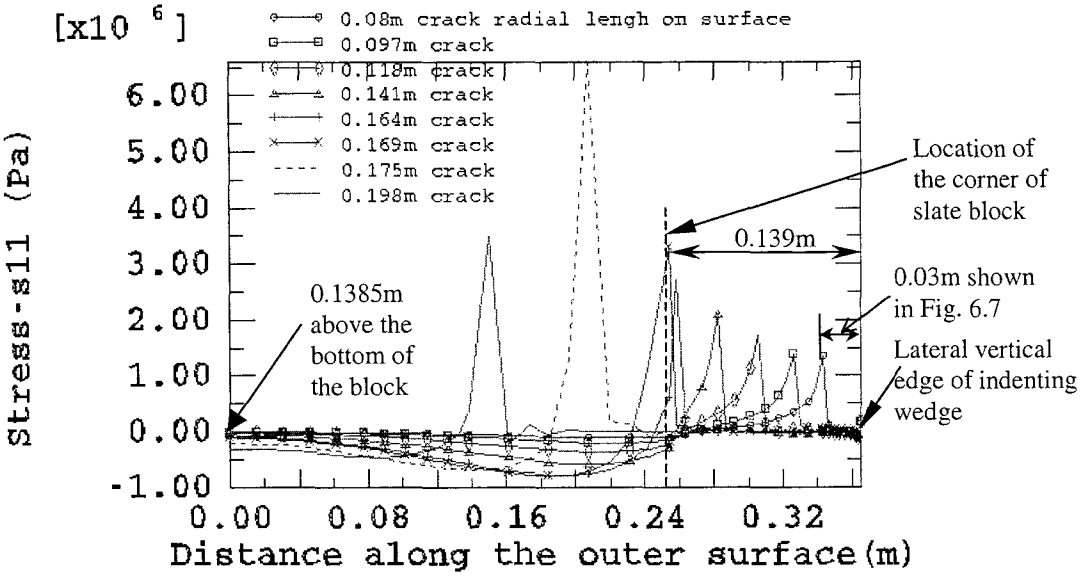

Figure 6.21: Variation of stress in local 1-direction along the outer periphery of the specimen.

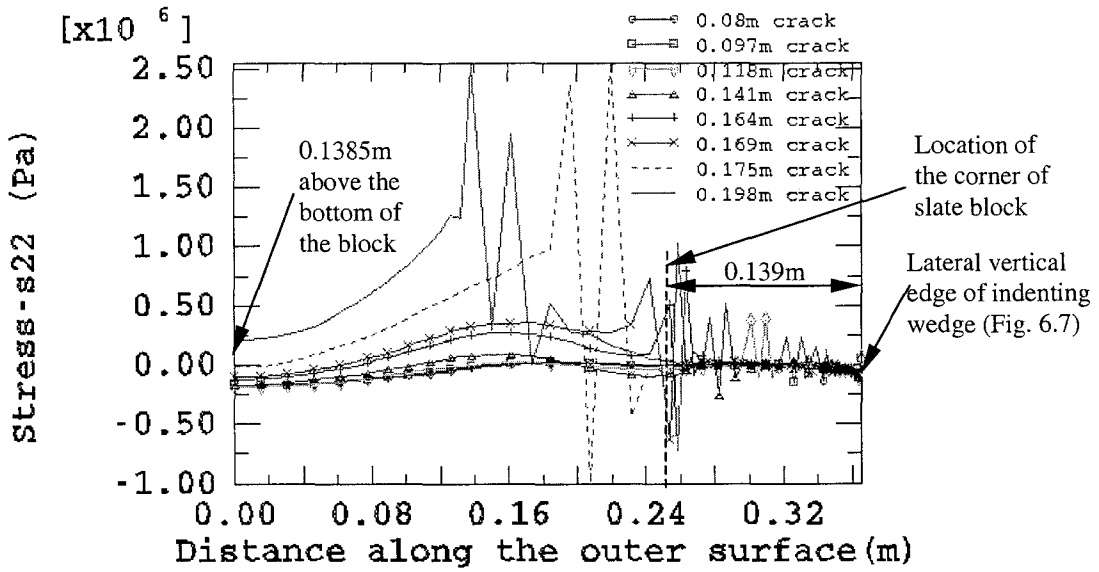

Figure 6.22: Variation of stress in local 2-direction along the outer periphery of the specimen.

6.4 Crack Growth Prediction

Contour integral option available in ABAQUS finite element software was used to determine the stress intensity factors along a crack front for the propagation of the postulated crack front (see ABAQUS keynote user manual 6.3). In order to verify the tension force at the crack tip node, mode II stress intensity factors and sign of mode I stress intensity factor were examined. Mode II stress intensity factors were obtained as zero and mode I stress intensity factors were obtained as +ve for each step of crack growth. Since the model is quarter symmetric, only one side of the crack was modelled. During the analysis ABAQUS assumed the direction of the crack growth at each node on the crack front to be in the crack plane and normal to the crack front. The complete linear elastic growth prediction consisted of 30 crack positions as crack advanced.

The variation of load with respect to time, up to the region of interest (30^{th} crack front position) is shown in Figure 6.23. Variation of mode I stress intensity factors (SIF) with respect to time at first, middle, 20^{th} and last nodes of each crack front (including 30 crack positions on the crack plane 2-3 as crack front changed with respect to time) are shown in Figures 6.24 to 6.27. It is seen that SIFs vary irregularly at each crack front node as crack progresses with respect to time. However, the SIF of each crack front node increases up to 23^{rd} increment of crack length for first and middle crack front nodes and up to 26^{th} increment of crack length for the last crack front node; thereafter it starts to decrease slowly. The decrease of SIF at the 30^{th} crack position from its maximum value was less than 19%. On the other hand load decrease was obtained as 36.4%. From this observation it could be mentioned that SIFs are not only dependent on the external loading but also on other factors such as crack length and crack propagation velocity.

From the initial crack front to position of the 21st crack front (where the load reached its maximum value and surface crack points turned their directions from the horizontal to vertical edge) maximum SIFs increased in an irregular manner in the first crack front node (Figure 6.24). Thereafter the SIF decreased up to 10th crack front and then increased and decrease in the middle crack front node (Figure 6.25). It increased almost linearly in the outer surface nodes (Figures 6.26 & 6.27). However, variation of SIFs was similar for the crack front positions between 22nd to 30th, as shown in Figs. 6.24 and 6.25. The irregular variation of SIFs at the beginning of the crack propagation occurs due to the node release procedure adopted in the solution.

The variation of reaction force with respect to time at the outer periphery node of each crack front itself and at different positions crack front was shown in Figure 6.28. It is seen that reaction force increases linearly as the previous node is released in the node release technique applied in finite element software to simulate dynamic crack. It could also be said that ABAQUS software allows force to be released in a linear manner from the released node. The cross symbol line indicates the turning point of crack from the horizontal surface to the vertical edge.

Mode I stress intensity factors (SIF) for each node along the crack front was determined at every 5 increments of crack length along the propagation direction (crack front is given in Figure 6.7). This variation of SIFs is shown in Figure 6.29. From Figure 6.29, it was observed that the variation of SIFs along the crack front at each five increments of crack depth were similar except the outer surface nodes. The magnitude of SIFs varied within 15% of their average values. SIFs were also plotted at the first node, middle (11th node)

and outer surface point (21st node) of each crack front along the vertical plane and shown in Figures 6.30 to 6.32. It is seen that the variation of stress intensity factors is not exactly similar to those obtained earlier for plane strain equivalent 3D analysis. A difference of around 15% was observed up to a crack extension of 0.4 times the depth of specimen along the symmetry line (Figures 5.29 and 6.30). However, variation of SIFs was much more when the crack extended beyond this. In this case propagation of crack was different from those occurring in the plane strain equivalent 3D problem as crack path needed to travel in both horizontal and vertical directions. The differences in SIF values between maximum and minimum in Figures 6.30 and 6.31 were less than 20% and 25%, respectively. The probable reason for these gradual variations of SIFs may be attributed to variation of crack path (from a parabolic curve to another form of a curve) with respect to time and the change in crack velocity. From Figure 6.32 it is seen that SIF decreased by more than 50% of the average value at the position of crack front where horizontal surface and vertical edge met.

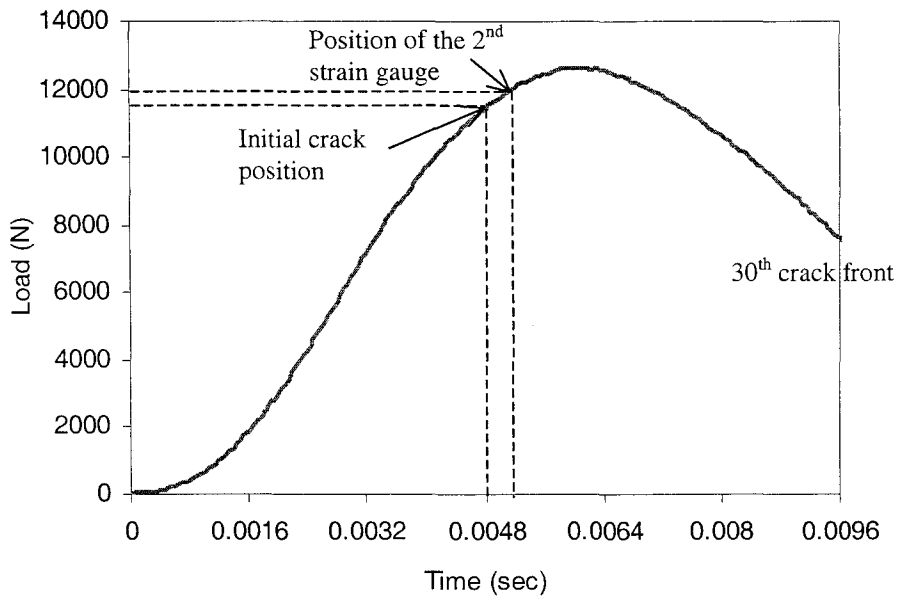

Figure 6.23: Variation of impact splitting force with time up to the region of interest.

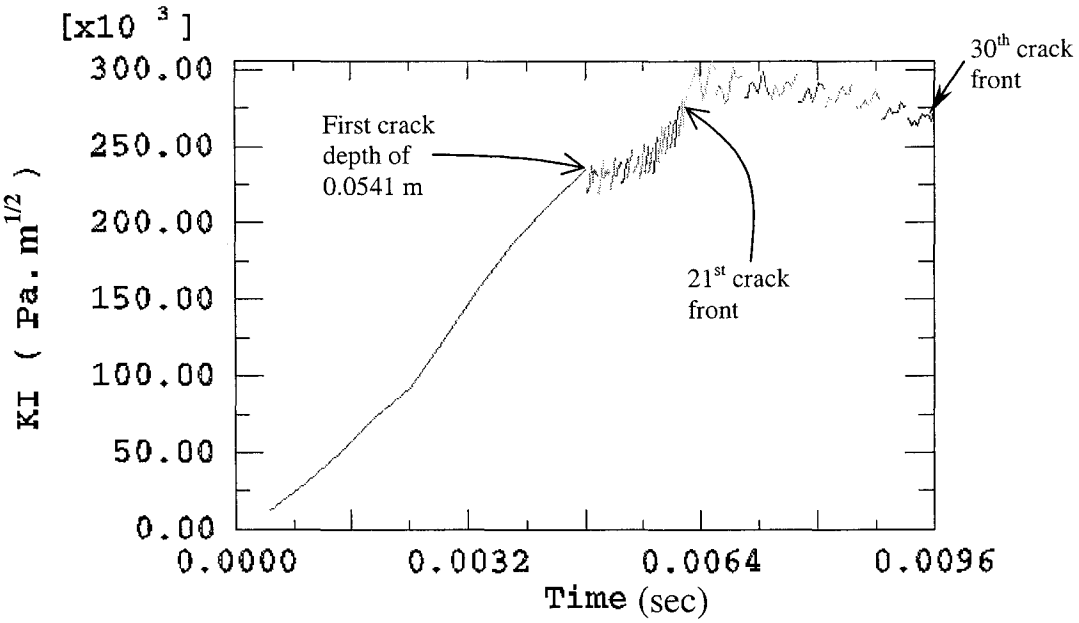

Figure 6.24: Variation of mode I stress intensity factor with respect to time along the symmetric plane 2-3 in direction-2 as crack propagating from an initial depth 0.0514m.

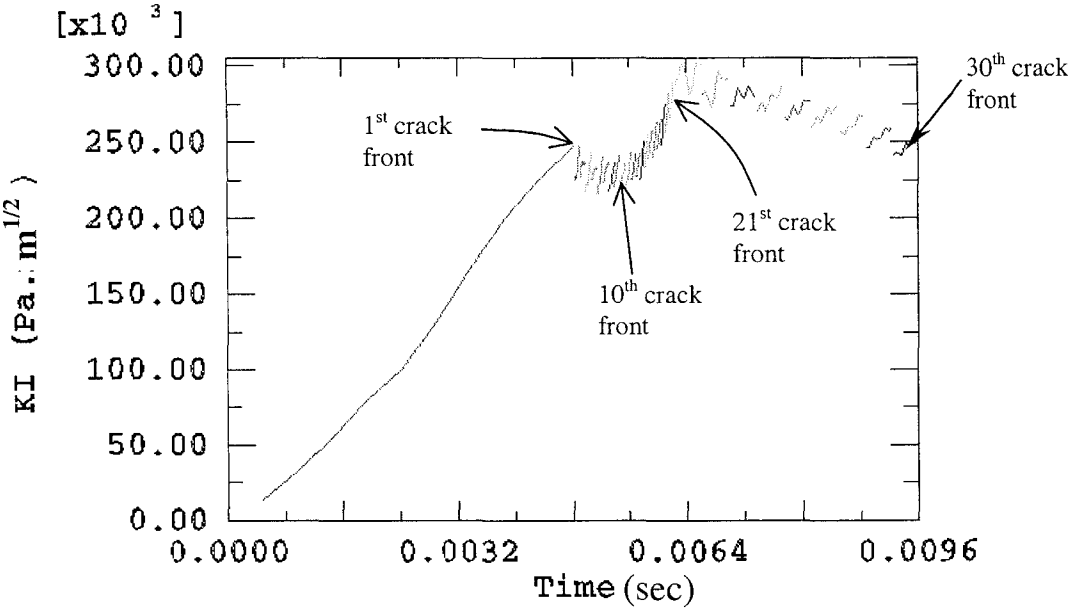

Figure 6.25: Variation of mode I stress intensity factor with respect to time along the middle point of all crack fronts shown in Figure 6.7.

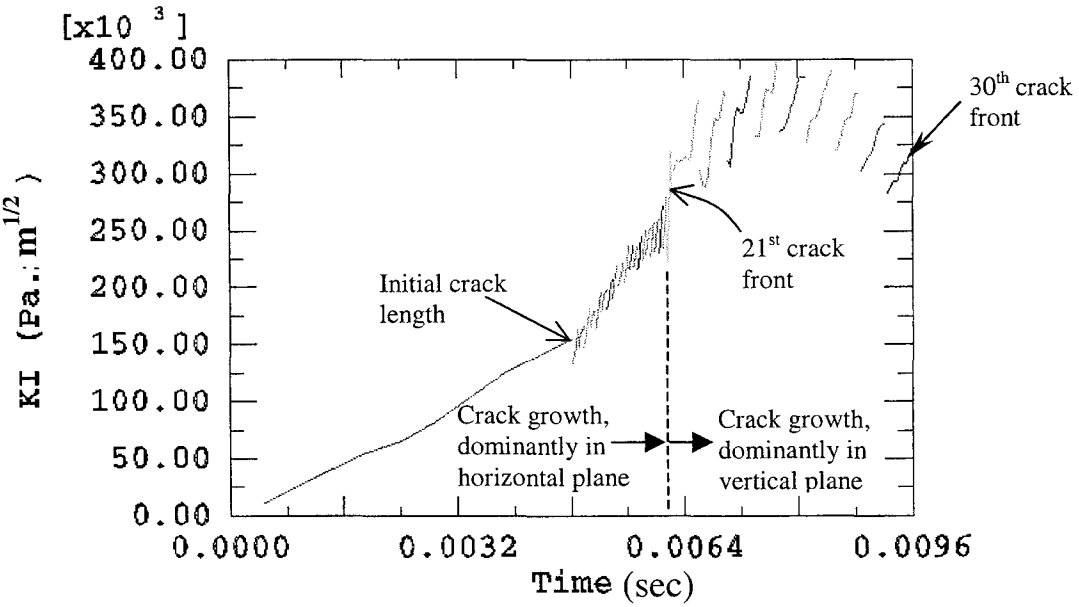

Figure 6.26: Variation of mode I stress intensity factor with respect to time along the crack propagation line one element (0.05 times the length of each crack front) inside the outer surface (20th crack front node) as crack propagated from an initial length of 0.08 m.

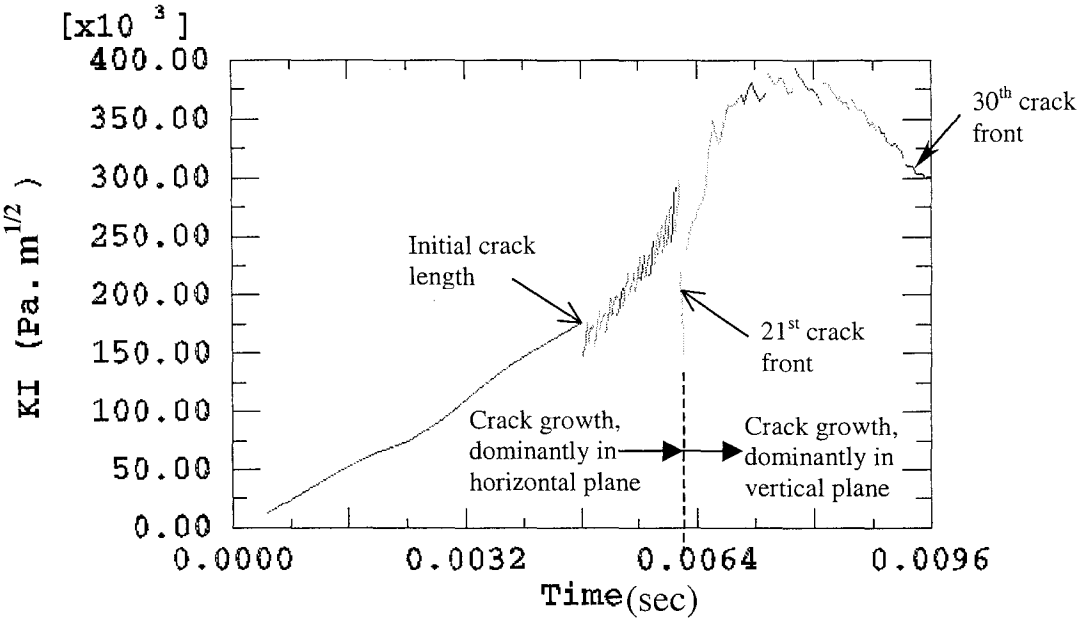

Figure 6.27: Variation of mode I stress intensity factor with respect to time along the crack propagation line at the outer surface of the specimen from an initial crack length 0.08 m.

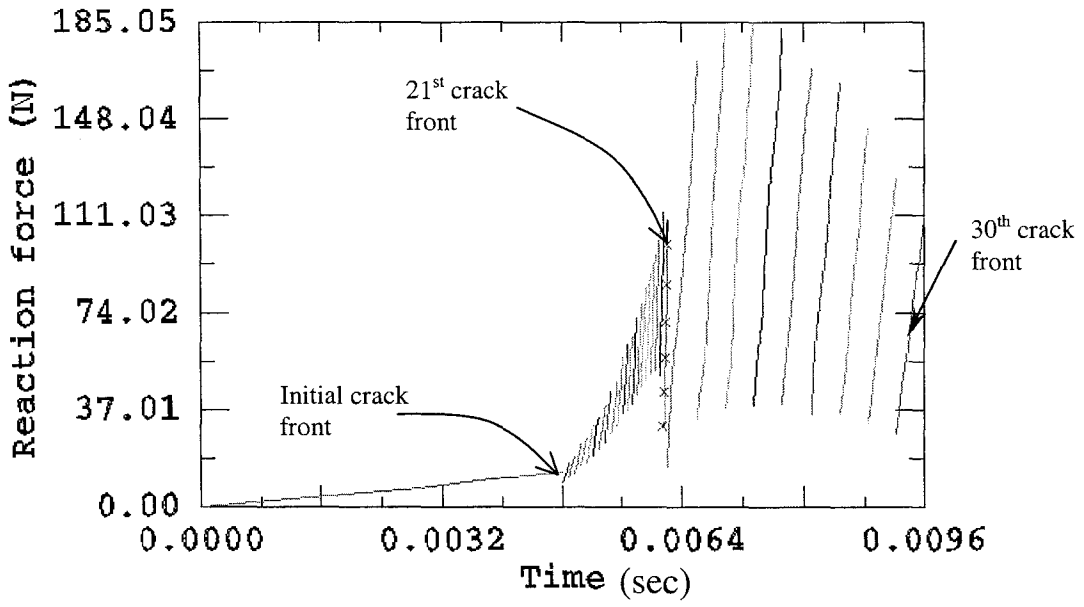

Figure 6.28: Variation of reaction force with respect to time at the crack front nodes on the outer surface of the specimen for each crack extension from its initial length 0.08 m.

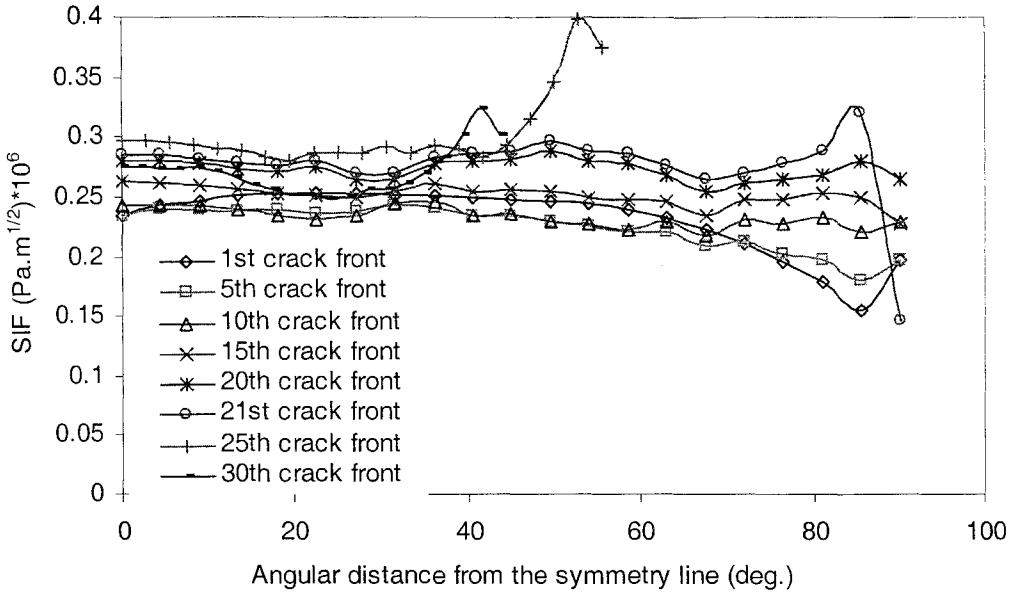

Figure 6.29: Variation of mode I stress intensity factor (SIF) along the crack front for various lengths of crack propagation as plane crack propagated along the symmetry plane.

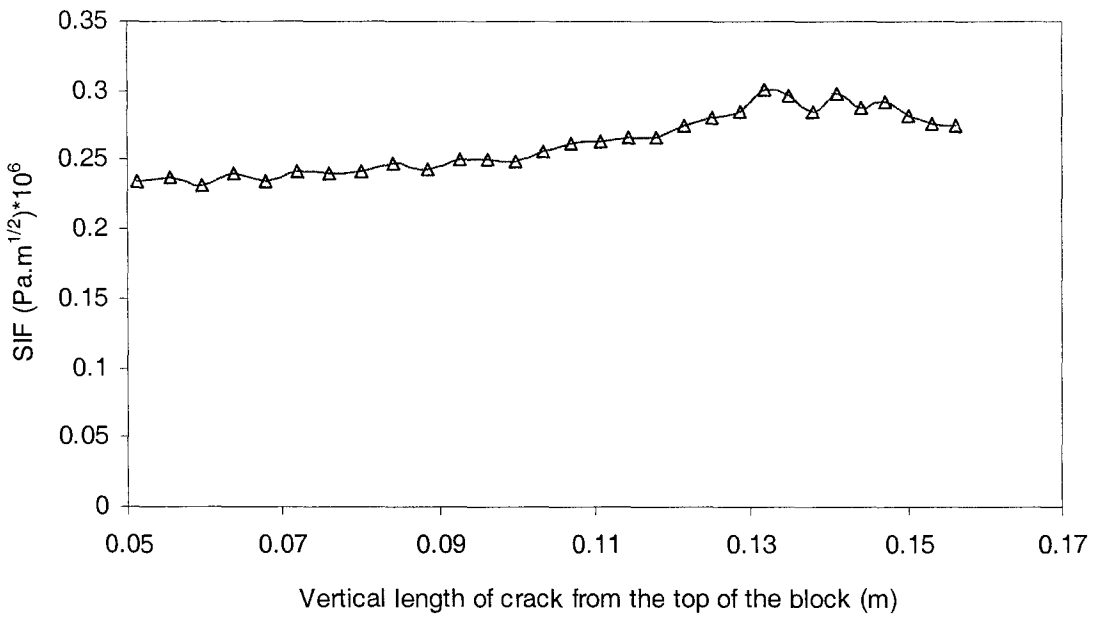

Figure 6.30: Variation of SIFs with crack length at the first node, along the vertical symmetry plane as plane crack propagated along symmetry plane

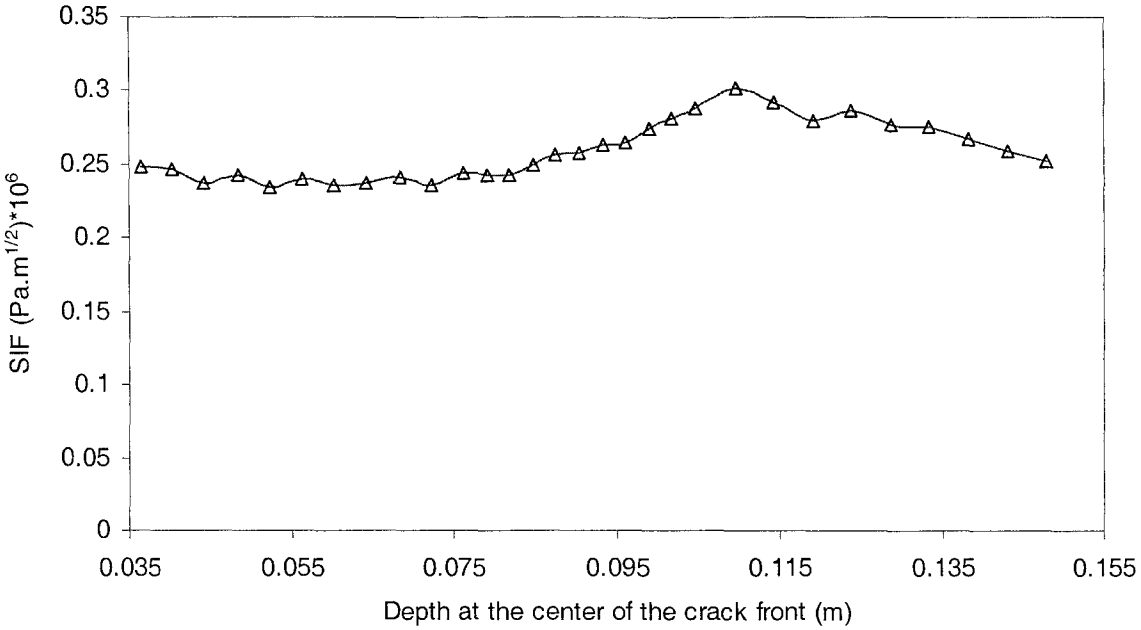

Figure 6.31: Variation of SIFs with crack length along the middle point of each crack front as plane crack propagated along symmetry plane.

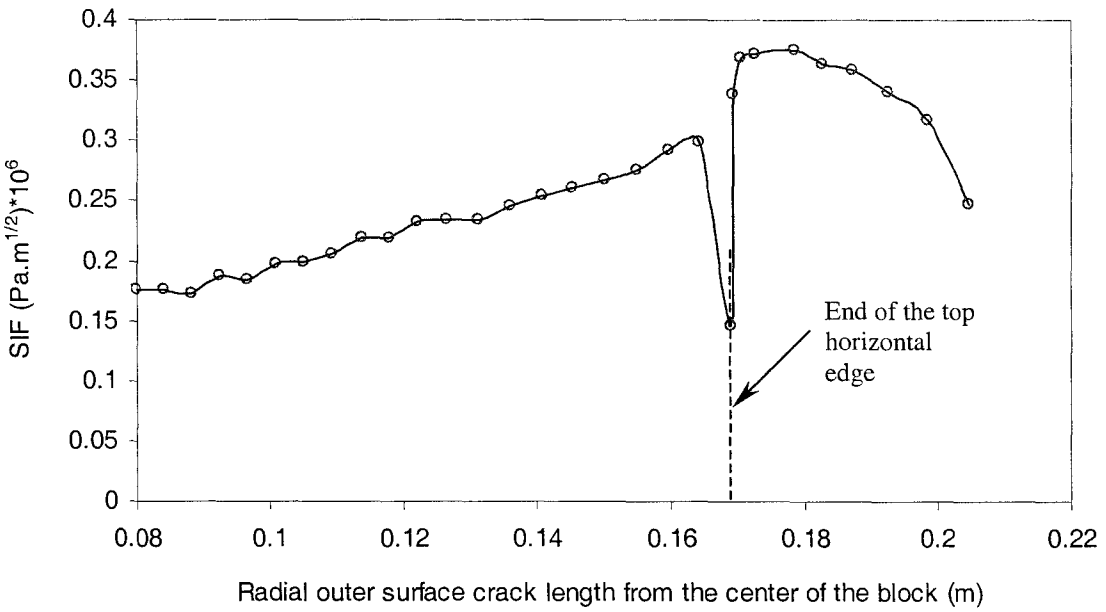

Figure 6.32: Variation of SIFs with crack length at 21st node, along the outer periphery of the specimen as plane crack propagated along symmetry plane.

Chapter 7

Interrelationships between Mode I Stress Intensity Factor, Splitting Load and Geometry of Slate Block

7.1 Introduction

Rocks in most of the cases are considered as brittle material and contain intrinsic cracks. Therefore, their fracturing process is basically caused by gradual initiation (coalescence of micro-crack) and propagation of the cracks. For this reason the failure of the cracked rock is governed by its fracture parameters rather than its elastic and plastic mechanical parameters (Whittaker, et. al. 1992, page 349). It is easier to make correlation between block size and their breaking load after carrying out extensive experimental studies on small scale and large scale tests. In this case accuracy of correlation equation depends on the test results. Good correlation could be obtained when scattering of data is less. In rock materials, the probability of less scattered data from the test program is rather dim. The disadvantage of obtaining correlation equation in this manner is that it requires a large number of test results both for small scale and large scale specimens (in the laboratory) as well as in the field. Further more, different testing procedures for determining breaking

load may yield substantially different results. Most of the laboratories are well equipped to carry out tests for material properties but not necessarily to break large sizes of rock blocks. The alternative to this is to develop a correlation equation based on material property based failure criteria and breaking load, using the geometric characteristics of the body by analyzing different sizes of specimens numerically. Fracture behavior of a rock can be determined by determining the fracture toughness of the rock material in the laboratory. Therefore it should be possible to study breaking force of rock of different sizes based on measured fracture toughness and small- and medium- scale laboratory tests. Material properties do not vary with the size and shape of the specimen to be tested for a specified environment (for a fixed temperature, humidity, etc.) in case of homogeneous materials. However, in case of rock this situation could be different, as most of the rock materials are not homogeneous due to the presence of inherent flaws (microcrack, planar discontinuity, material discontinuity, etc.). Material properties, specially the strength of rock material, would be affected more in this regard. However in mode I plane strain fracture toughness test cases, size effect might not affect the results very much as the test is carried out by introducing an initial crack in the test specimen and having very small micro crack process zone (due to brittle behaviour of rock material. This micro cracking phenomena in the micro crack process zone would remain unchanged even if the specimen sizes vary a lot.

Therefore, this property (mode I plane strain fracture toughness) could be considered as a unique material property of rock while analyzing the rock breaking problems. But breaking load varies with the geometry of body and the breaking conditions (plane strain or real 3D slate block) as seen in Chapter 4. Therefore, it could give the reliable

correlation equation for any sizes of specimen if it is possible to make correlation between fracture parameters, breaking load and the geometry of the body. Once the correlation equation is developed it will facilitate a more considered selection of rock cutting and excavation process in the field. In the present study such a type of correlation analysis was undertaken to develop appropriate relationships between stress intensity factor, breaking load and the geometry of the body by analyzing different sizes of slate blocks numerically using finite element method.

7.2 Factors Influence Rock Fracture Process

Heterogeneity, discontinuity, anisotropy, types of external loads with respect to direction of the state of stresses (uniaxial, biaxial, triaxial, polyaxial) and the state of stresses (tensile, compressive, and shear), distribution of the external loads (uniformly or nonuniformly distributed, tensile or compressive or bending or torsion), rate of the external loading (constant, gradually increasing, alternating or impact) and the environmental conditions (temperature, humidity and chemical environment) generally influence the fracture process in rock. The stability and the continuity of crack growth will be affected by the heterogeneity of rock due to the variations in crystal structure and local strength close to the extending crack. The work done at fracture, critical strain energy release rate or fracture toughness, as a function of fracture propagation orientation can vary with the anisotropy of the rock. The environmental conditions such as confining pressures, temperature, pore pressure, etc., can also substantially affect the fracture behaviour of rock (Whittaker, et. al. 1992).

7.3 Correlation Study between Geometry of Slate Blocks, K_{Id} and Splitting Forces

Correlation between mode I dynamic stress intensity factor, impact forces and geometry of plane strain slate block was obtained by using the multiple linear regression analysis using the results similar to that shown in Figures 5.36 and 5.39 in chapter 5. The stress intensity factors obtained from numerical analysis for the applied load, different crack lengths and specimen dimensions were correlated. The plane strain fracture toughness value ($K_{IC} = 0.292 \pm 0.0379$ MPa.m$^{1/2}$) obtained from earlier experiments was considered as a criteria for in-plane crack propagation within the specimen. Therefore, the time dependent splitting load corresponding to plane strain fracture toughness for a finite sized plane strain slate block was determined using the developed correlation formula. The formula obtained for this problem from multiple linear regression analysis available in Microsoft Excel 97 (1997) of numerical results is given as:

$$K_{Id}(t) = \frac{P(t)}{w^{1/2} l} Y \tag{7.1}$$

where

$$Y = \left[3.6374 - 11.21\frac{a(t)}{d} + 10.8968\frac{a(t)}{w} - 2.1295\frac{d}{w} + 8.5793\frac{a^2(t)}{d^2} - 3.8241\frac{a^2(t)}{w^2} + 0.2613\frac{d^2}{w^2} \right]$$

with the coefficient of determination being equal to 0.9678 and valid for,

$$0.12 \le a(t)/d \le 0.66\,,\ 0.167 \le a(t)/w \le 0.5\,,\ \frac{w}{d} \le 1 \tag{7.2a}$$

and,

$$P(t) = P_0(0.373835 + 0.458736\cos\omega t + 0.145906\cos 2\omega t + 0.0426553\cos 3\omega t)$$

for $t \leq T/2$ (7.2b)

$$\omega = \frac{2\pi}{T} \text{ and } T = 2 \times \text{total time (in Figure 7.1)}$$

$P(t)$ (in MN) is the time dependent impact splitting force per unit length which decreases as crack length $a(t)$ increases. w and d are the width and depth of the specimen, respectively. P_0 is the maximum impact load required to split the rock specimen apart. A constant transverse length (l) equal to 0.1 m is considered in this formulation. However, for generalized length considerations it is necessary to consider a unit length of the specimen. That can be provided by analyzing a plane strain problem of layered slate rock having a length of unity to determine mode I stress intensity factor. These stress intensity factors could then be used to develop correlation equation. For linear variation between load and transverse length, the above equations can be written as,

$$K_{Id}(t) = \frac{P(t)}{w^{1/2}} Y \tag{7.3}$$

where

$$Y = \left[3.6374 - 11.21\frac{a(t)}{d} + 10.8968\frac{a(t)}{w} - 2.1295\frac{d}{w} + 8.5793\frac{a^2(t)}{d^2} - 3.8241\frac{a^2(t)}{w^2} + 0.2613\frac{d^2}{w^2} \right]$$

for a unit length (1 meter) consideration and the limits specified above.

When the experimental P_0 is equal to 5500 N for the 0.10 m cubic block, use of equation 7.2 (b) gives an error + 2.10% for the maximum impact splitting load; it can be improved by taking additional Fourier coefficients.

The variation of empirical theoretical splitting force *P(t)* for a plane strain fracture toughness value and experimental splitting force for different crack lengths are shown in Figure 7.1 for a slate specimen having the dimensions 0.1 m × 0.1 m × 0.1 m. It is seen that the theoretical splitting force is larger than the experimental one by 58.15% at the peak value for the mean fracture toughness of 0.440 MPa.$m^{1/2}$ (obtained from the empirical equation of Bush (1976) and Ouchterlony (1980)). Instead of the empirical equation value, if the mean finite element value was used in the analysis, the maximum theoretical splitting load is + 4.96% larger than the experimental value. The finite element analysis obtained fracture toughness value seems to be closer to the correct value that should be obtained in the experiment. In this study maximum experimental breaking force was obtained as 5500 N for 0.1 m × 0.1 m × 0.1 m slate specimen. As mentioned earlier a part of this applied force is lost due to heat generated, sound produced and vibration damping etc. As could be seen from Figure 7.2 there is a very good correlation using only the four Fourier coefficients. The error is around + 2.1% when t = 0; this could be improved by taking additional Fourier harmonics. Table 7.1 gives a comparison between theoretical and experimental values based on mean fracture toughness values for various slate blocks broken experimentally under plane strain conditions. The errors obtained for smaller specimens are much larger, probably due to the steep variation of SIF for small crack depths and equation 7.2 being not good enough for small-sized specimens.

Using equation 7.3 and the finite element analysis computed fracture toughness value, the impact load for breaking a 2.0 m length, 1.0 m deep and 0.98 m thick slate rock with a 0.12 m initial crack, works out to 402.69 kN, while it works out to 1290.98 kN for a 4.0

m length, 4.0 m deep and 2.0 m thick slate rock with a initial crack of 0.48 m. The load seems to be a reasonable load that could be handled by a hydraulic device. This load could be reduced considerably if the load applied on the line of hydraulic actuators (used for applying the impact loads) is cascaded across the actuators (starting from the centrally placed actuators) with a small time delay. It must be mentioned that this load is only for a plane strain cracking. When the boundaries are constrained to provide a partial three-dimensional action, the required load may be a little higher.

The correlation between experimental 3D breaking loads and 3D numerical results could not be made since the 3D numerical analysis consumed so much of computational time. In order to give some numbers, it was found that the time taken, to prepare, analyze and process nearly 30 time steps in the numerical results given in section 6.3 of Chapter 6, was nearly 2 days. Hence in order to get some meaningful results for 3D analysis 100 to 120 separate runs had to be made and this would have consumed an enormous amount of computational hours. Hence no effort was made on this regard.

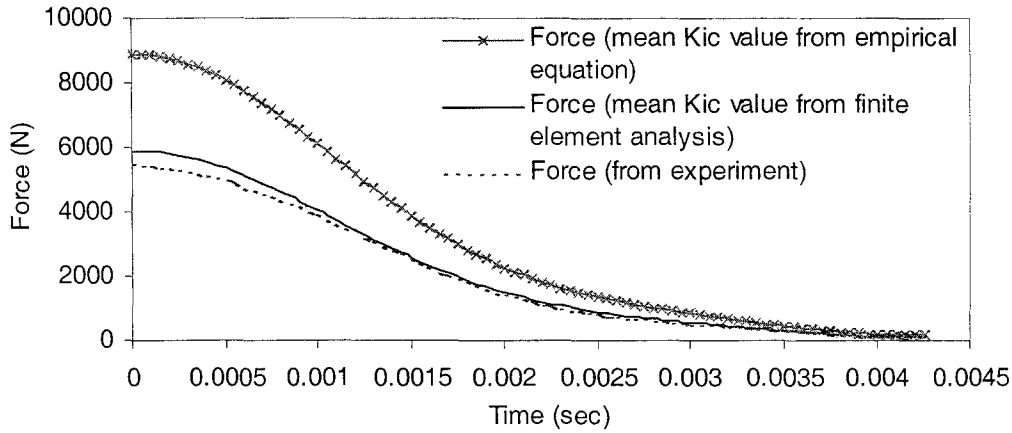

Figure 7.1: Variation of theoretical impact splitting loads obtained from empirical equation mean value (0.440 MPa.m$^{1/2}$) and finite element analysis mean value (0.292 MPa.m$^{1/2}$) and experimental breaking loads.

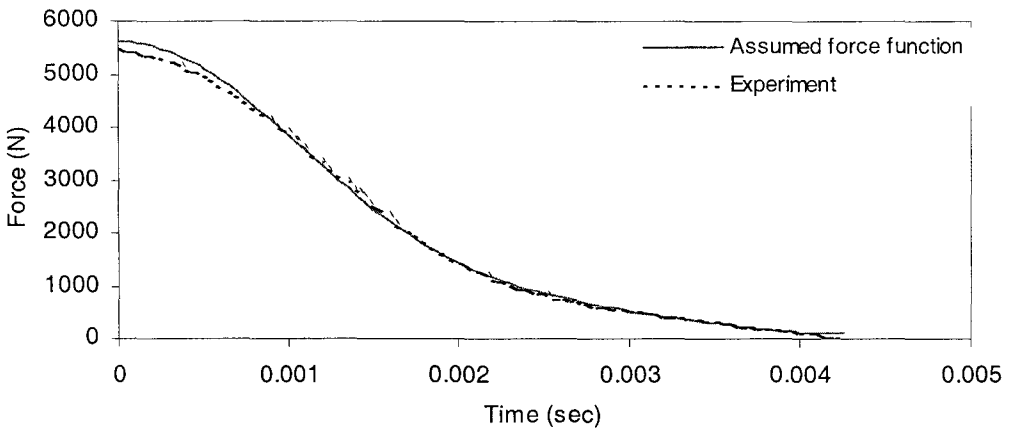

Figure 7.2: Variation of assumed force function with the consideration of four Fourier terms and the experimental force obtained during breaking of slate block having size 0.1 m $\times$ 0.1 m $\times$ 0.1 m.

Table 7.1: Comparison between theoretical impact splitting loads obtained from empirical equation mean value (0.440 MPa.m$^{1/2}$) and finite element analysis mean value (0.292 MPa.m$^{1/2}$) and experimental breaking loads.

Specimen size ($L \times W \times D$) in 'm'	Experimental breaking load		Theoretical breaking load (for mean K_{IC}) with empirical equation value of 0.440 MPa.m$^{1/2}$		Error	Theoretical breaking load (for mean K_{IC}) with finite element analysis value of 0.292 MPa.m$^{1/2}$		Error
	lbf	kN	lbf	kN	%	lbf	kN	%
0.100 × 0.050 × 0.100	977.00 *	4.345 *	1047.66	4.659	7.23	695.264	3.092	-32.34
0.100 × 0.076 × 0.100	1100.00 *	4.893 *	1544.94	6.871	40.43	1025.28	4.560	-6.80
0.100 × 0.100 × 0.100	1236.46 *	5.500 *	1955.92	8.698	58.15	1298.02	5.773	+4.96
0.100 × 0.100 × 0.127	1300.53	5.785	1975.55	8.786	51.86	1311.02	5.830	+0.78
0.100 × 0.100 × 0.152	1503.53 *	6.688 *	2066.07	9.188	37.38	1371.13	6.098	-8.82
0.100 × 0.100 × 0.178	1627.85	7.241	2203.74	9.800	35.34	1465.48	6.504	-10.18
0.100 × 0.100 × 0.203	1813.77 *	8.068 *	2376.60	10.569	30.99	1577.20	7.014	-13.06

* - Average value of the two specimens

Chapter 8

Numerical Investigation on Impact Splitting of a Slate Rock in the Field and Reduction of Wastage in Slate Manufacture

8.1 Introduction

The objective of this study is to break large sized slate blocks in the field so that they could be cut into smaller ones in the processing plant for producing different sizes of slate products, without much wastage. Geometry of slate rock for this problem is shown in Figure 8.1. Specimen used for numerical analysis is an idealized form of field situation after applying some assumptions on the geometry of the field problem as well as their material condition. Idealization for finite element anlysis and geometry of the domain of interest considered for finite element analysis are shown in Figures 8.2 and 8.3. Assumptions and modifications related to the geometry and material of this problem are as follows:

1. One side of the slate quarry is assumed to be opened or made open by using other methods such as saw cut, diamond wire cut, etc., and considered in finite element model as a traction free edge.
2. Numerous holes are made along the line in the three sides (bottom and two ends) shown in Figure 8.1 using the power drill and these are replaced by three layers (one

layer at the bottom and two layers on the two sides) of soft material having Young's modulus of elasticity three times less than the original material's Young's modulus of elasticity in finite element analysis. The existing continuous media of these three sides beyond the drilled holes are modelled using infinite elements.

3. The side opposite to the open side is treated as unbound domain. In finite element analysis it is modelled using infinite elements available in ABAQUS finite element software (ABAQUS 6.3, 2002).
4. A series of impacting wedges that is used to split or separate a part of slate rock from their original state (shown in Fig. 8.1) is idealized as a continuous indenting wedge similar to the problem discussed earlier in plane strain/3D analysis.
5. Material is taken to be homogeneous and transversely isotropic (observed from experimental results reported earlier).
6. Crack was assumed to be a plane crack and propagating along the vertical impact plane by maintaining the same depth of penetration in the transverse direction (direction-2), for each time step.
7. Load was assumed to be distributed uniformly at a height 20 mm above the tip of the indenting wedge.
8. It is assumed that when the wedge penetrates 10 mm deep into the slate rock, the crack is assumed to have grown to 25% of the field specimen depth.

In addition to the above, the chapter also briefly discusses the possible reduction of wastage of slate material that could be achieved, in the processing industries, by the use of impact splitting for the sizing of slate products.

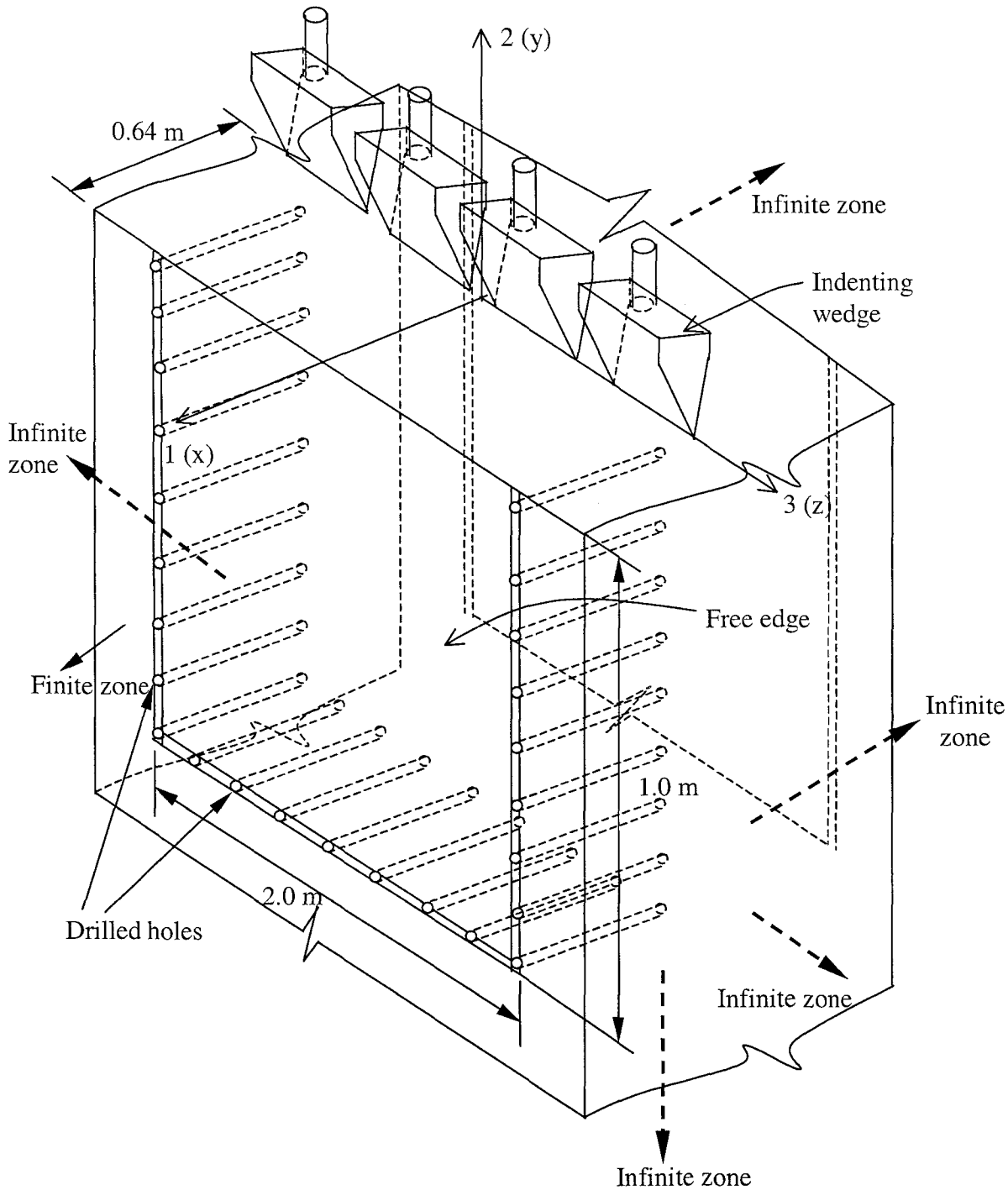

Figure 8.1: Geometry of a part of slate quarry ready for impact splitting

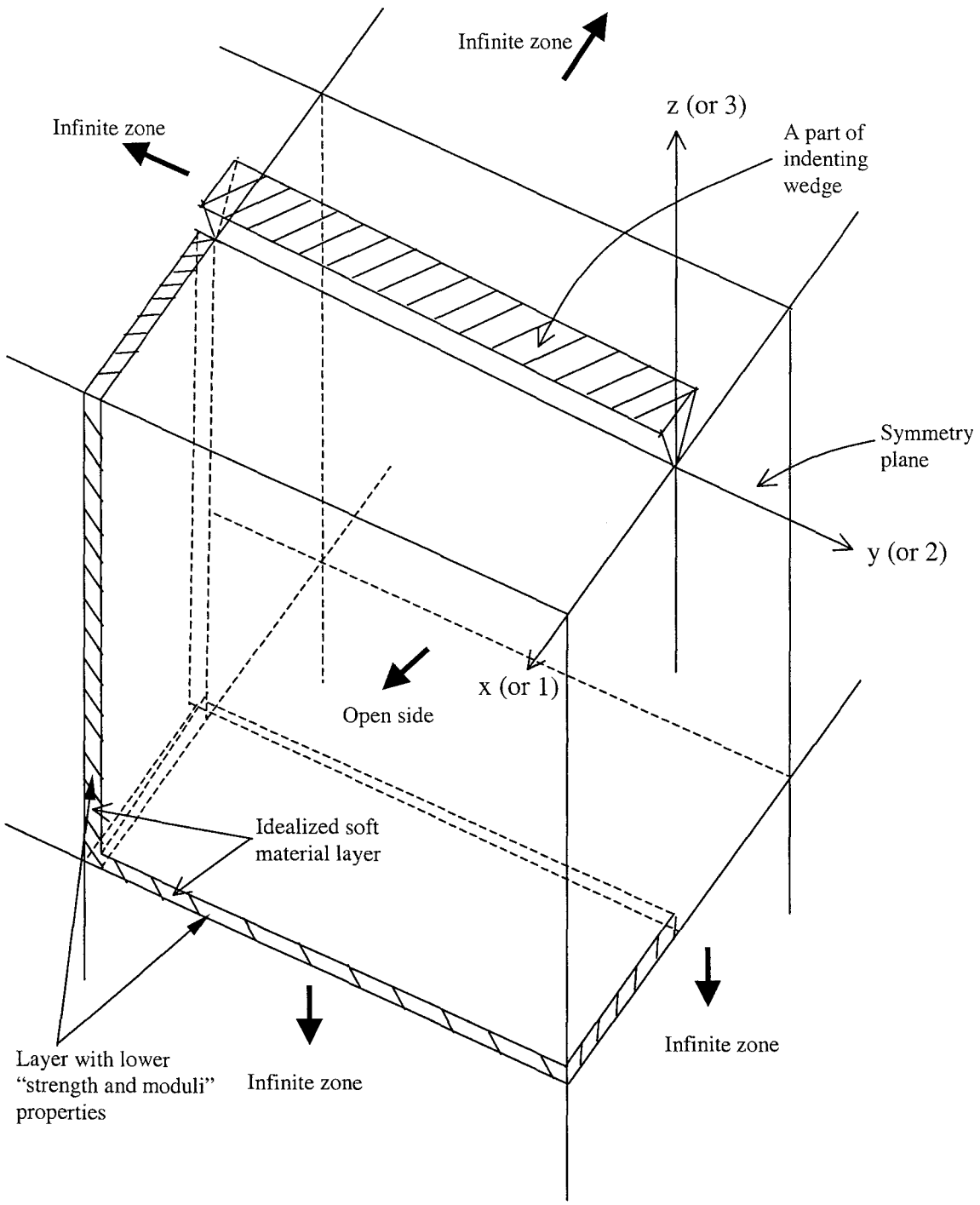

Figure 8.2: Idealization for finite element analysis

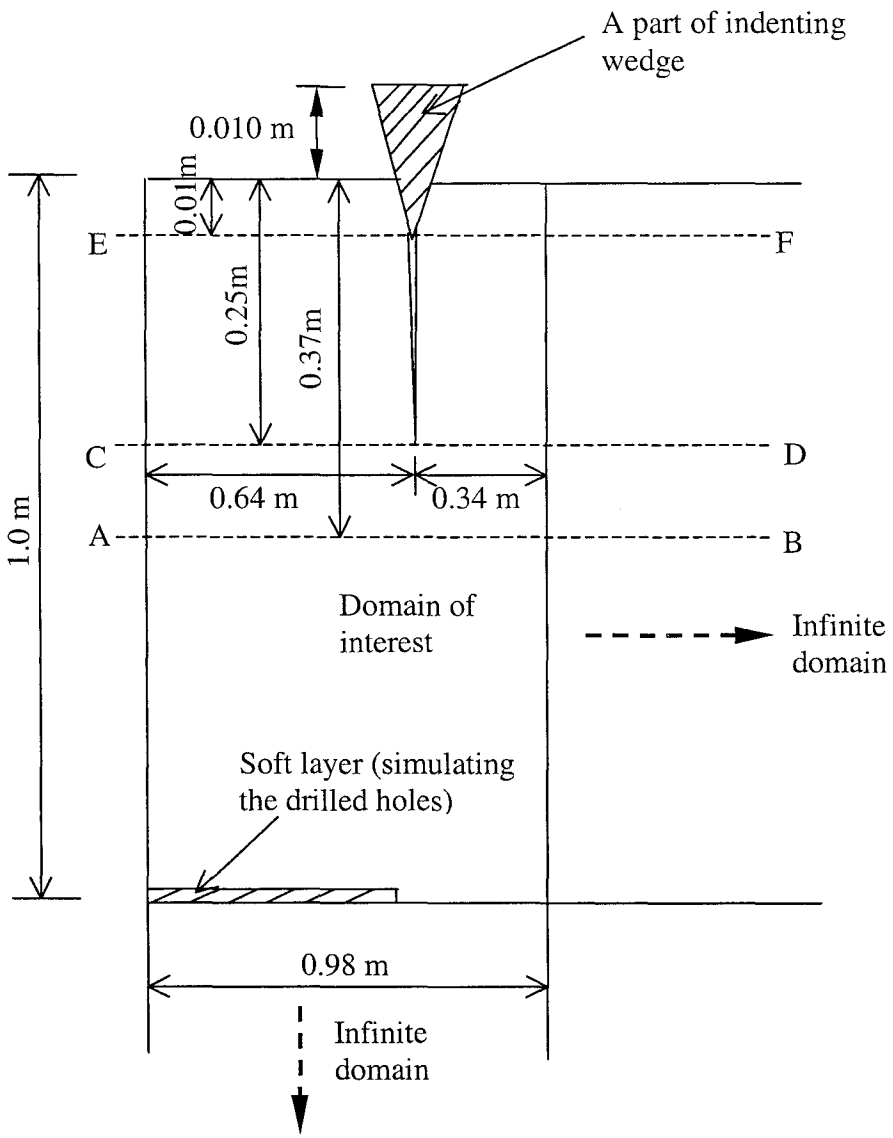

Figure 8.3: Geometry of finite element model

8.2 Finite Element Modelling and Processing of Results

A static finite element analysis was carried out to investigate the separation of a part of slate rock from the slate quarry. The node release technique used earlier for SIF computation could not be applied due to the presence of unsymmetric boundary conditions during the splitting of rock. Therefore, each crack depth was modelled separately and individually. However, half symmetry of the rock mass was taken into consideration due to the existence of symmetry in geometry, load, material and boundary conditions about the plane 1-3; this procedure helped to reduce the size of the problem. Since a series of impacting wedges [shown in Figs. 8.1 to 8.3] was to be used to separate a long slab of slate rock, a "line load" loading condition was assumed as an idealized form of load applied under real field situation.

Therefore, the distributed load on the wedge obtained at a height 0.01 m above the tip of wedge to break a 0.10 m cube slate block experimentally was used as applied load for this problem after making some modifications on load time diagram (shown in Figures 8.4 and 8.5) for their greater depth of cut. A necessary modification was made for the decaying part of load time diagram shown in Figure 8.4 based on the assumed crack propagation velocity (46.5 m/s). Since the depth of the field problem considered in this analysis was 10 times greater than 0.10 m cube slate block, breaking time should be higher for the crack to reach the crack to the bottom of the slab. The increasing part of the load-time diagram was not modified since the stiffness of the rock media and the indenting wedge were assumed to be the same as before. This increased portion of the time axis was incorporated into Fig. 8.5 without changing the load magnitude. The updated load vs. time diagram used to analyze the present problem is shown in Figure 8.5.

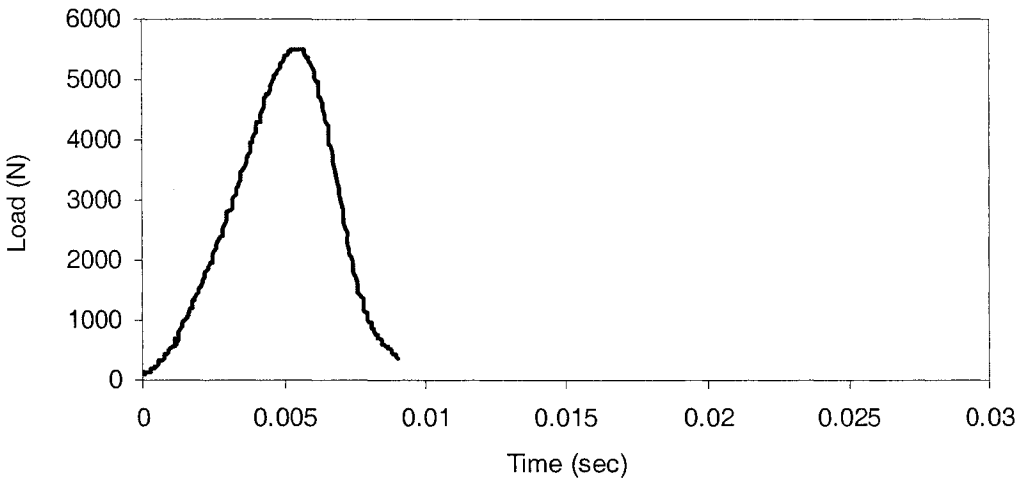

Figure 8.4: Varying part of breaking load with respect to time during impact splitting of a plane strain slate block having the dimensions, $L = 0.10$ m, $D = 0.10$ m and $W = 0.10$ m.

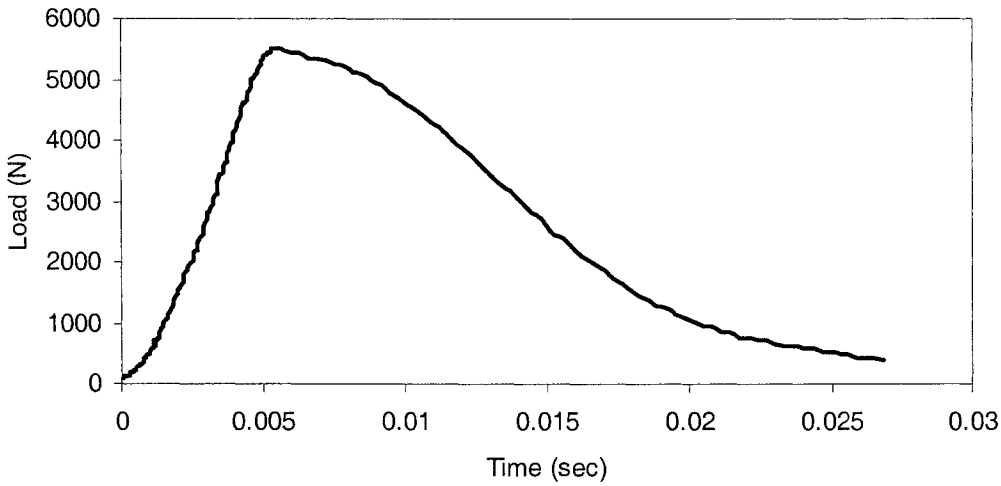

Figure 8.5: Updated breaking load variation with respect to time used to analyze the splitting process of the slate rock.

A load equal to the 0.75 times of the peak load was considered as the load for the first crack since crack started when load reached its peak value. Subsequent cracking load was determined based on the assumed velocity of crack propagation. When crack depth was increased, the magnitude of the applied load decreased. A constant velocity of crack propagation (46.5 m/s) was taken into consideration since variation of crack propagation velocity having low magnitude (constant or linearly variable) has a marginal effect on the value of stress intensity factor; this was discussed earlier in plane strain and 3D analysis of slate blocks (section 5.2 & 5.3 of Chapter 5). Five separate crack depths (in an increasing manner) were modelled and treated as five separate individual problems. 3D analyses were required to be carried out since plane strain analysis was not possible to be used in this situation. The entire body was discretized using eight-noded linear brick elements, six-noded wedge elements and infinite elements. A non-uniform mesh was introduced by employing relatively fine mesh (element size 3 mm by 1.5 mm by 5 mm) along the crack front and contact planes, and coarse mesh away from these critical zones. Wedge penetration was assumed to be 0.01 m in the beginning of the analysis.

Since contour integral option in ABAQUS finite element software does not support triangular/wedge elements in the contour regions considered to determine SIF or strain energy release rate, wedge elements were used a little away (after two rows) from the crack plane (as shown in Fig. 8.6). This became necessary to reduce the size of the overall finite element problem. A graded fine to coarse mesh size was used in the region away from the splitting surfaces. This transition was made after providing two rows of small sized brick elements near the crack plane. For this reason SIFs were obtained only from the first two contours. Contour integral does not also support material discontinuity

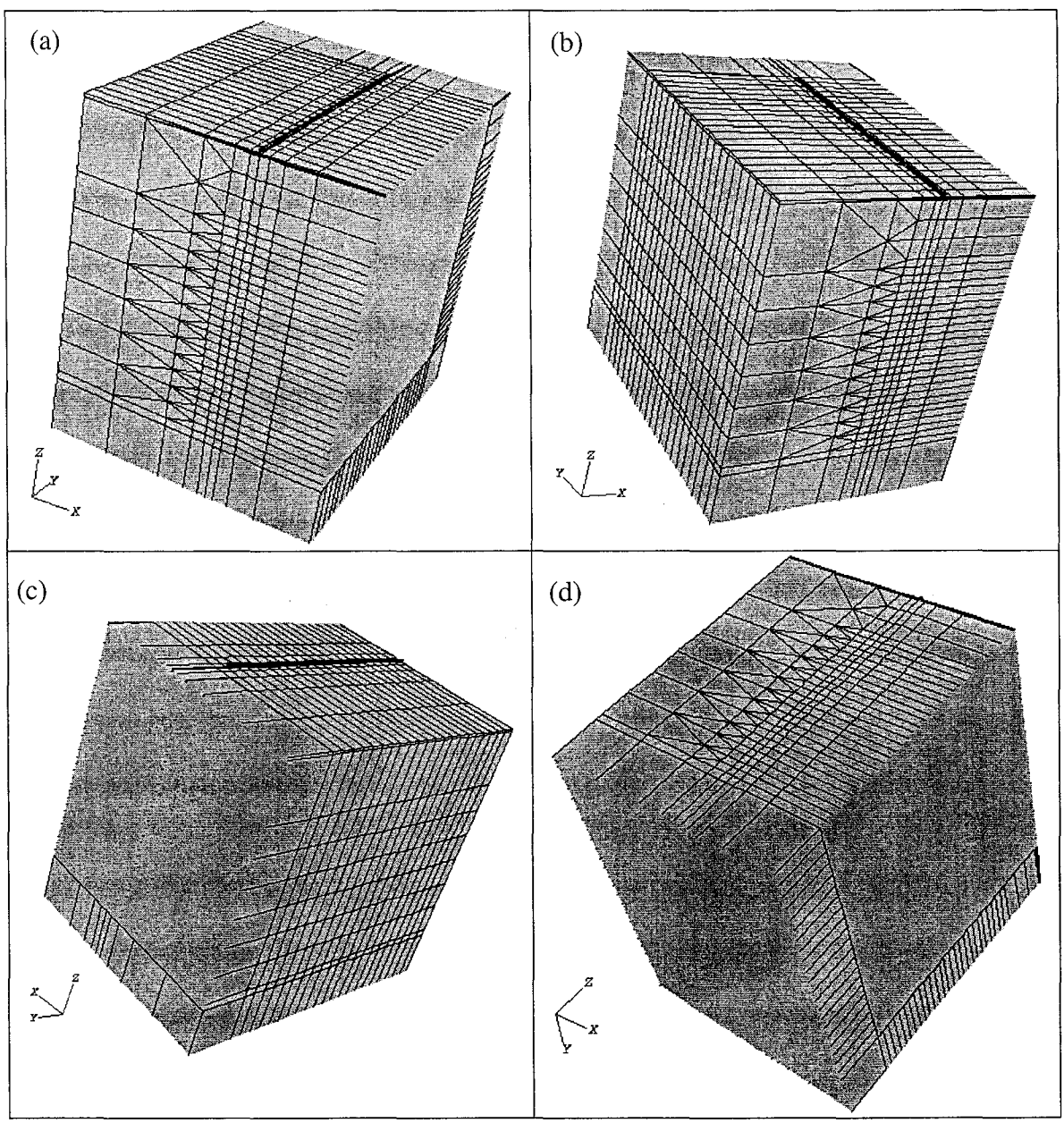
(a)
Z
Y
X
(b)
Z
Y
X
(c)
X
Z
Y
(d)
Z
X
Y

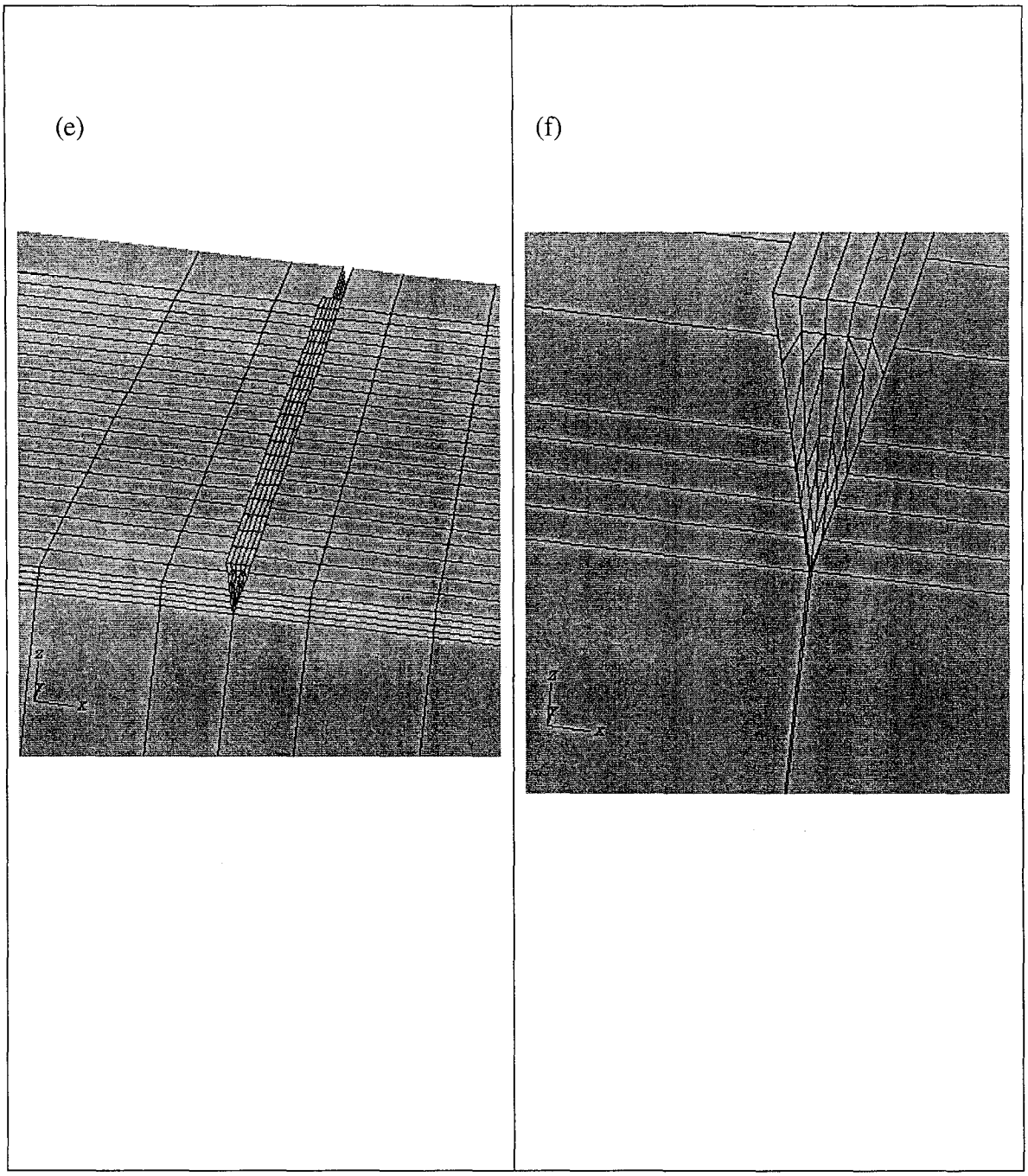

Figure 8.6: (a)-(d) Finite element discretization of a body of slate rock available in field situation from different views; (e) and (f) Enlarged mesh at the junction of indenting wedge and slate specimen.

/dissimilar materials at the crack tip node point (special treatment is required to incorporate material discontinuity/dissimilar materials at the crack tip node point). Therefore, SIFs were determined along the crack front up to a distance 0.90 m from the half symmetry plane. Soft layer was modelled using eight-noded linear brick elements and six-noded wedge elements. The finite element discretization for this problem has been given in Figures 8.6 (a)-(f).

Since at the beginning of wedge penetration, crushing of the material occurs due to very high contact pressures developed at the contact surface between wedge tip and slate rock within a very short (impact) time, a crushing width equal to 0.005m (0.0025 m on either side of the crack plane) was introduced at wedge location.

This problem was set up for time dependent load in static analysis (nature and magnitude of the impact load were kept same as needed for dynamic analysis) that was assumed to be an equivalent of dynamic impact load. Static analysis was carried out instead of dynamic analysis because of boundary modelling requirements that are to be introduced for using infinite elements to model unbounded (infinite) domains. Infinite elements provided stiffness in static solid continuum analyses and quiet boundaries for the finite element model in dynamic analyses (ABAQUS 6.3, 2002). In dynamic analysis wave reflection/refraction will occur while using infinite elements; therefore the dynamic analysis was terminated automatically by ABAQUS. Stresses and mode I stress intensity factors along the crack front were determined for different crack lengths and applied loading conditions.

Contour plots of stresses in local 1-direction for five different crack depths are shown in Figures 8.7 (a) to (e). It is seen that stress concentration point (at the crack tip) is not highlighted properly. This is due to coarse nature of finite element meshing used in this study. However, it can be seen clearly, by indicating the stress concentration points, developed at the crack tip when stresses (in local 1- and 3- directions) were plotted (shown in Figure 8.8 and 8.9) along the vertical line passing through the cracked and uncracked part of the body. The absence of highlighting (in contour plots) is due to the lesser number of colors available in ABAQUS post processor facility to show the contour plots. Use of very fine meshes at the crack tip region or use of singular elements at the crack tip would show the stress concentration locations clearly.

Stresses in local 1- and 3- directions of all nodes along the crack front were also determined (shown in Figures 8.10 and 8.11) for different crack depths and load values and magnitudes were also compared. These were also determined for a constant load application (0.75 times the peak value for all crack depths) and shown in Figures 8.12 and 8.13. It is observed from Figures 8.10 and 8.11 that as the crack depth increases, stresses in local 1- and 3- directions (along the crack front) decrease for decreasing magnitudes of applied load. However, for a constant load (see Figures 8.12 and 8.13) stresses decrease first and then increase as crack depth increases. This is expected to happen because the uncracked ligament (resistance comes from the lesser area of the body) decreases if crack depths are increased. It also shows that there is an effect of crack depth on stresses if crack depths are increased. In case of variable loads, stress in local 1- direction decreases more than the stress in local 3- direction. Due to the use of soft layer and infinite

elements at the end of wedge, a jump in stresses was observed. Use of lower Young's modulus of elasticity for the soft layer than the original slate rock produces this jump.

Variation of stresses in local 1- and 3- directions along the lines AB, CD and EF (shown in Figure 8.3) are shown in Figures 8.14 and 8.15. It is seen that stresses at the crack tip and the uncracked part of slate rock 0.12 m below the crack tip point are tensile and at the location of indenting wedge tip it is compressive. This happens due to the direct contact of wedge on line EF and indirect effect of wedge load at the crack tip.

(a)

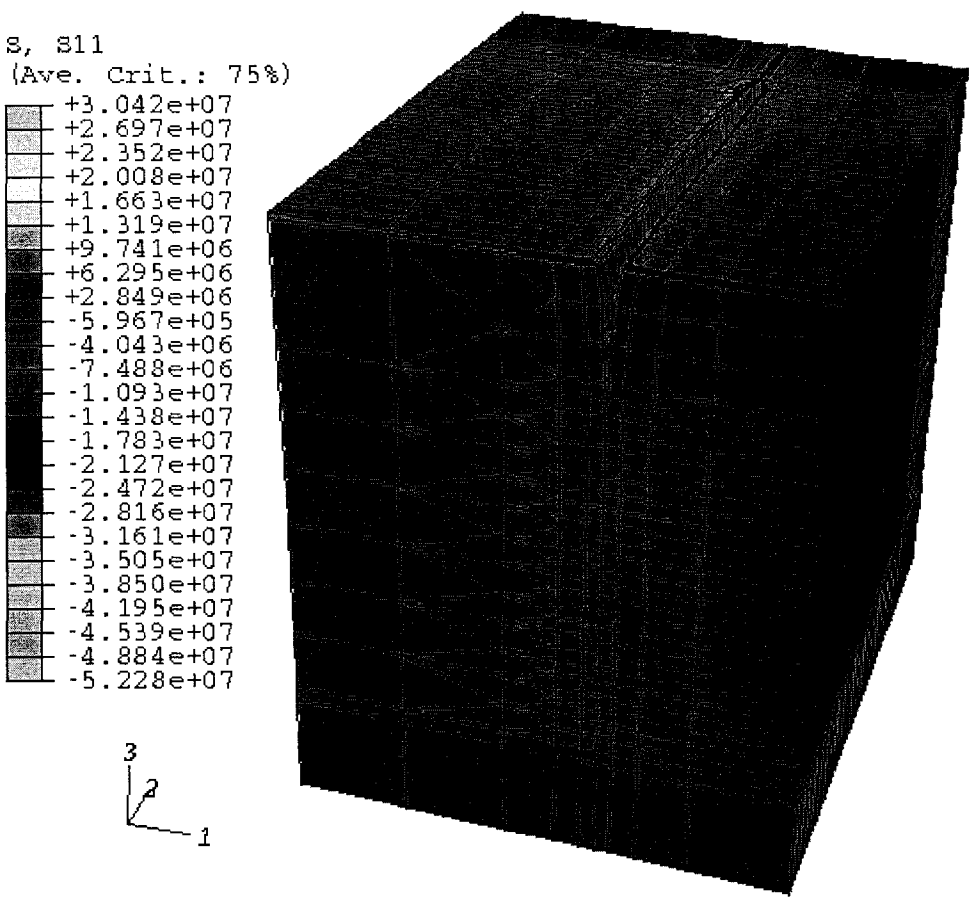

(b)

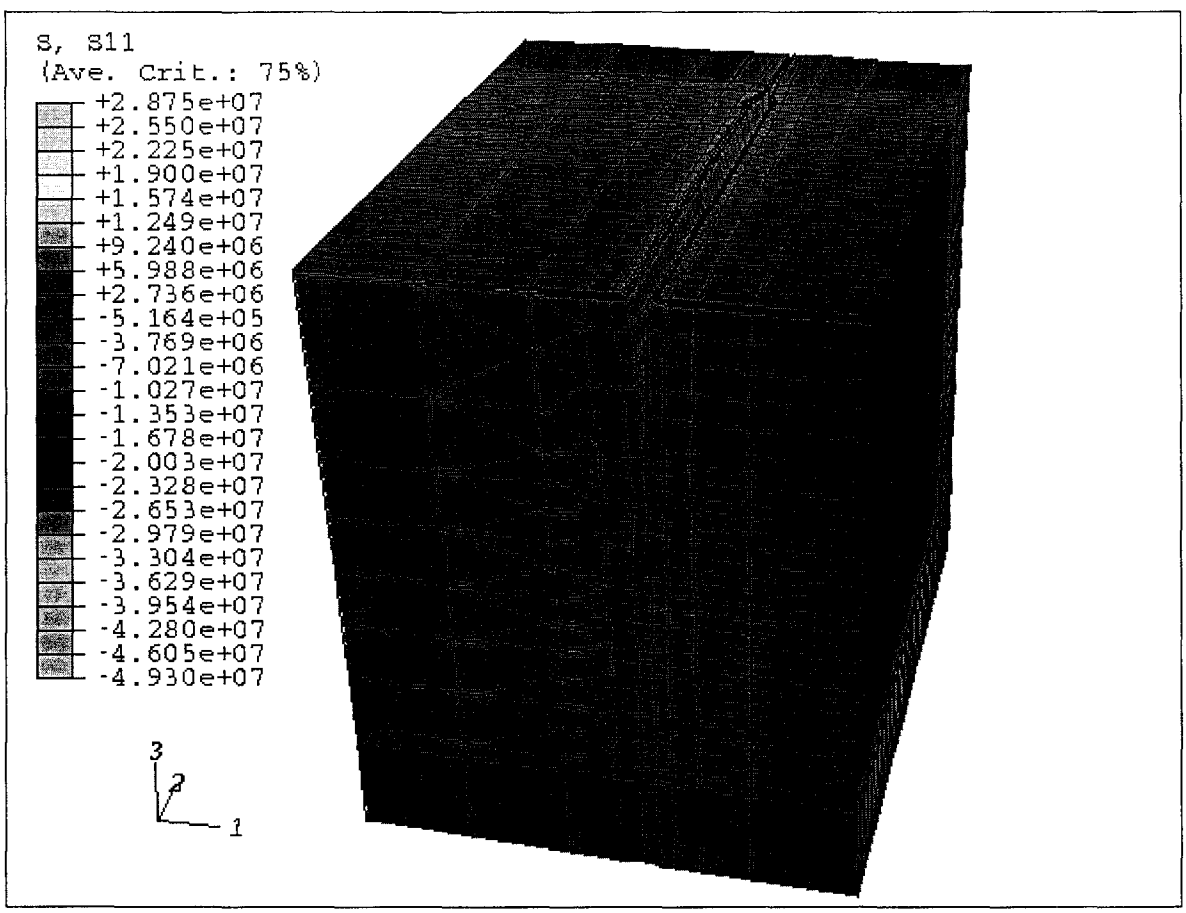
S, S11
(Ave. Crit.: 75%)
+2.875e+07
+2.550e+07
+2.225e+07
+1.900e+07
+1.574e+07
+1.249e+07
+9.240e+06
+5.988e+06
+2.736e+06
-5.164e+05
-3.769e+06
-7.021e+06
-1.027e+07
-1.353e+07
-1.678e+07
-2.003e+07
-2.328e+07
-2.653e+07
-2.979e+07
-3.304e+07
-3.629e+07
-3.954e+07
-4.280e+07
-4.605e+07
-4.930e+07
3
2
1

(c)

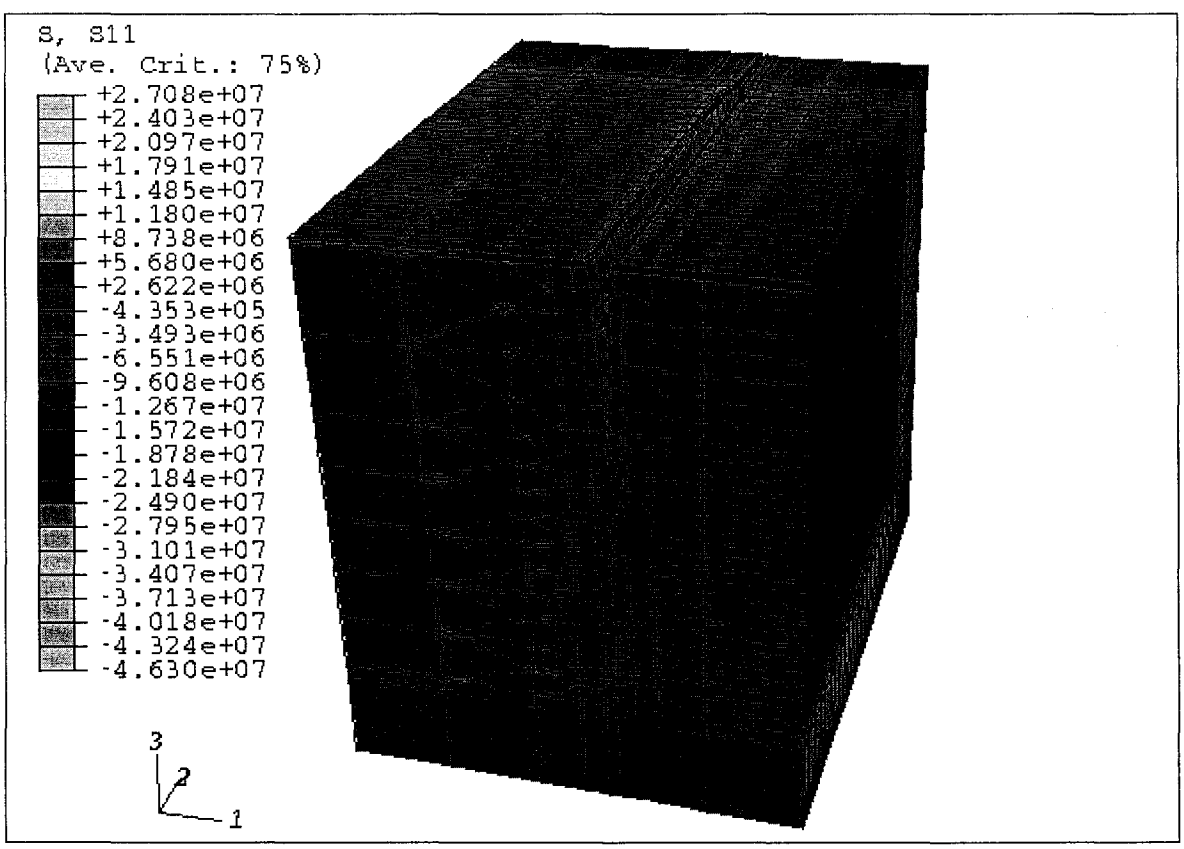
S, S11
(Ave. Crit.: 75%)
+2.708e+07
+2.403e+07
+2.097e+07
+1.791e+07
+1.485e+07
+1.180e+07
+8.738e+06
+5.680e+06
+2.622e+06
-4.353e+05
-3.493e+06
-6.551e+06
-9.608e+06
-1.267e+07
-1.572e+07
-1.878e+07
-2.184e+07
-2.490e+07
-2.795e+07
-3.101e+07
-3.407e+07
-3.713e+07
-4.018e+07
-4.324e+07
-4.630e+07
3
2
1

(d)

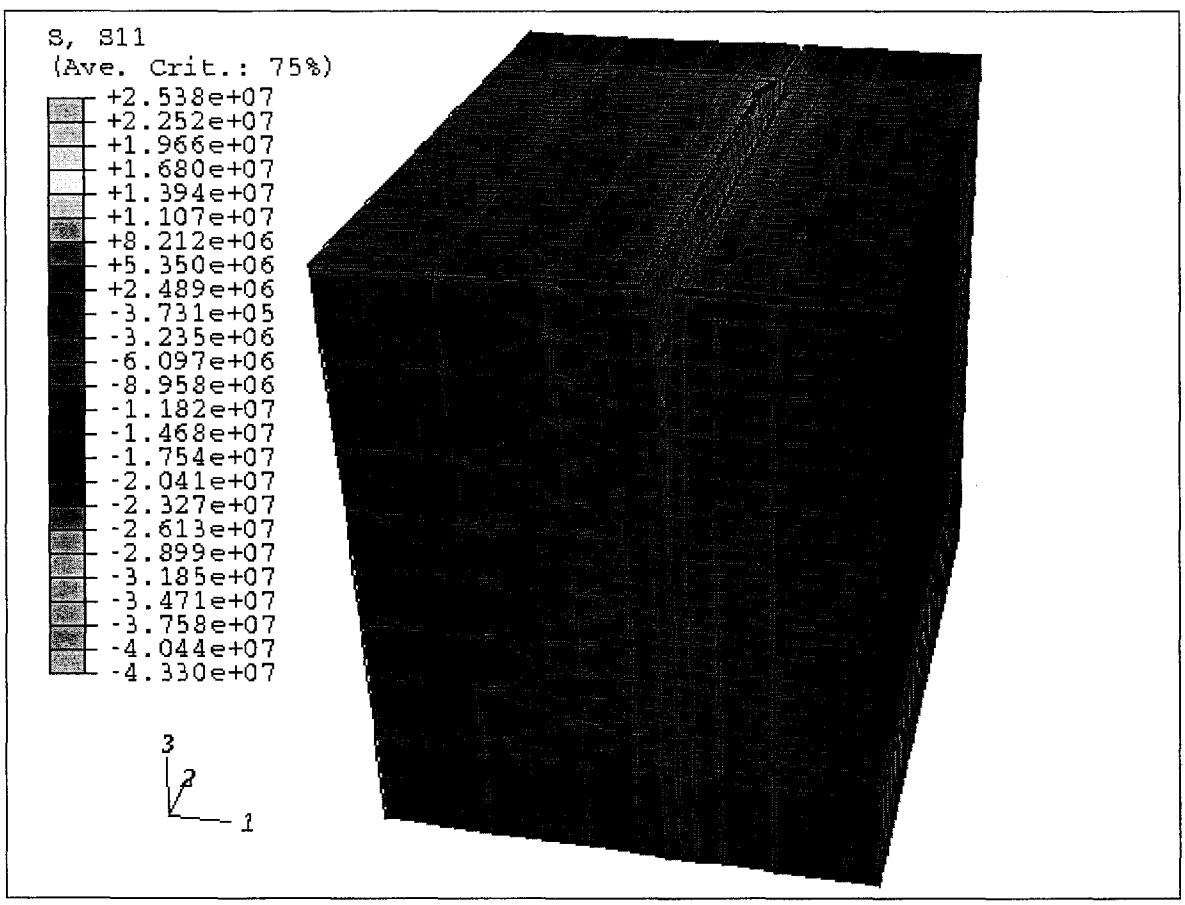
S, S11
(Ave. Crit.: 75%)
+2.538e+07
+2.252e+07
+1.966e+07
+1.680e+07
+1.394e+07
+1.107e+07
+8.212e+06
+5.350e+06
+2.489e+06
-3.731e+05
-3.235e+06
-6.097e+06
-8.958e+06
-1.182e+07
-1.468e+07
-1.754e+07
-2.041e+07
-2.327e+07
-2.613e+07
-2.899e+07
-3.185e+07
-3.471e+07
-3.758e+07
-4.044e+07
-4.330e+07
3
2
1

(e)

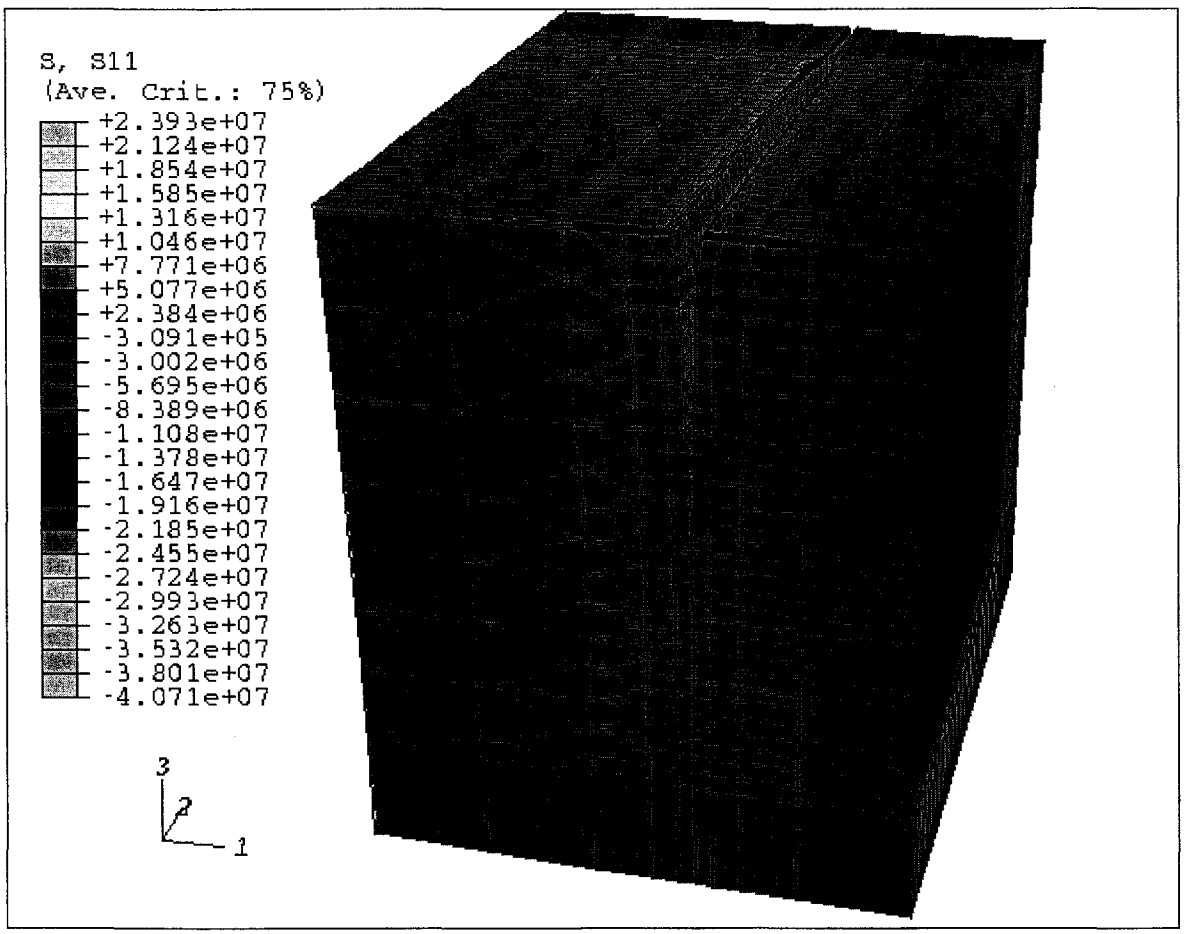

Figure 8.7: Contour plot of stress in local 1-direction for different crack depths: (a) 0.25 m crack depth; (b) 0.31 m crack depth; (c) 0.37 m crack depth; (d) 0.43 m crack depth and (e) 0.49 m crack depth.

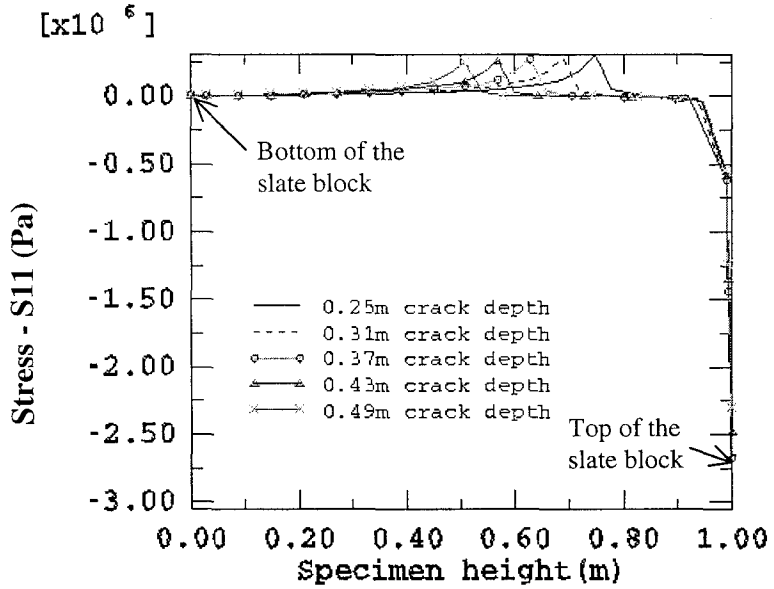

Figure 8.8: Variation of stress in local 1-direction along the height of the specimen for various depths of crack.

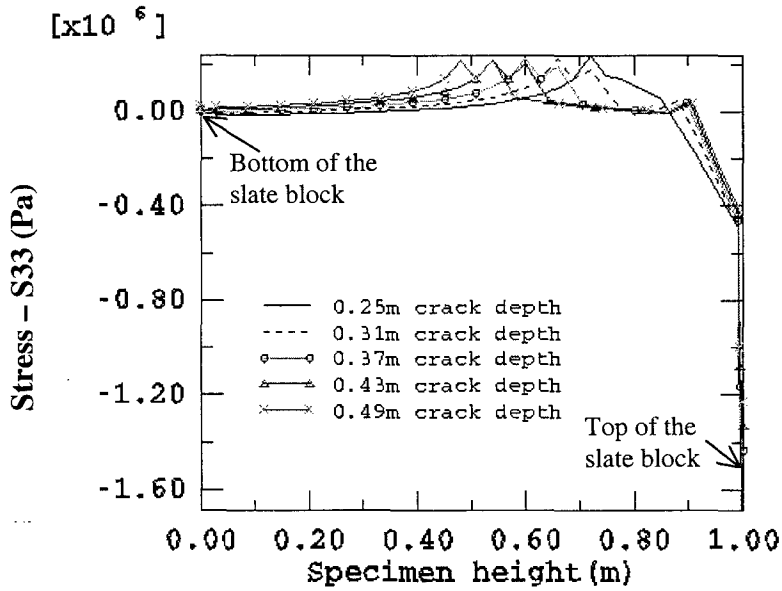

Figure 8.9: Variation of stress in local 3-direction along the height of the specimen for various depths of crack.

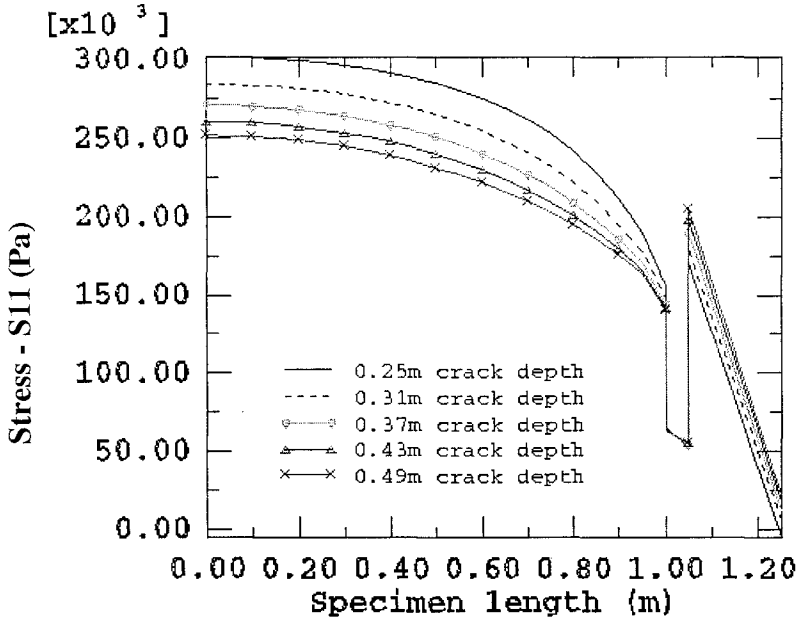

Figure 8.10: Variation of stress in local 1-direction along the crack front for various depths of crack as plane crack propagates (variable breaking load).

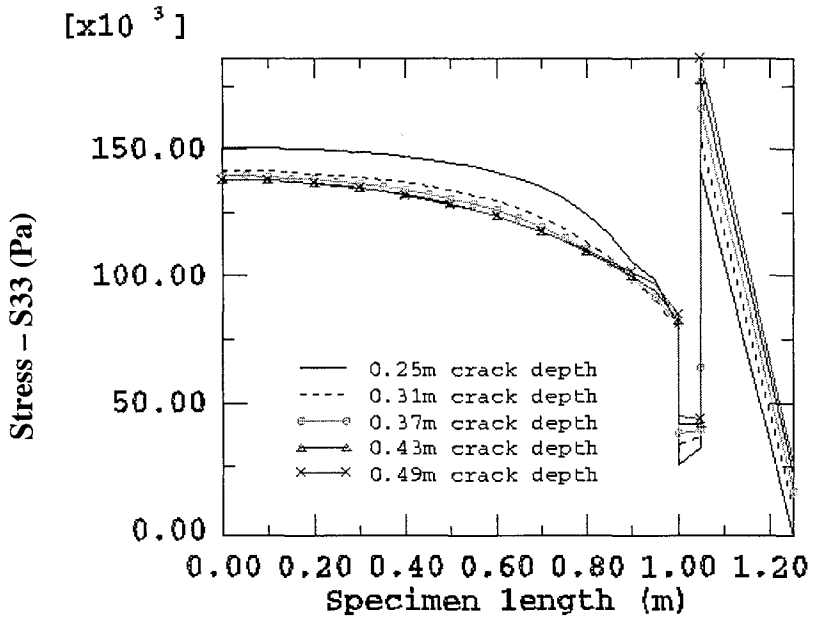

Figure 8.11: Variation of stress in local 3-direction along the crack front for various depths of crack as plane crack propagates (variable breaking load).

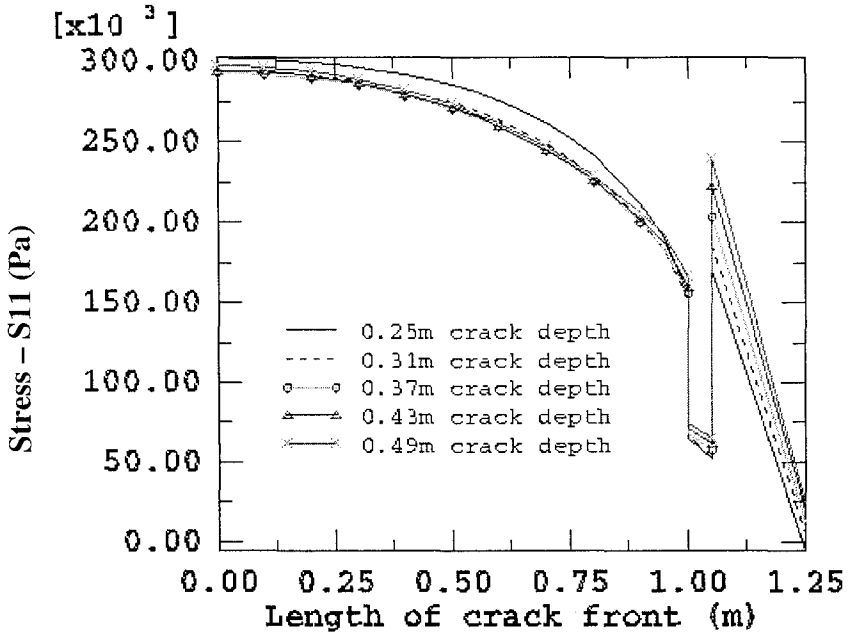

Figure 8.12: Variation of stress in local 1-direction along the crack front for various depths of crack as plane crack propagates (constant breaking load).

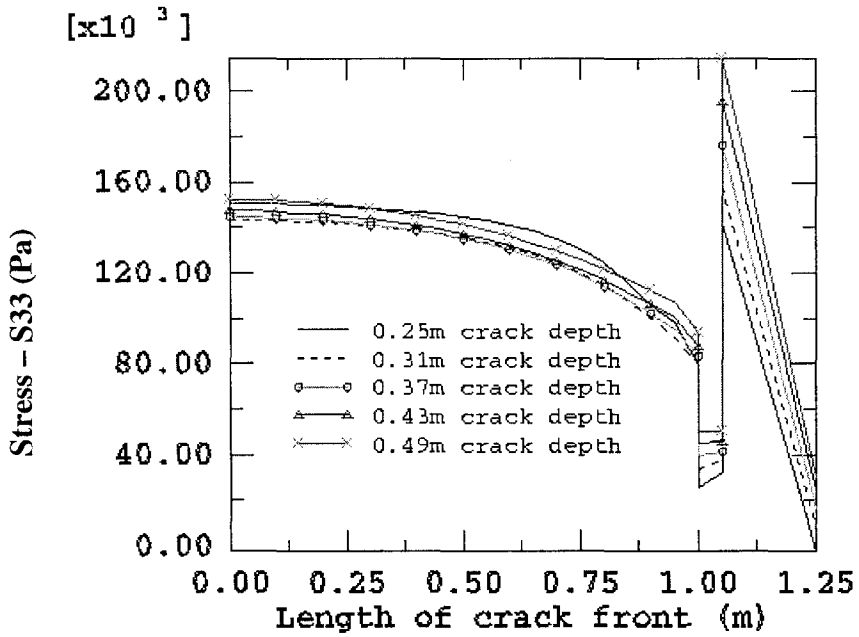

Figure 8.13: Variation of stress in local 3-direction along the crack front for various depths of crack as plane crack propagates (constant breaking load).

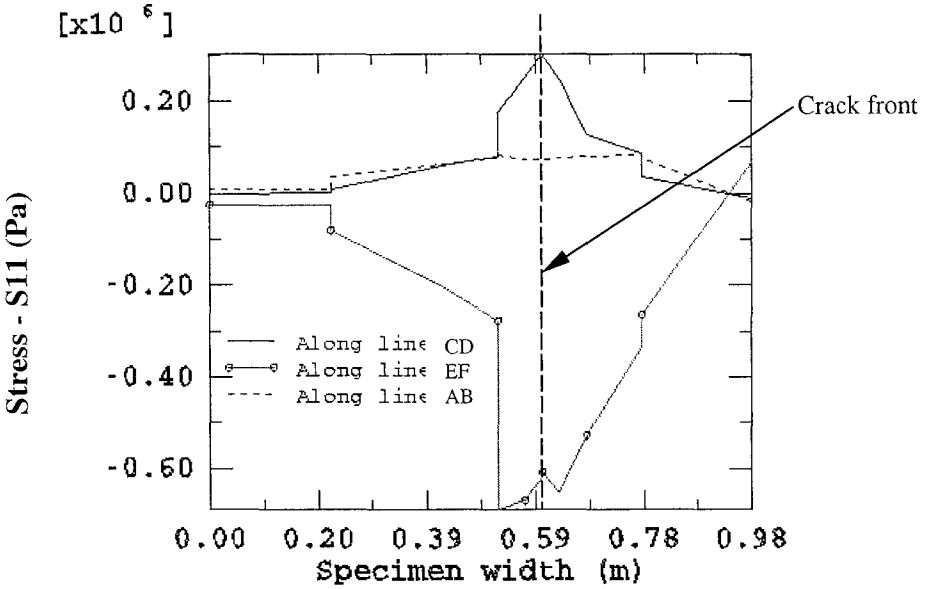

Figure 8.14: Variation of stresses in local 1-direction along the lines AB, CD and EF shown in Figure 7.3 for a crack depth 0.25 m.

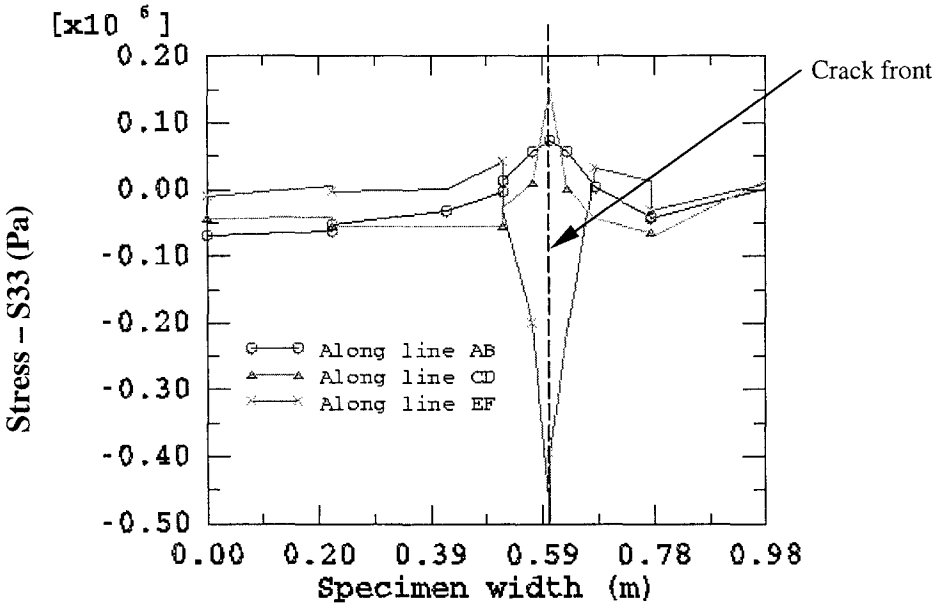

Figure 8.15: Variation of stresses in local 3-direction along the lines AB, CD and EF shown in Figure 7.3 for a crack depth 0.25 m.

Variation of stresses in local 1- and 3- directions along the line of the crack front and the lines 0.08 m left and 0.08 m right of the crack front were shown in Figures 8.16 and 8.17. It is seen that stresses along the line of the crack front always greater than the other two. Stresses in local 1-direction along the line 0.08 m left of the crack front line (on the cracking side of rock) was obtained to be greater than those obtained from the location, 0.08 m right (on the uncracking side of rock). The stress in local 3- direction along the line 0.08 m to the right of the crack front was obtained to be compressive. The existence of continuous slate rock at the right side of the crack front generates this variation of stresses.

Variation of mode I stress intensity factors (SIF) with respect to crack depth for assumed variable loads and constant load in static analysis, along the crack front, and at the crack tip point are shown in Figures 8.18 to 8.20. It is seen that SIFs decrease as crack depth increases for assumed variable loads. However, this change in SIF was not regular. When crack depth changed from 0.25 m to 0.31 m, SIF decreased by 6.054%; when it changed from 0.31 m to 0.37 m, SIF decreased by 4.784%; and subsequently, when crack depth changed from 0.37 m to 0. 43 m and 0.43 m to 0.49 m, SIF decreased by 4.03% and 3.34%, respectively. Improper consideration of crack propagation velocity that was used to determine the breaking load for the uncracked part of the slate rock could be a reason for this variation of SIFs. For the constant load case, mode I stress intensity factors decreased first and then started to increase as crack depth increased gradually (see figure 8.20). It is well known that mode I SIFs vary linearly with respect to the far field stress, the square root variation of crack depth and a factor related to the geometry of the body. Therefore, for constant load cases SIFs should increase as crack depth increases if other parameters

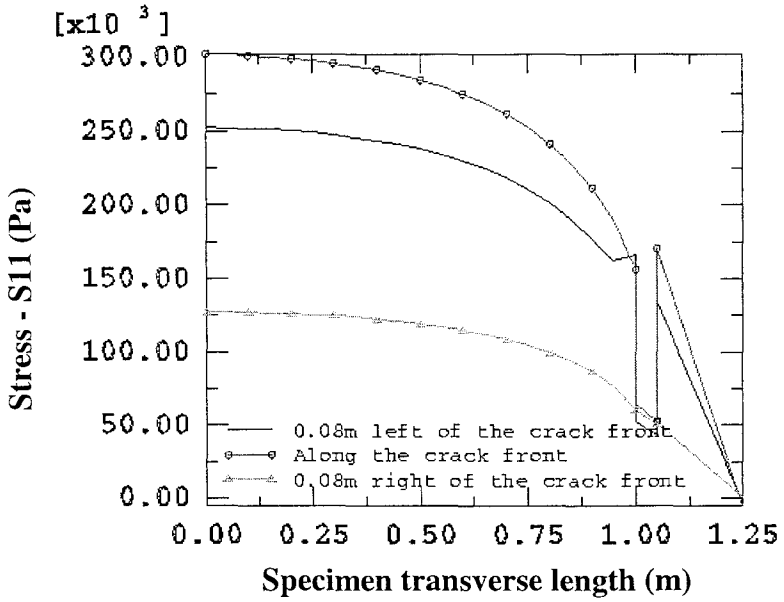

Figure 8.16: Variation of stresses in local 1-direction along the lines parallel to the crack front at different locations of the slate block.

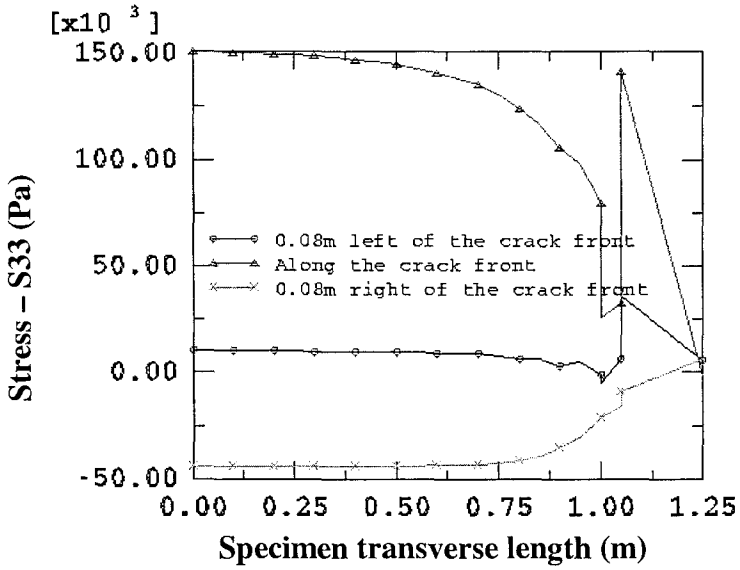

Figure 8.17: Variation of stresses in local 3-direction along the lines parallel to the crack front at different locations of the slate block.

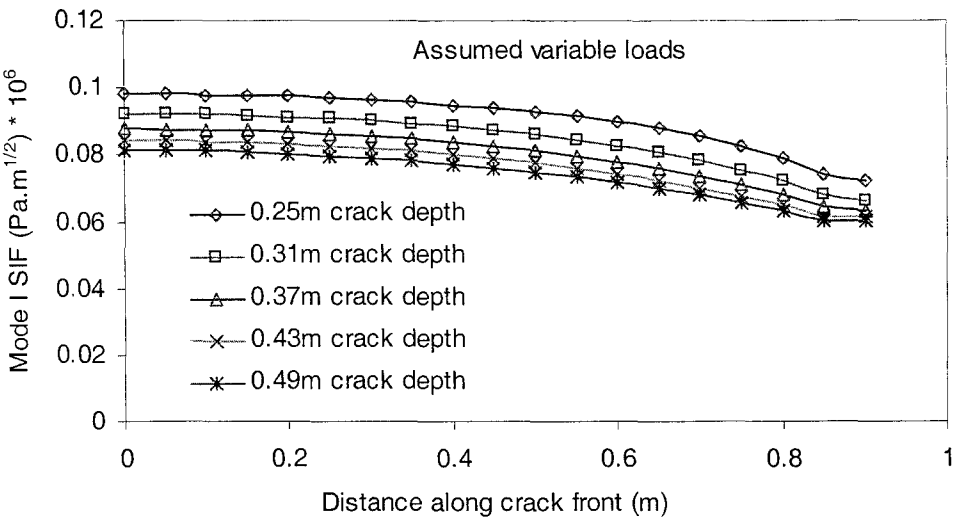

Figure 8.18: Variation of mode I stress intensity factor (SIF) along the crack front for various depths of crack as plane crack propagated along the splitting plane (variable breaking loads).

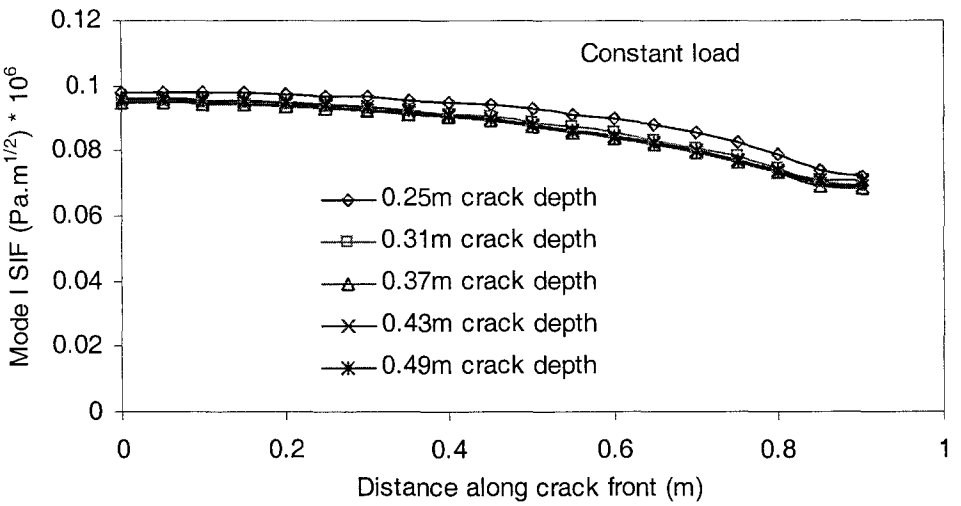

Figure 8.19: Variation of mode I stress intensity factor (SIF) along the crack front for various depths of crack as plane crack propagated along the splitting plane (constant load).

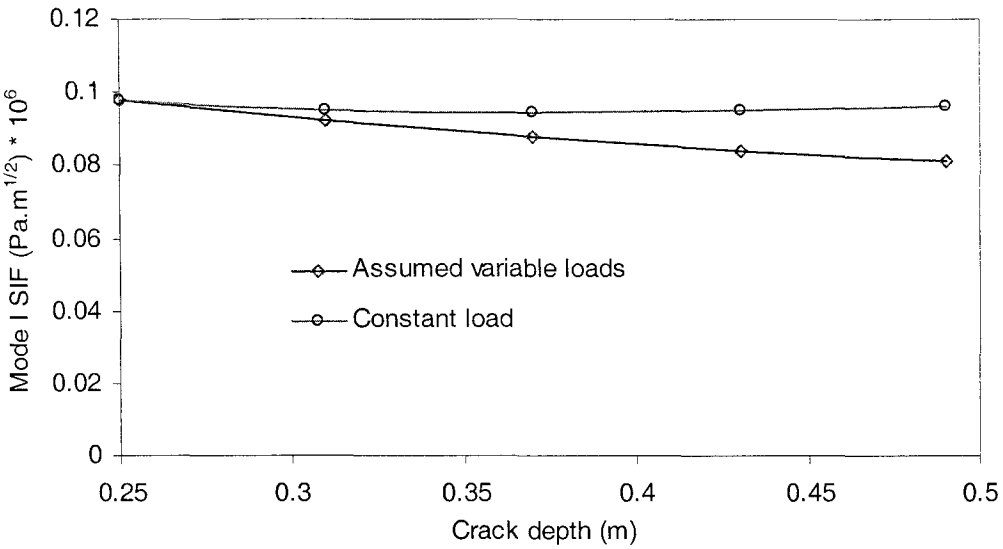

Figure 8.20: Variation of mode I stress intensity factor (SIF) with respect to crack depth at the crack tip point.

remain constant; whereas it remains a constant in this situation. Probably the factor related to the geometry of the body may be changing.

The load considered in this analysis was an assumed load obtained from the experimental breaking of the 0.10 m cubic plane strain slate block. This is not the actual breaking load for the present problem in which long and deeper slate slab needs to be separated from its original state. Breaking load for this case could be determined from the plane strain fracture toughness value of slate rock (0.292 ± 0.0379 MPa.m$^{1/2}$) by assuming that the stress intensity factors vary linearly with respect to the applied load. The load corresponding to mean plane strain fracture toughness obtained for the in-situ field problem having a size of 2.0 m (length) by 1.0 m (depth) by 0.98 m (width) slate slab (without taking into account unbounded domain) was 327.76 kN as the SIF value

was obtained as 0.098 MPa.m$^{1/2}$ for this block with 0.25 m initial crack length. This load (peak value of load time curve) was calculated by multiplying the distributed load obtained from the value of plane strain fracture toughness by the longitudinal area of the wedge at a height 0.02 m above the wedge tip. The load was obtained as 402.69 kN when the correlation equation (7.3) was applied for the same initial crack length. This is 22.56% more than the finite element analysis results. This shows that equation (7.3) is a reasonably good equation to estimate the breaking load of in-situ slate rock.

8.3 Reduction of Wastage in Slate Manufacture

As outlined in the first chapter, one of the possible outcomes of this study would be the great amount of reduction of wastage that could be achieved by the use of this method in the manufacture of slate products. It was observed from a careful examination of the impact breaking loads given in Tables 4.17, 4.18 and 4.19, 35 to 40% of the slate blocks gave loads lower or much lower than the expected impact load for the various individual blocks. It is surmised in this study that this reduction in the impact strength of slate blocks was most probably due to the presence of inherent flaws within the slate blocks. Therefore as a conservative estimate it is assumed that nearly 33% of slate material will be wasted due to the presence of cracks, damaged zones and presence of nonslaty material in the split slate blocks.

Since the blocks split in the field will have irregular boundaries due to splitting across the drilled holes, they have to be sized in the field into regular blocks by using the Hunter saw (given in Figure A8 in Appendix A). This would reduce the usable amount of slate to 80% to 85% during the initial stage of mining. Since the blocks are also to be

subsequently impact split by the use of hydraulic actuator and manual procedures (chisel and mallet – Appendix A6-IV and A6-V) another 33% of slate is also assumed to become unusable. Finally this will leave an usable amount of 25 to 30% of the initial amount of slate mined. This is nearly 5 to 6 times more than the present 5.0% of usable slate products mined (see section 1.1).

Chapter 9

Conclusions and Recommendations

9.1 Conclusions

An effort has been made to reasonably characterize the splitting process of naturally bedded layered slate rock. The main objectives of this study were: (i) To determine the physical and mechanical properties of slate (as a material) that were required for subsequent numerical analyses; (ii) To investigate the impact splitting of slate rock experimentally (from small scale to reasonably intermediate scales); and (iii) To carry out numerical analysis of the impact splitting of slate blocks having finite sizes (plane strain blocks, 3D blocks and field problems) using impact forces determined from experimental study in the laboratory. In addition an attempt has also been made to develop a correlation equation for the determination of the approximate impact splitting force for plane strain slate blocks, using the results obtained from numerical analysis of variously sized plane strain slate blocks.

From the literature review of the formation of slate rock, minerals content, and their characteristic properties it is seen that slate is a fine grained, crystalline rock that resulted

from sediments of clay and fine silt that were deposited on seabed, which can be easily split into almost parallel uniform layers. It was also observed that easy splitting of slate was possible due to the following reasons:

(i) presence of minute flaky minerals that had re-orientated themselves along defined planes, with, probably, some shearing action;

(ii) growth of new flaky minerals similarly orientated (an incipient schistosity); and

(iii) flattening of mineral particles and grain orientation perpendicular to compression direction due to intense pressure and consequent deformation.

An extensive and detailed laboratory testing was carried out to determine relevant physical and mechanical properties of slate that were required for the subsequent numerical investigation of impact splitting loads. From this study it is concluded that mechanical properties (elastic moduli, Poisson's ratio, compressive and tensile strengths, hardness, fracture toughness) determined experimentally were not constant for all test specimens; the mean and standard deviation of the determined properties were estimated. The mean Young's modulus of elasticity and Poisson's ratio with their standard deviation obtained from this study were E_{11} = 72.95 ± 15.33 GPa, E_{22} = 78.74 ± 17.62 GPa and E_{33} = 39.645 ± 3.85 GPa, and ν_{12} = 0.236 ± 0.085, ν_{13} = 0.171 ± 0.01434 and ν_{23} = 0.165 ± 0.041, and ν_{31} = 0.192 ± 0.078. Co-efficient of friction was obtained as 0.56 ± 0.0037. Material properties in a planar direction varied less than those obtained in the direction perpendicular to the plane although there were no well defined planes in the slate (from microscopic studies). Therefore, it was assumed that slate material is a transversely isotropic material. It must be mentioned here that the present results seem to have the

smallest variation in physical and mechanical properties when they are compared with the published results available in open literature.

Two types of fracture toughness values i.e, displacement based and stress based, were obtained. Displacement based fracture toughness values were obtained to be slightly larger (0.33 $MPa.m^{1/2}$) than the stress based fracture toughness values (0.292 $MPa.m^{1/2}$). Stress based fracture toughness was obtained when the load was applied parallel to the plane in three point bending test of cylindrical specimens. Displacement based fracture toughness was obtained when load was applied perpendicular to the plane in four point bending. The fracture toughness value selected for impact splitting parallel to the bedding planes was taken as the lowest of the two values measured namely (0.292 $MPa.m^{1/2}$).

From the scanning electron microscope study of slate, it was revealed that micro cracks existed at grain boundaries, discontinuities of layering were common features, and layer interfaces seemed to be well defined crack surfaces.

Experiments were also carried out to examine the impact splitting of slate blocks. The magnitude of the impact forces needed to split a number of finite sized slate blocks, both under in-plane strain and under non-plane strain test conditions. Crack propagation directions and the splitting surfaces were also examined visually. From the results obtained in these studies it was concluded that plane strain blocks started to break apart when the load reached the peak value; for non-plane strain blocks they started to split before the load reached its peak value. Breaking load was not consistent with the sizes of blocks in some cases. Some of the larger blocks took lesser loads to break than those found for relatively smaller blocks; this difference in behaviour was observed to be due to

the presence of pre-existing flaws. Split surface texture of load resisting parts of splitting surface was observed to be different from those of unresisting parts. Load resisting parts of splitting surfaces seemed to be fairly regular whereas the non-resisting parts (due to previous flaw) seemed to be irregular. Split of the plane strain block started by the extension of crack front horizontally over the cracked surface; the crack plane was almost vertical and the block broke exactly into two pieces. However, in case of non plane strain splitting, crack started first under the wedge tip and spread horizontally and vertically downward. Propagation of crack was observed to be unsymmetric.

Velocity of crack propagation was determined using strain gauge sensors fixed at some regular intervals on the surface of the slate block, perpendicular to the cracking plane. In most of the cases, irregular variation of crack propagation velocities was obtained. However, for a few cases almost linearly decreasing crack propagation velocities were obtained. The velocities were observed to vary between 2.0 m/s to 120 m/s. The crack velocity considered for numerical analysis was taken to vary between 55 to 38 m/s.

Impact splitting of slate rock for plane strain and non-plane strain specimens were analyzed numerically using the plane strain fracture toughness as a crack propagation criteria. In the numerical analysis, finite element method was used to determine the mode I stress intensity factors as a function of geometry of the body, crack depth and applied load. Though the stresses in local 1- and 2- directions of 3D finite element analysis were much lower than those obtained during plane strain finite element analysis, the SIFs (in both cases) showed very good agreement (<10%). Path independent contour integral was used to calculate SIFs as it was not influenced much by the size of the mesh used.

Linearly decreasing and constant crack propagation velocities were taken into consideration for this analysis (linearly varying between 55 to 38 m/s and constant at 46.5 m/s). The mode I stress intensity factors of a 0.10 m cubic slate block, in the range of propagating crack lengths of 0.0325-0.0550 m, agreed very well with the experimentally measured static fracture toughness values (0.292 $MPa.m^{1/2}$) for both the cases of crack velocity propagation. It was also observed that the crack propagation velocities had little or almost no effect on the variation of the SIFs. Size effect of the plane strain slate blocks on mode I stress intensity factor was also considered in this analysis. In this case 0.10 m cubic slate block was taken as the reference slate block. It was seen that SIFs varied in an inverse manner with respect to the width. Higher SIFs were obtained for specimens having a width less than the width of the reference slate block. SIFs also varied with the depth of the specimens but the variation was much less than that obtained for width. Variation of SIFs was less than 7.8% when depth of the block was increased to twice the depth of reference block by keeping other dimensions constant. SIF values were obtained higher by 10% for linearly decreasing crack propagation velocities than for constant crack propagation velocities, for both plane strain and 3D analyses.

From a review of literature available for plane crack propagation in real 3D bodies, it was observed that plane strain crack propagates in the body either in a cylindrical or elliptic manner. In this study it was observed that a cylindrical or elliptical crack front did not produce an almost constant stress intensity factor (SIF) along the crack front; hence a parabolic crack front was considered in this study. For the finite element analysis of 3D slate blocks a parabolic crack was assumed to propagate in a symmetric manner within the body under the edge of impacting wedge, since it produced an almost constant SIF (or

fracture toughness) along the crack front. Crack propagated both in horizontal and vertical directions. The variation of stress intensity factors in this case was not exactly similar to those obtained earlier for plane strain equivalent 3D analysis. A difference of around 15% was observed up to a crack extension of 0.4 times the depth of specimen along the symmetry line. However, variation of SIFs was much more when the crack extended beyond this. The magnitude of SIFs varied within 15% of their average values along the crack front at each five increments of crack except at the outer surface nodes. At the position of crack front where horizontal surface and vertical edge met together SIFs decreased by more than 50% of the average value.

Correlation between mode I stress intensity factors, splitting loads and geometry of plane strain slate blocks was established to find out the approximate breaking load for a limited size of plane strain slate blocks. Plane strain fracture toughness played a significant role in this regard. Experimentally determined fracture toughness values corresponding to breaking loads of different sized plane strain slate blocks were compared with those obtained from the numerical investigations, and the theoretical impact splitting load computed. A difference of around + 0.78 to – 32.34% was observed between the measured and numerically computed values.

Numerical investigations of an exact field problem (separation of long slate slab from the original rock state) were carried out using static finite element analysis. The breaking load obtained from this study was compared with that obtained from the correlation equation. A good agreement (difference was less than 15%) was obtained between them.

The study carried out in this thesis on the impact splitting of naturally bedded slate rocks could be used to design instrumentation (indenting wedge with hydraulic actuator) for breaking slate rocks in industries as well as under field situations that would produce regular sized slate blocks without much wastage.

9.2 Contributions Obtained from the Study

* The physical and mechanical characterization of Newfoundland slate (from Britannia Cove formation) was achieved for the first time.
* The impact load, obtained from the splitting test on a chosen slate block, produced a mode I SIF value (numerically computed) which was almost equal to the fracture toughness value obtained from earlier experimental measurements (see Figures 5.15, 5.29, 5.30 and 5.31). This was used for bench marking the subsequent computations.
* It was observed that in a three-dimensional crack propagation problem the crack front had to be parabolic to obtain an almost equal SIF (or fracture toughness) value along the crack front.
* A correlation equation was established between the experimental impact load and geometrical dimensions of slate block for blocks loaded under plane strain conditions.
* A field problem was also numerically examined to see whether the laboratory study can be used in the field context. It was found that the error between the established correlation equation, and numerical results were around 15%.
* It was also observed that a much higher reduction of wastage (approximately 30% to 35%) of slate material can be achieved through the use of this impact splitting procedure.

9.3 Recommendations for Future Study

The following additional investigations are required to complete the studies reported in this thesis:

1. More laboratory tests for small scale as well as large scale specimens need to be conducted to determine plane strain fracture toughness values of slate rocks used in this study. Probably a new test needs to be developed to examine whether the static fracture toughness values were the same as the critical SIF values obtained during impact splitting of rocks.
2. Determination of dynamic mechanical properties should be made to obtain the proper values that are to be used for numerical analysis.
3. Velocity of crack propagation needs to be determined using high sensitivity semiconductor strain gauges as well as photographic examinations using a high speed camera.
4. Size of the plane strain slate blocks other than 0.1m transverse length slate blocks need to be broken in the laboratory to determine generalized breaking loads.
5. The effectiveness of impact indenter splitting of slate rocks against the hydraulic splitter approach (with drilled holes) should be examined.
6. Plane strain splitting test needs to be carried out for specimens having an initial cut.
7. Analyses need to be carried out considering variable initial crack lengths starting from very small values (approximately 1% of the specimen depth). Higher order elements should be used in 3D analysis, to get better correlation between analysis and results.

8. Field problem needs to be analyzed considering drill holes instead of soft material layer. Dynamic analysis needs to be carried out by taking special care for the infinite elements.
9. Discontinuous indenting wedges, instead of the continuous wedge used in separating the long slab of slate rock from the slate quarry, need to be considered for the finite element analysis.
10. To develop proper correlation equations for 2-D (plane strain) and 3-D situations, considerably more results need to be obtained from numerical analysis of various sizes of slate blocks. Some numerical investigations carried out in this thesis, support the relationship developed in this study; but restriction on some of important factors such as depth and width of the specimen as well as boundary conditions (continuous media in field situation) and initial crack depth need to be relaxed for developing a generalized relationship.

References

ABAQUS, 1991. Fracture Mechanics (manual), Hibbitt, Karlsson & Sorensen, Inc., Pawtucket, RI 02860-4847.

ABAQUS/Standard 5.7, 1997. "User Manual", Vol. 1, Hibbitt, Karlsson & Sorensen, Inc.

ABAQUS/Standard 6.3, 2002. "User Manual", Vol. 1, Hibbitt, Karlsson & Sorensen, Inc.

ABAQUS 6.3, 2002. "Keynote Manual", Hibbitt, Karlsson & Sorensen, Inc.

Abrate, S., 1998. Impact on composite structures, Cambridge University Press, 289p.

Attewell, P. B., and Taykor, R. K., 1969. "A microtextural interpretation of a Welsh slate", Int. J. Rock. Mech. Min. Sci., Vol. 6, pp. 423-438.

Bakewell, R., 1815. An Introduction to Geology, Harding, London, 2nd ed., 492p.

Barsoum, R. S., 1976. "A Degenerate Solid Element for Linear Fracture Analysis of Plate Bending and General Shells", International Journal for Numerical Methods in Enginering, Vol. 10, pp. 551-564.

Bear, T. J. and Barr, B., 1977. "Fracture Toughness Tests for Concrete", Int. Journal of Fracture, Vol. 13, pp. 92-96.

Begley, J. A. and Landes, J. D., 1972. "The J-Integral as a Fracture Criterion", Fracture Toughness, Proceedings of the 1971 National Symposium on Fracture Mechanics, Part II, ASTM STP 514, American Society for Testing and Materials, pp. 1-20.

Bieniawski, Z. T., 1968b. "Fracture Dynamics of Rock", The International Journal of Fracture Mechanics, Vol. 4, no. 4, pp. 415-430.

Bieniawski, Z. T., 1967. "Mechanism of Brittle Fracture of Rock Part I – Theory of the Fracture Process", International Journal of Rock Mechanics and Mining Science, Vol. 4, pp. 395-406.

Bieniawski, Z. T., 1966. "Fracture Velocity of Rock", Report of the South African Council of Scientific and Industrial Research No. MEG 517

Bilek, Z., 1980. "Some Comments on Dynamic Crack Propagation in a High Strength Steel. Crack Arrest Methodology and Applications", ASTM STP 711, G. T. Hahn and M. F. Kanninen, Eds., American Society for Testing and Materials, pp. 240-247.

Bligh, T. P., 1974. "Principles of Breaking Rock Using High Pressure Gases", Proc. 3rd Int Cong. on Rock Mech., Denver, IIB, US Nat. Acad. Sci., 1421-1427.

Blackwood, G., 1993. "Geological Report on the Britannia Cove Slate Quarry", Newfoundland slate Incorporated, unpublished report, 106 pages. [2C/04 (60)]

Bolotin, V. V., 2001. "Mechanics of Delaminations in Laminate Composite Structures", Mechanics of Composite Materials, Vol. 37, no. 5/6, pp. 367-380.

Boutinguiza, M., Lusquinos, F., Pou, J., Soto, J., Quintero, F., and Perez-Amor, M., 2002. "Cutting of Slate Tiles by CO_2 Laser", Journal of Laser Applications, Vol. 14, No. 1, pp. 9-12.

Broek, D., 1974. Elementary Engineering Fracture Mechanics, Noordhoff International Publishing, A division of A. W. Sijthoff International Publishing Company B. V., Leyden, The Netherlands, 408 p.

Browning, B., Cook, G. and Timbrell, C., 2001. "Predicting Large Scale Crack Growth in 3D Finite Element Models", 2001 ABAQUS Users' Conference.

Brown, W. F. and Srawley, J. E., 1965. "Fracture Toughness Testing", Fracture Testing Special Technical Publication ASTM No. 381, pp. 133-196.

Bush, A. J., 1976. "Experimentally determined stress intensity factor for single-edge crack round bar loaded in bending", Expl. Mech., 1976,Vol. **16**, 249-257.

C 120 – 52 (1981), 1984. "Method of Flexure Testing of Slate (Modulus of Rupture, Modulus of Elasticity)", Annual Book of ASTM Standards, section 4, Vol. 04.08, pp. 12-14.

C 170 – 50 (1981), 1984. "Test Method for Compressive Strength of Natural Building Stone", Annual Book of ASTM Standards, section 4, Vol. 04.08, pp. 17-19.

C 406 – 58 (1981), 1984. "Specification for Roofing Slate", Annual Book of ASTM Standards, section 4, Vol. 04.08, pp. 26-28.

C 1327 – 99, 2000. "Standard Test Method for Vickers Indentation Hardness of Advanced Ceramics", Annual Book of ASTM Standards, Vol. 03.01, pp. 480–487.

C 1421 – 99, 2000. "Standard Test Methods for Determination of Fracture Toughness of Advanced Ceramics at Ambient Temperature", Annual Book of ASTM Standards, pp. 641–672.

Challinor, J., 1967. "A Dictionary of Geology", Cardiff University of Wales Press, Third Edition, pp. 298.

Chan, S., Tuba, I. S., and Wilson, W. K., 1970. "On the Finite Element Method in Linear Fracture Mechanics", Eng. Frac. Mech. 2, 1, pp. 1-18

Chow, C-Lun. and Burns, S. J., 1980. "K_{Id} - Values Deduced from Shear Force Measurements on Double Cantilever Beam Specimens", Crack Arrest Methodology and Applications, ASTM STP 711, G. T. Hahn and M. F. Kanninen, Eds., American Society for Testing and Materials, pp. 228-239.

Christensen, R. M., 1975. "Wave Propagation in Layer Elastic Media", Journal of Applied Mechanics, pp. 153-158.

Cook, G., Timbrell, C. and Claydon, P., 1990. "Automatic and Adaptive Finite Element mesh Generation for Full 3D Fatigue Crack Growth", STRUCENG & FEMCAD Conference, Grenoble, France, 1990.

Craig A. B., Eber, L. and Fyfe, I. M., 1998. "A Study of Failure in Small Pressurized Cylindrical Shells Containing a Crack", A report prepared for Langley Research Center under Grant NAG1-1586, NASA/CR-1998-208454.

D 3148 – 80, 1984. "Test Method for Elastic Moduli of Intact Rock Core Specimens in Uniaxial Compression", Annual Book of ASTM Standards, section 4, Vol. 04.08, pp. 501-507.

D 2930 – 78, 1984. "Direct Tensile Strength of Intact Rock Core Specimens", Annual Book of ASTM Standards, section 4, Vol. 04.08, pp. 455-459.

Dally, J. W., 1979. "Dynamic Photoelastic Studies of Fracture", Experimental Mechanics, 19, 349-361.

Dally, J. W., Shukla, A., and Kobayashi, T., 1980. "A Dynamic Photoelastic Study of Crack Propagation in a Ring Specimen", Crack Arrest Methodology and Applications, ASTM STP 711, G. T. Hahn and M. F. Kanninen, Eds., American Society for Testing and Materials, pp. 161-177.

Daniel, P., 1993. "Slate Without Waste", Industrial Diamond Review, Vol. 53, pp. 200-204.

Darwin, C., 1846. Geological Observations on South America, Smith-Elder, London, 279 pp.

Davies, J. D. and Stagg, K. G., 1970. "Splitting Tests on Rock Specimens", Proceedings of the Second Congress of the International Society for Rock Mechanics, Vol. 2, Themes 3-48.

Delph, T. J., and Herrmann, G., 1983. "An Effective Dispersion Theory for Layered Composites", Journal of Applied Mechanics, Vol. 50, pp. 157-164.

Duckworth, W. H., 1951. "Precise Tensile Properties of Ceramic Bodies", J. Am. Cer. Soc., Vol. 34, No. 1, pp. 1-9.

E 384 – 99, 2000. "Standard Test Method for Microindentation Hardness of Materials", Annual Book of ASTM Standards, Vol. 15.01, pp. 409–432.

E 140 – 97, 2000. "Standard Hardness Conversion Tables for Metals, Relationship among Brinell Hardness, Vickers Hardness, Rockwell Hardness, Superficial Hardness, Knoop Hardness and Scleroscope Hardness", Annual Book of ASTM Standards, Vol. 03.01, pp. 409–432.

Evans I., 1962., "A Theory of the Basic Mechanics of Coal Ploughing", Proceedings of the International Symposium on Mining Research, (G. Clark, Ed.), Vol. 2, 761-798, Pergamon Press, Oxford.

Gabriel, B. L., 1985. "SEM: A User's Manual for Materials Science", American Society for Metals, Metals Park, OH.

Gdoutos, E. E., 1990. Fracture Mechanics Criteria and Applications, Kluwer Academic Publishers, 313p.

Gdoutos, E. E., 1993. Fracture Mechanics: An Introduction, Kluwer Academic Publishers, 307p.

Griffith, A. A., 1921. "The Phenomena of Rupture and Flow in Solids", Phil. Trans. Roy. Soc. London, Series A, Vol. 221, pp.163-198.

Griffith, A. A., 1924. "The Theory of Rupture", Proc. 1st Int. Cong. Appl. Mech., Delft, pp. 55–63.

Haisty, B. S. and Springer, W.T., 1985. "The Longitudinal Vibration Characteristics of a Uniform Beam Containing Two Symmetric Discontinuities", Proceedings of the Society for Experimental Mechanics, Spring conference, pp. 389-393.

Haisty, B. S. and Springer, W.T., 1988. "A General Beam Element for Use in Damage Assessment of Complex Structures", Journal of Vibration, Acoustics, Stress and Reliability in Design, Vol. 110, pp. 389-394.

Hakalehto, K. O., 1970. "A note on the Fracture of Rock under Impulses", Proceedings of the Second Congress of the International Society for Rock Mechanics, Vol.2, Themes 3-32.

Hardy, M. P., 1973. "Fracture Mechanics Applied to Rock", Ph. D. Thesis, Faculty of the Graduate School, University of Minnesota, 231p.

Hegemier, G. A., and Nayfeh, A. H., 1973. "A Continuum Theory for Wave Propagation in Laminated Composites/case1: Propagation Normal to the Laminates", Journal of Applied Mechanics, pp. 503-510.

Hegemier, G. A., and Bache, T. C., June 1973. "A Continuum Theory for Wave Propagation in Laminated Composites/case II: Propagation Parallel to the Laminates", Journal of Elasticity, Vol. 3, No. 2, pp. 125-140.

Hoek, E. and Bieniawski, Z. T., 1965. "Brittle Fracture Propagation in Rock Under Compression", Int. J. Fract. Mech., Vol. 1, pp. 137-155.

Inglis, C. E., 1913. "Stresses in a Plate Due to the Presence of Cracks and Sharp Corners", Transactions of the Institute of Naval Architects, 55, 219–214.

Irwin, G. R., 1948. "Fracture Dynamics, Fracture of Metals", A. S. M., Cleveland, pp. 147-166.

Irwin, G. R., 1957. "Analysis of stresses and strains near the end of a crack traversing a plate", Journal of Applied Mechanics, Trans. ASME 24, pp. 361-364.

ISRM: 1988. "Suggested Methods for Determining the Fracture Toughness of Rock", F. Ouchterlong (Working Group Co-ordinator), International Journal of Rock Mechanics and Mining Sciences & Geomechanics Abstracts, 25, pp. 71-96.

Jih, C. J. and Sun, C. T., 1990. "Evaluation of a Finite Element Based Crack-Closure Method for Calculating Static and Dynamic Strain Energy Release Rates", Engineering Fracture Mechanics, 37: no. 2, 313–322.

Judd, W. R., 1964. Rock Stress, Rock Mechanics and Research, State of Stress in the Earth's Crust, W. R. Judd (Ed.), New York, Elsevier, pp. 5-51.

Kassir, M. K. and Bandyopadhyay, K. K., 1983. "Impact Response of a Cracked Orthotropic Medium", Journal of Applied Mechanics, Vol. 50, pp. 630-636.

Klepaczko, J. R., Bassim, M. N. and Hsu, T. R., 1984. "Fracture Toughness of Coal Under Quasi-Static and Impact Loading", Engineering Fracture Mechanics, Vol. 19, No. 2, pp. 305-316.

Kobayashi, T. and Dally, J. W., 1980. "Dynamic Photoelastic Determination of the $\dot{a} - K$ Relation for 4340 Alloy steel", Crack Arrest Methodology and Applications, ASTM STP 711, G. T. Hahn and M. F. Kanninen, Eds., American Society for Testing and Materials, pp. 189-210.

Kobayashi, A. S., 1993. Handbook on Experimental Mechanics, Second Revised Edition, Society for experimental mechanics, U. S. A., ISBN 1-56081-640-6 VCH Publishers, 1074p.

Kostrov, B. V., 1975. "On the Crack Propagation with Variable Velocity", International Journal of Fracture, 11, 47-56.

Krueger, R., 1999. "A Shell/3D Modelling Technique for Delaminations in Composite Laminates", In Proceedings of the American Society for Composites, 14th Technical Conference, Technomic Publishing, ISBN 1-56676-791-1, pp. 843-852.

LabView 5.1, 1999. National Instruments Corporation.

Lama, R. D., 1969. "Effect of Nonhomogeneities and Discontinuities on Deformational Behaviour and Strength of Rocks. Metals and Minerals Review", Vol. VIII, No. 8, pp. 3-10.

Lama, R. D. and Vutukuri, V. S., 1978. Handbook on Mechanical Properties of Rocks, Trans Tech Publications, Clausthal, Germany, ISBN 0-87849-021-3, Vol-II, 481p.

Labuz, J. F., Shah, S. P. and Dowding, C. H., 1985. "Experimental Analysis of Crack Propagation in Grinite", Int. J. Rock Mech. Min. Sci. & Geomech. Abstr. Vol.22, No. 2, pp. 85-98.

Lee, J. H., Peacor, D. R., Lewis, D. D. and Wintsch, R. P., 1984. "Chlorite-illite/muscovite Interlayered and Interstratified Crystals: A TEM/STEM Study", Contrib. Mineral Petrol., vol. 88, pp. 372-385.

Liu, G. R. and Xi, Z. C., 2002. "Elastic Waves in Anisotropic Laminates", CRC press, pp.1-20.

Logan, D. L., 2002. "A First Course in the Finite Element Method", Brooks/cole, Wadsworth Group, Thomson learning, USA, Third edition, 696p.

Mall, S. and Luz, J., 1980. "Use of Eight-node Element for Fast Fracture Problem", International Journal of Fracture, **16:** 33-36.

Mall, S., Kobayashi, A. S. and Loss, F. J., 1980. "Dynamic Fracture Analysis of Notch Bend Specimens", Crack Arrest Methodology and Applications, ASTM STP 711, G. T. Hahn and M. F. Kanninen, Eds., American Society for Testing and Materials, pp. 70-85.

Malluck, J. F. and King, W. W., 1980. "Fast Fracture Simulated by Conventional Finite Elements: A Comparison of Two Energy-Release Algorithms", Crack Arrest Methodology and Applications, ASTM STP 711, G. T. Hahn and M. F. Kanninen, Eds., American Society for Testing and Materials, pp. 38-53

Martha, L. F., Wawrzynek, P. A. and Ingraffea, A. R., 1990. "Simulation of Arbitrary Crack Propagation in Three-Dimensions", Proc. 5th Int. Conf. on Num. Meth. in Frac. Mech., Frieburg.

Mazur, C. J., 1985. Fracture Toughness Testing of Coal. Masters Thesis, Department of Mechanical Engineering, West Virginia University, United State America.

Mertin, W., 1983. Once Upon A Mine: Story of Pre-Confederation Mines on the Island of Newfoundland, The Canadian Institute of Mining and Metallurgy, Special Volume 26, 98 pages.

Microsoft Excel 97 SR-2, 1997. Microsoft Corporation.

Mikkola, T. P. J., Leinonen, M., Niemi, H. and Talja, H., 1990. "Automated fracture analysis with three-dimensional finite elements models", Proceedings of the 5th international conference on Numerical methods in Fracture Mechanics, Freiburg, Federal Republic of Germany, pp. 545-556.

Moon, F. C., 1973. "One-Dimensional Transient Waves in Anisotropic Plates", Journal of Applied Mechanics, pp. 485-490.

Mott, N. F., 1948. "Fracture of Metals: Theoretical considerations", Engineering, 165, 16-18.

Murry, A. and Howley, J. P., 1989. "Reports of the Geological Survey of Newfoundland from 1881 to 1909", Newfoundland Mines and Energy, Open File [Nfld.(652)]

Nemat-Nasser, S., 1972. "General Variational Methods for Waves in Elastic Composites", Journal of Elasticity, Vol. 2, No. 2, pp. 73-90.

Nillson, F., 1972. "Dynamic Stress Intensity Factor for Finite Strip Problems", International Journal of Fracture, 8, pp. 403-411.

Nishioka, T. and Atluri, S. N., 1980. "Numerical Modeling of Dynamic Crack Propagation in Finite Bodies, by Moving Singular Elements Part 1: Formulation", Journal of Applied Mechanics, **47:** pp. 570–576.

Nishioka, T. and Atluri, S. N., 1980. "Numerical Modeling of Dynamic Crack Propagation in Finite Bodies, by Moving Singular Elements Part 2: Results", Journal of Applied Mechanics, **47:** pp. 577–582.

Nishimatsu, Y., 1972. "The Mechanics of Rock Cutting", Int. J. Rock Mech. Min. Sci., Vol. 9, pp. 261-270.

Nwosu, D.I., 1993. "Fatigue Strength Analysis of Offshore Tubular Welded Joints under Constant Amplitude Loading: Local Strain and Fracture Mechanics Approach", Ph.D.

Thesis, Memorial University of Newfoundland St. John's, Canada, pp. 90-96, 121-124, 139-149.

Olofsson, T., Fransson, L. and Sandkvist, J., 1991, "Ice Crushing Failure Mechanism", A Joint Project Report between SSPA Maritime Consulting AB and div. of Structural Engineering, University of Lulea.

Orowan, E., 1947. "Notch Brittleness and the Strength of Metals", Trans. Inst. Engineers and Shipbuilders, paper 167

Ouchterlony, F., 1980c. "A New Core Specimen for the Fracture Toughness Testing of Rocks", Swedish Detonic Res. Foundation Rept., DS, P10, Stockholm, Sweden, 1980c.

Paterson, M. S., 1978. Experimental Rock Deformation - the brittle field, Springer – Verlag Berlin . Heidelberg, ISBN 3-540-08835-0, 254p.

Paul, B., 1960. "Prediction of Elastic Constants of Multiphase Materials", Trans. A. I. M. E., Vol. 218, 1960, pp. 36-41.

Perkins, T. M. and Krech, W. W., 1966. "Effect of Cleavage Rate and Stress Level on Apparent Surface Energies for Rock", Soc. Pet. Eng. J., pp. 308–314.

Popelar, C. H., 1980. "A Model for Dynamic Crack Propagation in a Double-Torsion Fracture Specimen", Crack Arrest Methodology and Applications, ASTM STP 711, G. T. Hahn and M. F. Kanninen, Eds., American Society for Testing and Materials, pp 24-37.

Remzi, E. M., Blackburn, W. S. and Hellen, T. K., 1990. "Automatic Growth of Planar Cracks in Three Dimensional Geometries", Proc. 5th Int. Conf. on Num. Meth. in Frac. Mech., Frieburg.

Rzhevsky, V., and Novik, G., 1971. The Physics of Rocks, MIR Publishers, Moscow.

Sansalone, M., Carino, N. J. and Hsu, N. N., 1987. " Finite Element Studies of Transient Wave Propagation", Review of Progress in Quantitative Nondestructive Evaluation, Vol. 6 A, pp. 125-134.

Schmidt, R. A., 1976. " Fracture Toughness Testing of Limestone", Expl. Mech., 16, 161-167.

Schardin, H., 1959. "Velocity Effects in Fracture", Fracture (B. L. Averbach et. al., Eds.), Wiley, N. Y., pp. 297-329.

Sedgwick, A., 1835. "Remarks on the Structure of Large Mineral Masses, and Especially on the Chemical Changes Produced in the Aggregation of Stratified Rocks During Different periods After Their Deposition", Trans. Geol. Soc. Lond., 2nd Ser., Vol. 3, pp. 461-486.

Sharpe, D., 1849. " On Slaty Cleavage", Q. J. Geol. Soc. Lond., Vol. 5, pp. 111-115.

Sharpe, D., 1847. " On Slaty Cleavage", Q. J. Geol. Soc. Lond., Vol. 3, pp. 74-104.

Shephard, M. S., Yehia, N. A. B., Burd, G. S. and Weidner, T. J., 1985. "Automatic Crack Propagation Tracking", Comp. Struc., **20**, pp. 211-223.

Shih, C. F., Moran, B. and Nakamura, T., 1986. "Energy Release Rate Along a Three-dimensional Crack Front in a Thermally Stressed Body", International Journal of Fracture, Vol. 30, pp. 79-102.

Shi, G. C., Ravera, R. S. and Embley, G. T., 1972. "Impact Response of a Finite Crack in Plane Extension", International Journal of Solids and Structures, 8, pp. 977-993.

Sih, G. C. (ed), 1977. Mechanics of Fracture, Vol. 4, Elastodynamic Crack Problems, Noordhoff Int. Publ., The Netherlands.

Sih, G. C. and Chen, E. P., 1972. "Crack Propagating in a Strip of Material Under Plane Extension", International Journal of Engineering Sciences, 10, 537-551

Sih, G. C., 1970. "Dynamic Aspects of Crack Propagation, in Inelastic Behavior of Solids", (eds M. F. Kenninen, W. F. Adler, A. R. Rosenfield and R. I. Jaffee), McGraw-Hill, pp. 607-639.

Singh, M. M., 1970. "Rock Breakage by High-Speed Impact", Proceedings of the Second Congress of the International Society for Rock Mechanics, Beograd, Vol. III - Themes 5–8.

Solenhofen, Archae, January 11, 2003. http://www.geocities.com/unforbidden_geology/rock_properties.htm

Sorby, H.C., 1853., " On the Origin of Slaty Cleavage", New Philos. J . (Edinb.), Vol. 55, pp. 137-148.

Sorby, H.C., 1856a., " On the Theory of the Origin of Slaty Cleavage", Philos. Mag., Vol. 12, pp. 129-129.

Srawley, J. E. and Gross, B., 1976. "Side-Cracked Plates Subjected to Combined Direct and Bending Forces", Cracks and Fractures, ASTM STP 601, pp. 559-579

Sun, C. T. and Jih, C. J., 1995. "Quasi-Static Modeling of Delamination Crack Propagation in Laminates Subjected to Low-Velocity Impact", Composites Science and Technology, Vol. 54, pp. 185-191.

Sun, C. T. and Potti, S. V., 1996. "A Simple Model to Predict Residual Velocities of Thick Composite Laminates Subjected to High Velocity Impact", International Journal of Impact Engineering, Vol. 18, No. 3, pp. 339-353.

Sun, C. T. and Han, C., 2001. "Dynamic Mode I Fracture Toughness Test of Composites Using a Kolsky Bar", Proceedings of 2001 ASME International Mechanical Engineering Congress and Exposition, New York, AMD-Vol. 247, pp. 41-53.

Sutherland, R. B., 1963. "Some Dynamic and Static Properties of Rocks", Fifth Symposium on Rock Mechanics, University of Minnesota, pp. 473-491.

Tedesco, J. W., Hayes, J. R. and Landis, D. W., 1987. "Dynamic Response of Layered Structures Subject to Blast effects of Non-nuclear Weaponry", Computer & Structures, Vol. 26, No. 1/2, pp. 79-86.

Timbrell, C., Claydon, P. and Cook, G., 1994. "Application of ABAQUS to Analysis of 3D Cracks and Fatigue Crack Growth Prediction", ABAQUS User' Conference, Rhode Island, U. S. A.

Tsai, Y. M., 1973. "Propagation of a Brittle Crack at Constant and Accelerating Speeds", International Journal of Solids and Structures, 9, pp. 625-642.

United Kingdom Production of Minerals, 1997 – 2003, http://www.defra.gov.uk/ Environment /statistics/index.htm

Vutukuri, V. S., Lama, R. D. and Saluja, S. S., 1974. Handbook on Mechanical Properties of Rocks, Trans Tech Publications, Vol. 1, 280p.

Weber, P., 1971. "The Finite Element Method, Applied to Fracture Mechanics", Rock Fracture, Symp. Int'l. Soc. Rock Mech., Nancy paper II-7.

Weibull, W. U., 1939. "A Statistical Theory of Strength of Materials", Ing. Vetenskaps. Akad. Handl. 151, pp. 5-44.

White, S. H. and Johnston, D. C., 1981. "A Microstructural and Microchemical Study of Cleavage Lamellae in a Slate", Journal of Structural Geology, Vol. 3, No. 3, pp. 279-290.

White, S. H., and Knipe, R. J., 1978. "Microstructure and Cleavage Development in Selected Slates", Contrib. Mineral. Petrol., Vol. 66, pp. 165-174.

Whittaker, B. N. and Szwilski, A. B., 1973. "Rock Cutting by Impact Action", Int. J. Rock. Mech. Min. Sci. & Geomech. Abstr., Vol.10, pp. 659-671.

Whittaker, B. N. and Frith R. C., 1990. Tunnelling – Design, Stability and Construction, IMM London, 460p.

Whittaker, B. N., Singh, R. N. and Sun, G., 1992. Rock Fracture Mechanics: Principles, Design, and Applications, Elsevier Publication, 570p.

Williams, W. L., 1961. "The Bending Stress Distribution at the Base of a Stationary Crack", Journal of Applied Mechanics, Transaction ASME Series E, Vol. 82, pp. 78-82.

Windes, S. L., 1949. "Physical Properties of Mine Rock", Part I, Bureau of Mines, Report of Investigation 4459, Department of the Interior, United States, 76 pp.

Xia, Y. R., 1988. "Behaviour of a Two-layered Beam Under Impact Loading", International Journal of Impact Engineering, Vol. 7, No. 4, pp. 415-428.

Xia, Y. R. and Ruiz, C., 1989. "Response of Layered Plates to Projectile Impact", Inst. Phys. Conf. Ser. No. 102: Session 11, Paper presented at Int. Conf. Mech. Prop. Materials at High Rates of Strain, Oxford, pp. 573-580.

Yanng, W., Suo, Z., and Shih, S. F., 1991. "Mechanics of Dynamic Debonding", Proc. R. Soc., Lond. A, 443, pp. 679–697.

Younathan, Y. Y., 1970. "Dynamic Physical Properties of Rocks: Part II, Experimental Results, Proceedings of the Second Congress of the International Society for Rock Mechanics, Beograd, Vol. 1, pp. 1-26

http://www.gov.nf.ca/mines&en/geosurvey/dimension/dimension.stm Updated: Feb.24, 2005.

http://www.traditionaltimberframe.com, 2005

http://gocanada.about.com/od/mapsnewfoundland/, 2005

http://www.nr.gov.nl.ca/mines&en/geosurvey/dimension/dimension.stm, 2000

http://www.msnucleus.org/membership /html/jh/earth/sedimentary/lesson4/ sedimentary4b.html, 2005

http://www.concretenetwork.com/concrete/demolition/hydraulic_splitter.htm, 2004

http://www.ur.com/files/corp/ catalog/104_rock_powertools.pdf, 2004

http://www.ceejaytool.com/downloads/pdf/sm_hds62.pdf, 2005

http://mathworld.wolfram.com/ContourIntegration.html, Wolfram Research, Inc., 1999-2005, CRC Press LLC.

http://www.stoneworld.com/CDA/ArticleInformation/features/BNP_features_Item/0,4046,63535,00.html, 2005, BNP Media.

http://www.dingo.ws/html/att (cruncher_splitter.htm), 2005

Appendix - A

Slate rock could form vertically or at some inclination (with respect to the horizontal) in nature. Some of geological features of this rock are shown in Figures A1 - A3. Slate extraction procedures from the quarry are also shown in Figures A4 – A5 in addition to different slate tiles manufacturing procedures (Figures A6-I to A6-VII) currently used in Hurleys Slatework Company. Field application of hydraulic fracturing procedures used for breaking a large rock block and concrete wall are also shown in Figures A7-I and A7-II. Hunter saw used for cutting of slate slab is given in Figure A8.

Figure A1: Geology of slate

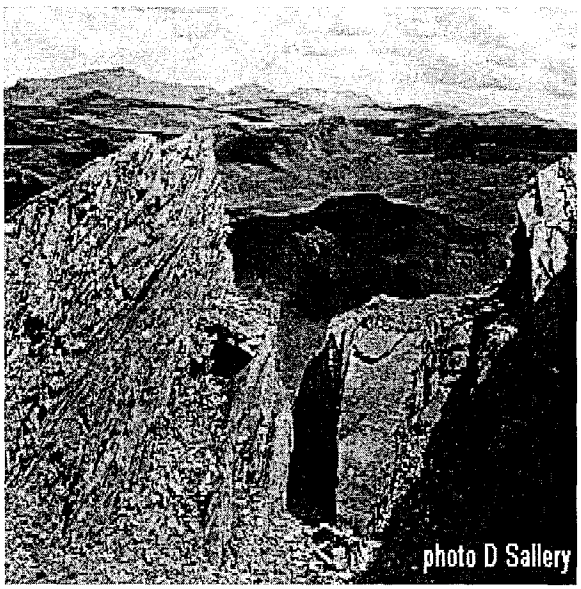

Figure A2: Geology of slate

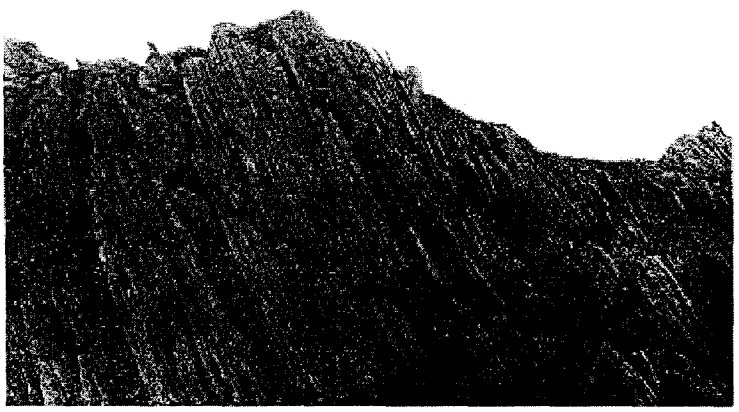

Figure A3: Geology of slate

Figure A4: Open quarry technique

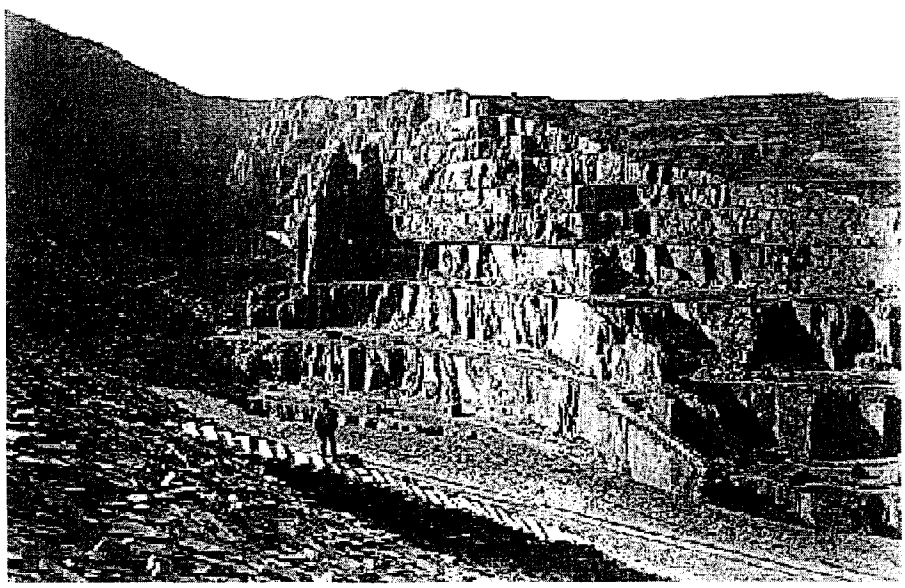

Figure A5: Under ground tunnel to extract slate block

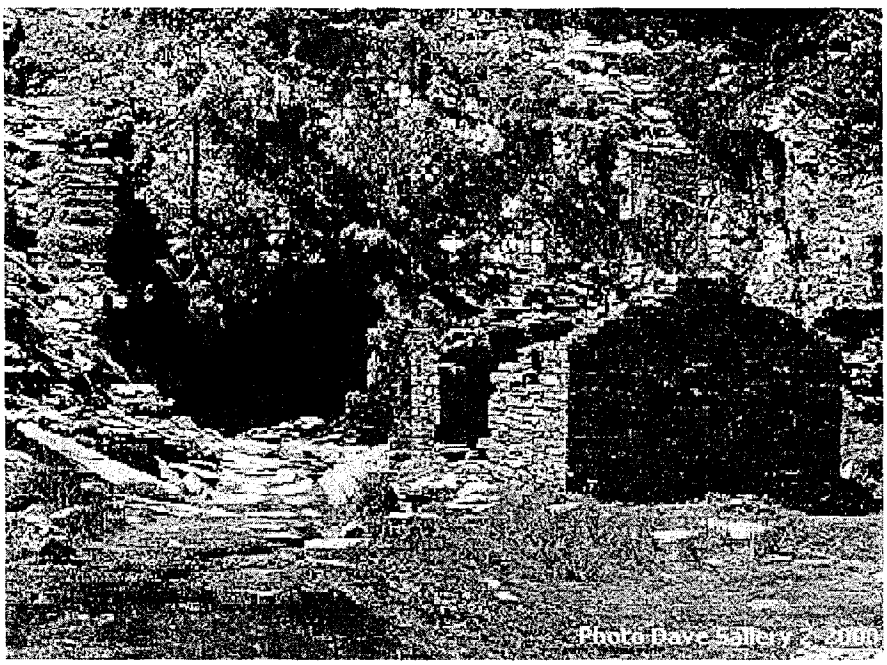

Figure A6-I: Breaking process of the large block of slate

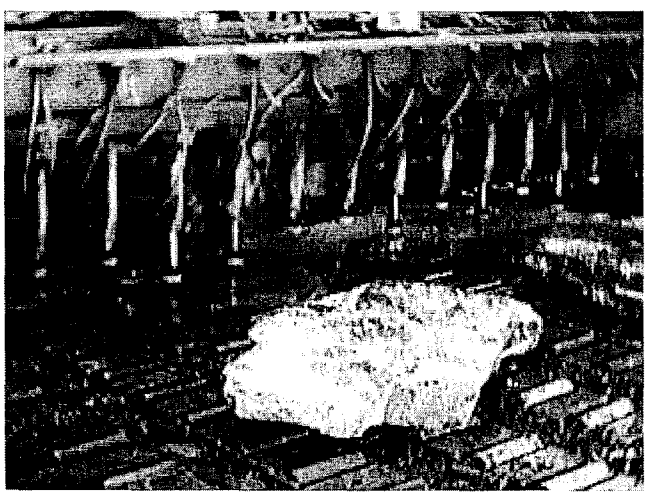

Figure A6-II: Processing for a reducible size of slate block

Figure A6-III: Splitting of slate (manually)

Figure A6-IV: Splitting of slate from thicker piece to a sizable piece along the layer (manually)

Figure A6-V: Splitting of slate according to the requirement of size of tiles (manually)

Figure A6-VI: Trimming of slate tiles

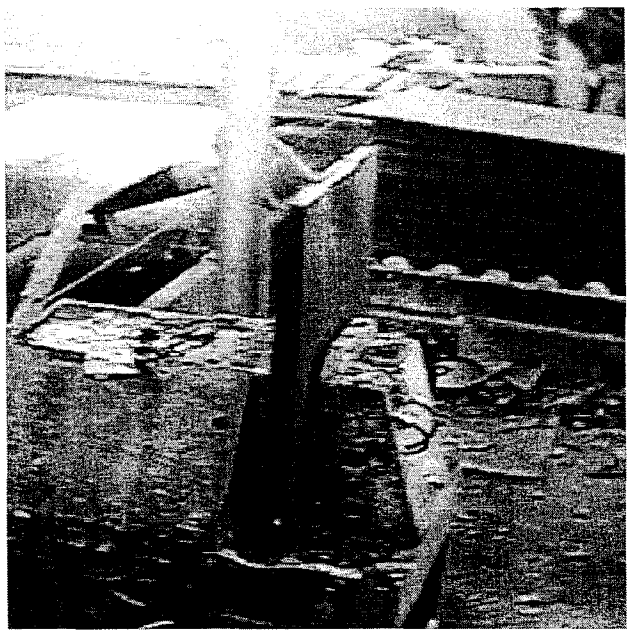

Figure A6-VII: Finished roofing slate tiles

Figure A7-I: Rock mass is split using hydraulic splitter http://www.ur.com/files/corp/catalog/104_rock_powertools.pdf).

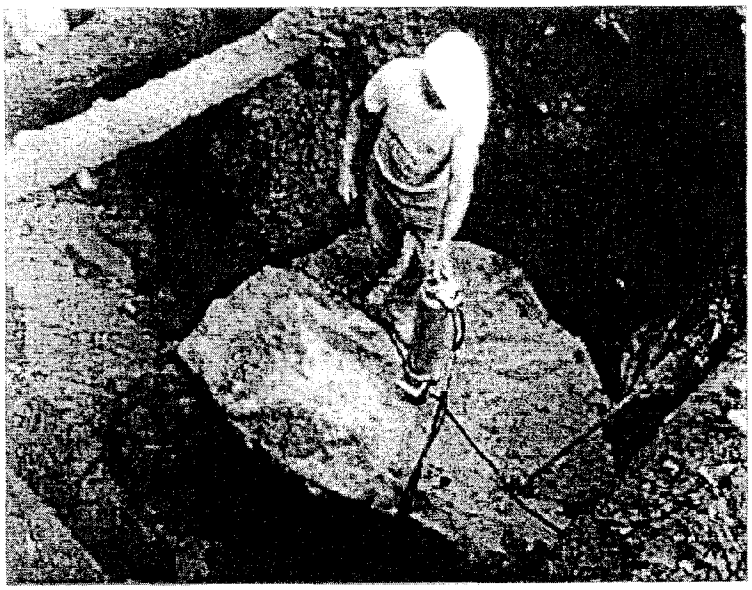

Figure A7-II: Concrete wall is split using hydraulic splitter (http://www.dingo.ws/html/att/cruncher_splitter.htm)

Figure A8: Hunter saw used for slate rock cutting

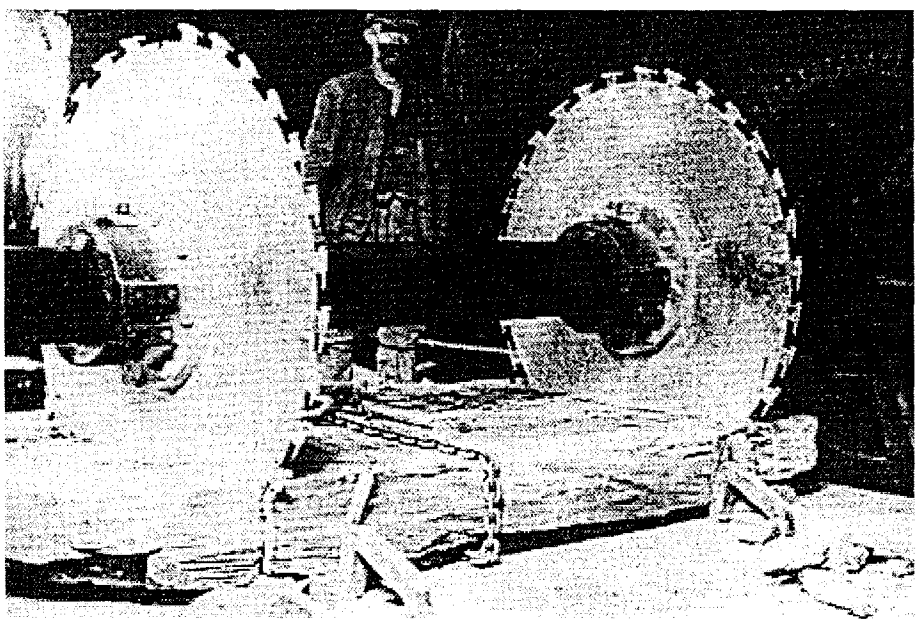

Appendix B

Constitutive relationships of isotropic, transversely isotropic and orthotropic materials are given in sections I, II and III for plane stress, plane strain and 3D dimensional cases.

I. Isotropic material

i. Plane stress formulation

$$\begin{Bmatrix}\sigma_x\\ \sigma_y\\ \sigma_{xy}\end{Bmatrix}=\frac{E}{(1-\nu^2)}\begin{bmatrix}1 & \nu & 0\\ \nu & & 0\\ 0 & 0 & \dfrac{1-\nu}{2}\end{bmatrix}\begin{Bmatrix}\varepsilon_x\\ \varepsilon_y\\ \gamma_{xy}\end{Bmatrix} \qquad \text{B-1}$$

ii. Plane strain formulation

$$\begin{Bmatrix}\sigma_x\\ \sigma_y\\ \sigma_{xy}\end{Bmatrix}=\frac{E}{(1+\nu)(1-2\nu)}\begin{bmatrix}(1-\nu) & \nu & 0\\ \nu & (1-\nu) & 0\\ 0 & 0 & \dfrac{(1-2\nu)}{2}\end{bmatrix}\begin{Bmatrix}\varepsilon_x\\ \varepsilon_y\\ \gamma_{xy}\end{Bmatrix} \qquad \text{B-2}$$

and, $\sigma_z=\nu(\sigma_x+\sigma_y)$

iii. Three dimensional formulation

$$[D]=\frac{E}{(1+\nu)(1-2\nu)}\begin{bmatrix}1-\nu & \nu & \nu & 0 & 0 & 0\\ & 1-\nu & \nu & 0 & 0 & 0\\ & & 1-\nu & 0 & 0 & 0\\ & & & \dfrac{1-2\nu}{2} & 0 & 0\\ & & & & \dfrac{1-2\nu}{2} & 0\\ \textit{Symmetry} & & & & & \dfrac{1-2\nu}{2}\end{bmatrix} \qquad \text{B-3}$$

II. Transversely Isotropic material

i. Plane stress formulation

$$[D]=\begin{bmatrix} \dfrac{E_x}{1-\nu_{xy}\nu_{yx}} & \dfrac{\nu_{xy}E_y}{1-\nu_{xy}\nu_{yx}} & 0 \\ \dfrac{\nu_{yx}E_x}{1-\nu_{xy}\nu_{yx}} & \dfrac{E_y}{1-\nu_{xy}\nu_{yx}} & 0 \\ 0 & 0 & G_{12} \end{bmatrix} \tag{B-4}$$

ii. Plane strain formulation

$$[D]=\frac{1}{Z(\nu_{xy}+\nu_{zy}\nu_{xz})}\begin{bmatrix} \dfrac{E_x(1-\nu_{zy}\nu_{yz})}{(1-\nu_{zx}\nu_{xz})} & \dfrac{E_x(\nu_{yx}+\nu_{zx}\nu_{yz})}{(1-\nu_{zx}\nu_{xz})} & 0 \\ \dfrac{E_p(\nu_{xy}+\nu_{zy}\nu_{xz})}{1-\nu_{zx}\nu_{xz}} & E_p & 0 \\ 0 & 0 & G_{xy}Z(\nu_{xy}+\nu_{zy}\nu_{xz}) \end{bmatrix} \tag{B-5}$$

where,

$$Z=\frac{1-\nu_{zx}\nu_{xz}-\nu_{zy}\nu_{yz}-\nu_{xy}\nu_{yx}-\nu_{yx}\nu_{zy}\nu_{xz}-\nu_{xy}\nu_{zx}\nu_{yz}}{(\nu_{xy}+\nu_{zy}\nu_{xz})(1-\nu_{zx}\nu_{xz})},\quad E_y=E_z=E_p$$

iii. Three dimensional formulation

$$[D]=\begin{bmatrix} \dfrac{1-\nu_{\alpha z}\nu_{z\alpha}}{E_\alpha E_z\nabla} & \dfrac{\nu_\alpha+\nu_{z\alpha}\nu_{\alpha z}}{E_\alpha E_z\nabla} & \dfrac{\nu_{z\alpha}-\nu_\alpha\nu_{z\alpha}}{E_\alpha E_z\nabla} & 0 & 0 & 0 \\ \dfrac{\nu_\alpha+\nu_{\alpha z}\nu_{z\alpha}}{E_z E_\alpha\nabla} & \dfrac{1-\nu_{z\alpha}\nu_{\alpha z}}{E_z E_\alpha\nabla} & \dfrac{\nu_{z\alpha}+\nu_{z\alpha}\nu_\alpha}{E_z E_\alpha\nabla} & 0 & 0 & 0 \\ \dfrac{\nu_{\alpha z}+\nu_\alpha\nu_{\alpha z}}{E_\alpha^2\nabla} & \dfrac{\nu_{\alpha z}(1+\nu_\alpha)}{E_\alpha^2\nabla} & \dfrac{1-\nu_\alpha^2}{E_\alpha^2\nabla} & 0 & 0 & 0 \\ 0 & 0 & 0 & G_{z\alpha} & 0 & 0 \\ 0 & 0 & 0 & 0 & G_{z\alpha} & 0 \\ 0 & 0 & 0 & 0 & 0 & \dfrac{E_\alpha}{2(1+\nu_\alpha)} \end{bmatrix} \tag{B-6}$$

where,

$$\nabla = \frac{(1-\nu_\alpha)(1-\nu_\alpha - 2\nu_{\alpha z}\nu_{z\alpha})}{E_\alpha^2 E_z} \text{ and for symmetric matrix requirement,}$$

$$\frac{\nu_\alpha + \nu_{z\alpha}\nu_{\alpha z}}{E_\alpha E_z \nabla} = \frac{\nu_\alpha + \nu_{\alpha z}\nu_{z\alpha}}{E_z E_\alpha \nabla}$$

$$\frac{\nu_{z\alpha} + \nu_{z\alpha}\nu_\alpha}{E_z E_\alpha \nabla} = \frac{\nu_{\alpha z}(1+\nu_z)}{E_\alpha^2 \nabla}$$

$$\frac{\nu_{z\alpha} + \nu_\alpha \nu_{z\alpha}}{E_\alpha E_z \nabla} = \frac{\nu_{\alpha z} + \nu_\alpha \nu_{\alpha z}}{E_\alpha^2 \nabla}$$

where, E_α and ν_α are the symmetry plane (x, y) Young's modulus and Poisson's ratio and $E_{\alpha z}$ and $\nu_{z\alpha}$ are the Young's modulus and Poisson's ratio in the z direction, $G_{z\alpha}$ is the shear modulus in the z-direction.

III. Orthotropic material

Three dimensional formulation

$$[D] = \begin{bmatrix} \frac{1-\nu_{yz}\nu_{zy}}{E_y E_z \nabla} & \frac{\nu_{yx}+\nu_{yz}\nu_{zx}}{E_y E_z \nabla} & \frac{\nu_{zx}+\nu_{yx}\nu_{zy}}{E_y E_z \nabla} & 0 & 0 & 0 \\ \frac{\nu_{yx}+\nu_{yz}\nu_{zx}}{E_y E_z \nabla} & \frac{1-\nu_{xz}\nu_{zx}}{E_x E_z \nabla} & \frac{\nu_{zy}+\nu_{xy}\nu_{zx}}{E_x E_z \nabla} & 0 & 0 & 0 \\ \frac{\nu_{zx}+\nu_{yx}\nu_{zy}}{E_y E_z \nabla} & \frac{\nu_{zy}+\nu_{xy}\nu_{zx}}{E_x E_z \nabla} & \frac{1-\nu_{xy}\nu_{yx}}{E_x E_y \nabla} & 0 & 0 & 0 \\ 0 & 0 & 0 & G_{yz} & 0 & 0 \\ 0 & 0 & 0 & 0 & G_{xz} & 0 \\ 0 & 0 & 0 & 0 & 0 & G_{xy} \end{bmatrix} \quad \text{(B-7)}$$

where,

$$\nabla = \frac{\left(1 - \nu_{xy}\nu_{yx} - \nu_{yz}\nu_{zy} - \nu_{xz}\nu_{zx} - 2\nu_{yx}\nu_{zy}\nu_{xz}\right)}{E_x E_y E_z}$$

$$\frac{\nu_{yx} + \nu_{zx}\nu_{yz}}{E_y E_z \nabla} = \frac{\nu_{xy} + \nu_{xz}\nu_{zx}}{E_z E_x \nabla}$$

$$\frac{\nu_{zy} + \nu_{zx}\nu_{xy}}{E_z E_x \nabla} = \frac{\nu_{zy} + \nu_{xz}\nu_{yz}}{E_x E_y \nabla}$$

$$\frac{\nu_{zx} + \nu_{yx}\nu_{yz}}{E_y E_z \nabla} = \frac{\nu_{xz} + \nu_{xy}\nu_{yz}}{E_x E_y \nabla}$$

Appendix - C

Variation of stress vs. strain obtained during the carrying out of laboratory tests for modulus of elasticity and Poisson's are shown in Figures C1 - C4. Load variations with respect to crack mouth opening displacement and back face strain are shown in Figures C5 – C10. Variation of impact splitting force with respect to time, during the splitting of different sizes of plane strain and non-plane slate blocks using indenting wedge, are shown in Figures from C-11 to C-20. Crack propagation velocities determined for different sized slate blocks is shown in Figures C12-C25 and Tables C-1 to C-5.

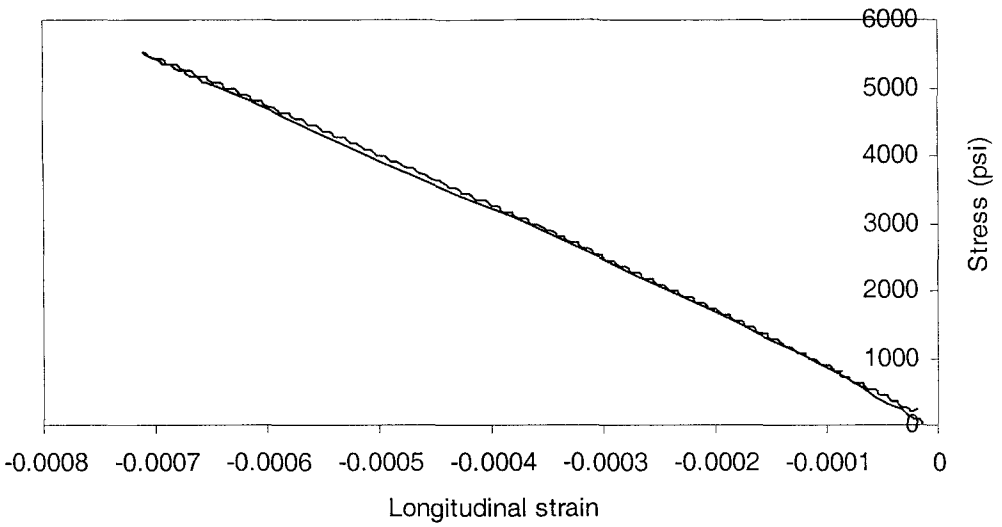

Figure C-1: Variation of stress vs. longitudinal strain up to ultimate failure under compressive load applied parallel to the layering on a test specimen (used in determination of Young's modulus of elasticity and Poisson's ratio).

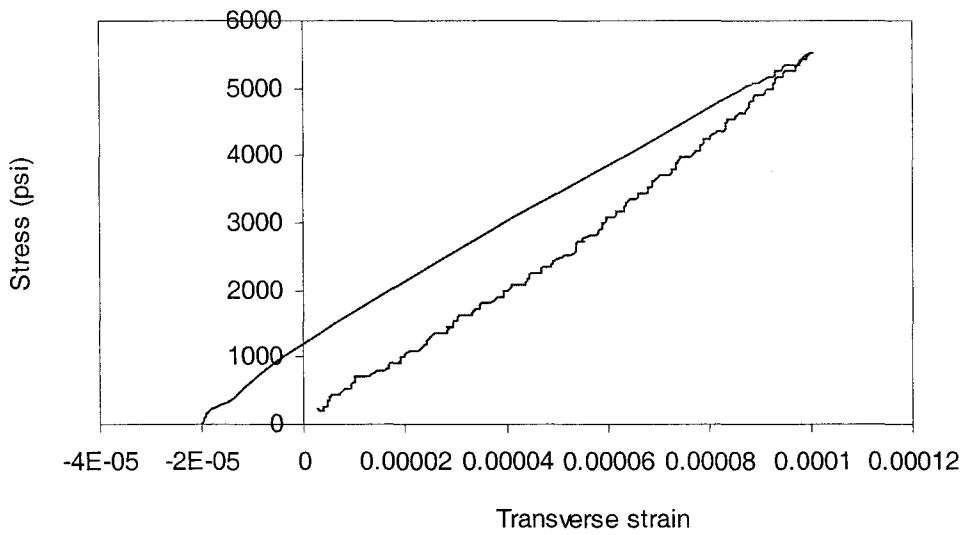

Figure C-2: Variation of stress vs. transverse strain up to ultimate failure under compressive load applied parallel to the layering on a test specimen (used in determination of Young's modulus of elasticity and Poisson's ratio).

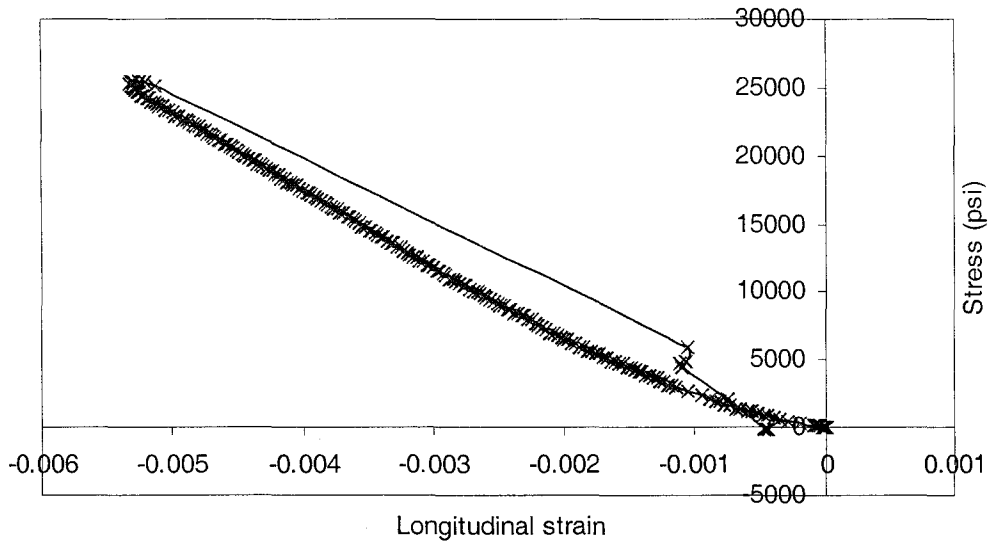

Figure C-3: Variation of stress vs. longitudinal strain up to ultimate failure under compressive load applied perpendicular to the layering on a test specimen (used in determination of Young's modulus of elasticity and Poisson's ratio).

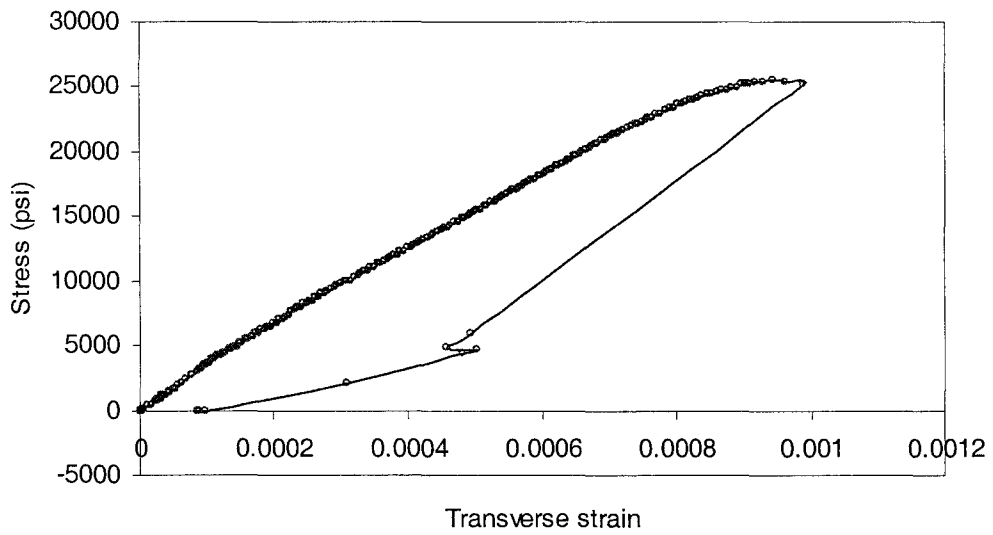

Figure C-4: Variation of stress vs. transverse strain up to ultimate failure under compressive load applied perpendicular to the layering on a test specimen (used in determination of Young's modulus of elasticity and Poisson's ratio).

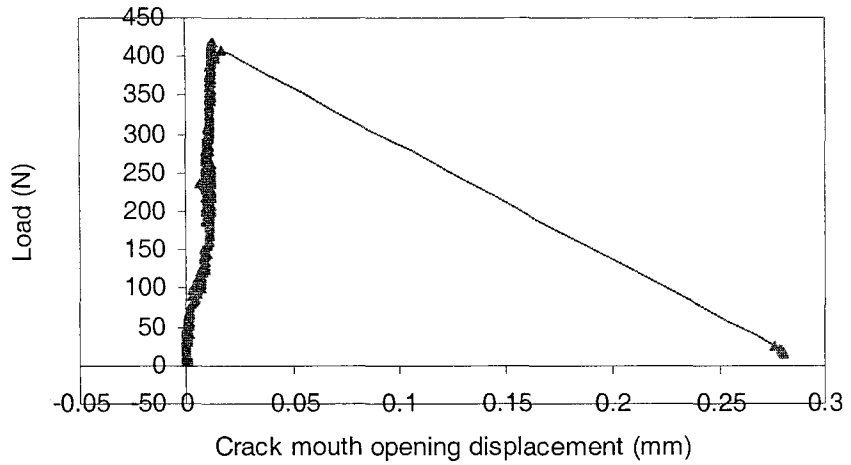

Figure C-5: Variation of load with CMOD (crack mouth opening displacement) up to ultimate failure under 3PB (three-point-bending) fracture toughness test of cylindrical specimen. Load is applied parallel to the layering. (d = 1.375″, a = 0.500″, a/d = 0.364)

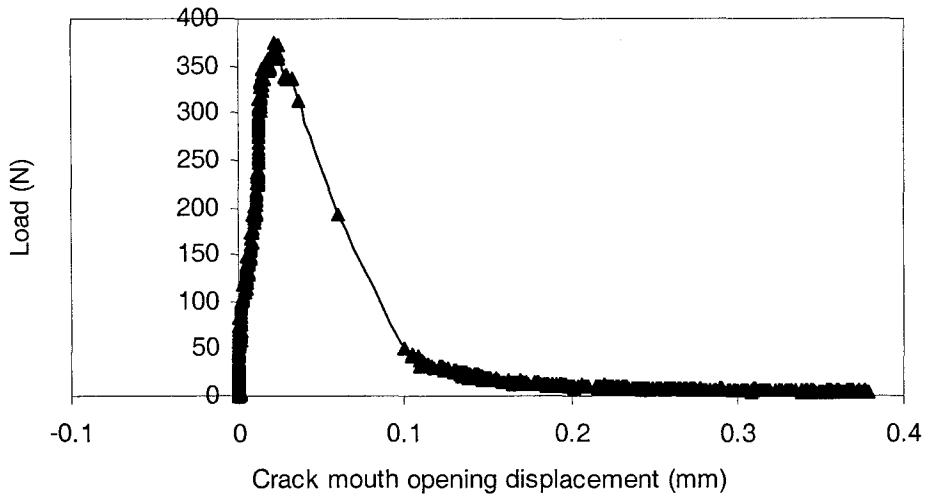

Figure C-6: Variation of load with CMOD (crack mouth opening displacement) up to ultimate failure under 3PB (three-point-bending) fracture toughness test of cylindrical specimen. Load is applied parallel to the layering. (d = 1.375″, a = 0.563″, a/d = 0.410)

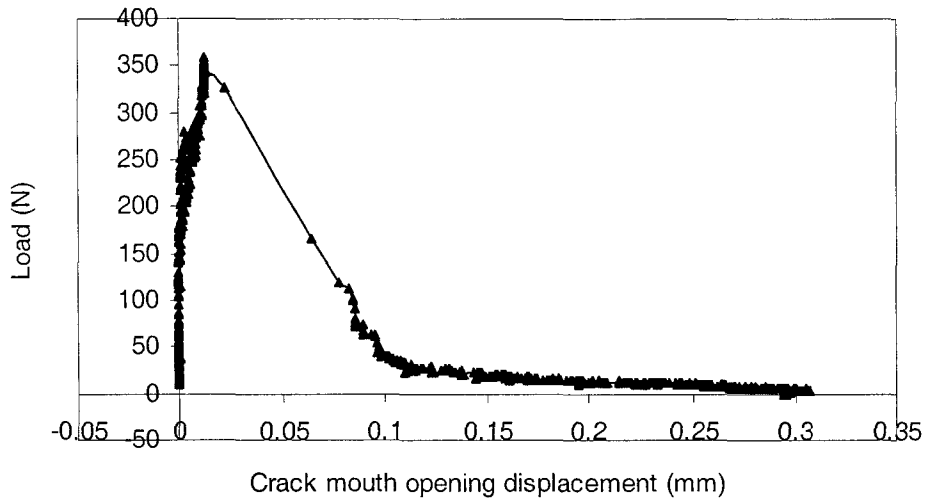

Figure C-7: Variation of load with CMOD (crack mouth opening displacement) up to ultimate failure under 3PB (three-point-bending) fracture toughness test of cylindrical specimen. Load is applied parallel to the layering. (d = 1.375″, a = 0.516″, a/d = 0.375)

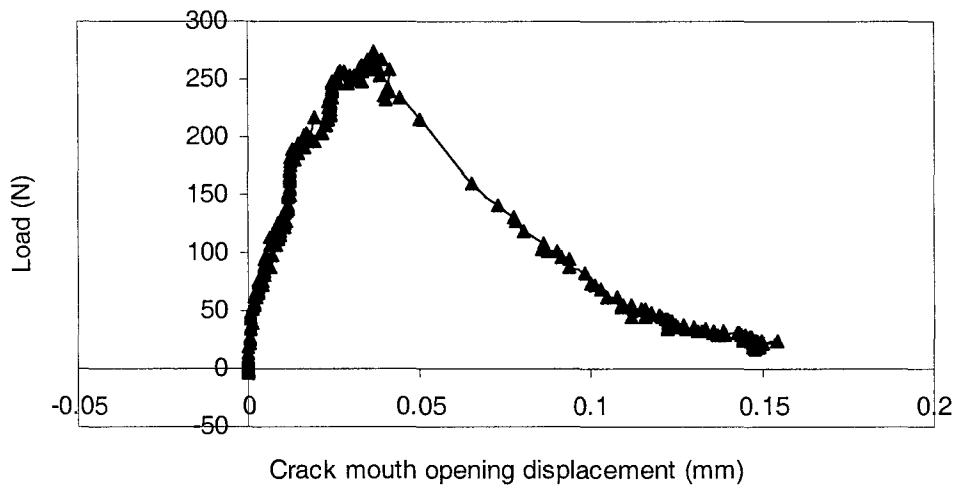

Figure C-8: Variation of load with CMOD (crack mouth opening displacement) up to ultimate failure under 3PB (three-point-bending) fracture toughness test of cylindrical specimen. Load is applied parallel to the layering. (d = 1.375″, a = 0.641″, a/d = 0.466)

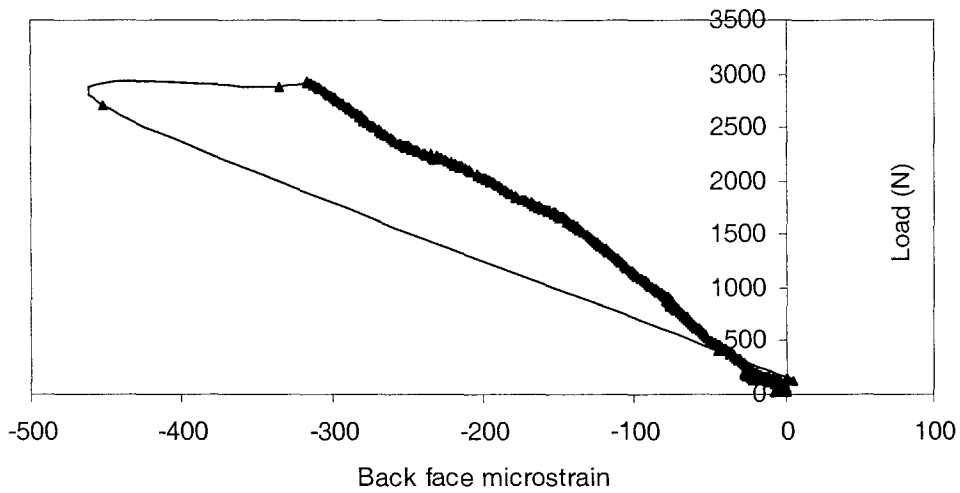

Figure C-9: Variation of load with back face strain up to ultimate failure under 4PB (four-point-bending) fracture toughness test of rectangular specimen. Load is applied perpendicular to the layering. (t = 1.47″, a = 0.672″, a/t = 0.457)

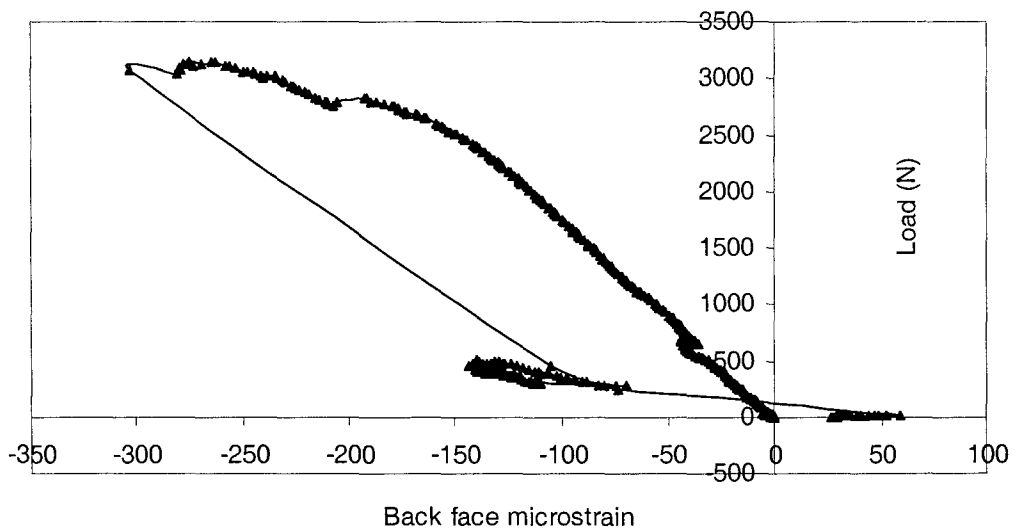

Figure C-10: Variation of load with back face strain up to ultimate failure under 4PB (four-point-bending) fracture toughness test of rectangular specimen. Load is applied perpendicular to the layering. (t = 1.47″, a = 0.656″, a/t = 0.447)

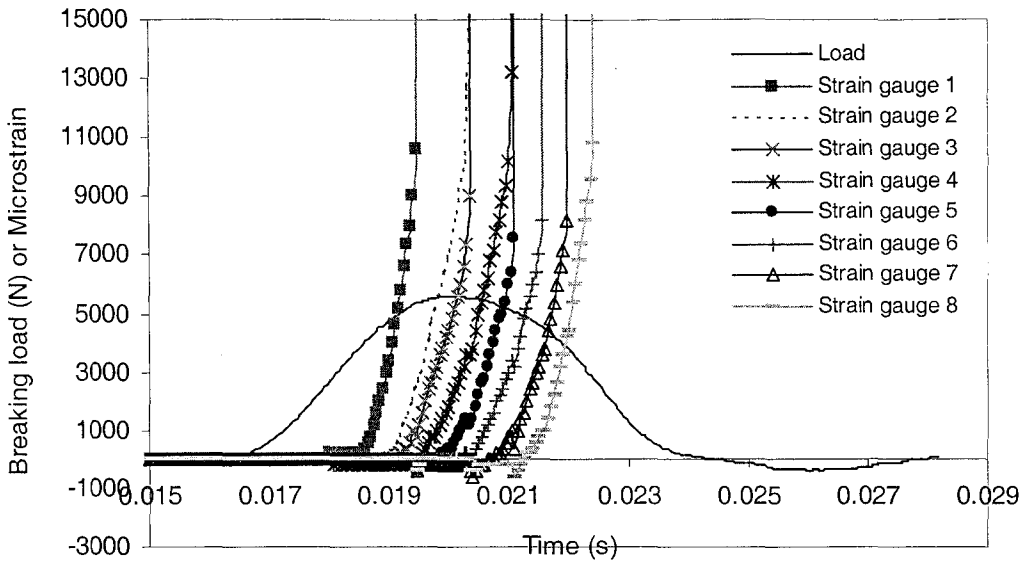

Figure C-11: Variation of breaking load or microstrain with respect to time during impact splitting of slate block having dimensions, L = 4.33 inch, W = 4.0 inch and H = 5.12 inch. (Wedge length, L_1 = 4 inch, clear height between wedge and specimen before hit = 1.5 inch, wedge penetration depth = 0.394 inch).

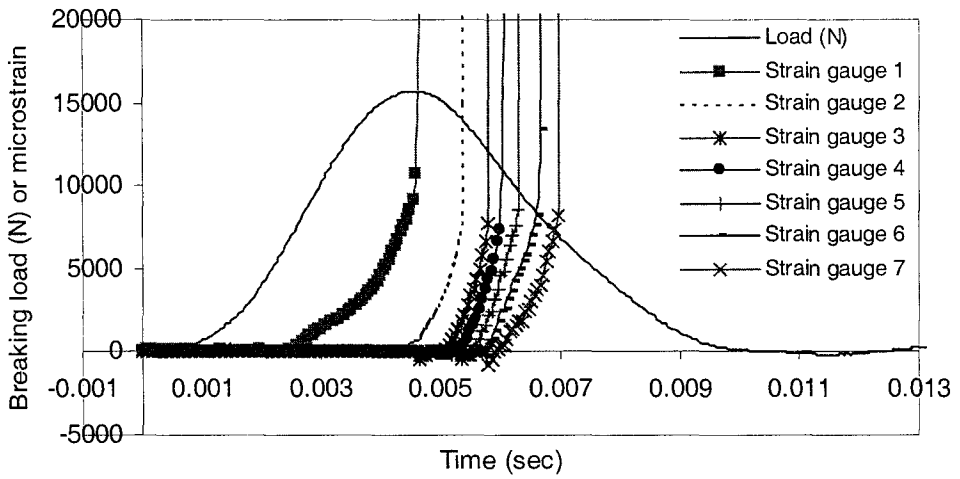

Figure C-12: Variation of breaking load or microstrain with respect to time during impact splitting of slate block having dimensions, L = 5 inch, H = 6 inch and W = 6.18 inch. (Wedge length, L_1 = 4 inch, clear height between wedge and specimen before hit = 1.5 inch, wedge penetration depth = 0.394 inch)

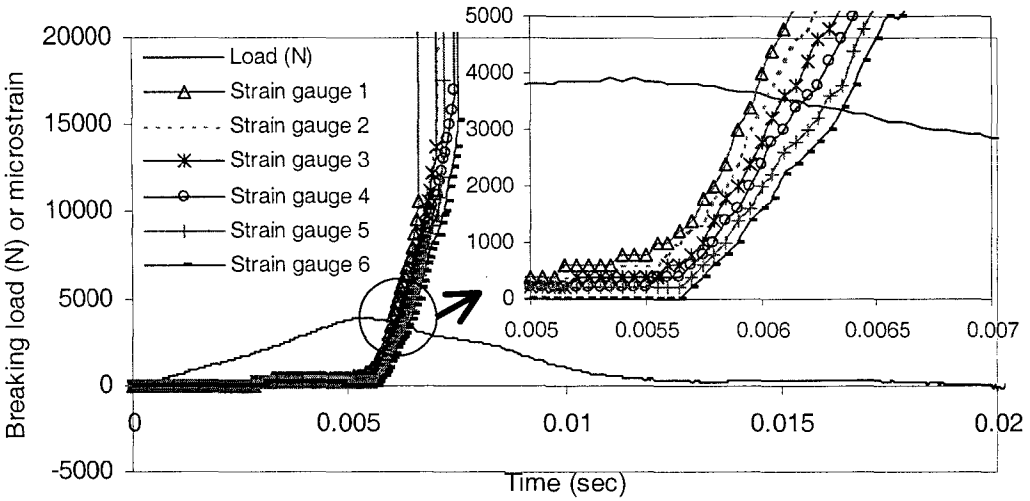

Figure C-13: Variation of breaking load or microstrain with respect to time during impact splitting of slate block having dimensions, L = 4.25 inch, H = 6.45 inch and W = 5.9 inch. (Wedge length, L_1 = 4 inch, clear height between wedge and specimen before hit = 1.5 inch, wedge penetration depth = 0.394 inch)

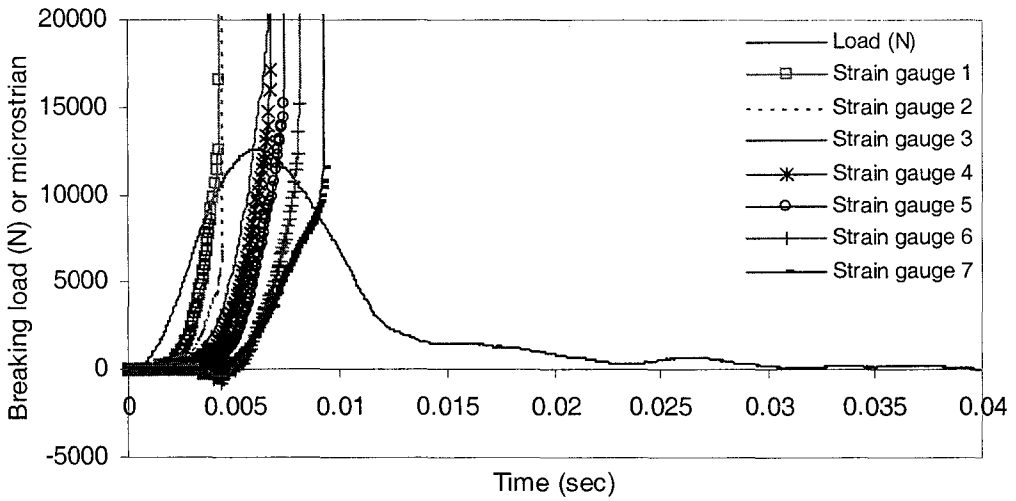

Figure C-14: Variation of breaking load or microstrain with respect to time during impact splitting of slate block having dimensions, L = 13.125 inch, H = 10.0 inch and W = 5.8125 inch. (Wedge length, L_1 = 4 inch, clear height between wedge and specimen before hit = 2.36 inch, wedge penetration depth = 0.5 inch).

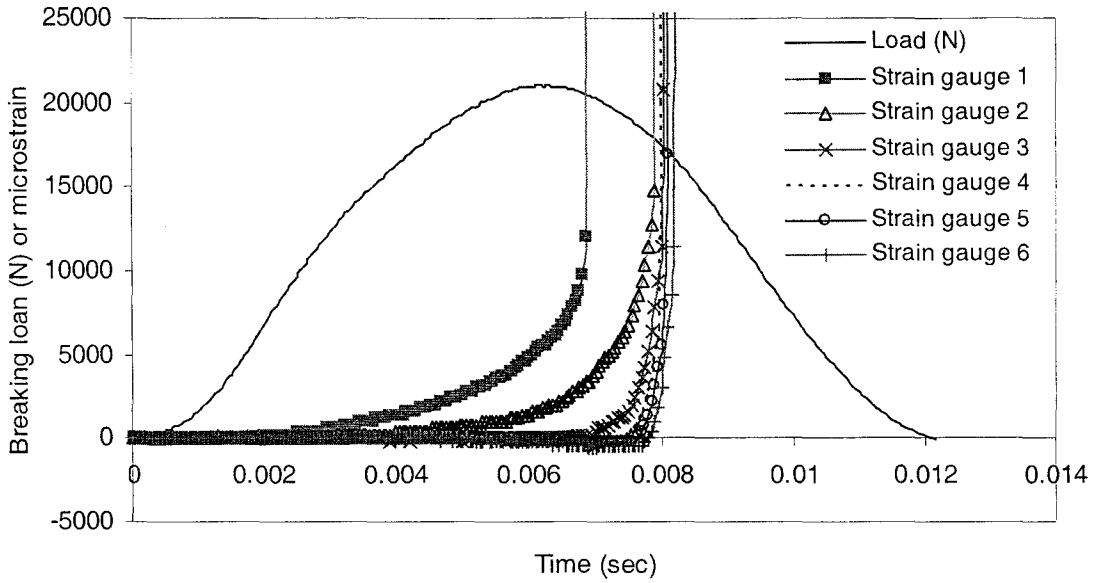

Figure C-15: Variation of breaking load or microstrain with respect to time during impact splitting of slate block having dimensions, L = 10.0 inch, H = 8.0 inch and W = 5.0 inch. (Wedge length, L_1 = 4 inch, clear height between wedge and specimen before hit = 1.97 inch, wedge penetration depth = 0.5 inch).

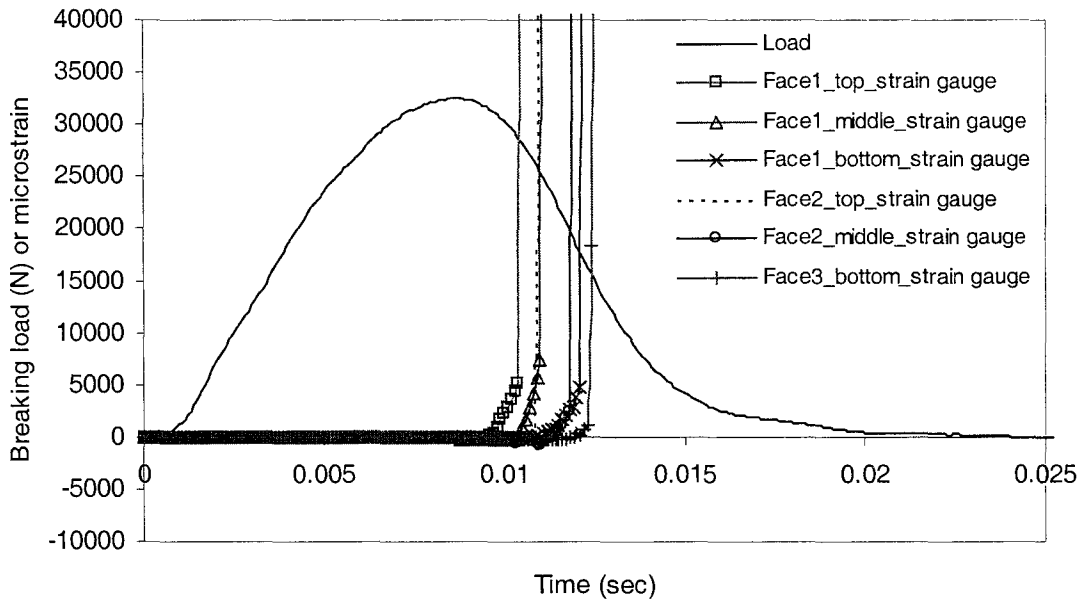

Figure C-16: Variation of breaking load or microstrain with respect to time during impact splitting of slate block having dimensions, L = 13.3125 inch, H = 12.5 inch and W = 3.1 inch. (Wedge length, L_1 = 4 inch, clear height between wedge and specimen before hit = 2.5 inch, wedge penetration depth = 0.5 inch).

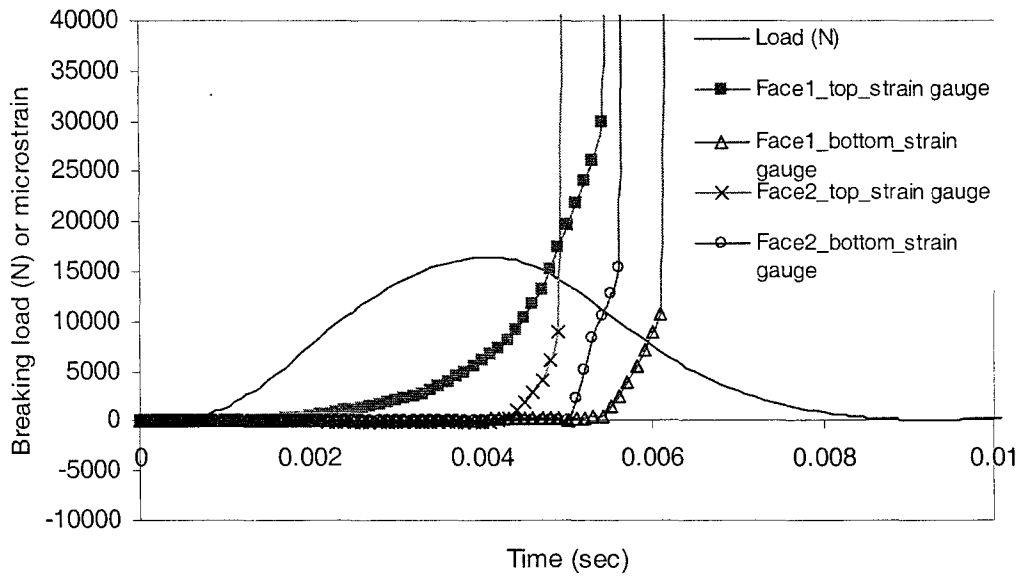

Figure C-17: Variation of breaking load or microstrain with respect to time during impact splitting of slate block having dimensions, L = 9.375 inch, H = 6.75 inch and W = 3.375 inch. (Wedge length, L_1 = 4 inch, clear height between wedge and specimen before hit = 2.5 inch, wedge penetration depth = 0.5 inch).

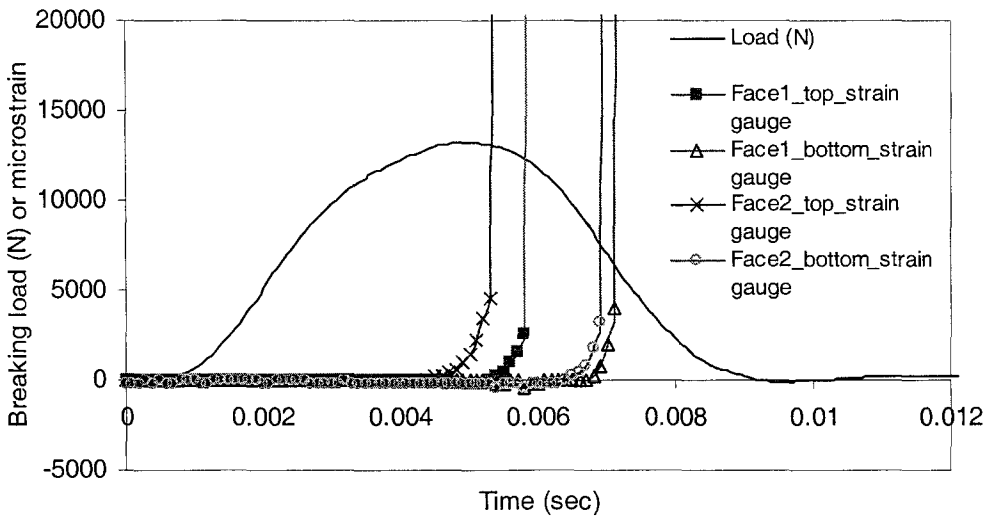

Figure C-18: Variation of breaking load or microstrain with respect to time during impact splitting of slate block having dimensions, L = 8.8125 inch, H = 9.625 inch and W = 2.375 inch. (Wedge length, L_1 = 4 inch, clear height between wedge and specimen before hit = 2.5 inch, wedge penetration depth = 0.5 inch).

Figure C-22

Figure C-22: Crack propagation velocity during impact splitting of slate blocks

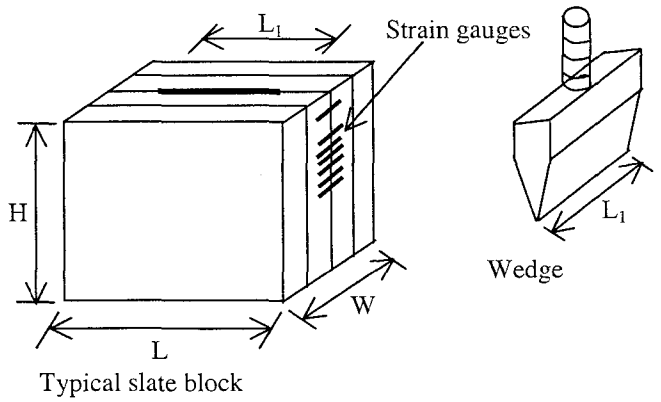

Specimen dimensions, L = 4.25 inch, W = 5.9 inch and H = 6.45 inch, Wedge length, L_1 = 4 inch, clear height between wedge and specimen = 1.5 inch, wedge penetration depth = 0.394 inch.

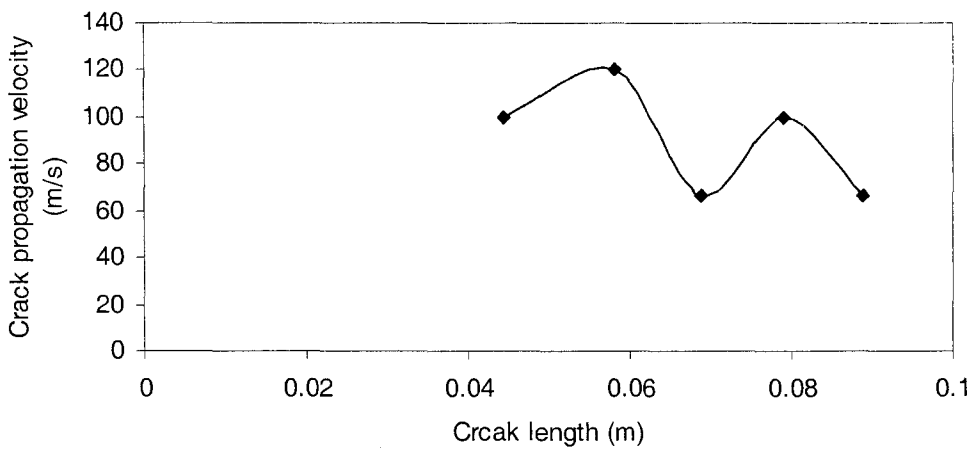

Table C-2: Crack propagation velocity during impact splitting of slate blocks

Crack length (m)	Crack velocity (m/s)	Average velocity (m/s)
0.0445	100	
0.058	120	
0.069	66.67	90.67
0.079	100	
0.089	66.67	

Figure C-23: Crack propagation velocity during impact splitting of slate blocks

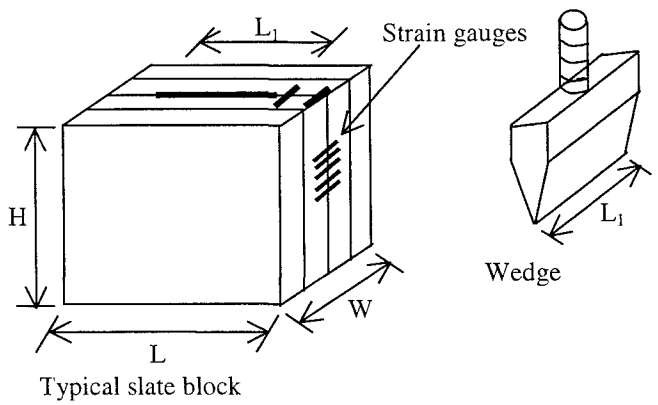

Specimen dimensions, L = 12.0 inch, W = 6.0 inch and H = 10.0 inch, Wedge length, L_1 = 4 inch, clear height between wedge and specimen = 2.0 inch, wedge entered into the specimen = 0.75 inch.

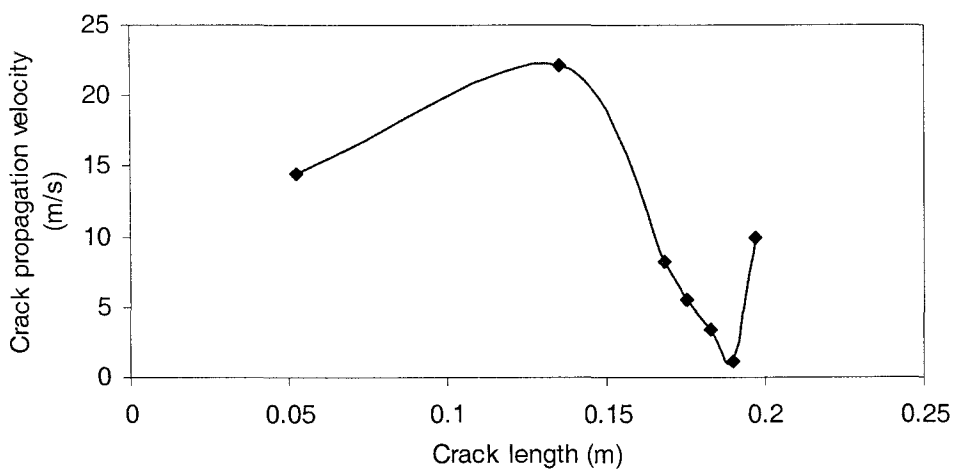

Table C-3: Crack propagation velocity during impact splitting of slate blocks

Crack length (m)	Crack velocity (m/s)	Average velocity (m/s)
0.0525	14.49	
0.1350	22.22	
0.1685	8.24	
0.1755	5.60	9.306
0.1825	3.41	
0.1895	1.18	
0.1965	10.00	

Figure C-24: Crack propagation velocity during impact splitting of slate blocks

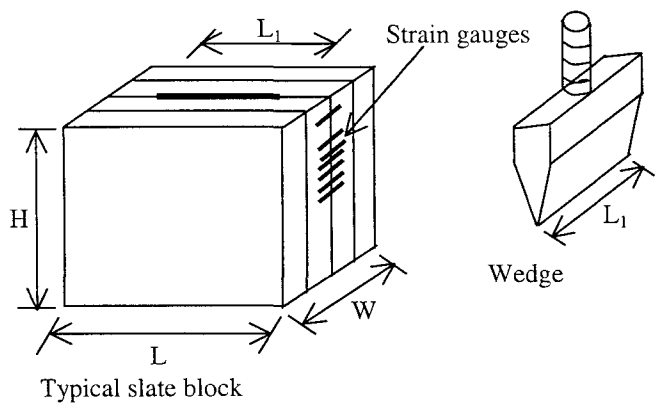

Specimen dimensions, L = 4.4 inch, W = 6.0 inch and H = 6.0 inch, wedge length, L_1 = 4 inch, clear height between wedge and specimen = 1.5 inch, wedge penetration depth = 0.394 inch.

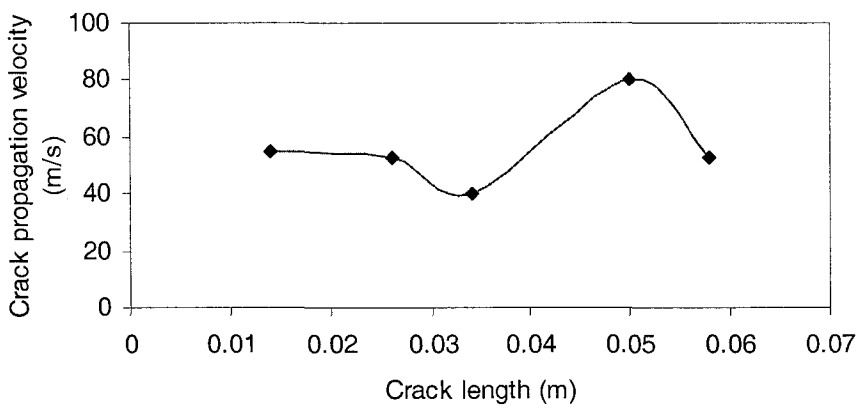

Table C-4: Crack propagation velocity during impact splitting of slate blocks

Crack length (m)	Crack velocity (m/s)	Average velocity (m/s)
0.014	55	
0.026	53	
0.034	40	56.20
0.05	80	
0.058	53	

Figure C-25: Crack propagation velocity during impact splitting of slate blocks

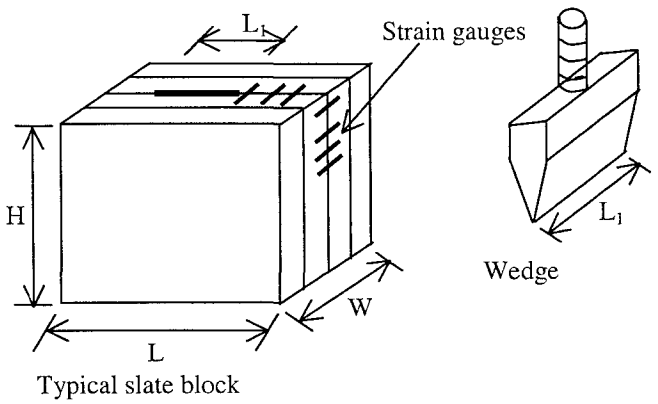

Specimen dimensions, L = 13.125 inch, W = 5.75 inch and H = 10.0 inch, wedge length, L_1 = 4 inch, clear height between wedge and specimen = 1.5 inch, wedge penetration depth = 0.394 inch.

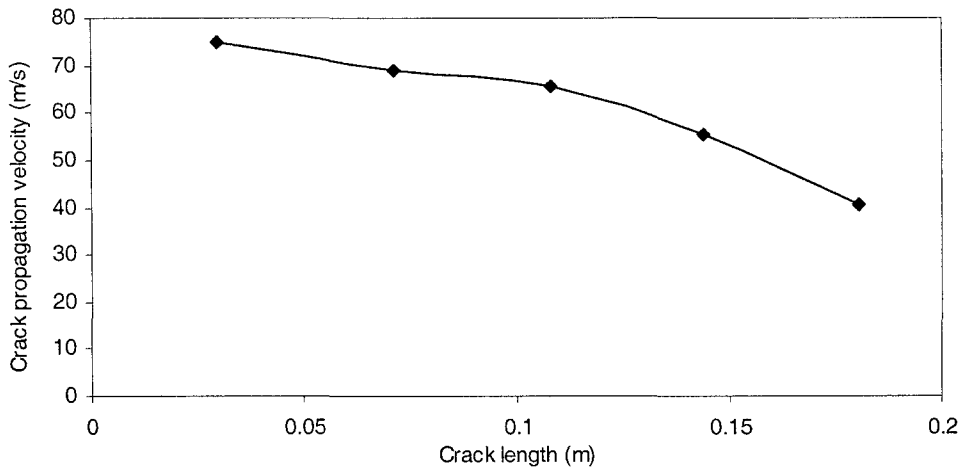

Table C-5: Crack propagation velocity during impact splitting of slate blocks

Crack length (m)	Crack velocity (m/s)	Average velocity (m/s)
0.0295	75	
0.071	69.1	
0.108	65.45	61.104
0.144	55.38	
0.18	40.59	